Controlling purely elastic instabilities

Thesis submitted in accordance with the requirements of
the University of Liverpool for the degree of Doctor in Philosophy
by
Mahdi Davoodi

June 2019

Abstract

In the last twenty-five years, research into the flow of complex viscoelastic fluids has highlighted that, even in the absence of inertial forces (i.e. so called "creeping" flow), instabilities can be observed solely due to the presence of the non-linear elastic forces which are known as "purely-elastic" instabilities (Larson et al., 1990). In fluid mechanics related applications, the presence of these instabilities may be considered beneficial from mixing (Poole et al., 2014b) and heat transfer enhancement (Abed et al., 2017) point of view or an unwanted phenomenon once they appear in rheometry (Fardin et al., 2014). In rheometry, the Taylor-Couette (Fardin et al., 2014) and cross-slot geometries (Haward et al., 2012b) are used frequently to investigate flow behaviour and rheological properties of viscoelastic fluids for shear and elongational or extensional viscosities, respectively. In order to ensure a constant shear rate in the gap between the inner and outer cylinders in the Taylor-Couette geometry or a uniform elongational flow in cross-slot geometries, these measurements are restricted up to a limited deformation rate where such an instability is triggered. In this thesis, using a combination of analytical, numerical and experimental approaches, a series of control mechanisms are introduced and studied that can play an important role in the onset criteria of these instabilities. The Taylor-Couette (TC) geometry is one of the most widely studied geometries in the whole of fluid mechanics. Usually the ratio of the height of the fluid to the distance between the cylinders ("the gap") is made very large such that, in conjunction with this gap being "narrow" with respect to the radii of the two cylinders, a linear velocity distribution is obtained. In this thesis, what happens when this "aspect ratio" (Λ =height/gap) is made finite by the imposition of end walls for viscoelastic fluids is studied. In the narrow-gap inertialess limit, this problem simplifies to planar Couette flow in a rectangular duct and an exact analytical solution to this problem is represented and compared with previously reported Newtonian solution in the literature (Theofilis et al., 2004) and full non-linear simulations using an open source computational fluid dynamics code (OpenFoam). Subsequently a perturbation technique is used to derive an approximate analytical solution for the Oldroyd-B model to show that, for any non-zero value of the Weissenberg number (Wi=(elastic force)/(viscous force)), a steady secondary flow must exist in the TC geometry driven by gradients of normal stresses (in combination with curvature). This, in itself, is an important result

as secondary flows in viscoelastic TC flow have hitherto been associated with the occurrence of purely-elastic instabilities (Larson et al., 1990). Subsequently the accuracy and range of validity of this approximate solution is checked with full non-linear simulations. Finally using novel experiments conducted by Prof. Sandra Lerouge (Université Paris Diderot, France) it is confirmed that the Newtonian flow remains quasilinear but that for elastic Boger fluids a steady secondary flow does indeed appear. These results also show that the aspect ratio can be used to successfully control the onset of the purely-elastic instability.

The cross-slot stagnation point flow is one of the benchmark problems in fluid mechanics as it allows large strains to develop and can therefore be used in extensional rheometry (Haward et al., 2012b). In such a flow, for purely-elastic cases in creeping flow regimes, beyond a critical value of the Weissenberg number, elasticity can break symmetry which is perhaps an unwanted phenomenon if used as a rheometer and will limit the maximum deformation rate in which these tests can be performed, or beneficial once used as mixing device. As a first step, the investigation in this thesis focuses on the effect of elongational dominated flow on the onset criteria of symmetry-breaking purely-elastic instability in the cross-slot geometry by applying a fundamental change on the kinematics of the flowfield in this region. Here, the standard geometry is modified by adding a cylinder at the geometric centre and replacing the free stagnation point by pinned stagnation points at the cylinder walls. These results suggest that in the limit that the cylinder size tends to zero, although the important kinematic properties of the flow has fundamentally changed in the elongational dominated region, the nature of instability remains the same and the onset criteria for the instability tends toward to its critical value in the standard cross-slot geometry. These results suggest that the instability driven region should not be located at the stagnation point and it is most probably located near the re-entrant corners. These new results suggest that once the cylinder size is sufficiently large enough, addition of the cylinder in the geometry may have a stabilizing effect, once again enabling effective control.

Finally, the stabilizing effect of the surface tension in two phase viscoelastic fluid flows in cross-slot geometries is simulated using a volume of fluid method (Hirt and Nichols, 1981). The combined effects of the capillary number (the ratio of viscous force to the surface tension force), β, Wi, α of each of phase and the ratio of the total viscosities of each phase (the K parameter) are investigated. It is shown that the surface tension force plays an important role in the shape of the interface of two fluids. By reducing the surface tension force, the interface of the two fluids becomes curved and this can consequently change the curvature of streamlines in this region. In this scenario, for fixed values of β, Wi, α and K parameters, the surface tension is shown to have a stabilising effect on the associated steady symmetry-breaking instability in the cross-slot. The K parameter is shown to change the location of the stagnation point and the

interface position of the two fluids. By increasing the K parameter, the local value of the Weissenberg number near the corners of the geometry is significantly increased and this can consequently lead to a time-dependent purely-elastic instability.

Overall, the results in the thesis suggest a number of novel ways to predict and control the onset of purely-elastic instability in prototypical shear-dominated (TC) and extensional-dominated (cross-slot) geometries.

Contents

List of Figures

Acknowledgement

As I am approaching the end of my PhD program, I would like to take this opportunity to express my sincerest gratitude to all those people who helped and supported me during these years.

First and foremost I want to thank my supervisor Professor Robert J. Poole. I appreciate all his contributions of time, ideas, and funding to make my Ph.D. experience productive and stimulating. The joy and enthusiasm he has for his research was contagious and motivational for me, even during tough times in the Ph.D. pursuit. I am also thankful for the excellent example he has provided in both my academic and personal lives. He has shown me that how great the quality of a research work can be and how enjoyable academic world can be. Being in contact with him was one of the greatest things that happened to me and I am honored to be associated as one of his PhD students.
I would also like to express my gratitude to Prof. Morton Denn from the city college of New York who initially recommended me for this PhD program. If it wasn't for his help and support, I would probably never have the opportunity to do my PhD here and join Prof. Robert J. Poole's research group. I feel privileged to be in contact with such a great researcher and to receive feedback from him on my research works.

There are no words that can express my gratitude for the help and support that these two people provided me.

Besides my main supervisor, I would like to thank Dr. David J. C. Dennis, for his valuable comments and encouragement which incented me to widen my research from various perspectives. Also I sincerely thank Prof. Sandra Lerouge from Université Paris Diderot who conducted the experiments relating to the Taylor-Couette chapter in this thesis and provided me with her insightful comments during the study.

I thank my fellow colleagues, Dr Bayode Owolabi, Mr. Allysson Domingues, Mr. Rishav Agrawal, Dr. Chaofan Wen, Dr Waleed Abed and Dr. Haonan Xuin for the stimulating discussions and for all the fun we have had in the last four years. In partic-

ular, I am grateful to Dr. Henry Ng for the numerous help he provided me in different steps of my experiments.

Last but not the least, I would like to thank my family: my Father and to my sisters Mona and Maryam for supporting me spiritually throughout writing this thesis and my life in general.

Chapter 1

Introduction

Beyond a critical flow rate such that the ratio of the inertial to the viscous stress is large enough, inertial instabilities can often be observed in Newtonian fluid flows. In recent decades, an increasing attention has been allocated to understand and use such phenomenon in mixing processes and other industrial applications. Pioneering work relating to inertial instabilities was undertaken by Reynolds (1883) by characterising the conditions in which the flow of water in straight pipes transitions from laminar flow to turbulent flow. In this study, the fluid streamlines for different flow rates were visualized by injecting a small jet of dyed water at the centre of flow. When the ratio of inertial stress to the viscous stress (now termed the Reynolds number) was low, the dyed layer remained distinct through the entire length of the long tube. By increasing the Reynolds number (Re) beyond a critical value, the layer broke up and convected throughout the fluid's cross-section. This critical value is known as the transition point from laminar to turbulent flow and Reynolds found it was sensitive to the precise inlet conditions. For many decades after this insight of Reynolds regarding such instabilities, scientists were not able to successfully predict the onset of the instability in a pipe. Today, we know this difficulty is related to the non-linear form of the instability, and pipe flow still remains an outstanding challenge and the subject of many studies (see e.g. Eckhardt et al. (2007); Mullin (2011)). In contrast to such rectilinear flows, for hydrodynamic problems with curved streamlines, stability analysis has proved to be much more successful due to the linear nature of instabilities (Taylor, 1923; Görtler, 1944). In such flows, the appropriate dimensionless number appearing in the disturbance equation is the Görtler number (Görtler, 1944):

$$G = \sqrt{\frac{\tilde{\Theta}^*}{\tilde{\Re}} \frac{\tilde{\rho}\tilde{U}\tilde{\Theta}^*}{\tilde{\eta}_s}}, \tag{1.1}$$

where $\tilde{\Theta}^*$ is the boundary layer thickness, $\tilde{\Re}$ is the streamline curvature, $\tilde{\rho}$ is the density of the fluid, $\tilde{U}$ is a reference velocity and $\tilde{\eta}_s$ is the viscosity. Note, throughout this thesis dimensional variables will be indicated using a tilde. The first term on the right hand side of this equation is a dimensionless parameter showing the ratio of two

important characteristic lengths in the problem and the second term is just a Reynolds number defined based on the characteristic boundary layer length. This term scales the destabilizing effect of a pressure difference $\Delta\tilde{p} \approx \tilde{\rho}\tilde{U}^2$.

Interestingly, in viscoelastic fluids, even in cases that there is a vanishingly small inertial stress, a similar type of instability can be observed but in these cases it is related to the elastic stress: such instabilities are called "purely elastic" (Larson et al., 1990). These types of instabilities are generally triggered when a combination of the elastic normal stress in the streamwise direction is coupled with streamline curvature. A well known dimensionless parameter which rationalizes these types of "curved streamlines" instabilities is the M parameter introduced by McKinley et al. (1996a) (often referred to as the "Pakdel-McKinley" criteria) which is defined as:

$$M = \sqrt{\frac{\tilde{\lambda}\tilde{U}}{\tilde{\Re}} \frac{\tilde{\tau}_{ss}}{\tilde{\eta}_0 \tilde{\dot{\gamma}}}}, \tag{1.2}$$

where $\tilde{\tau}_{ss}$ is the normal elastic stress in the streamwise direction, $\tilde{\eta}_0$ is the zero shear rate viscosity of the fluid and $\tilde{\dot{\gamma}}$ is the magnitude of the shear rate. This parameter can be considered as the viscoelastic complement of the Görtler number as can be seen by comparison of equations 1.1 and 1.2. In equation 1.2, the first term on the right hand side shows the ratio of a characteristic length $\tilde{\lambda}\tilde{U}$ over which disturbance information is convected before it decays to the streamline curvature (this term can also be referred to as a local Deborah number, showing the ratio of the relaxation time of the fluid to the time a disturbance takes to travel along a streamline). The second term on the right hand side of equation 1.2 is added to scale properly the effect of the normal stress in the streamwise direction with a reference stress scale. This term is generally in the same order of magnitude as a local Weissenberg number which is the destabilizing term in the disturbance equation (McKinley et al., 1996a) (equivalent to the Reynolds number in equation 1.1). Equation 1.2 proposes that the kinematic and dynamic conditions corresponding to the curvature of the flow and the tensile elastic stress along the streamlines respectively can be combined into a single dimensionless criterion that must be exceeded for the onset of purely elastic instabilities.

In this thesis, to better understand this phenomenon, "purely elastic" instabilities in two geometries, namely Taylor-Couette and so called "cross-slot" geometries, will be investigated using numerical, experimental and analytical methods to explore the possibility of controlling (i.e. promoting, delaying or removing entirely) this type of instability with different controlling mechanisms that may, potentially, influence the parameters in equation 1.2. As the field of "purely elastic" instabilities is rather broad, having been observed in a wide range of geometries (Su and Khomami, 1992; Joo and Shaqfeh, 1991; Shull et al., 2000; Pakdel and McKinley, 1996; Arora et al., 2002; Pan

et al., 2013; Berti et al., 2008; Sahin, 2013; Burghelea et al., 2007), the following literature review will primarily be focussed on these two geometries.

1.1 Taylor-Couette and related geometries and onset of secondary flows

The flow between two concentric cylinders has routinely been studied by researchers due to its wide range of applications especially in rheometry (Walters, 1975; Morrison, 2001; Tanner, 2000). For rheometrical applications, a laminar viscometric assumption is necessary. In most of the cases rheologists are dealing with, the fluids are highly viscous or the geometry is designed to be sufficiently small so the creeping flow assumption is applicable. In these situation for Newtonian fluids the flow is laminar and instabilities can usually be neglected especially at low rotation speeds. Historical studies mainly focused on potential instabilities of Newtonian fluids at higher Reynolds numbers (i.e. the ratio of inertia to viscous stresses). In these cases, inertia proved to be the driving force for the instabilities.

Pioneering works in this geometry prior to instability were carried out by Couette (1888) and Mallock (1889) who derived an analytical solution for the flow between concentric cylinders. The height of the cylinders is considered to be $2\tilde{b}$ with $\tilde{R}_i$ and $\tilde{R}_o$ as the radii of inner and outer cylinders, respectively (Figure 1.1 shows the geometrical definition of the problem). The ratio of the gap between two cylinders and the height of cylinder were considered to be small enough so they can eliminate the effect of walls on the top and bottom of cylinders. The resulting one-dimensional analytical solution they derived was presented in the following form:

$$\tilde{U}_\theta(\tilde{r}) = \tilde{A}\tilde{r} + \frac{\tilde{B}}{\tilde{r}}, \tilde{A} = -\frac{(\frac{\tilde{R}_i}{\tilde{R}_o})^2\tilde{\omega} - \tilde{\omega}_o}{1-(\frac{\tilde{R}_i}{\tilde{R}_o})^2},\ \tilde{B} = \frac{\tilde{\omega} - \tilde{\omega}_o}{1-(\frac{\tilde{R}_i}{\tilde{R}_0})^2}\tilde{R}_i^2, \tag{1.3}$$

where, $\tilde{\omega}$ and $\tilde{\omega}_o$ are the inner and outer rotation speed. As shown in equation 1.3, the solutions were calculated assuming axisymmetric flow so the flow can be only a function of radial location. For the stationary outer cylinder cases, using the definition of the local shear stress and shear rate at the wall we obtain:

$$\tilde{\tau}|_{\tilde{r}=\tilde{R}_i} = \frac{\tilde{T}}{4\pi\tilde{b}\tilde{R}_i^2}, \tag{1.4}$$

$$\tilde{\dot{\gamma}}|_{\tilde{r}=\tilde{R}_i} = -\tilde{r}\frac{\partial}{\partial\tilde{r}}(\frac{\tilde{U}_\theta(\tilde{r})}{\tilde{r}})|_{\tilde{r}=\tilde{R}_i} = \frac{2\tilde{B}}{\tilde{R}_i^2}, \tag{1.5}$$

where, $\tilde{T}$ is the measured torque from the experiment on the inner cylinder. Then, the apparent (shear) viscosity of the material is simply given by $\tilde{\eta} = \frac{\tilde{\tau}}{\tilde{\dot{\gamma}}}$. Experiments conducted by Couette (1888) and Mallock (1889) showed that viscosity is only constant

for low rotation speeds and increasing the rotation speed of the cylinder above a critical value can lead to a bogus shear-thickening behaviour for the apparent viscosity even for constant-viscosity Newtonian fluids which is the signature of instability of the flow.

Since these early works, this geometry has received such a great deal of attention

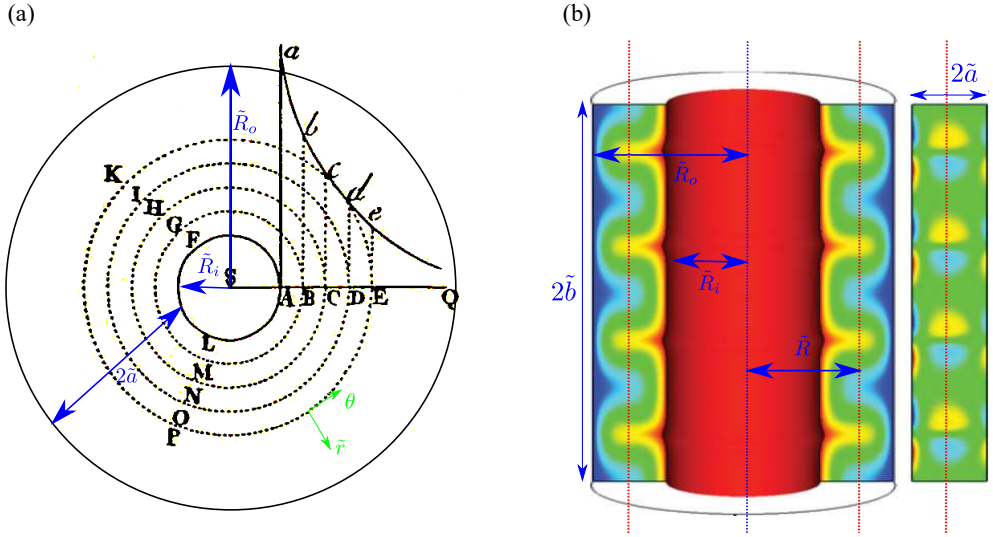

Figure 1.1: Comparison between (a) the base flow (adopted from Taylor (1923)) and (b) the Taylor cellular flow (adopted from Fardin et al. (2014))

from researchers that it has been referred to as the 'hydrogen atom of fluid dynamics' (Tagg, 1994; Fardin et al., 2014). The Taylor-Couette (TC) geometry has several advantages over the pipe studied by Reynolds and many others since; first of all, in the small-gap limit, the shear rate is constant across the gap (note that equations 1.3 - 1.5 show the large gap limit). From equation 1.3 one can calculate the shear rate simply as $\tilde{\dot{\gamma}} = 2\tilde{B}/\tilde{r}^2$. When the gap size is small, $2\frac{\tilde{a}}{\tilde{R}_i} < 1$, knowing that $\tilde{R}_o = \tilde{R}_i + 2\tilde{a}$ and applying a Taylor-expansion one can obtain the shear rate to be $\tilde{\dot{\gamma}} = |\tilde{\omega} - \tilde{\omega}_o|\tilde{R}_i^3/2\tilde{a}\tilde{r}^2$. Knowing that in this limit $\frac{\tilde{R}_i}{\tilde{r}} \approx 1$, one can obtain the shear rate as $\tilde{\dot{\gamma}} = |\tilde{\omega} - \tilde{\omega}_o|\tilde{R}_i/2\tilde{a}$ (i.e. constant). Secondly, streamlines are curved, so the nature of the instability in this geometry is linear, and therefore it could be dealt with much easier than pipe flow. Upon eliminating the effect of confining walls on the top and the bottom of the TC geometry, and assuming axisymmetry, i.e. one-dimensional (1D) flow assumption, the fluid must have a rectilinear velocity distribution with no secondary flow. Taylor showed that, beyond a critical rotation speed, by adding a small perturbation, a non-linear distribution of the main flowfield with pairs of steady secondary flows replaces the previous rectilinear distribution (for instance see Figure 1.1(b)). In such situations, there is a competition between centrifugal force which has a destabilizing effect and viscous force as the stabilizing factor. According to Wendt (1933), Prandtl was the first person who noted for the stationary outer-cylinder cases, that Taylor's critical condition for the onset of instability can be approximated by a simple correlation as:

$$Ta_{cr} = \frac{\tilde{\omega}\tilde{R}_i 2\tilde{a}}{\tilde{\nu}}\sqrt{\frac{2\tilde{a}}{\tilde{R}_i}} = 41.2, \tag{1.6}$$

where, $\tilde{\nu}$ is the kinematic viscosity of the fluid and the dimensionless number on

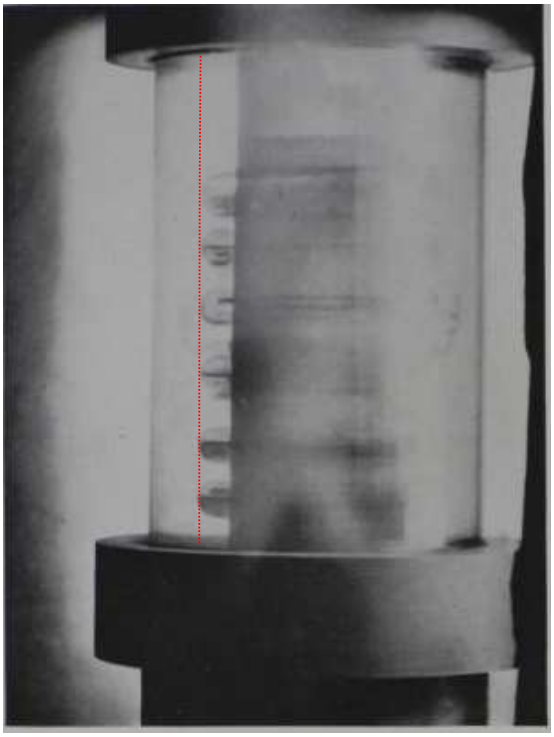

Figure 1.2: Presence of the nodal surface in counter-rotating instability of TC systems (Taylor, 1923)

the left hand side of this equation is called the Taylor number and can be written as a multiplication of Reynolds number by the square root of curvature ratio (CF the Görtler number in equation 1.1). Donnelly and Fultz (1960) noted that in the counter-rotating cases, an imaginary surface appears between the gap of two cylinders such that they called it a "nodal surface" (Figure 1.2). This nodal surface has a width of $2\vartheta a$ and shows the position of the zero velocity line between two counter-rotating cylinders. In this definition ϑ is defined as:

$$\vartheta = \frac{Re_i}{Re_i - Re_o}, \tag{1.7}$$

here, Re_i and Re_o are the Reynolds numbers calculated based on the rotation speeds of inner and outer cylinders, respectively. This definition provided a more general criterion for the instability of TC flow and showed that the wavelength of TC cellular structure scales as $2\vartheta a$.

Nowadays the TC geometry is considered a benchmark geometry in the fluid mechanics community, and devices with different aspect ratio (height/gap) Λ (ranging

from as small as 0.2) have been used for various purposes (Muller et al., 1989; Berret et al., 1997; Lerouge et al., 2000; Mullin et al., 2002; Hu and Lips, 2005; Lee et al., 2005; Liberatore et al., 2006; Gurnon et al., 2014; López-Barrón et al., 2015). For example, TC cells with aspect ratios $3 < \Lambda < 12$ are commonly used for both small-angle neutron scattering (Hu and Lips, 2005; Liberatore et al., 2006; Gurnon et al., 2014; López-Barrón et al., 2015) and flow birefringence experiments (Muller et al., 1989; Berret et al., 1997; Lerouge et al., 2000; Mullin et al., 2002; Lee et al., 2005). The confining effect of walls on the stability and bifurcation of Newtonian fluids in inertial regimes was studied by Benjamin (1978a) using the existence theory due originally to Leray and Schauder (1934). Benjamin (1978a) concluded that the supercritical nature of the instability, which was previously reported by Taylor (1923), based on an idealized 1D assumption for the base state, will not typically be observed in a physical flow between two finite concentric cylinders. Following this argument, a different process whereby the primary flow undergoes 'morphogenesis' was predicted by including the effect of the walls on the top and bottom of the geometry (as shown in Figure 1.3). In

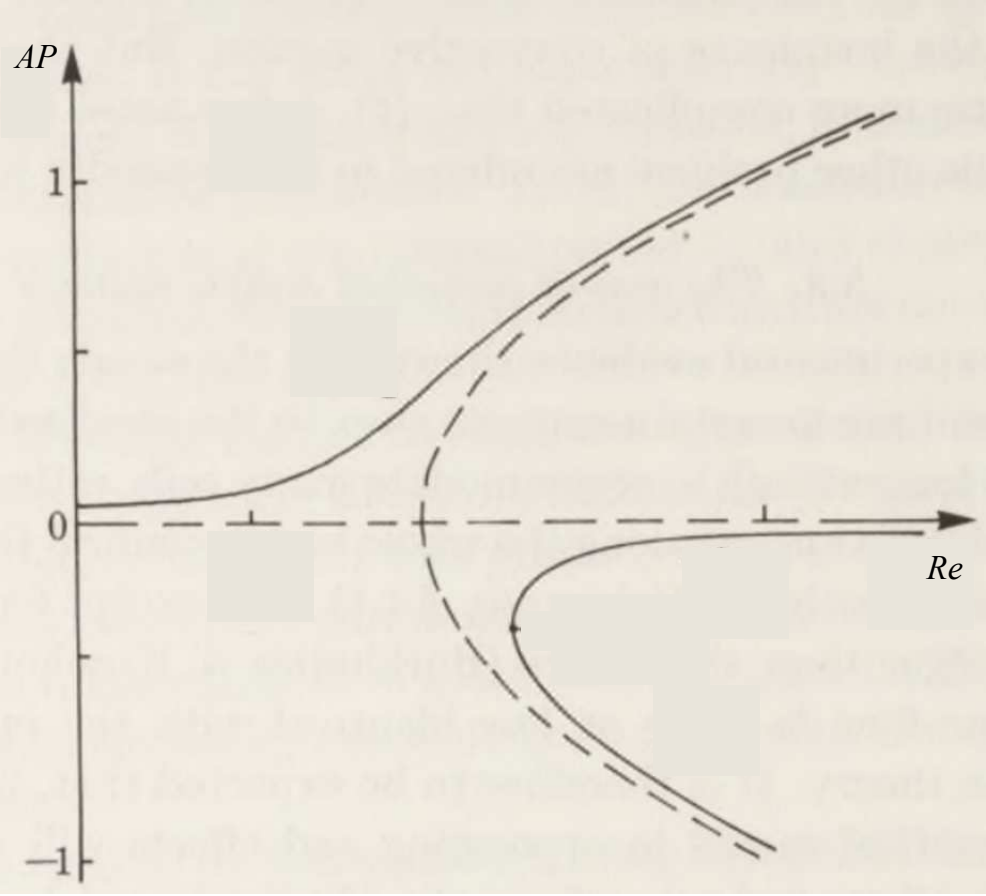

Figure 1.3: Prediction of Benjamin (1978a) for decoupling of bifurcation phenomenon in a confined Taylor-Couette geometry. Variation of asymmetry parameter (i.e. AP) versus Re number.

a following experimental study (Benjamin, 1978b), support for the theoretical part was provided showing a decoupling of the supercritical bifurcation for finite-aspect-ratio TC geometries. The results clearly showed that, once the inner cylinder starts to rotate from the stationary state, a secondary motion appears, which gets more intensified with increasing Reynolds number (see Figure 1.4). Similar qualitative results were obtained

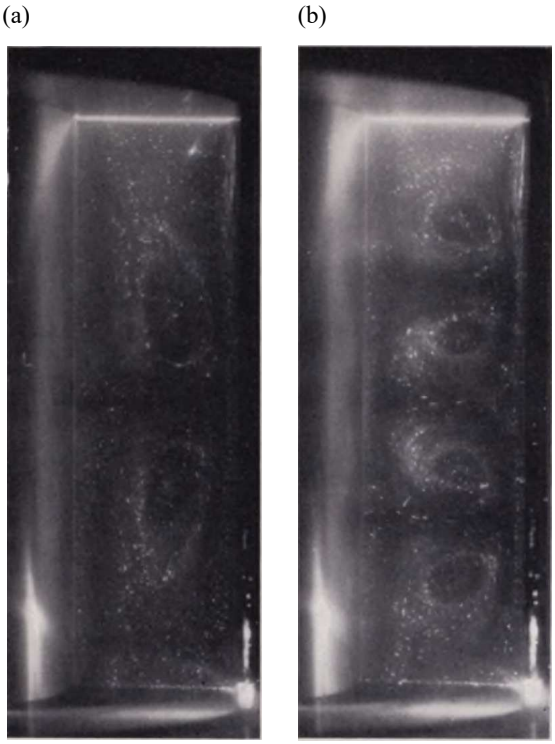

Figure 1.4: Experimental results conducted by Benjamin (1978a) in a confined Taylor-Couette geometry showing (a) presence of a pair of vortices in the base flow before onset of any instability and (b) a cellular structure of flowfield after instability.

in a numerical study by De Roquefort and Grillaud (1978) and a theoretical analysis by Schaeffer (1980), which used a homotopy approach to include the physically realistic effect of the fixed wall on the end faces of the cylinders. Thus, the use of end walls in Newtonian Taylor-Couette flow has been used to modify critical conditions for onset of inertial instability.

Görtler (1944), showed that most of the criteria for TC instability can be directly compared with more general curved boundary-layer flow (equation 1.1). Following Görtler's work, a great number of studies have been conducted to investigate effects of curvature and centrifugal forces. The main difference between flow in curved boundary layers and TC flow is related to the fact that in the TC system the fluid experiences a wall-driven motion while in curved ducts or curved boundary layers it is usually pressure-driven. Seminal papers by Dean (1927, 1928) tried to capture the structure of Taylor–Görtler vortices in curved pipes, which were previously studied experimentally

by Eustice (1911). Dean (1927, 1928) implemented a perturbation method, using the ratio of the pipe radius over the curvature radius as the perturbation parameter for the pressure-driven flow inside a curved pipe. Owing to the presence of centrifugal forces, pressure gradients in the lateral directions of the pipe appear, stimulating a pair of steady secondary vortices (as shown schematically in Figure 1.5). In this case, the centrifugal force causes fluid particles to move from the inner side of the curvature towards the outer side, while conservation of mass requires a replacement of particles and consequently a pair of secondary flow vortices appear. As a consequence of this pioneering study, these vortices are usually called "Dean's vortices". A similar method by Winters (1987) extended the analysis to flow in curved rectangular ducts. Sugiyama et al. (1983) experimentally investigated the flow patterns of Newtonian fluids in curved rectangular channels for wide ranges of the curvature ratio and aspect ratio. From flow visualisation, it was observed that the number of secondary flow vortices changes with increasing the Reynolds number as shown in Figure 1.6. In this work, it has been shown that at low values of the Reynolds number only one pair of secondary vortices appears but by increasing the Reynolds number the flow pattern may change and an additional pair of vortices start to grow. Thus, it is now well known that the combination of inertia and curvature leads to secondary flow for Newtonian fluids.

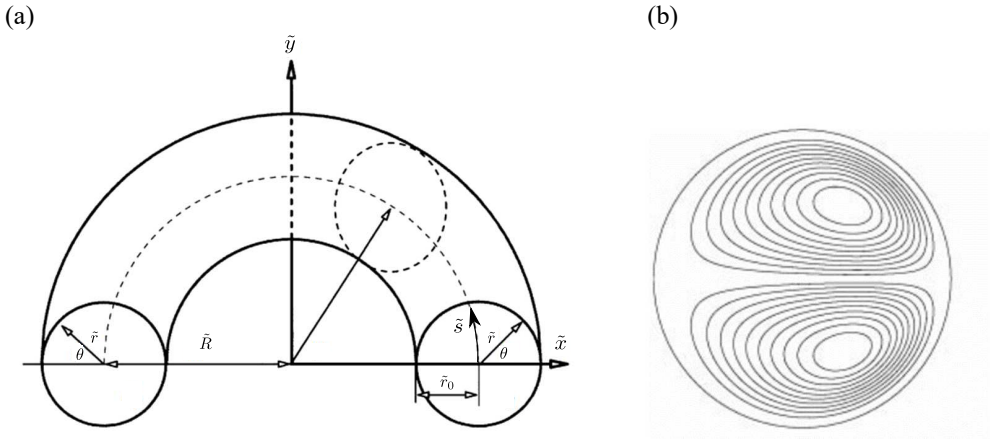

Figure 1.5: (a) Geometry configuration and (b) streamlines representing the secondary flow in a curved pipe (adopted from Fan et al. (2001))

In contrast, for viscoelastic fluids a secondary flow develops even in the inertialess limit for the curved pipe geometry, and such studies have received a great deal of attention because of their applications in mixing and other systems (Akiyama and Cheng, 1974; Finlay, 1989; Kumar et al., 2006; Ali et al., 2010; Keshavarz-Motamed and Kadem, 2011; Hayat et al., 2012; Hoque et al., 2013). Fan et al. (2001), based on an order-of-magnitude analysis, derived an equation for the Oldroyd-B model in such curved pipe flows, showing a correlation between the so-called 'hoop' stress (the normal

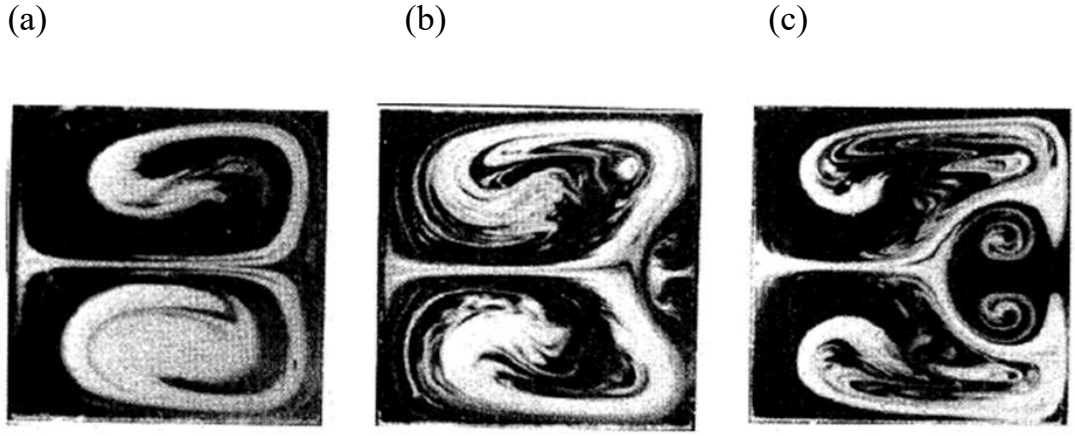

Figure 1.6: Flow patterns in the channel of aspect ratio 1 and curvature ratio 8(a) $Re = 265$ (b) $Re = 393$ (c) $Re = 518$ (Sugiyama et al., 1983)

stress in the azimuthal direction τ_{ss}) and centrifugal force. Considering the fact that lateral components of velocity are generally two orders of magnitude smaller than the main velocity ($V_r \approx V_\theta << V_s$ and so $\tau_{r\theta} \approx \tau_{rr} << \tau_{ss}$), the momentum equation in the "$\tilde{r}$" direction of the pipe (see Figure 1.5), far from wall and near the core region, can be reduced to:

$$Re\frac{{U_s}^2}{r} = -\frac{\partial p}{\partial r} + \frac{\tau_{ss}}{r}. \tag{1.8}$$

where $Re = \frac{\tilde{\rho}\tilde{U}_B\tilde{r}_0}{\tilde{\eta}_0}$ and $\tilde{\rho}$ is the density of fluid, $\tilde{U}_B$ is the bulk velocity, $\tilde{\eta}_0$ is the zero shear rate viscosity and $\tilde{r}_0$ is the radius of pipe and the azimuthal velocity is made dimensionless with bulk velocity $U_s = \frac{\tilde{U}_s}{\tilde{U}_B}$, r is the variable defined in the cylindrical coordinate system and is made dimensionless with radius of the pipe (i.e. $r = \frac{\tilde{r}}{\tilde{r}_0}$) and pressure and hoop stress are made dimensionless as $p = \frac{\tilde{p}}{\frac{\tilde{\eta}_0\tilde{U}_B}{\tilde{r}_0}}, \tau_{\theta\theta} = \frac{\tilde{\tau}_{\theta\theta}}{\frac{\tilde{\eta}_0\tilde{U}_B}{\tilde{r}_0}}$, respectively. Equation 1.8 shows that fluid inertia and hoop stress τ_{ss} are two significant and competitive forces near the core region, which contribute to establishing a pressure gradient and consequently the presence of Taylor-Görtler secondary flow. Poole et al. (2013) in a numerical simulation, showed that for creeping flow of a viscoelastic fluid in "serpentine" channels a pair of secondary flow vortices exists that is absent for the equivalent inertialess Newtonian flow. These secondary flows can be attributed to the effect of curvature and elastic normal stress similar to the Dean flow structure except that in the viscoelastic case there is no inertia. Within a similar context, Robertson and Muller (1996) and Jitchote and Robertson (2000) captured combined effects of elastic force and centrifugal force in curved pipes. In these papers, similar to the previous works by Dean (1927, 1928), a perturbation method was employed to show that, even in the absence of inertia, a combined effect of elastic normal-stresses and curvature are able to create hoop stresses and generate secondary flows. The presence of these secondary flows, consequently generates a second normal-stress difference for

Oldroyd-B fluids. With a similar interest, Yue et al. (2008) conducted a theoretical investigation using the Giesekus model and showed even in the absence of curvature, similar secondary motion of fluids may appear in non-circular pipes which is due to an inherit prediction of the non-vanishing second normal-stress difference in pure-shear flow in the employed constitutive model. Norouzi et al. (2010) in a numerical work tried to show the combined effects of first and second normal-stress differences in creeping flow through a square curved duct. It is shown that these two normal stresses have an opposite influence on the creation of secondary flows and the dominant force is the elastic first normal-stress difference.

In the last century, research into complex viscoelastic fluids has highlighted that, even in the absence of inertial forces (i.e. creeping flow), similar mechanisms to inertial instabilities can be generated solely due to the nonlinear elastic forces; such instabilities are called 'purely elastic' (Shaqfeh, 1996). The flow between two concentric cylinders (TC flow described above) has routinely been studied by researchers in viscoelastic fluids due to its wide range of applications especially in rheometry (Mallock, 1889; Taylor, 1923). Following the studies already discussed on the effect of inertial instabilities in the TC system and Dean flows (Dean, 1928), a number of researchers tried to extend this scenario to the case of viscoelastic fluids. The modifying effects of viscoelasticity on the inertial TC instabilities were investigated by Giesekus (1966, 1972) both experimentally and analytically using the second-order fluid model. It is shown that adding small amount of polymeric particles to the fluid can stabilize the inertial TC instabilities and the critical value of Taylor number will be increased. They also showed that the wavelength of the cellular structure of the vortices is not a function of viscoelasticity in these cases. Although, as the polymeric concentration reaches 1000 p.p.m this trend will change and viscoelasticity will show a destabilizing effect. Giesekus (1966), using a theoretical approach, tried to capture the influences of the first and second normal-stress differences in the limiting case that the Taylor number is zero (creeping flow). He concluded that in cases where the second normal-stress difference is positive and strong enough purely-elastic TC instabilities can be observed. For the purpose of this investigation a second order fluid constitutive equation was used. In nature, the second normal-stress difference of most fluids has negative sign and are very small so Giesekus' zero inertial instability is not expected to be observed. Generally, a second-order fluid is the lowest-order form of a mathematical constitutive equation after the Newtonian fluid (first-order solution) so is only suitable for simulation of slow and slowly varying flow, while in the case of purely viscoelastic instabilities, driven by nonlinear effects, this assumption is not strictly valid (Bird et al., 1987). Muller et al. (1989) showed experimentally that, in the absence of significant second normal-stress differences, using a Boger fluid (an elastic fluid with a constant viscosity (Boger, 1977)), a purely-elastic

instability can be observed. They showed that, unlike the steady nature of TC vortices, in the purely-elastic case the structure has an oscillatory form the wavelength of which decreases with time. Figure 1.7 shows the structure of TC instability for both Newtonian and viscoelastic fluids. From these seminal results, it can be deduced that the first normal-stress difference should play a key role in purely-elastic instabilities.

(a) (b) (c)

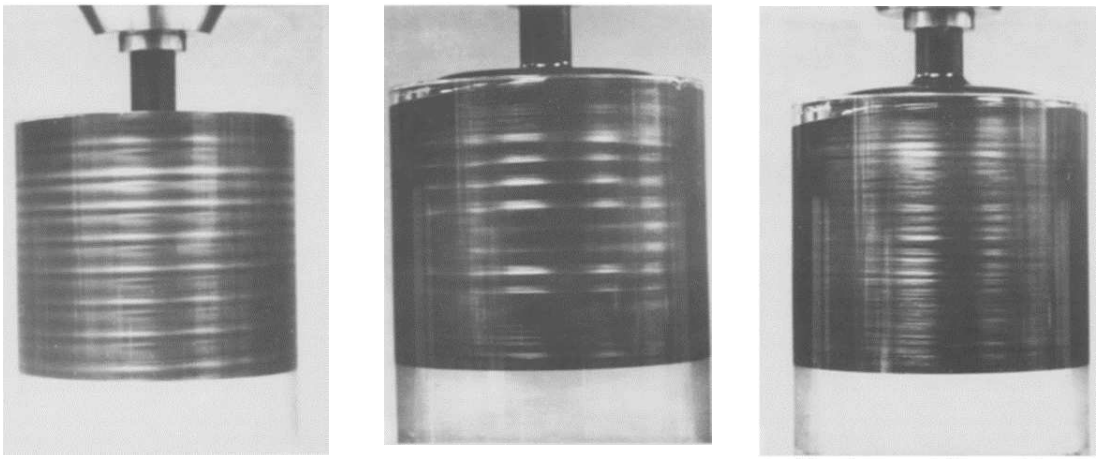

Figure 1.7: Photographs of Taylor-Couette flow. Small mica flakes were suspended in the test fluid. These plate-like particles reflect light in a manner that is highly dependent on their orientation; hence the variations in reflected light intensity are due to their alignment by the flow. (a) Newtonian Taylor cells in a solution of glycerol and water (b) Initial development of elastic vortices for viscoelastic fluids (c) Long-time, small wavelength elastic vortices (Muller et al., 1989)

A reasonably up-to-date review on viscoelastic flows in the TC system and different types of instabilities can be found in Muller (2008). A theoretical study to estimate the onset conditions of purely elastic instabilities was carried out by Larson et al. (1990). Using a linear stability analysis, they employed a perturbation method to predict the threshold of this instability. Larson et al. (1990) eliminated the effect of confining walls on the top and bottom of the geometry, and disturbed an initially 1D axisymmetric flow using a time-periodic function and showed that only after a critical shear rate did an instability in the form of a time-dependent secondary flow occur, in qualitative agreement with experiments of Muller et al. (1989). The previous studies in the literature for viscoelastic fluids suggested that the presence of secondary flows was only attributed to the onset of a purely elastic instability in the TC geometry (Giesekus, 1966, 1972; Muller et al., 1989; Larson et al., 1990).

1.1.1 Notable research gaps in the Taylor-Couette geometry for viscoelastic fluids

The previously conducted research has shown that a combination of inertial stress with curvature of streamlines in confined Taylor-Couette geometries leads to the presence of secondary flows that may potentially play an important role in the onset criteria of hydrodynamic instability for Newtonian fluids (Benjamin, 1978a,b). However, although there has been several studies conducted to investigate the effect of elastic stress on the onset criteria of purely-elastic instability Muller et al. (1989); Shaqfeh (1996); Muller (2008), the modifying effect of confining walls has not been addressed so far in the literature. In the previously studied geometries, the ratio of the gap size to the height of cylinders were mainly considered to be large enough so the 1D assumption of the base flow can be applied. In this thesis it will be shown that, by considering the effect of confining walls, even before the onset of any potential purely elastic instability, a pair of steady secondary vortices exists in the region near the corner of the moving wall and the stationary wall. Indeed, viscoelastic flow through finite-aspect-ratio curved ducts is characterized by secondary flows which are driven by a combination of curvature and stress gradients near the duct walls that significantly affect the primary flow. Although never previously studied, in a TC system this issue is likely to play an important role in both the base-state solutions and the purely elastic instability threshold of viscoelastic fluids in the TC system, especially for shallow geometries (i.e. small aspect ratios). Thus, the aim is to see if the finite aspect ratio can be used to "control" (promote or delay) the onset of the purely-elastic instability which is known to occur. In this thesis, this gap in the literature will be addressed by investigating finite end effects for the narrow-gap concentric-cylinder geometry under inertialess conditions for viscoelastic fluids using both an approximate analytical perturbation approach and full nonlinear simulations with the Oldroyd-B model.

1.2 Cross-slot stagnation point and related geometries

As already discussed, instabilities in Newtonian fluid flows occur frequently due to the nonlinear nature of the inertial force not only in viscometric flows like TC flow but also in more complex flows with extensional flow components. Extensional flow occurs when a fluid experiences a deformation in the streamwise flow direction and can be observed in many different situations such as flow through expansions (Abbott and Kline, 1962) or contractions (Rothstein and McKinley, 1999) and at stagnation point flows like flow through intersections (such as T- shaped (Kockmann et al., 2003) or cross-slot (Poole et al., 2014a) geometries) or flow passing an obstacle (Eckerle and Langston, 1986; Proudman and Pearson, 1957; Taylor and Acrivos, 1964). Generally,

beyond a critical value of the Reynolds number the "simple" solution branch of the base state (i.e. steady and/or symmetric) in such flows bifurcates to a more complex flow distribution. Taylor (1934), was one of the first researchers who started to investigate

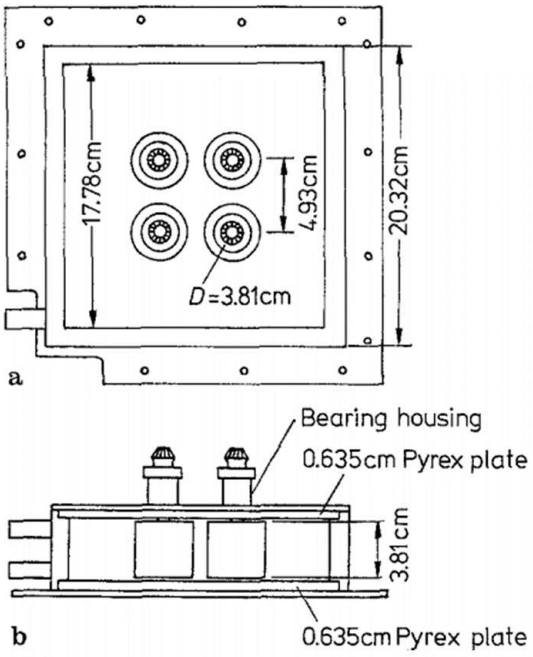

Figure 1.8: Schematic of four-fill mill; (a) top view; (b) side view (Lagnado and Leal, 1990)

different flow-type behaviours using a "four-roll mill" designed configuration. Taylor's four-roll mill geometry allows the generation of strong extensional flows by trapping a matrix fluid at the stagnation point and applying deformation on any suspended droplets. A schematic of apparatus is shown in Figure 1.8. Lagnado and Leal (1990) have used the four-roll mill apparatus previously introduced by Taylor (1934), to study instability of the flowfield in extensional dominated flows. At low Reynolds number, the rotation of rollers have been constrained to generate an approximately two-dimensional pure planar elongational flow at the geometric center of the apparatus. As the Reynolds number increases a combination of the inertial stress and curvature of the streamlines lead to growth of steady, symmetrically positioned Dean vortices near the top and bottom walls of the container. As the Reynolds number is increased beyond a critical value, the reported Dean vortices join together and creates a vortex stretching along the exit channel resulting in the loss of symmetry in the flow pattern. Here, the loss of symmetry in the flowfield is attributed to the influence of elongational flow on the Dean vortices. Figures 1.9 show this transition from top and side views.

Perhaps one of the most well studied, symmetry-breaking bifurcation instabilities is related to the flow of Newtonian fluids passing through planar sudden expansions (Cherdron et al., 1978). In such geometries, due to a sudden change in the cross-section

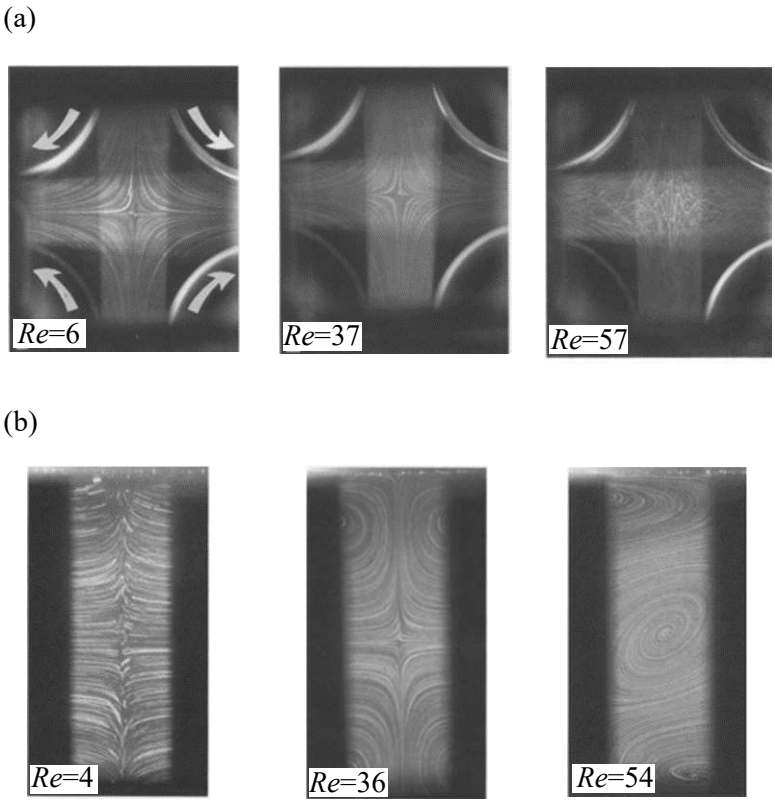

Figure 1.9: Flow patterns of Newtonian fluids in four-mill apparatus at different Reynolds numbers; (a) Top view (b) side view photographs. Results based on the experiments conducted by Lagnado and Leal (1990)

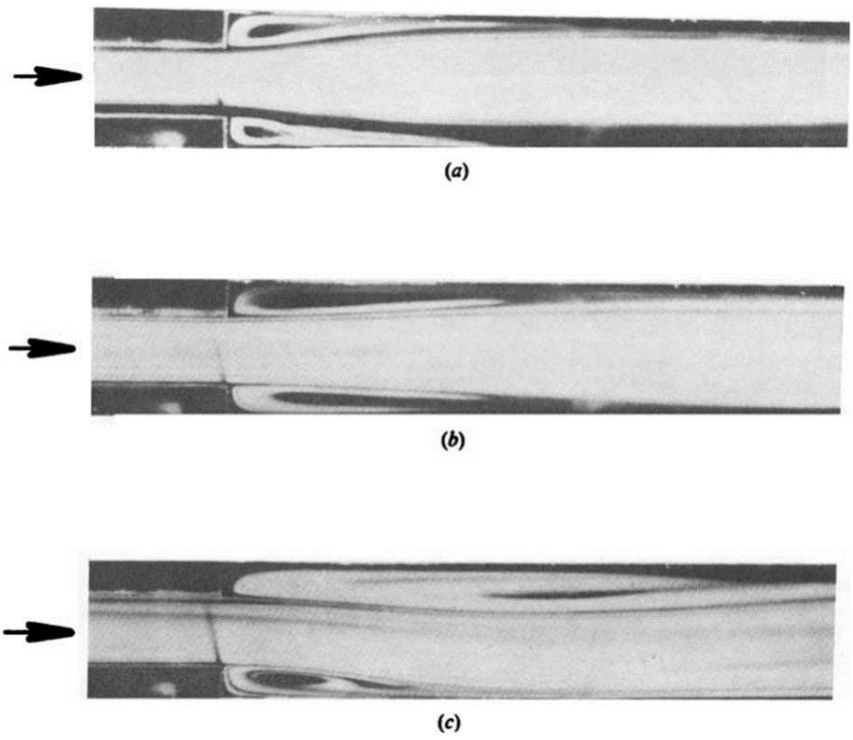

Figure 1.10: Flow patterns at different, Reynolds numbers for an aspect ratio of 8 and an expansion ratio of 2. (a) $Re = 110$. (b) $Re = 150$. (c) $Re = 500$ based on the experiments conducted by Cherdron et al. (1978)

of the geometry a fluid particle experiences a complex combination of extensional and shear dominated flows. For Newtonian fluids, above a critical value of the Reynolds number, the flowfield finds a steady asymmetric distribution. As previous reported (Abbott and Kline, 1962; Drikakis, 1997), the asymmetry of the flowfield appears in the form of two stable antisymmetric flow states which each correspond to a recirculation region attached to one of the two downstream walls (Abbott and Kline, 1962). The critical Reynolds number for the onset of the instability is reported to be a function of both the expansion ratio (i.e. the ratio of the width of the downstream to upstream channels) and, for three dimensional flows, the aspect ratio (i.e. the ratio of the inlet channel height to its width). Figure 1.10 presents experimental results capturing this phenomenon based on the results previously reported by Cherdron et al. (1978).

One of the popular mixing geometries in microfluidics is the planar T-channel which was firstly presented by Kockmann et al. (2003). In this geometry, two channels with opposite streams join through a 90^o turn into an outlet channel. The numerical study by Kockmann et al. (2003) found a similar type of instability in a T-channel problem to the one previously observed in the four-roll mill geometry. This study reported the bifurcation of flow from a steady-symmetry to steady-asymmetry distribution. At low

Reynolds number flows, streamlines follow the geometry walls in an almost unidirectional distribution. As inertial effects become more important, due to the presence of a 90^o turn, Dean-like vortices appear in the outlet channel. Finally, above a critical value of the Reynolds number, the symmetry of the flow breaks and the vortices merge into a single vortex.

The so-called "cross-slot" geometry is another popular geometry which is used frequently in extensional-flow related studies. This geometry consists of four bisecting rectangular channels with two sets of opposite inlets and outlets. These opposing inlets and outlets produce a flowfield with a free stagnation point located at the centre of the geometry. At this point the velocity field is zero and a finite gradient of velocity in the streamwise direction appears. In principle, due to the zero velocity field at this point, a fluid element is trapped for an infinite time generating a significant strain and potentially enabling "steady-state" extentional flow kinematics to be realised which is a hall-mark of this geometry and the reason it is often proposed as an extensional rheometer (Haward et al., 2012b). Poole et al. (2014a) using a numerical procedure studied the effect of inertial stresses in a 2D cross-slot geometry to explore the inertial instabilities in this geometry. They have shown that by increasing the Re number, four identical standing recirculating vortex are initially formed starting at the four corners of the geometry which is caused by a combination of inertial stress and the curvature of streamlines. A schematic of the problem is shown in Figure 1.11. As Reynolds number increases to higher values, a bifurcation of the flowfield from its symmetry distribution appears by changing the size of theses vortices. Figure 1.12 represent the symmetry-breaking mechanism which appears in the outlet arms before and after the critical Reynolds number (Poole et al., 2014a). The instability in this geometry is similar in nature to the one previously reported in flow passing through planar expansions (Abbott and Kline, 1962).

In following research, Haward et al. (2016b) extended the study of the inertial symmetry-breaking instability in the cross-slot geometry to analyse the effect of the cross-section aspect ratio using both numerical and experimental methods, i.e. to real geometries of finite aspect ratio. In this study, it has been shown that when the Reynolds number is smaller than the critical value for the onset of instability but non-zero, due to the presence of curved streamlines, the centrifugal force leads to growth of four symmetrically positioned Dean vortices (with respect to centre planes). By increasing the Reynolds above a critical value the flow undergoes a bifurcation to a steady asymmetry state with a single spiral vortex along the outlet channels of the geometry (see Figure 1.13). The time evolution of this transformation is presented in Figure 1.14. The results suggest that the observed transition follows the same trend as was previously reported in the four-roll mill geometry (Lagnado and Leal, 1990) which is known to appear due to the presence of a stagnation point and the stretching of a

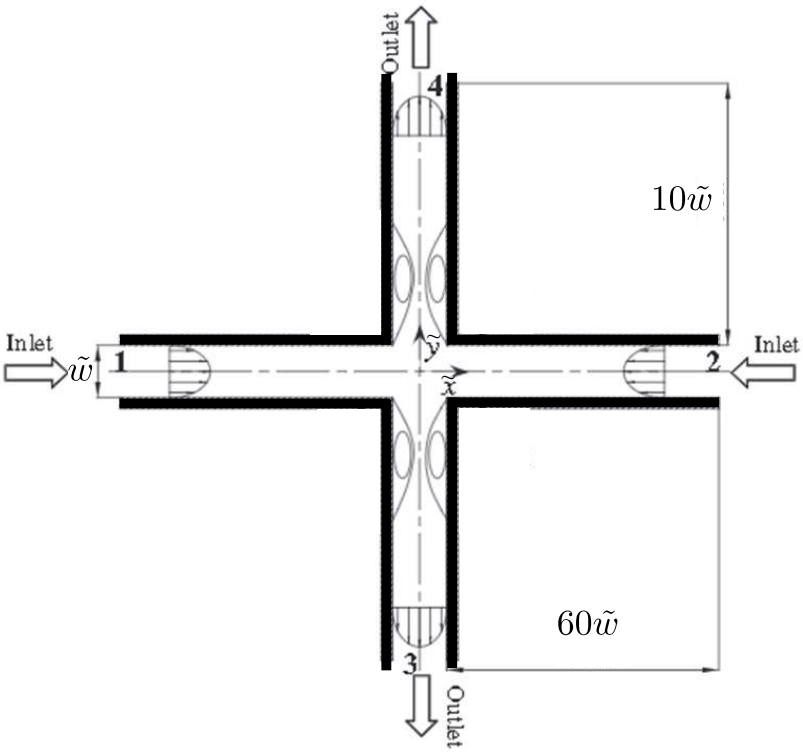

Figure 1.11: Schematic of cross-slot geometry (Poole et al., 2014a)

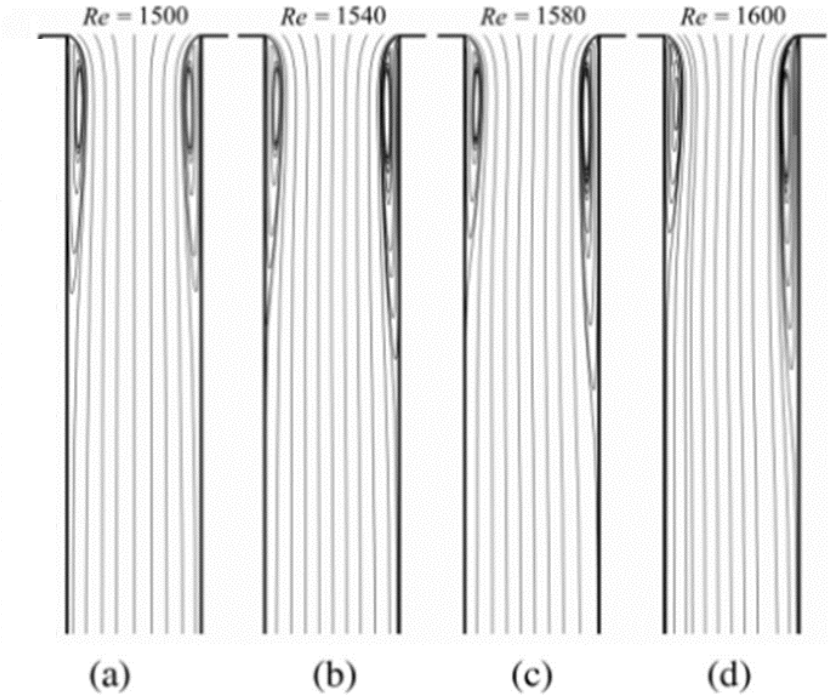

Figure 1.12: Size of recirculation zones close to critical conditions (a)$Re = 1500$; asymmetric growth of recirculation regions beyond bifurcation: (b)$Re = 1540$; (c)$Re = 1580$ and (d)$Re = 1600$. based on the numerical study conducted by Poole et al. (2014a)

vortex in planar elongational flows.

Many industrial processes deal with highly extensional flows of polymeric fluids. As already discussed, in most of these cases, a purely-elastic instability may occur that is absent for its equivalent Newtonian creeping flows (Poole et al., 2007a; Zilz et al., 2014). During the last few decades, significant attention has been placed on such flows to characterise the physics behind these types of instabilities especially in shear flows (McKinley et al., 1996a; Larson et al., 1990), however understanding of this type of elastic instability in extensional-dominated flows is not as advanced as in shear-flow dominated flows (Haward et al., 2016a).

The cross-slot geometry, shown in Figure 1.11, is a common flow geometry that has been extensively utilized for generating controllable planar, uniaxial and biaxial elongational flowfields and to study the stretching dynamics of polymers (Afonso et al., 2010; Haward et al., 2012b, 2016a). A numerical study carried out by Afonso et al. (2010) suggested the use of modified three-dimensional cross-slot geometries to simulate different standard types of elongational flows. Two different flow configurations were presented to simulate uniaxial and biaxial elongational flowfields near the stagnation point. The numerical results showed that the flow is symmetric relative to the centreline at low values of the Weissenberg number while, for Weissenberg numbers above a critical value, the elastic stress can trigger an instability and the flow becomes asymmetric, while remaining steady. As a consequence of the loss of symmetry, it has been shown that the uniform elongational dominated flow around the stagnation point will be replaced by a complex asymmetric flowfield. Subsequently, as the Weissenberg number (the ratio of the elastic stress to the viscous stress) increases to higher values, the flow becomes unsteady (Sousa et al., 2018).

A similar type of stagnation point flow can be observed when fluid passes objects such as a cylinder or a sphere (Walters and Tanner, 1992). If the obstacle is a solid object the stagnation point is pinned at the surface of the geometry and cannot move, while for example in the case of falling/raising drops, the stagnation point is located at the surface of moving droplets and in principle is free to move and change the shape of the droplet (Bisgaard, 1983; McKinley, 2002; Davoodi and Norouzi, 2016). As a consequence of the no-slip condition and mass continuity, the local velocity gradient and the velocity field are zero for a pinned stagnation point while for a free stagnation point the strain rate can have finite non-zero values. In both types of flows, beyond a critical value of strain rate a symmetry-breaking of the flow distribution can be observed for both the pinned (Afonso et al., 2012) and free stagnation point flows (Bisgaard, 1983). Soulages et al. (2009) studied two different geometries to investigate the kinematic differences between a pinned stagnation point flow at the wall and a free stagnation point

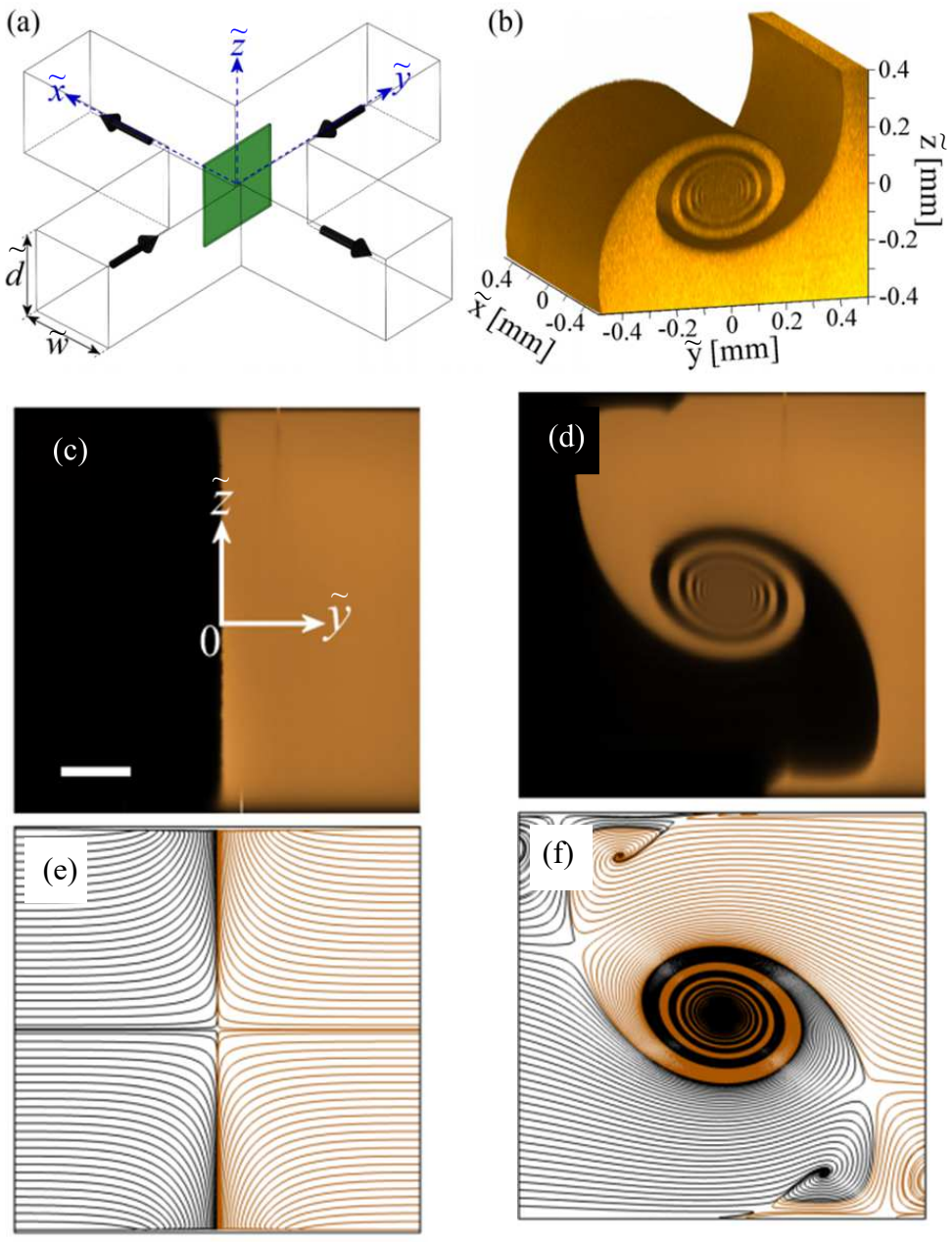

Figure 1.13: (a) Schematic diagram of a cross-slot geometry with aspect ratio = 1 (flow enters along y and exits along x). (b) Three-dimensional rendering of a vortex structure observed for the flow of water at $Re = 75.8$. Confocal imaging (c, d) and numerically generated streamlines (e, f) showing the evolution of flow structures in the $x = 0$ plane (Haward et al., 2016b).

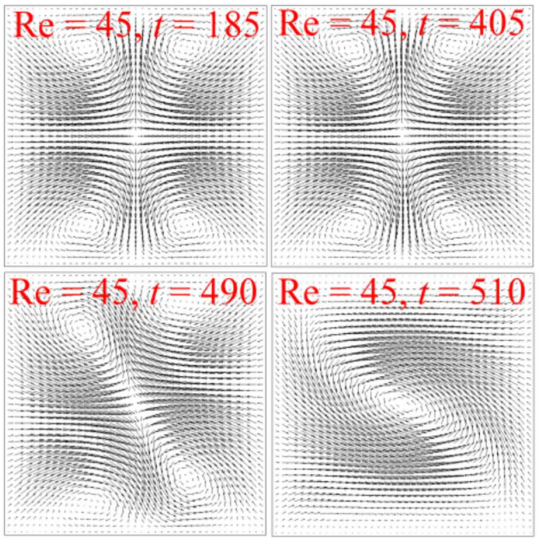

Figure 1.14: Dynamic evolution of velocity vector fields and centre point vorticity computed from time-dependent numerical simulations at the centeral plane $x = 0$ (Haward et al., 2016b).

flow by adding a recirculating cavity opposite to the outlet arm of a T-shaped channel. They showed that the critical value of flow rate for the onset of an unsteady 3D instability is delayed to higher values of the Weissenberg number for the free stagnation point flow geometry with a cavity compared to the pinned case without a cavity. Also, a new type of steady asymmetric instability was reported in this modified geometry that was suppressed for the cases in which the stagnation point was pinned at the wall.

Early research conducted by Gardner et al. (1982) was the first which reported that a steady flow asymmetry can occur for viscoelastic flows in cross-slot geometries. In this geometry, although nominally extensional dominated, fluid particles passing through the cross section in between the corner and the stagnation point experience both significant shear flow near these re-entrant corners (Dean and Montagnon, 1949; Moffatt, 1964; Hinch, 1993; Davies and Devlin, 1993) and elongational-dominated flow near the stagnation point (Öztekin et al., 1997; Haward et al., 2016a). The combination of this complex deformation with the non-linear elastic stresses for viscoelastic materials can enable disturbances to grow and trigger a purely-elastic instability. Although firstly observed by Gardner et al. (1982), it was not until Arratia et al. (2006) that this effect was clearly associated with a purely-elastic instability and suitably characterised. In this geometry, for Newtonian fluids and viscoelastic materials before onset of any instability, fluids injected from the inlet arms divide equally into two outlets. By increasing the Weissenberg number to a critical value, at a given instant, the dyed solution no longer divides equally between the two outlets (as shown in Figure 1.15). Supporting numerical simulations for this phenomenon were presented by Poole et al.

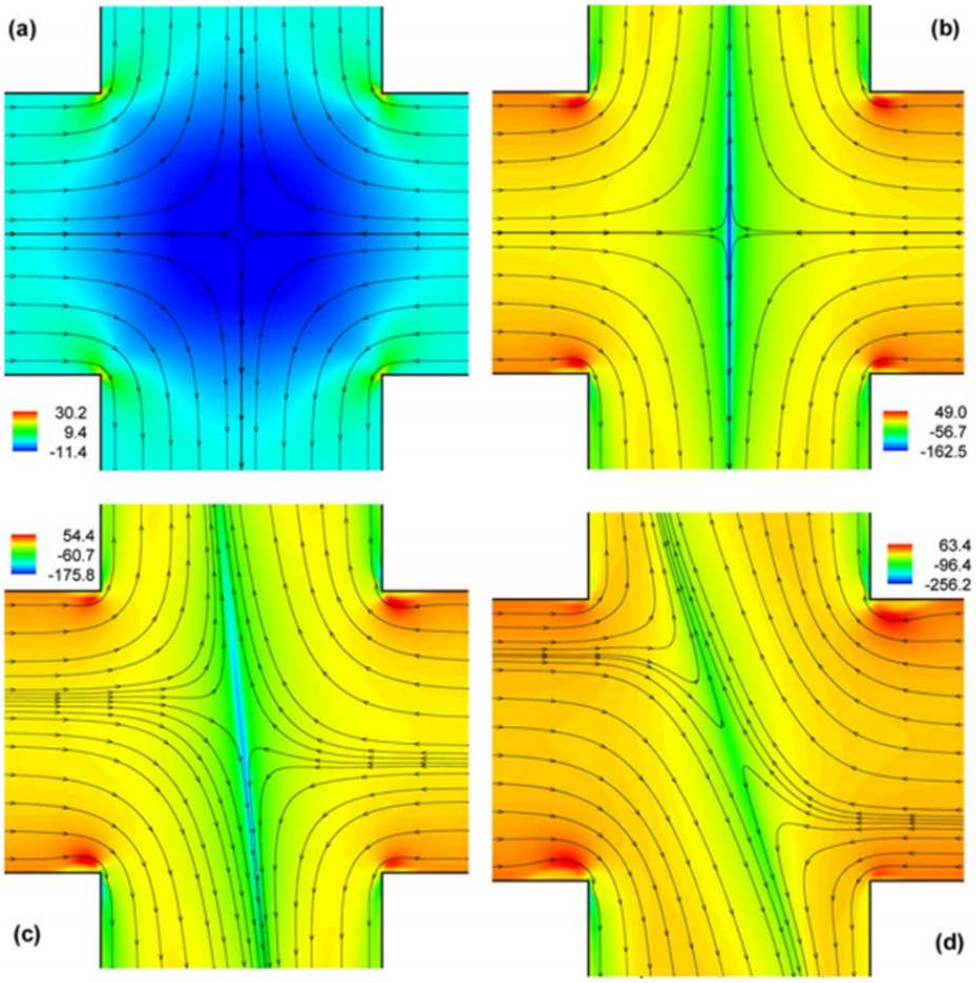

Figure 1.15: Streamline patterns superimposed onto contour plots of the first normal-stress difference, for (a) Newtonian fluid, (b) viscoelastic (symmetry flow distribution), (c) and (d) viscoelastic (asymmetry flow distributions for two different values of the Wi number) (Poole et al., 2007b).

(2007b), where it was shown that once the instability appears, the shape of the velocity profile along a line between the corner of the cross-slot geometry and the free stagnation point changes from convex into concave.

Recently, Cruz et al. (2016) have used the M parameter (equation 1.2) to plot its spatial variation in the cross-slot geometry for both the upper-convective Maxwell (UCM) and simplified Phan-Thien Tanner (sPTT) fluids. Previous studies for flow around sharp re-entrant corners both for Newtonian (Dean and Montagnon, 1949; Moffatt, 1964), and UCM fluids (Davies and Devlin, 1993; Hinch, 1993) suggest that although the velocity field at the corner is zero, the velocity gradient, and consequently the magnitude of stress tensor, are singular. At such corners the combination of high shear rate along with high curvature of the streamlines can thus provide a suitable mechanism for a disturbance to grow and trigger an instability. The numerical simulations of Cruz et al. (2016) for a geometry with sharp square re-entrant corners (standard-shape cross-slot) suggest that instability should be triggered at a region near the corner of the geometry (see Figure 1.16). These results support the earlier work by Rocha et al. (2009) who showed the instability is delayed to higher values of the Weissenberg number once the sharp square corner is replaced with a sufficiently rounded corner.

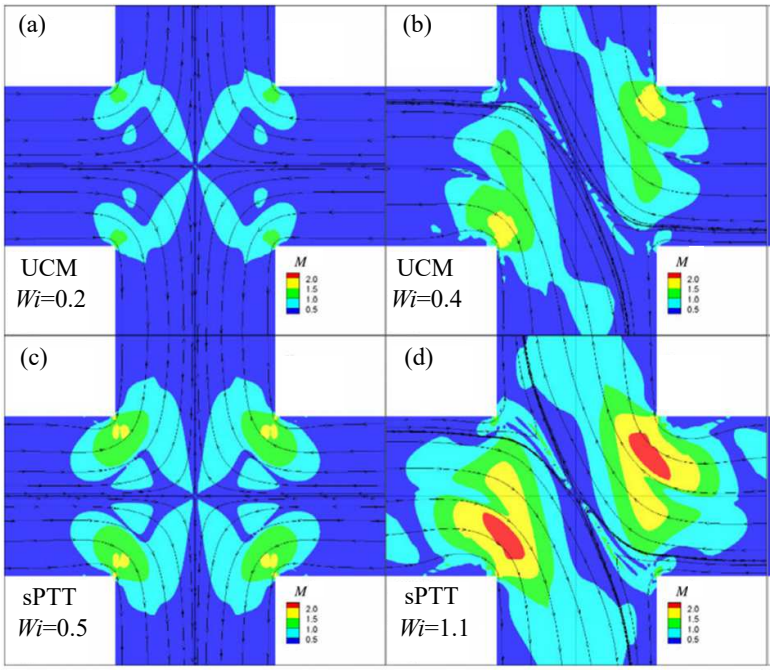

Figure 1.16: Contour maps of the modified Pakdel–McKinley criterion M for cross-section aspect ratio of 2.3, at the highest simulated Wi prior to each flow transition. The constitutive model, Wi number is given in each panel. Maps are shown (a, c) prior to the steady bifurcation and (b, d) prior to the onset of time-dependent flow (Figures are adopted from Cruz et al. (2016)).

To obtain an ideal planar elongational flowfield, Haward et al. (2012b) suggested to optimise the standard shape of the cross-slot geometry using a numerical approach and termed the resulting shape the Optimized Shape Cross-slot Elongation Rheometry geometry ("OSCER"). In a follow on study, Haward et al. (2016a) using the OSCER geometry, showed that once the ideal planar elongation flowfield is obtained, although the deformation rate has a small value at the stagnation point, the curvature of the streamline exhibits a large value near this region and the maximum value of the M parameter (equation 1.2) appears in the vicinity of the stagnation point.

1.2.1 Research gap in cross-slot geometry problems for viscoelasic fluids

Previous studies in cross-slot geometries has shown in the absence of inertia, a purely-elastic instability may be triggered due to the non-linear nature of the elastic force, but it is still not clear if instabilities in the cross-slot are driven via curvature and high shear near the stagnation point (Haward et al., 2016a) or from a region closer to the corner (or even at the corner) (Rocha et al., 2009). For Newtonian fluids, and inertial instabilities, previous studies have shown that base-flow modifications using a passive control device in the *wavemaker* region, i.e. a region of the flow where physical mechanisms giving rise to a self-sustained flow oscillation are active, will alter the stability properties of flows and consequently the suppression of vortex shedding inertial instability for a flow past a cylinder (Marquet et al., 2008; Strykowski and Sreenivasan, 1990; Hill, 1992). In this thesis, to better understand the purely-elastic instability in the cross-slot geometry, using a series of numerical simulations supported by experimental and analytical tools, the standard-shape cross-slot geometry will be modified by replacing the free stagnation point flow with pinned stagnation points by the addition of a control cylinder at the geometric centre of the domain. Using this modification, the curvature of streamlines close to the geometric centre will be affected by the presence of the cylinder and will exhibit an opposite sign in comparison to the curvature of the streamlines near the corners of the geometry. A change in the relative size of the cylinder (i.e. changing the "blockage ratio" parameter) will allow the local value of streamline curvature to be controlled along with the average value of the velocity passing through the gap between the corner of the cross-slot and the cylinder. It will be shown that the introduced modification acts as a passive control-mechanism that can be used to delay the critical flow rate in which the instability is triggered. Also, due to conservation of mass and the no-slip boundary condition, once a cylinder is added, the finite non-zero value of the strain rate at the stagnation point seen for the standard shape cross-slot geometry is replaced by stagnation-point where the strain rate is zero. Considering the above issues, one can state that the addition of the cylinder at the

geometrical centre of the cross-slot geometry significantly changes the flow distribution near the stagnation point while the flow distribution close to the corners will stay relatively unchanged (at least for small cylinders).

For viscoelastic fluids, all previous studies in the cross-slot were restricted to a single fluid phase. Therefore, a series of two-phase flow simulations will be performed to investigate the effect of interfacial tension applied at the boundary of two fluids for the case where two immiscible fluids are injected from the opposite inlets of the cross-slot geometry. By increasing the interfacial tension between the two fluids one can influence both the streamline curvature $\tilde{\Re}$ and the strain rate magnitude in the vicinity of the free stagnation-point located at the geometrical centre of the problem. Thus, the interfacial tension can be used as another means to control the symmetry-breaking instability.

1.3 Thesis aim and objectives

The aim of this thesis is to investigate the laminar creeping flow structure and discuss the possible influences of geometrical and rheological parameters on the threshold of purely-elastic instabilities. To achieve this aim, two different problems are studied. One which is shear dominated (the Taylor-Couette geometry) and one which is extensional dominated (the cross-slot geometry).
The objectives in the Taylor-Couette problem are:

- To derive an analytical solution as a benchmark solution for the confined TC system of creeping flow of a viscoelastic fluid.
- To analyse the effect of confining walls at the top and the bottom of the Taylor-Couette system on the structure of the main flow.
- To investigate the effect of viscoelasticity on the secondary flow structure and its possible influences on the threshold rotation speed of purely-elastic instabilities in a finite aspect ratio Taylore-Couette system.

The objectives in the cross-slot problem is:

- To investigate the effect of addition of a cylinder at the geometrical centre of the problem and replacement of a finite strain rate free-stagnation point with zero strain rate pinned stagnation points.
- To derive an analytical expression to predict the onset of the purely-elastic instability of viscoelastic fluids in the modified geometry.
- To analyse the kinematic properties of flow at a fixed cylinder size by replacing the no-slip boundary condition with a complete slip at the cylinder wall.
- To conduct a series of numerical simulations for two-phase flow in this geometry.
- To analyse the effect of interfacial tension and the total viscosity ratio of two fluids on the flowfield and the interface shape of two fluids.
- To investigate the effect of interfacial tension on the curvature of streamlines at the vicinity of the stagnation point region and threshold of purely-elastic instability in the cross-slot two-phase flow problem.
- To investigate the effect of the total viscosity ratio of two fluids on the onset of purely-elastic instability.

Chapter 2

Viscoelastic models and their responses to simple flows and numerical methods

2.1 Constitutive equations

For a fluid which is Newtonian, the stress tensor $\tilde{\boldsymbol{\tau}}_{\boldsymbol{s}}$ has a linear relationship with the deformation rate $\tilde{\dot{\gamma}}$ as:

$$\tilde{\boldsymbol{\tau}}_{\boldsymbol{s}} = \tilde{\eta}_s \tilde{\dot{\gamma}}, \tag{2.1}$$

where $\tilde{\eta}_s$ is the viscosity of the fluid and is a constant at a specified temperature and pressure and is not a function of deformation rate or the previous state of the fluid particles. Any fluid which has a deviation from this behaviour is known as a non-Newtonian fluid. A wide variety of non-Newtonian fluids exists. In this thesis, in particular, we are interested in a group of these fluids known as viscoelastic fluids which exhibit a mixed behaviour of solid elastic materials and viscous fluids, simultaneously. Viscoelastic fluids exhibit a number of counter intuitive phenomena due to the existence of fluid memory from the history of the deformation. These specific behaviours for viscoelastic materials suggests that in order to predict their behaviour correctly, an alternative constitutive equation to equation 2.1 should be employed. Here, four different differential constitutive equations, namely the upper-convective Maxwell (UCM), the Oldroyd-B (Oldroyd, 1950), the simplified Phan-Thien and Tanner (sPTT) (Phan-Thien and Tanner, 1977) and the finitely extensible non-linear elastic (FENE-P) (Bird et al., 1980) models, have been chosen to investigate the effect of viscoelasticity on the flow fields of the problems to be studied.

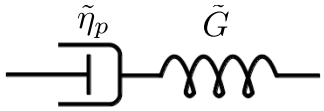

Figure 2.1: Representation of the Maxwell model as a combination of a dash-pot and a spring.

2.1.1 Upper-convective Maxwell and Oldroyd-B models

Maxwell (1867) was the first researcher who mathematically represented viscoelastic behaviour via a linear combination of fluid like and elastic response as a dash-pot and a spring in series as shown in figure 2.1.

For a shearing flow, Maxwell suggested that fluids exhibiting viscoelastic behaviour could be simply expressed by Newton's law of viscosity together with Hooke's law of elasticity as:

$$\tilde{\boldsymbol{\tau}} + \tilde{\lambda}\frac{\partial \tilde{\boldsymbol{\tau}}}{\partial \tilde{t}} = \tilde{\eta}_p(\nabla\tilde{\boldsymbol{u}} + \nabla\tilde{\boldsymbol{u}}^T), \tag{2.2}$$

where $\tilde{\lambda} = \frac{\tilde{\eta}_p}{\tilde{G}}$ is the "relaxation" time of the fluid, $\tilde{\eta}_p$ is the viscosity of the fluid and $\tilde{G}$ is the elastic modulus. Although this model includes a relaxation time and therefore elasticity, the prediction is only valid for small amplitude displacements, since it is not independent of reference frame (Oldroyd, 1950).

Following the concepts presented by Maxwell (1867), the upper-convected Maxwell (UCM) model was proposed by Oldroyd (1950) as a generalisation of the Maxwell material for the case of large deformations using an upper-convected time derivative. The model can be written as:

$$\tilde{\boldsymbol{\tau}} + \tilde{\lambda}\overset{\nabla}{\tilde{\boldsymbol{\tau}}} = \tilde{\eta}_p(\nabla\tilde{\boldsymbol{u}} + \nabla\tilde{\boldsymbol{u}}^T), \tag{2.3}$$

in continuum mechanics, including fluid dynamics, an upper-convected time derivative, is the rate of change of a tensor property of a fluid that is written in the coordinate system rotating and stretching with the fluid. The upper-convective derivative of the extra-stress tensor, $\overset{\nabla}{\tilde{\boldsymbol{\tau}}}$, is therefore defined as:

$$\overset{\nabla}{\tilde{\boldsymbol{\tau}}} = \frac{D}{D\tilde{t}}(\tilde{\boldsymbol{\tau}}) - (\tilde{\boldsymbol{\tau}}.\nabla\tilde{\boldsymbol{u}} + \nabla\tilde{\boldsymbol{u}}^T.\tilde{\boldsymbol{\tau}}), \tag{2.4}$$

where the material derivative of an arbitrary matrix $\tilde{\boldsymbol{Q}}$ is defined as $\frac{D}{D\tilde{t}}(\tilde{\boldsymbol{Q}}) = (\frac{\partial\tilde{\boldsymbol{Q}}}{\partial\tilde{t}} + \tilde{\boldsymbol{u}}.\nabla\tilde{\boldsymbol{Q}})$.

The Oldroyd-B model is one of the simplest constitutive models used to describe the flow of viscoelastic fluids that includes the history of the flow. This model is equivalent to an assembled Maxwell element in parallel with a Newtonian solvent counterpart as illustrated in figure 2.2. The total stress $\tilde{\tau}_t$ in this model can be calculated as:

$$\tilde{\boldsymbol{\tau}}_t = \tilde{\boldsymbol{\tau}} + \tilde{\boldsymbol{\tau}}_s, \tag{2.5}$$

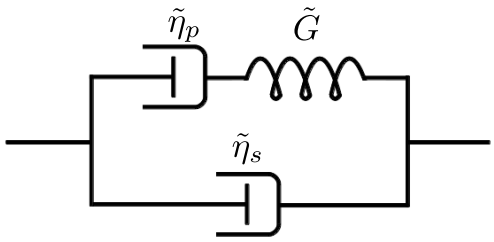

Figure 2.2: Representation of the Oldroyd-B model as a combination of dash-pots and spring.

where $\tilde{\boldsymbol{\tau}}_{\boldsymbol{s}}$ and $\tilde{\boldsymbol{\tau}}$ can be calculated from equations 2.1 and 2.3, respectively and in the limiting case that $\tilde{\eta}_s = 0$ the UCM model will be recovered.

2.1.2 Simplified Phan-Thien and Tanner model

The simplified Phan-Thien and Tanner constitutive model (sPTT) is derived from network theory (Phan-Thien and Tanner, 1977) and is a suitable model for simulation of shear-thinning polymeric fluids (Bird et al., 1987). Similar to the Oldroyd-B model, the total stress $\tilde{\boldsymbol{\tau}}_t$ can be calculated as a summation of a Newtonian solvent contribution $\tilde{\boldsymbol{\tau}}_s$ and an extra tensor $\tilde{\boldsymbol{\tau}}$ representing the polymeric contribution of the stress tensor as in equation 2.5, where the extra-stress tensor using the simplified Phan-Thien and Tanner (sPTT) model may be calculated as follows:

$$f_1\tilde{\boldsymbol{\tau}} + \tilde{\lambda}\overset{\nabla}{\tilde{\boldsymbol{\tau}}} = \tilde{\eta}_p(\nabla\tilde{\boldsymbol{u}} + \nabla\tilde{\boldsymbol{u}}^T). \tag{2.6}$$

Here, the f_1 function for the linear-sPTT model is defined as follows:

$$f_1 = 1 + \alpha\frac{\tilde{\lambda}}{\tilde{\eta}_p}Tr(\tilde{\boldsymbol{\tau}}), \tag{2.7}$$

where α is the extensibility parameter and in the limiting case that $\alpha = 0$ the sPTT constitutive equation reduces to the Oldroyd-B model. Additionally, if $\tilde{\eta}_s = 0$ the UCM model is recovered.

2.1.3 Finitely extensible non-linear elastic model

One other constitutive equation which has frequently been used to simulate the shear-thinning behaviour of viscoelastic materials is the finitely extensible non-linear elastic (FENE-P) model (Bird et al., 1980). This model is based on a molecular, coarse-grained treatment of the polymer molecules as a collection of beads and springs. The model suggests that dilute polymeric fluids are a mixture of the solvent and polymer, where the solvent can stretch and convect the polymer molecules that are assumed to behave like elastic springs. In the limiting case of the spring being able to be stretched

infinitely, the model becomes the simpler macroscopic Oldroyd-B model. The FENE-P model may be presented in the following form:

$$\tilde{\tau} + \tilde{\lambda}(\frac{\overset{\nabla}{\tilde{\boldsymbol{\tau}}}}{f_2}) = \frac{a\tilde{\eta}_p}{f_2}(\nabla\tilde{\boldsymbol{u}} + \nabla\tilde{\boldsymbol{u}}^T) - a\tilde{\eta}_p(\frac{D}{D\tilde{t}}(\frac{1}{f_2}))\boldsymbol{I}, \tag{2.8}$$

where $a = \frac{L^2}{L^2-3}$ and L^2 is also called the extensibility parameter. The f_2 function for the FENE-P model is defined as:

$$f_2 = \frac{L^2 + \frac{\tilde{\lambda}}{a\tilde{\eta}_p}Tr(\tilde{\boldsymbol{\tau}})}{L^2 - 3}. \tag{2.9}$$

In the limiting case that the extensibility parameter aproaches infinity (i.e. $L^2 \to \infty$) the model reduces to the Oldroyd-B model. Additionally once the solvent viscosity is set to zero (i.e. $\tilde{\eta}_s = 0$), the UCM model is recovered.

2.1.4 Conformation law for viscoelastic fluids

For polymeric fluids, the constitutive equations can often be defined as a function of a state variable known as the conformation tensor $\boldsymbol{A}$. One can regard the conformation tensor as a measure of an internal strain (see Leonov (1976), Dashner and VanArsdale (1981)) or as a quantity that is directly measurable in optical measurements (see Peterlin (1976)). In this formulation, an evolution equation for the conformation tensor can be written as:

$$\tilde{\lambda}\ \overset{\nabla}{\boldsymbol{A}} = \boldsymbol{F(A)}, \tag{2.10}$$

where the tensor $F(\boldsymbol{A})$ takes different forms in various models. For the Oldroyd-B model, this function can be presented as

$$F(\boldsymbol{A}) = \boldsymbol{I} - \boldsymbol{A}, \tag{2.11}$$

where $\boldsymbol{I}$ is the identity tensor. For the sPTT model, the $F(\boldsymbol{A})$ function may presented as:

$$F(\boldsymbol{A}) = (1 + \alpha(Tr(\boldsymbol{A}) - 3))(\boldsymbol{I} - \boldsymbol{A}). \tag{2.12}$$

In this presentation, the extra-stress tensor for the Oldroyd-B and sPTT models can be calculated as:

$$\tilde{\boldsymbol{\tau}} = \frac{\tilde{\eta}_p}{\tilde{\lambda}}(\boldsymbol{A} - \boldsymbol{I}). \tag{2.13}$$

In the FENE-P model, the $F(\boldsymbol{A})$ function may expressed as:

$$F(\boldsymbol{A}) = \frac{\boldsymbol{I}}{1 - 3/L^2} - \frac{\boldsymbol{A}}{1 - Tr(\boldsymbol{A})/L^2}. \tag{2.14}$$

The extra-stress tensor for the FENE-P model can be calculated as:

$$\tilde{\boldsymbol{\tau}} = \frac{\tilde{\eta}_p}{\tilde{\lambda}} \frac{1}{1-(Tr(\boldsymbol{A})/L^2)}(\boldsymbol{A} - \frac{1-\frac{Tr(\boldsymbol{A})}{L^2}}{1-3/L^2}\boldsymbol{I}). \tag{2.15}$$

2.2 Standard rheological flows

Experimental rheologists have reported a vast literature of observations on viscoelastic fluids, in standard "rheological" flows. Before we start to use the described viscoelastic constitutive equations in complex flows, in this section, some of the non-Newtonian effects that these constitutive equations are capturing in simple flows will be discussed first. The two flows studied in this section (i.e. simple shear and simple elongational flows) may be considered as *the* classic flows frequently used in rheological measurements.

2.2.1 Steady simple shear flow (SSSF)

Steady simple shear flow is the most common flow type investigated in rheology. Figure 2.3 shows a two-dimensional schematic of the velocity profile in simple shear flow. In a simple shear flows, the flowfield is known to have a rectilinear distribution with layers of fluid sliding past each other. In this type of flow, the velocity only varies in one direction, in the $\tilde{x}_2$ direction as illustrated in figure 2.3. In practical rheometery, this flow distribution is only achieved in the narrow gap limit (when $\tilde{H} \to 0$), and at relatively small Reynolds numbers when inertial effects are insignificant.

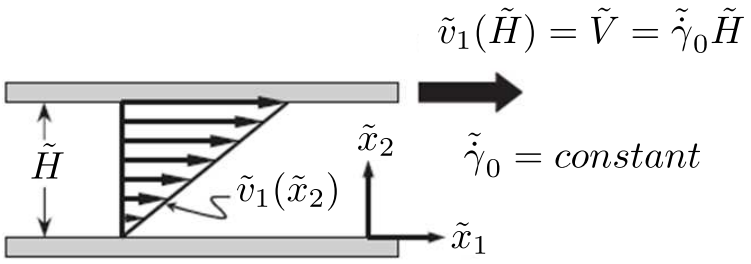

Figure 2.3: Flowfield in simple shear (Morrison, 2001).

Steady simple shear flow can be generated by putting a fluid sample between two parallel walls and moving one of the walls at a constant velocity in a specific direction. There are several configuration which experimentalists use to generate an approximate simple shear flow and in Figure 2.4 some of them are presented.

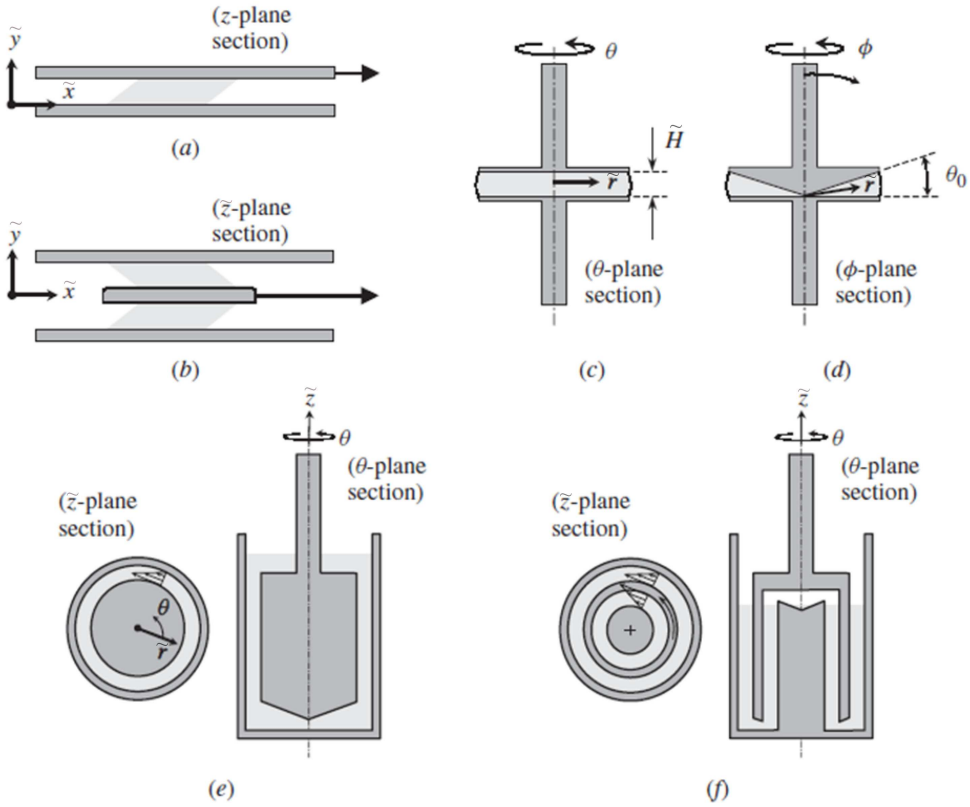

Figure 2.4: Geometries used to produce shear flow in commercial and research rheometers. (a) Rectilinear parallel plate. (b) Rectilinear double parallel plate. (c) Torsional parallel plate or parallel disk. (d) Torsional cone and plate. (e) Couette or cup and bob. (f) Double-walled Couette (Morrison, 2001).

In the following subsections the steady simple shear flow problem will be solved for the UCM, Oldroyd-B, sPTT and FENE-P models.

Upper-convective Maxwell and Oldroyd-B models

Here, the response of both the UCM and Oldroyd-B models in simple shear flows will be investigated. Knowing that the velocity vector for simple shear flow in Cartesian coordinates is defined as:

$$\boldsymbol{u} = (\tilde{\dot{\gamma}}\tilde{x}_2, 0, 0)_{\tilde{x}_1,\tilde{x}_2,\tilde{x}_3}, \tag{2.16}$$

now the tensor $\nabla \boldsymbol{u}$ is:

$$\nabla \boldsymbol{u} = \begin{pmatrix} 0 & 0 & 0 \\ \tilde{\dot{\gamma}} & 0 & 0 \\ 0 & 0 & 0 \end{pmatrix}, \tag{2.17}$$

so the UCM model (i.e. equation 2.3) in tensor form can be written as:

$$\begin{pmatrix} \tilde{\tau}_{xx} & \tilde{\tau}_{xy} & \tilde{\tau}_{xz} \\ \tilde{\tau}_{xy} & \tilde{\tau}_{yy} & \tilde{\tau}_{yz} \\ \tilde{\tau}_{xz} & \tilde{\tau}_{yz} & \tilde{\tau}_{zz} \end{pmatrix} - \begin{pmatrix} \tilde{\lambda}\tilde{\dot{\gamma}}\tilde{\tau}_{xy} & 0 & 0 \\ \tilde{\lambda}\tilde{\dot{\gamma}}\tilde{\tau}_{yy} & 0 & 0 \\ 0 & 0 & 0 \end{pmatrix} - \begin{pmatrix} \tilde{\lambda}\tilde{\dot{\gamma}}\tilde{\tau}_{xy} & \tilde{\lambda}\tilde{\dot{\gamma}}\tilde{\tau}_{yy} & 0 \\ 0 & 0 & 0 \\ 0 & 0 & 0 \end{pmatrix} = \begin{pmatrix} 0 & \tilde{\eta}_p\tilde{\dot{\gamma}} & 0 \\ \tilde{\eta}_p\tilde{\dot{\gamma}} & 0 & 0 \\ 0 & 0 & 0 \end{pmatrix}, \tag{2.18}$$

which gives the following scalar equations:

$$\tilde{\tau}_{yy} = \tilde{\tau}_{yz} = \tilde{\tau}_{zz} = \tilde{\tau}_{xz} = 0, \tag{2.19}$$

$$\tilde{\tau}_{xx} = 2\tilde{\lambda}\tilde{\dot{\gamma}}\tilde{\tau}_{xy}, \tag{2.20}$$

$$\tilde{\tau}_{xy} - \tilde{\lambda}\tilde{\dot{\gamma}}\tilde{\tau}_{yy} = \tilde{\eta}_p\tilde{\dot{\gamma}}. \tag{2.21}$$

From equation 2.19 and 2.21 one can obtain:

$$\tilde{\tau}_{xy} = \tilde{\eta}_p\tilde{\dot{\gamma}}. \tag{2.22}$$

From equation 2.22 and 2.20 one can obtain :

$$\tilde{\tau}_{xx} = 2\tilde{\lambda}\tilde{\eta}_p\tilde{\dot{\gamma}}^2. \tag{2.23}$$

As the Oldroyd-B model is thus equal to the UCM model plus a Newtonian solvent, the total stress for the Oldroyd-B model in SSSF can be presented as:

$$\tilde{\boldsymbol{\tau}} = \begin{pmatrix} 2\tilde{\lambda}\tilde{\eta}_p\tilde{\dot{\gamma}}^2 & (\tilde{\eta}_p + \tilde{\eta}_s)\tilde{\dot{\gamma}} & 0 \\ (\tilde{\eta}_p + \tilde{\eta}_s)\tilde{\dot{\gamma}} & 0 & 0 \\ 0 & 0 & 0 \end{pmatrix} \tag{2.24}$$

One can realize that the presence of the polymers has made two changes to the Newtonian stress: firstly, the shear viscosity is changed from $\tilde{\eta}_s$ to $\tilde{\eta}_p + \tilde{\eta}_s$. Secondly, there is a difference between the two diagonal stress components $\tilde{\tau}_{xx}$ and $\tilde{\tau}_{yy}$. This difference is called the first normal-stress difference (i.e. $N_1 = \tilde{\tau}_{xx} - \tilde{\tau}_{yy} = 2\tilde{\lambda}\tilde{\eta}_p\tilde{\dot{\gamma}}^2$). As a stress

acting along the flow lines (xx-direction) it has the opposite sign to pressure so it acts like a tension: the streamlines are like stretched rubber bands. N_1 is the driving force behind the rod-climbing experiment (shown in Figure 2.5) also known as the "Weissenberg" effect (Bird et al., 1987). In this problem, the rod in the middle is rotated, causing a shear flow round the outside. The streamlines are circular, so their tension causes the fluid to move to the middle (the only place it can go is therefore up the rod). Similar to the first normal-stress difference one can define the second normal-stress difference as $N_2 = \tilde{\tau}_{yy} - \tilde{\tau}_{zz}$ in which the Oldroyd-B model predicts a zero value (i.e. $N_2 = 0$) in SSSF.

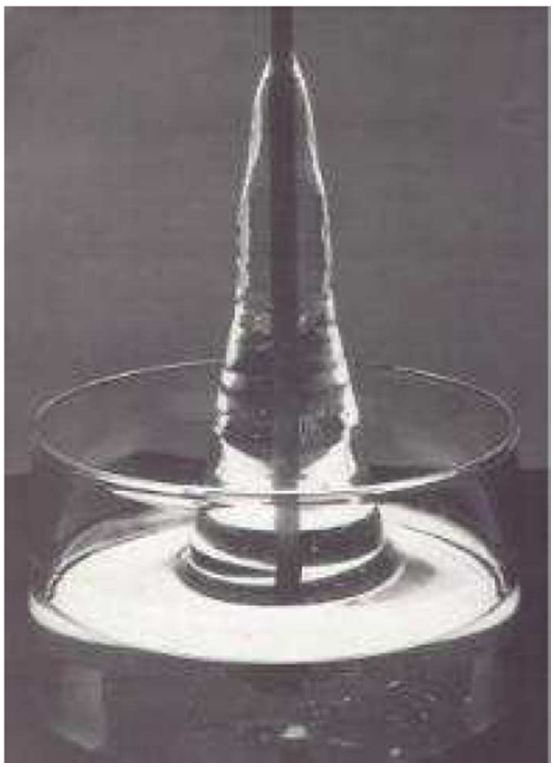

Figure 2.5: Rod-climbing experiment (Boger and Walters, 2012).

Simplified Phan-Thien and Tanner model

The sPTT model in its matrix form can be represented as:

$$\begin{aligned}(1+\frac{\tilde{\lambda}\alpha}{\tilde{\eta}_p}(\tilde{\tau}_{xx}+\tilde{\tau}_{yy}+\tilde{\tau}_{zz}))\begin{pmatrix}\tilde{\tau}_{xx} & \tilde{\tau}_{xy} & \tilde{\tau}_{xz}\\ \tilde{\tau}_{xy} & \tilde{\tau}_{yy} & \tilde{\tau}_{yz}\\ \tilde{\tau}_{xz} & \tilde{\tau}_{yz} & \tilde{\tau}_{zz}\end{pmatrix} - \begin{pmatrix}\tilde{\lambda}\tilde{\dot{\gamma}}\tilde{\tau}_{xy} & 0 & 0\\ \tilde{\lambda}\tilde{\dot{\gamma}}\tilde{\tau}_{yy} & 0 & 0\\ 0 & 0 & 0\end{pmatrix}\\ - \begin{pmatrix}\tilde{\lambda}\tilde{\dot{\gamma}}\tilde{\tau}_{xy} & \tilde{\lambda}\tilde{\dot{\gamma}}\tilde{\tau}_{yy} & 0\\ 0 & 0 & 0\\ 0 & 0 & 0\end{pmatrix} = \begin{pmatrix}0 & \tilde{\eta}_p\tilde{\dot{\gamma}} & 0\\ \tilde{\eta}_p\tilde{\dot{\gamma}} & 0 & 0\\ 0 & 0 & 0\end{pmatrix},\end{aligned} \tag{2.25}$$

which gives the following scalar equations:

$$\begin{aligned}(1+\frac{\tilde{\lambda}\alpha}{\tilde{\eta}_p}(\tilde{\tau}_{xx}+\tilde{\tau}_{yy}+\tilde{\tau}_{zz}))(\tilde{\tau}_{yy}) = (1+\frac{\tilde{\lambda}\alpha}{\tilde{\eta}_p}(\tilde{\tau}_{xx}+\tilde{\tau}_{yy}+\tilde{\tau}_{zz}))(\tilde{\tau}_{yz}) \\ = (1+\frac{\tilde{\lambda}\alpha}{\tilde{\eta}_p}(\tilde{\tau}_{xx}+\tilde{\tau}_{yy}+\tilde{\tau}_{zz}))(\tilde{\tau}_{zz}) = 0,\end{aligned} \tag{2.26}$$

$$(1+\frac{\tilde{\lambda}\alpha}{\tilde{\eta}_p}(\tilde{\tau}_{xx}+\tilde{\tau}_{yy}+\tilde{\tau}_{zz}))\tilde{\tau}_{xx} = 2\tilde{\lambda}\tilde{\dot{\gamma}}\tilde{\tau}_{xy}, \tag{2.27}$$

$$(1+\frac{\tilde{\lambda}\alpha}{\tilde{\eta}_p}(\tilde{\tau}_{xx}+\tilde{\tau}_{yy}+\tilde{\tau}_{zz}))\tilde{\tau}_{xy} - \tilde{\lambda}\tilde{\dot{\gamma}}\tilde{\tau}_{yy} = \tilde{\eta}_p\tilde{\dot{\gamma}}. \tag{2.28}$$

From equation 2.26 one can say $\tilde{\tau}_{yy} = \tilde{\tau}_{yz} = \tilde{\tau}_{zz} = 0$ (due to the non-homogeneous form of equation 2.28 the $(1+\frac{\tilde{\lambda}\alpha}{\tilde{\eta}_p}(\tilde{\tau}_{xx}+\tilde{\tau}_{yy}+\tilde{\tau}_{zz}))$ term cannot be equal to zero so $\tilde{\tau}_{yy} = \tilde{\tau}_{yz} = \tilde{\tau}_{zz} = 0$). From equation 2.27 we have:

$$(1+\frac{\tilde{\lambda}\alpha}{\tilde{\eta}_p}(\tilde{\tau}_{xx}+\tilde{\tau}_{yy}+\tilde{\tau}_{zz})) = \frac{2\tilde{\lambda}\tilde{\dot{\gamma}}\tilde{\tau}_{xy}}{\tilde{\tau}_{xx}} \tag{2.29}$$

substituting equation 2.29, into equation 2.28, one can obtain $\tilde{\tau}_{xy}$ as a function of $\tilde{\tau}_{xx}$ as follows:

$$\tilde{\tau}_{xx} = \frac{2\tilde{\lambda}}{\tilde{\eta}_p}\tilde{\tau}_{xy}^2, \tag{2.30}$$

Now, by replacing equation 2.30 into equation 2.29, one can calculated the shear stress as:

$$\tilde{\tau}_{xy} = \tilde{\eta}_p\left(\frac{1}{6}\frac{6^{1/3}(\tilde{\dot{\gamma}}^3(\sqrt{3}\sqrt{\frac{27\alpha\tilde{\dot{\gamma}}^2\tilde{\lambda}^2+2}{\tilde{\lambda}^2\alpha}}+9\tilde{\dot{\gamma}})\tilde{\lambda}^4\alpha^2)^{1/3}}{\tilde{\lambda}^2\tilde{\dot{\gamma}}\alpha} - \frac{1}{6}\frac{\tilde{\dot{\gamma}}6^{2/3}}{(\tilde{\dot{\gamma}}^3(\sqrt{3}\sqrt{\frac{27\alpha\tilde{\dot{\gamma}}^2\tilde{\lambda}^2+2}{\tilde{\lambda}^2\alpha}}+9\tilde{\dot{\gamma}})\tilde{\lambda}^4\alpha^2)^{1/3}}\right). \tag{2.31}$$

From equation 2.31 one can realize that as $\tilde{\dot{\gamma}} \to \infty$ the extra shear stress should scale as $\tilde{\tau}_{xy} \propto \tilde{\dot{\gamma}}^{1/3}$. Consequently, a combination of this scaling with equation 2.30 would suggest that in the limit that $\tilde{\dot{\gamma}} \to \infty$ the extra normal-stress should scale as $\tilde{\tau}_{xx} \propto \tilde{\dot{\gamma}}^{2/3}$.

Defining the viscosity of a viscoelastic fluid as $\tilde{\eta} = \frac{\tilde{\tau}_{t,xy}}{\tilde{\dot{\gamma}}}$ where $\tilde{\tau}_{t,xy} = \tilde{\tau}_{xy} + \tilde{\eta}_s\tilde{\dot{\gamma}}$, one can realize that unlike the Oldroyd-B model, the viscosity of sPTT fluids in not constant but depends on $\tilde{\dot{\gamma}}$, α and $\tilde{\lambda}$. In steady simple shear flows, the analysis suggests a non-zero value for the first normal-stress difference N_1 and a zero second normal-stress difference N_2. Figure 2.6 represents the variation of the shear viscosity of sPTT fluids versus $\tilde{\lambda}\tilde{\dot{\gamma}}$ for different extensibility parameter α at a constant solvent-to-total viscosity ratio $\beta = 1/9$. As shown, for a typical sPTT fluid, the viscosity of the fluid varies with shear rate. At small shear rates, as the shear rate approaches zero, the viscosity reaches to a constant value know as the zero shear rate viscosity. As shear rate increases and asymptotes to infinity, the shear viscosity exhibits another constant value which is equal to the viscosity of the solvent part of the fluid (β in dimensionless form). In between

these two limits, by increasing the shear rate, the viscosity reduces from the zero shear rate viscosity to the value of the solvent viscosity. As shown in Figure 2.6, by increasing the value of the extensibility parameter α the shear-thinning behaviour of the sPTT fluids starts at smaller values of shear rate. The inset in Figure 2.6, shows variation

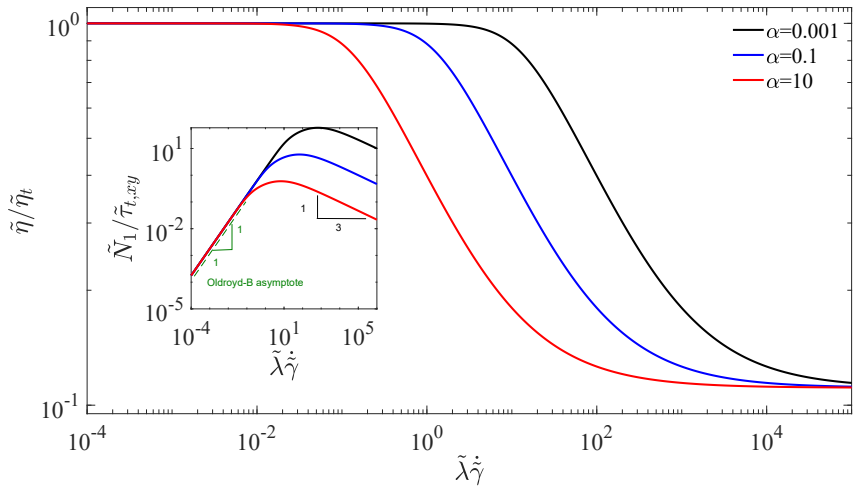

Figure 2.6: Variation of shear viscosity and normal-stress with shear rate for different values of the extensibility parameter α with $\beta = 1/9$.

of the first normal-stress difference made dimensionless by the total shear stress (i.e. $\tilde{\tau}_{t,xy} = \tilde{\tau}_{xy} + \tilde{\eta}_s\dot{\tilde{\gamma}}$). As shown in Figures 2.6 - 2.7, in the small shear rate limit (i.e. $\dot{\tilde{\gamma}} \to 0$), the viscosity of the fluid tends toward the constant value predicted by the Oldroyd-B model and from equation 2.31 one can deduce that the stress should scale linearly and the normal stresses should scale as $\tilde{\tau}_{xx} \propto \dot{\tilde{\gamma}}^2$ (identical to the Oldroyd-B prediction). As discussed earlier, by increasing the shear rate and approaching the $\dot{\tilde{\gamma}} \to \infty$ limit, the normal-stress scales as $\tilde{\tau}_{xx} \propto \dot{\tilde{\gamma}}^{2/3}$. By including the contribution of the solvent shear stress in the total shear stress (i.e. $\tilde{\tau}_{t,xy}$) the dominant term in the high shear rate limit would be the Newtonian contribution and will scale as $\tilde{\tau}_{t,xy} \propto \dot{\tilde{\gamma}}$. So, as $\dot{\tilde{\gamma}} \to \infty$ the normalized normal-stress would scale as $N_1/\tilde{\tau}_{t,xy} \propto \dot{\tilde{\gamma}}^{-1/3}$ as shown in Figure 2.6 - 2.7. The presented results also suggest that at a constant shear rate in the shear-thinning regime, by increasing the extensibility parameter α, both the shear viscosity and the maximum dimensionless normal-stress decrease.

Figure 2.7 represents the shear-thinning behaviour of sPTT fluids for different values of the solvent-to-total viscosity ratio parameter β. From equation 2.31 and the definition of the shear viscosity one can show for $\beta = 0$ (i.e. $\tilde{\eta}_s = 0$), in the limit that the shear rate goes to infinity, the shear viscosity should asymptote to zero as $\tilde{\eta} = \tilde{\eta}_p \propto \dot{\tilde{\gamma}}^{2/3}$. In this specific case (no solvent contribution), the dimensionless normal-stress scales as $N_1/\tilde{\tau}_{t,xy} \propto \dot{\tilde{\gamma}}^{1/3}$ (see Figure 2.7). As illustrated in Figure 2.7, by adding the solvent

contribution, the dimensionless first normal-stress difference decreases which is related to the growth of the $\tilde{\tau}_{t,xy}$ term. Also, by increasing the shear rate, the viscosity of the fluid tends toward the dimensionless viscosity of the solvent β.

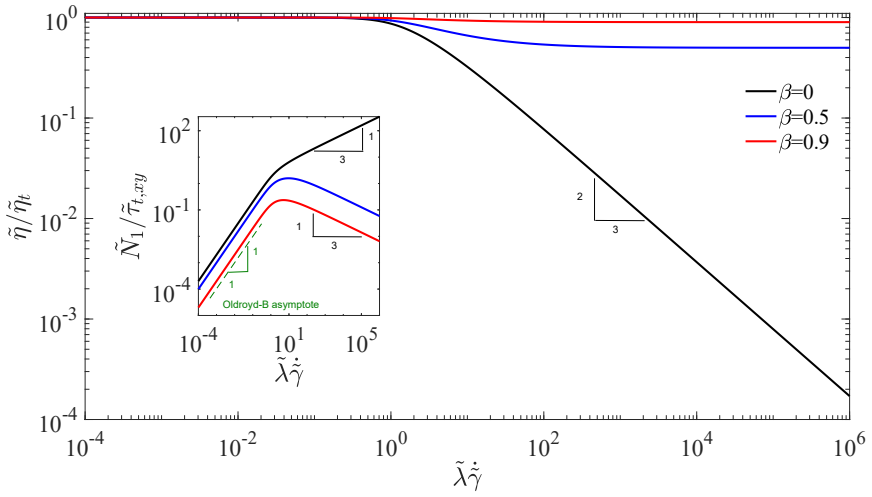

Figure 2.7: Variation of shear viscosity and normal-stress with shear rate for different values of solvent-to-total viscosity ratio with $\alpha = 0.1$.

FENE-P model

Expanding the upper-convective derivative in equation 2.8, the FENE-P model can be rewritten as:

$$\tilde{\tau} + \tilde{\lambda}((\overset{\nabla}{\tilde{\boldsymbol{\tau}}}\ \frac{1}{f_2}) + \tilde{\boldsymbol{\tau}}(\overset{\nabla}{\frac{1}{f_2}})) = \frac{a\tilde{\eta}_p}{f_2}(\nabla\tilde{\boldsymbol{u}} + \nabla\tilde{\boldsymbol{u}}^T) - a\tilde{\eta}_p(\frac{D}{D\tilde{t}}(\frac{1}{f_2}))\boldsymbol{I}. \tag{2.32}$$

In ideal steady-state shear/extensional flows, the terms $(\overset{\nabla}{\frac{1}{f_2}})$ and $a\tilde{\eta}_p(\frac{D}{D\tilde{t}}(\frac{1}{f_2}))\boldsymbol{I}$ are equal to zero, so the FENE-P model reduces to (Oliveira, 2009):

$$f_2\tilde{\boldsymbol{\tau}} + \tilde{\lambda}\ \overset{\nabla}{\tilde{\boldsymbol{\tau}}} = a\tilde{\eta}_p(\nabla\tilde{\boldsymbol{u}} + \nabla\tilde{\boldsymbol{u}}^T). \tag{2.33}$$

The FENE-P model in its matrix form for pure shear flow can the be represented as:

$$f_2\begin{pmatrix}\tilde{\tau}_{xx} & \tilde{\tau}_{xy} & \tilde{\tau}_{xz}\\ \tilde{\tau}_{xy} & \tilde{\tau}_{yy} & \tilde{\tau}_{yz}\\ \tilde{\tau}_{xz} & \tilde{\tau}_{yz} & \tilde{\tau}_{zz}\end{pmatrix} - \begin{pmatrix}\tilde{\lambda}\dot{\tilde{\gamma}}\tilde{\tau}_{xy} & 0 & 0\\ \tilde{\lambda}\dot{\tilde{\gamma}}\tilde{\tau}_{yy} & 0 & 0\\ 0 & 0 & 0\end{pmatrix} - \begin{pmatrix}\tilde{\lambda}\dot{\tilde{\gamma}}\tilde{\tau}_{xy} & \tilde{\lambda}\dot{\tilde{\gamma}}\tilde{\tau}_{yy} & 0\\ 0 & 0 & 0\\ 0 & 0 & 0\end{pmatrix} = a\begin{pmatrix}0 & \tilde{\eta}_p\dot{\tilde{\gamma}} & 0\\ \tilde{\eta}_p\dot{\tilde{\gamma}} & 0 & 0\\ 0 & 0 & 0\end{pmatrix}, \tag{2.34}$$

which gives three scalar equations:

$$f_2\tilde{\tau}_{yy} = f_2\tilde{\tau}_{yz} = f_2\tilde{\tau}_{zz} = f_2\tilde{\tau}_{xz} = 0, \tag{2.35}$$

$$f_2\tilde{\tau}_{xx} = 2\tilde{\lambda}\dot{\tilde{\gamma}}\tilde{\tau}_{xy}, \tag{2.36}$$

$$f_2\tilde{\tau}_{xy} - \tilde{\lambda}\tilde{\dot{\gamma}}\tilde{\tau}_{yy} = a\tilde{\eta}_p\tilde{\dot{\gamma}}, \tag{2.37}$$

From equation 2.35 one can say $\tilde{\tau}_{yy} = 0$. From equation 2.36 we have:

$$f_2 = \frac{2\tilde{\lambda}\tilde{\dot{\gamma}}\tilde{\tau}_{xy}}{\tilde{\tau}_{xx}}. \tag{2.38}$$

Substituting equation 2.38, into equation 2.37, one can obtain $\tilde{\tau}_{xy}$ as a function of $\tilde{\tau}_{xx}$ as follows:

$$\tilde{\tau}_{xx} = \frac{2\tilde{\lambda}}{a\tilde{\eta}_p}\tilde{\tau}_{xy}^2. \tag{2.39}$$

Now, by using equations 2.38 and 2.39, one can calculated the shear stress as:

$$\tilde{\tau}_{xy} = \tilde{\eta}_p\left(\frac{1}{6}\frac{6^{1/3}ff}{\tilde{\lambda}(L-3)} - \frac{1}{6}\frac{L^2 6^{2/3}}{\tilde{\lambda}ff}\right), \tag{2.40}$$

where function ff is defined as:

$$ff = \left(L^2\left(\sqrt{3}\sqrt{\frac{(27L\tilde{\dot{\gamma}}^2\tilde{\lambda}^2 - 81\tilde{\dot{\gamma}}^2\tilde{\lambda}^2 + 2L^2)}{(L-3)}} + 9\tilde{\dot{\gamma}}\tilde{\lambda}\right)(L-3)^2\right)^{(1/3)}. \tag{2.41}$$

Using the definition of viscosity, one can show that unlike the Oldroyd-B model (but like the sPTT model), the shear viscosity of the FENE-P model is not constant and depends on $\tilde{\dot{\gamma}}$, L^2 and $\tilde{\lambda}$. Also, the first normal-stress difference has a positive value and second normal-stress difference is equal to zero in SSSF.

In Figures 2.8 - 2.9 the variation of the shear viscosity and the first normal-stress difference with shear rate for different values of the extensibility parameter L^2 and solvent-to-total viscosity ratio parameter β is plotted. As shown, at low shear rates, the viscosity of fluids following the FENE-P model tends to a constant zero shear rate viscosity value. By increasing the shear rate, the fluid initially exhibits a shear-thinning behaviour. As the shear rate goes to higher values, the polymeric contribution of the viscosity tends to zero and the viscosity asymptotes to the value of the solvent. As also shown in Figure 2.8, by increasing the value of the extensibility parameter L^2 the shear-thinning behaviour of the fluid starts at higher values of shear rate which consequently increases the maximum normal-stress magnitude. One can show (see equation 2.40 and 2.41) that at low shear rates the normal-stress scales with $\tilde{\dot{\gamma}}$. On the other hand, in the high shear rate limit (i.e. $\tilde{\dot{\gamma}} \to \infty$), from equation 2.40, one can realize that the extra shear stress should scale as $\tilde{\tau}_{xy} \propto \tilde{\dot{\gamma}}^{1/3}$. Consequently, a combination of this result with equation 2.39 would suggest that in the limit that $\tilde{\dot{\gamma}} \to \infty$ the extra normal-stress should scale as $\tilde{\tau}_{xx} \propto \tilde{\dot{\gamma}}^{2/3}$. This matter suggests that the shear viscosity and normal-stress should scale similarly to sPTT model in the $\tilde{\dot{\gamma}} \to \infty$ limit (as shown in Figures 2.8 - 2.9).

Figure 2.9 show the variation of the shear viscosity with the solvent-to-total viscosity ratio parameter β which is similar to the behaviour seen in the sPTT model.

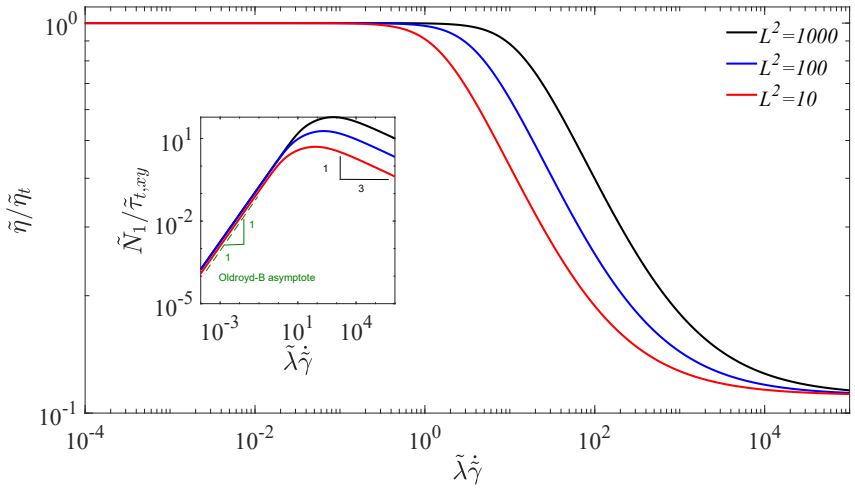

Figure 2.8: Variation of shear viscosity and normal-stress with shear rate for different values of the extensibility parameter L^2 with $\beta = 1/9$.

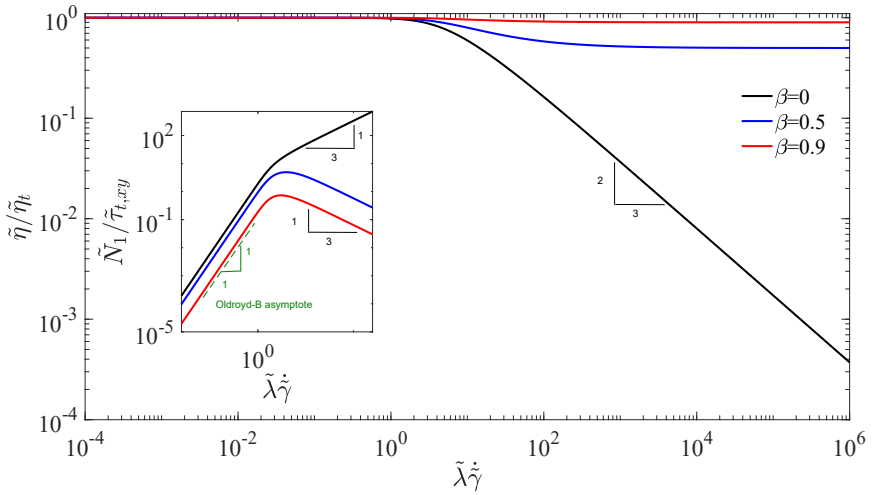

Figure 2.9: Variation of shear viscosity and normal-stress with shear rate for different values of solvent to tall viscosity ratio with $L^2 = 100$.

2.2.2 Shear-free flows

In general, standard simple flows divide into two main categories; shear and shear-free flows. As discussed in section 2.2.1, flows with non-zero off-diagonal components of the deformation tensor $\tilde{\boldsymbol{D}} = \nabla\tilde{\boldsymbol{u}} + \nabla\tilde{\boldsymbol{u}}^T$ are known as shear flows. Elongational flow is a shear-free flow, that experiences a streamwise gradient of velocity. In these types of flow, all the off-diagonal components of the deformation tensor are zero. The diagonal components of the stress tensor are known as the normal-stresses. The off-diagonal components of the stress tensor are presenting the shear stress in different directions. There are three types of simple, shear-free flows that are commonly discussed in rheology, and, like shear flow, they are defined in terms of their velocity profiles (Bird et al., 1987) as:

1-UNIAXIAL ELONGATIONAL FLOW

This type of flow, uniaxial elongational, mainly appears in polymer-processing operations such as fiber spinning and injection molding. Near the centreline of the flow in fibre spinning, for example, fluid particles are stretched uniformly (Figure 2.10).

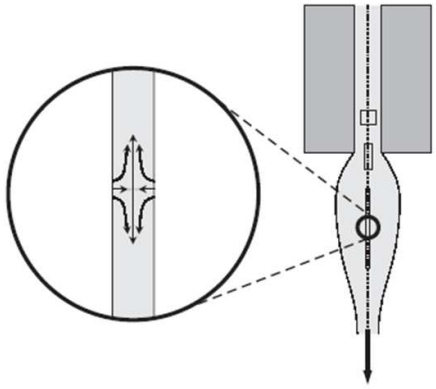

Figure 2.10: uniaxial extension flow appearing in fiber-spinning (Morrison, 2001).

The idealized form of this stretching flow is known as uniaxial extensional flow which is defined by a velocity profile as follows:

$$\tilde{\boldsymbol{u}} = (-\frac{\dot{\epsilon}}{2}x_1, -\frac{\dot{\epsilon}}{2}x_2, \dot{\epsilon}x_3), \qquad \dot{\epsilon} > 0 \tag{2.42}$$

where, $\dot{\epsilon}$ is known as the elongation rate which has a positive value. As shown in equation 2.42, the velocity profile has a 3D distribution with a high elongational flow appearing in one of the dimensions and contraction occurring in other two dimensions, equally. The graphical representation of the velocity profile is shown in Figure 2.11.

2- BIAXIAL STRETCHING FLOW

Once the fluid element is subjected to squeezing in between two lubricated surfaces,

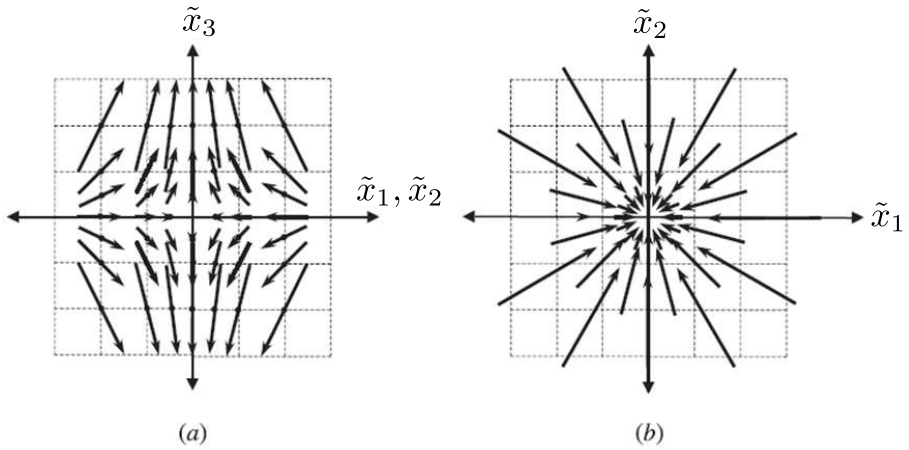

Figure 2.11: Two-dimensional representations of the velocity field in uniaxial elongational flow. (a) The velocity field is the same in in any planes that includes the $\tilde{x}_3$ axis. (b) Velocity field in the $\tilde{x}_1 - \tilde{x}_2$ plane with a stagnation point at the geometric center of the problem (Morrison, 2001).

or once a liquid film is inflating (Figure 2.12), typically, the velocity profile represents a biaxial elongational flow. In this type of flow, the velocity profile follows the same distribution as the uniaxial elongational flows but with $\dot{\epsilon} < 0$, as:

$$\tilde{\boldsymbol{u}} = (-\frac{\dot{\epsilon}}{2}x_1, -\frac{\dot{\epsilon}}{2}x_2, \dot{\epsilon}x_3), \qquad \dot{\epsilon} < 0 \tag{2.43}$$

Maybe a proper way to describe the difference between uniaxial and biaxial elon-

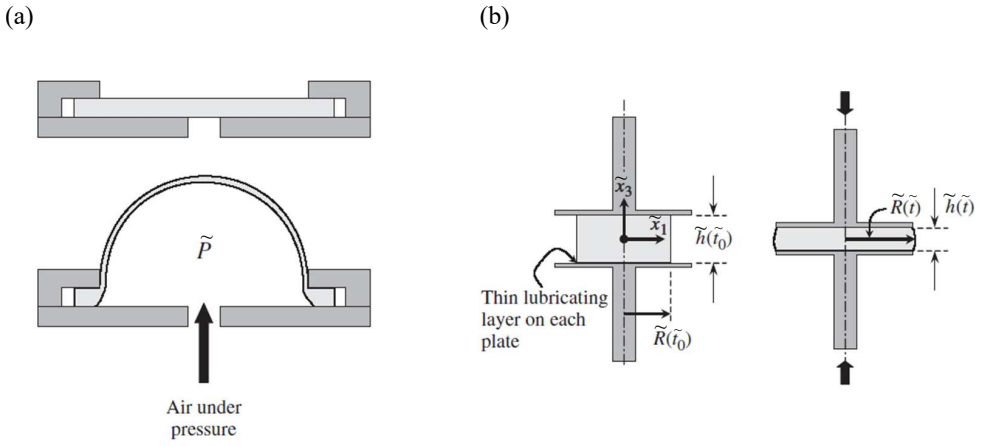

Figure 2.12: Testing configuration that produces biaxial flow by (a) inflating a liquid film and (b) lubricated squeezing (Morrison, 2001).

gational flows is by looking at the deformation of a fluid element in these flows. In uniaxial elongational flow, the fluid element is stretched in one direction, while in the other two directions it is contracting. As an example, for a cube of an incompressible fluid undergoing an uniaxial elongational deformation, the fluid element would be deformed into a cuboid of rectangular shape. One side of the cube would experience a

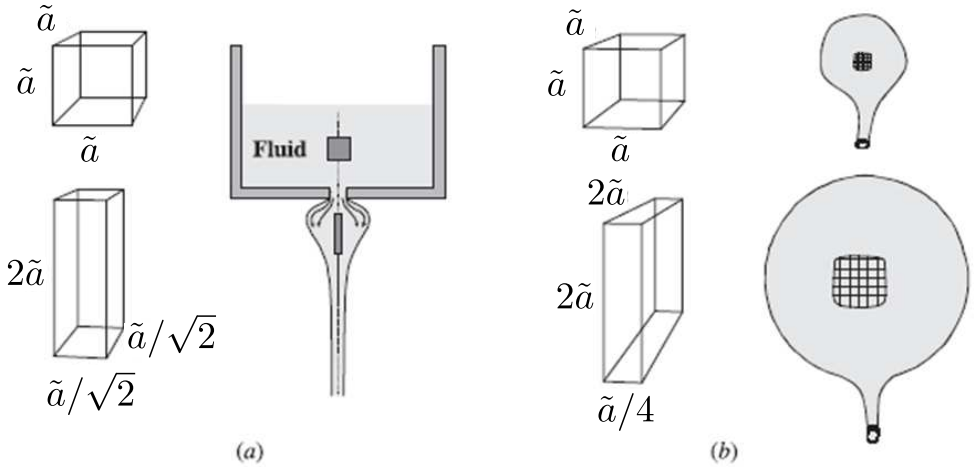

Figure 2.13: Schematics of the deformation (shape change) produced by (a) uniaxial elongational flow, (b) biaxial stretching flow (Morrison, 2001).

stretch and become twice as long as it was, while the other two sides would compress by a factor of $1/\sqrt{2}$. On the other hand, once an incompressible cubic element of the fluid experiences a biaxial elongational flow, in the main direction of deformation, the fluid element will be contracted by a factor of 1/4 and will be stretched in the other two direction by a factor of two. This matter is illustrated in Figure 2.13

3-PLANAR ELONGATIONAL FLOW

One another type of shear-free flow that is in particular interest to this thesis is the planar elongational flow that occurs for example in cross-slot flows.

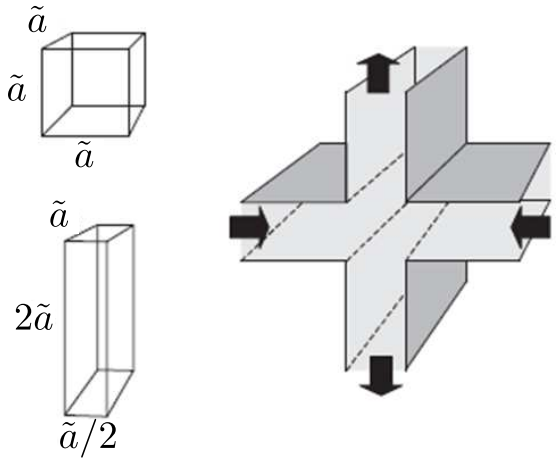

Figure 2.14: Schematics of the deformation (shape change) produced by planar elongational flow (Morrison, 2001).

The velocity profile describing an ideal planar elongation flow may be described as follows:

$$\tilde{\boldsymbol{u}} = (\dot{\epsilon} x_1, -\dot{\epsilon} x_2, 0). \qquad \dot{\epsilon} > 0 \tag{2.44}$$

As one can expect, the planar elongational flow occurs in a two-dimensional planar flow (so no deformation is allowed in the third direction (i.e. $u_3 = 0$)). This flow is of particular interest for researchers, since adding a constraint on one of the directions makes the numerical simulations or experimental studies much easier.

The deformation applied on a cube of an incompressible fluid in planar elongation flow is illustrated in Figure 2.14. If one side of the cube is stretched to twice its length in the flow direction, then the cube must contract by a factor of 2 along the other direction to satisfy conservation of mass.

Planar elongational flows of upper-convective Maxwell and Oldroyd-B fluids

Here, the response of the UCM and Oldroyd-B models in planar elongational flows will be investigated. Knowing that the velocity vector for simple shear flow in Cartesian coordinates is defined as presented in equation 2.44, now the tensor $\nabla \boldsymbol{u}$ is:

$$\nabla \boldsymbol{u} = \begin{pmatrix} \dot{\epsilon} & 0 \\ 0 & -\dot{\epsilon} \end{pmatrix}, \tag{2.45}$$

so the UCM model 2.3 in tensor form can be written:

$$\begin{pmatrix} \tilde{\tau}_{xx} & \tilde{\tau}_{xy} \\ \tilde{\tau}_{xy} & \tilde{\tau}_{yy} \end{pmatrix} - \begin{pmatrix} \tilde{\lambda}\dot{\epsilon}\tilde{\tau}_{xx} & \tilde{\lambda}\dot{\epsilon}\tilde{\tau}_{xy} \\ -\tilde{\lambda}\dot{\epsilon}\tilde{\tau}_{xy} & -\tilde{\lambda}\dot{\epsilon}\tilde{\tau}_{yy} \end{pmatrix} - \begin{pmatrix} \tilde{\lambda}\dot{\epsilon}\tilde{\tau}_{xx} & -\tilde{\lambda}\dot{\epsilon}\tilde{\tau}_{xy} \\ \tilde{\lambda}\dot{\epsilon}\tilde{\tau}_{xy} & -\tilde{\lambda}\dot{\epsilon}\tilde{\tau}_{yy} \end{pmatrix} = 2 \begin{pmatrix} \tilde{\eta}_p\dot{\epsilon} & 0 \\ 0 & -\tilde{\eta}_p\dot{\epsilon} \end{pmatrix}, \tag{2.46}$$

which gives three scalar equations:

$$\tilde{\tau}_{xy} = 0, \tag{2.47}$$

$$\tilde{\tau}_{xx} - 2\tilde{\lambda}\dot{\epsilon}\tilde{\tau}_{xx} = 2\tilde{\eta}_p\dot{\epsilon}, \tag{2.48}$$

$$\tilde{\tau}_{yy} + 2\tilde{\lambda}\dot{\epsilon}\tilde{\tau}_{yy} = -2\tilde{\eta}_p\dot{\epsilon}, \tag{2.49}$$

From equations 2.47 - 2.49 one can obtain:

$$\tilde{\tau}_{xy} = 0, \tilde{\tau}_{xx} = \frac{2\tilde{\eta}_p\dot{\epsilon}}{1 - 2\tilde{\lambda}\dot{\epsilon}}, \tilde{\tau}_{yy} = -\frac{2\tilde{\eta}_p\dot{\epsilon}}{1 + 2\tilde{\lambda}\dot{\epsilon}}. \tag{2.50}$$

In a Newtonian fluid we have:

$$\tilde{\boldsymbol{\tau}}_s = \begin{pmatrix} 2\tilde{\eta}_s\dot{\epsilon} & 0 \\ 0 & -2\tilde{\eta}_s\dot{\epsilon} \end{pmatrix}. \tag{2.51}$$

Using the definition of the extensional viscosity $\tilde{\eta}_e$ as:

$$\tilde{\eta}_e = \frac{\tilde{\tau}_{xx} - \tilde{\tau}_{yy}}{\dot{\epsilon}}. \tag{2.52}$$

Using this definition, the Oldroyd-B fluid has extensional viscosity of:

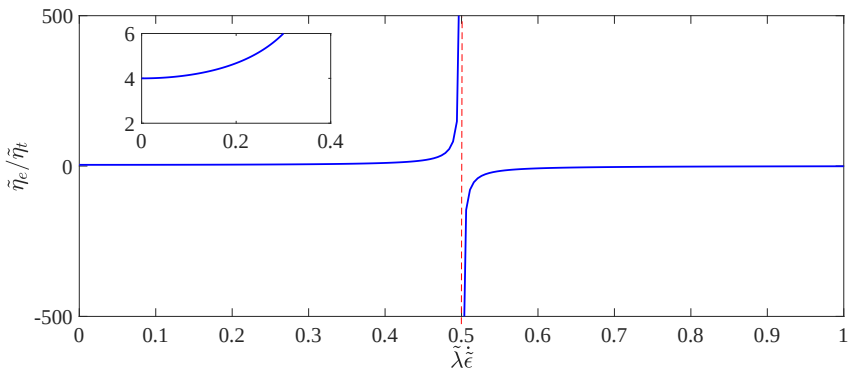

Figure 2.15: Variation of elongational viscosity with strain rate for Oldroyd-B fluids for $\beta = 1/9$.

$$\tilde{\eta}_e = 4\tilde{\eta}_s + \frac{4\tilde{\eta}_p}{1 - 4\tilde{\lambda}^2\dot{\tilde{\epsilon}}^2}. \tag{2.53}$$

Figure 2.15 represents the variation of the viscosity with strain rate for the Oldroyd-B fluids in a planar elongational flows. Using a comparison between the stress distribution of Newtonian fluids (equations 2.51) and Oldroyd-B fluids (equation 2.50) one can realize that the addition of polymer to the flow may add a dependency of the elongational viscosity to both the strain rate and relaxation time of the fluid (as also shown in equation 2.53). This strain dependency of the Oldroyd-B fluids predicts a strain-hardening behaviour (the viscosity increases with increasing strain rate) for low strain rates but for higher strain rates disaster appears; the viscosity diverges at $\tilde{\lambda}\dot{\tilde{\epsilon}} = 0.5$ and at higher strain rates, the model predicts a negative value for the steady-state elongational viscosity! One should note that the Oldroyd-B model initially was designed based on the linear deformation of a spring in shear flows, where the stretch is fairly moderate; for elongational flows as observed here, a linear spring can stretch indefinitely and therefore give infinite stress. The standard approach to circumnavigate this difficulty at this point is to use a non-linear spring law similar to a finite extensibility non-linear elasticity model (i.e. family of FENE models). Similar to the method presented for the Oldroyd-B fluids, one should be able to solve the stress distribution for the sPTT and FENE-P model in planar elongational flow and to extend these analysis to obtain elongational viscosity functions in this type of flowfield (Purnode and Crochet, 1998). Due to the large size of the equations involved in the solution the analytical solutions are not presented here but the results are presented and discussed.

In Figure 2.16 the variation the planar elongational viscosity with strain rates for different values of the extensibility parameters in both the sPTT and FENE-P models are presented. Unlike the Oldroyd-B model which predicts a singularity followed by non-physical negative values of the elongational viscosity after a critical strain rate, in

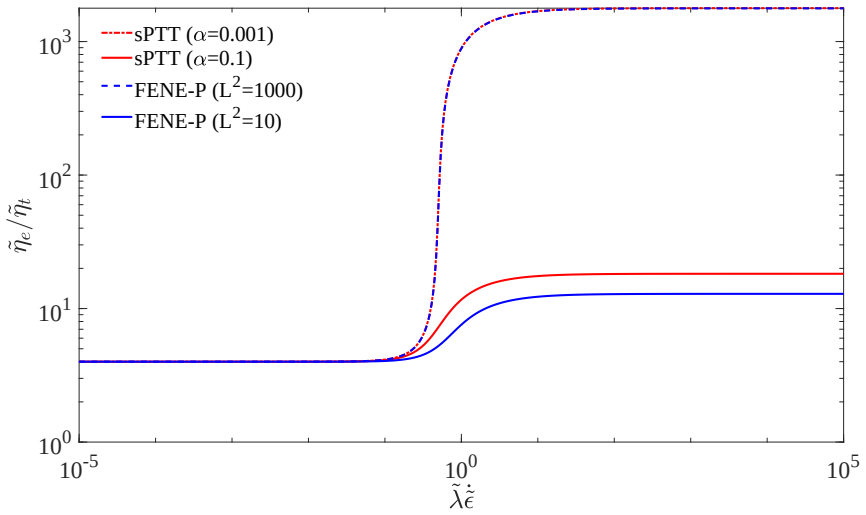

Figure 2.16: Variation of planar elongational viscosity with strain rate for different values of the extensibility parameters in sPTT and FENE-P models for $\beta = 1/9$.

the sPTT and FENE-P models the elongational viscosity varies between two bounded values. In both of these models, at small strain rates the dimensionless elongational viscosity approaches to four which is the Newtonian prediction. In the sPTT model, by increasing the α parameter the maximum value of the elongational viscosity reduces as the strain rate increases. A similar trend can be observed by reducing the L^2 parameter in the FENE-P model.

In Figure 2.17 the variation of the elongational viscosity for different values of solvent-to-total viscosity ratio parameters β is presented. As can be seen, by increasing the value of β, the maximum value of the elongational viscosity at high shear rates reduces. The same trend can be observed for the FENE-P model which is related to the reduction of the polymeric stress contribution.

2.2.3 On the similarity of FENE-P and sPTT models in simple shear flows

As discussed earlier, after expanding the upper convective derivative in the FENE-P model, in the limit where L^2 finds a large value, $a \approx 1$ and the FENE-P model reduces to (Oliveira, 2009):

$$(1 + \frac{\tilde{\lambda}(Tr(\tilde{\boldsymbol{\tau}}))}{\tilde{\eta}_p L^2})\tilde{\boldsymbol{\tau}} + \tilde{\lambda}\overset{\nabla}{\tilde{\boldsymbol{\tau}}} = \tilde{\eta}_p(\nabla\tilde{\boldsymbol{u}} + \nabla\tilde{\boldsymbol{u}}^T). \tag{2.54}$$

This issue suggests that in "viscometric" flows, assuming $L^2 >> 1$, both the FENE-P and sPTT models are identical when $\alpha = \frac{1}{L^2}$. In Appendix E and Figure E.1, this

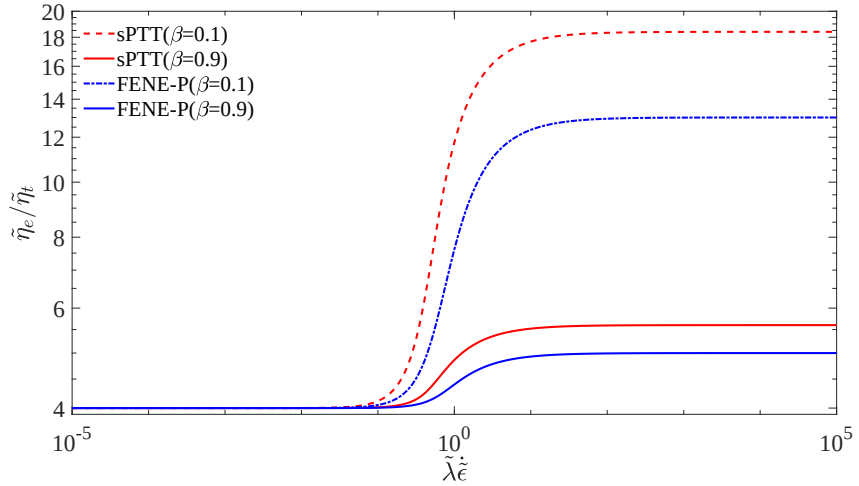

Figure 2.17: Variation of elongational viscosity with strain rate for different values of the solvent-to-total viscosity ratio parameters β in sPTT (α=0.1) and FENE-P ($L^2 = 10$) models.

point is illustrated by plotting viscometric functions of both the SPTT and FENE-P models with $\alpha = 2e - 4$ and $L^2 = 5000$, respectively, with $\beta = 1/9$. In appendix E this effect is investigated in the cross-slot geometry to see if matching steady-state materiel properties alone is sufficient to observe the same flow behaviour in a complex flow.

2.3 Numerical methods

In this section, a brief overview of the employed numerical methods used in this thesis are presented. The governing equations related to the estimation of the extra stress tensor in viscoelastic fluids were represented in section 2.1. In section 2.3.1 a discussion on the governing equation which are required to be coupled with the extra stress tensor for simulations of single-phase flow problems is presented. In section 2.3.2, the equations governing the motion of two-phase fluid flows is discussed using a volume of fluid (VOF) method.

Here the rheoTool platform in the OpenFOAM is used which was previously introduced by Pimenta and Alves (2017). In these types of solvers, instead of dealing with large values of stress components in the global coordinate system, the logarithm of the eigenvalues of the stress tensor in a local coordinate system consisting of the eigenvectors of the stress tensor (i.e. principal axis) are calculated and solved (Afonso et al., 2012; Fattal and Kupferman, 2004). More details about this approach are provided in section 2.3.3. In Appendix A, we develop an analytical platform for the time/space evolution of the extra stress tensor to apply a transformation based on the bounded properties of *arctangent* function (i.e. *Atan*). This analytical platform is embedded in the rheoFoam solver and the merit of this newly-introduced formulation is benchmarked

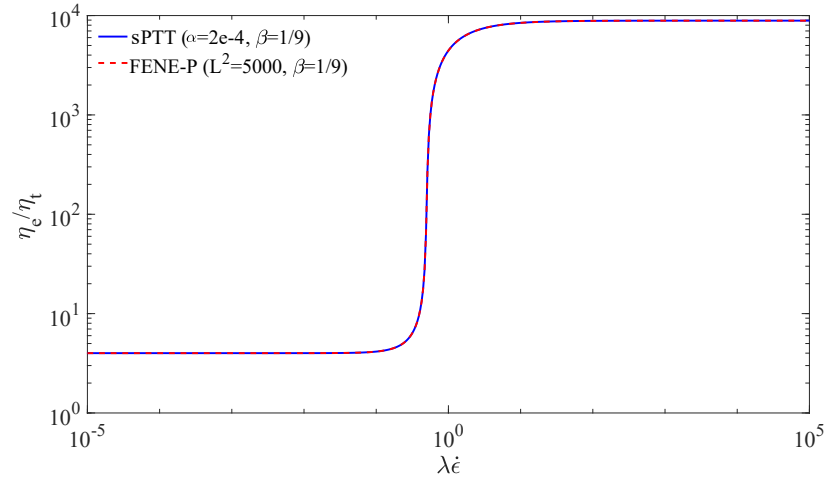

(a)

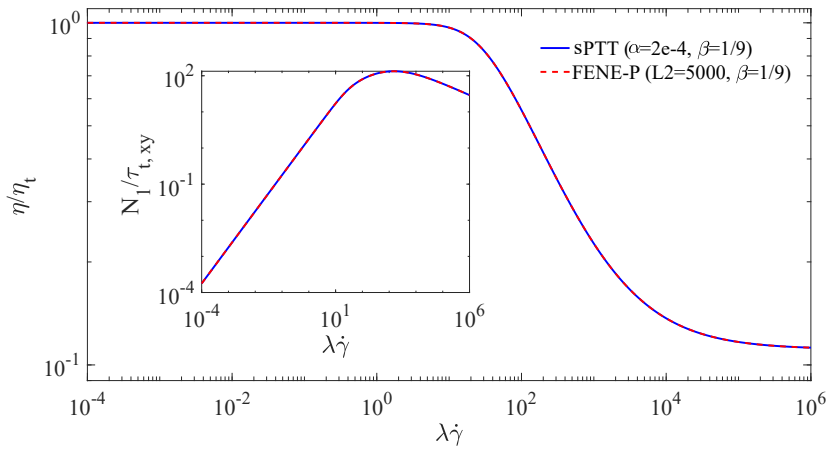

(b)

Figure 2.18: Comparison of rheological properties; (a) elongational viscosity, (b) shear viscosity and the first normal-stress, between sPTT ($\alpha = 2e-4$) and FENE-P ($L^2 = 5000$) models with $\beta = 1/9$, in standard pure shear and planar elongational flows.

in three different geometries.

2.3.1 Governing equation in single-phase flow problems

The governing equations for the motion of single-phase fluids assuming incompressibility are conservation of mass and momentum:

$$\nabla.\tilde{\boldsymbol{u}} = 0, \tag{2.55}$$

$$\tilde{\rho}(\frac{\partial \tilde{\boldsymbol{u}}}{\partial \tilde{t}} + \tilde{\boldsymbol{u}}.\nabla\tilde{\boldsymbol{u}}) = -\nabla\tilde{p} + \nabla.\tilde{\boldsymbol{\tau}} + \tilde{\eta}_s\nabla^2\tilde{\boldsymbol{u}}, \tag{2.56}$$

where $\tilde{\rho}$ is the density of the fluid, $\tilde{\boldsymbol{u}}$ is the velocity vector, $\tilde{\eta}_s$ is the solvent viscosity and $\tilde{\boldsymbol{\tau}}$ is the extra-stress tensor containing the polymeric contribution to the stress (as discussed in subsections 2.1.1 and 2.1.3).

In computational fluid dynamics (CFD), a number of different numerical methods can be applied for discretization of the governing equations used for the simulation of the fluid flow. Amongst these, one of the most popular approaches is the Finite Volume (FV) method in which the computational domain is decomposed into a number of smaller finite control-volumes (Versteeg and Malalasekera, 2007; Baliga and Patankar, 1983; Moukalled et al., 2016). The governing equations describing the problem are integrated over the control volume, and after applying Gauss's theorem, the unknown values related to the control volumes are calculated using an iterative approach (Versteeg and Malalasekera, 2007). Here, in numerical simulations of the single-phase flow problem, the governing equations are solved using a finite volume method in the rheoFoam solver (Pimenta and Alves, 2017).

2.3.2 Governing equation in two-phase flow problems

To simulate a two phase flowfield, there have been various numerical procedures suggested. These numerical approaches may generally be divided into two main categories known as "interface tracking" and "interface capturing" methods. Amongst the interface tracking methods, such as immersed boundary (Peskin, 1982; Mittal and Iaccarino, 2005), front-tracking (Tryggvason et al., 2001) and boundary integral (Peterlin, 1976) methods have received considerable attention due to their accurate prediction of the shape of the interface at the boundary of the two fluids. In such methods, a moving sharp boundary is considered to track the interface of the two fluids. Tracking methods are known to be accurate for most flows but due to singularity issues in problems with morphological change such as the ones observed in droplet breakup and coalescence (Jacqmin, 1999; Yue et al., 2004; Magaletti et al., 2013) cannot be used for these types of simulations. Also, due to the presence of a moving mesh (which needs to be updated and reconstructed in every time step in the simulation), one can realize such methods to be expensive with respect to their simulation computational time.

In contrast, in the numerical simulations involving interface capturing methods, the mesh is static (i.e. fixed grid distribution) and the interface between the two fluids is defined based on the variation of a scalar phase indicator parameter C. The Volume of fluid (VOF) and phase-field (PF) methods are probably the most popular interface capturing methods. For VOF and PF, this scalar quantity is usually related to a volume fraction or a mass concentration. In these methods, the scalar parameter C varies in between two limits (mostly $0 \leq C \leq 1$), and C equal to the lower and upper limits are indicative of the fluid-1/fluid-2, respectively. The interface of the two fluids is specified where C exhibits a mid-value in between of these two limits of 0.5.

In the VOF method, in order to find the evolution of the C parameter, generally, the classic transport diffusion equation is solved, while in the phase-field model, this equation has an additional double well potential term in comparison to the classic diffusion equation. In these methods, the system is dealt with as one single fluid with variable properties. By solving the transport equation for the C parameter, one can define different properties in space and time based on the regions that different fluid flows and treat the interfacial tension as a body force.

In this thesis, the VOF method is used to deal with the simulation of two-phase flow problems. To find the variation of the C parameter in the space and time domain, the standard diffusion transport equation is solved as:

$$\frac{\partial C}{\partial \tilde{t}} + \tilde{\boldsymbol{u}}.\nabla C. \qquad 0 \leq C \leq 1 \tag{2.57}$$

For a binary fluid composed of fluid-1 and fluid-2, the rheological properties of each phase such as the viscosity, density and the the relaxation time should remain constant in the bulk of each phase domain and vary across the interface. Once the space/time distribution of the C parameter is found one can define any different property of the simulated fluid as a linear function of C as follows:

$$\tilde{\rho} = C\tilde{\rho}_1 + (1-C)\tilde{\rho}_2, \tag{2.58}$$

$$\tilde{\eta}_s = C\tilde{\eta}_{s,1} + (1-C)\tilde{\eta}_{s,2}, \tag{2.59}$$

$$\tilde{\eta}_p = C\tilde{\eta}_{p,1} + (1-C)\tilde{\eta}_{p,2}, \tag{2.60}$$

$$\tilde{\lambda} = C\tilde{\lambda}_1 + (1-C)\tilde{\lambda}_2, \tag{2.61}$$

where indices 1 and 2, indicates properties of fluid-1 and fluid-2. The governing equations for the motion of this fluid are conservation of mass, assuming incompressibility, and momentum:

$$\nabla.\tilde{\boldsymbol{u}} = 0, \tag{2.62}$$

$$\tilde{\rho}(\frac{\partial \tilde{\boldsymbol{u}}}{\partial \tilde{t}} + \tilde{\boldsymbol{u}}.\nabla\tilde{\boldsymbol{u}}) = -\nabla\tilde{p} + \nabla.\tilde{\boldsymbol{\tau}} + \tilde{\eta}_s\nabla^2\tilde{\boldsymbol{u}} + \tilde{\boldsymbol{F}}. \tag{2.63}$$

In this presentation, $\tilde{\boldsymbol{F}}$ is the body force applied at the interface of the two fluids due to the existence of the interfacial tension and is calculated as (Figueiredo et al., 2016; Brackbill et al., 1992):

$$\tilde{\boldsymbol{F}} = \tilde{\sigma}\tilde{\kappa}\boldsymbol{n}\tilde{\delta}_i, \tag{2.64}$$

where $\tilde{\sigma}$ is the surface tension coefficient, $\tilde{\kappa}$ is the interface curvature and is calculated using the HF method (Francois et al., 2006), $\boldsymbol{n}$ is the normal vector to the interface and $\tilde{delta}_i$ is the δ-function at the interface. To solve the series of equations presented in 2.57 - 2.63 along with the appropriate constitutive equation for the calculation of the extra stress-tensor the rheoInterFoam solver in OpenFoam, introduced previously in the rheoTool package is used (Pimenta and Alves, 2017).

2.3.3 Kernel-conformation approach

For polymeric fluids, constitutive laws for the extra stress tensor can often be defined as a function of the conformation tensor $\boldsymbol{A}$ as already discussed in section 2.1.4 (Morrison, 2001). Describing the effect of advection and deformation of the flowfield on the conformation tensor using an upper convective derivative, most of these models which are used to describe evolution of the polymeric stress in time and space can be written in the following generic format (Bird et al., 1987):

$$\frac{\partial \boldsymbol{A}}{\partial t} + (\boldsymbol{u}.\boldsymbol{\nabla})\boldsymbol{A} = \boldsymbol{A}\nabla\boldsymbol{u} + \nabla\boldsymbol{u}^{\boldsymbol{T}}\boldsymbol{A} + \frac{F(\boldsymbol{A})}{Wi}H(\boldsymbol{A}), \tag{2.65}$$

where $\boldsymbol{u}$ is the non-dimensional velocity vector. The Weissenberg number is defined as $Wi = \frac{\tilde{U}\tilde{\lambda}}{\tilde{L}}$, where $\tilde{\lambda}$ is the relaxation time and $\tilde{U}$ and $\tilde{L}$ are the reference velocity and length scales. $F(\boldsymbol{A})$ and $H(\boldsymbol{A})$ are scalar and tensor parameters that allow the definition of specific constitutive models such as Oldroyd-B, Phan-Thien and Tanner and FENE-type models (Bird et al., 1987). The conformation tensor is a symmetric positive definite (SPD) tensor and during computational steps in numerical simulations should, in theory, remain SPD (positive definite matrix is a symmetric matrix whose eigenvalues are all positive).

The loss of positive definiteness, often related to the so-called High Weissenberg Number Problem (HWNP) (Afonso et al., 2012) is thought to be a consequence of the failure of employed computational approaches to balance the large growth of the conformation tensor and the convection terms in the evolution equation (Joseph, 1990; Afonso et al., 2012; Fattal and Kupferman, 2004, 2005; Balci et al., 2011). Recalling that any SPD tensor can be diagonalized, the conformation tensor $\boldsymbol{A}$ in a nominal Cartesian coordinate system x_1, x_2, x_3 may be written as follows (Morrison, 2001):

$$[\boldsymbol{A}]_{x_1,x_2,x_3} \equiv \boldsymbol{A} = \begin{pmatrix} A_{11} & A_{12} & A_{13} \\ A_{21} & A_{22} & A_{23} \\ A_{31} & A_{32} & A_{33} \end{pmatrix}_{x_1,x_2,x_3}, \tag{2.66}$$

where the subscribe x_1, x_2, x_3 on the matrix indicates that the coefficients are written in the x_1, x_2, x_3 coordinate system. This matrix can be also written in a *principal frame* with the basis vector χ_1, χ_2, χ_3 in a diagonal form as (Morrison, 2001; Myint-U and Debnath, 2007):

$$[\boldsymbol{A}]_{\chi_1,\chi_2,\chi_3} \equiv \boldsymbol{\Theta} = \begin{pmatrix} \Gamma_{11} & 0 & 0 \\ 0 & \Gamma_{22} & 0 \\ 0 & 0 & \Gamma_{33} \end{pmatrix}_{\chi_1,\chi_2,\chi_3}, \tag{2.67}$$

where, the rotation matrix $\boldsymbol{O}$ that transforms the matrix $\boldsymbol{A}$ in the x_1, x_2, x_3 coordinate system to the diagonal matrix $\boldsymbol{\Theta}$ in the χ_1, χ_2, χ_3 coordinate system may be calculated using (Morrison, 2001; Fattal and Kupferman, 2004, 2005; Afonso et al., 2012):

$$\boldsymbol{O^T A O} = \boldsymbol{\Theta}. \tag{2.68}$$

In this presentation, $\boldsymbol{O}$ embodies the orthogonal coordinate system in which the conformation tensor only has extensional components (i.e. the elements of the diagonal matrix $\boldsymbol{\Theta}$). Here, $\boldsymbol{O}$ and $\boldsymbol{\Theta}$ show the unitary eigenvector and eigenvalues of the conformation tensor, respectively. Once the rotation matrix is calculated from the eigenvalue problem in equation 2.68, one can calculate the coefficients of χ_1, χ_2, χ_3 of the principal coordinate system in x_1, x_2, x_3 coordinate system as $[\chi_i]_{\chi_1\chi_2\chi_3} = \boldsymbol{O^T}[x_i]_{x_1x_2x_3}$. Knowing that the positive definiteness is a tensor property that is independent of the chosen coordinate system, equation 2.68 suggests that the diagonal components of $\boldsymbol{\Theta}$ to have positive values. To deal with the HWNP, Fattal and Kupferman (2004, 2005) suggested applying a logarithmic transformation on the conformation tensor to reduce the magnitude of the stress tensor components. To avoid negative values when the log function is applied, it has been suggested to solve the problem in the coordinate system which is defined by the eigenvectors of the conformation tensor and to apply the log function on the elements of the diagonal matrix $\boldsymbol{\Theta}$ (which are known to have positive values). This transformation is now known as the "log-conformation transformation" and has been shown to be an effective approach in computational rheology, especially for simulation of problems dealing with singularities of the conformation tensor. Indeed, the log-conformation approach is used in the majority of results in this thesis. Following on from the original work carried out by Fattal and Kupferman (2004, 2005), Balci et al. (2011) suggested another approach to deal with the loss of positive definiteness of the conformation tensor. In this work, they suggested to use a square root instead of a log function to alleviate the HWNP. In this approach, knowing a positive-definite conformation tensor has a unique symmetric square root, they have shown that the evolution equation for the conformation tensor can be calculated without obtaining the eigenvalue and eigenfunction of the conformation tensor, that can significantly reduce the computational cost in the numerical simulations. In a later study, Afonso et al. (2012) extended these scenarios to a more general case and have shown that the evolution of the conformation tensor can be written in the form of a "kernel-conformation" for

any continuous, invertible matrix transformation function. Afonso et al. (2012) investigated a large group of transformations for the conformation tensor including $Log_a(\boldsymbol{A})$, $root^a(\boldsymbol{A})$, the linear shifted transformation of $\boldsymbol{A}$ and others to analyse the effect of the applied function on the outcome of numerical simulations. To analyse the efficiency of these nominal functions for the transformation of the conformation matrix, the flow of an Oldroyd-B model fluid past a confined cylinder was investigated for different values of Weissenberg numbers using different meshes. It was concluded that the efficiency of these nominal functions for the transformation of the conformation tensor is ultimately related to the type of singularity appearing in the problem and that some of theses functions may eventually fail to cope with the large values of the conformation tensor observed in this problem near the downstream stagnation point.

To illustrate the kernel conformation approach, as initially suggested by Fattal and Kupferman (2004, 2005), the transpose of the velocity gradient is split into one symmetric (i.e. $\boldsymbol{B}$) and two anti-symmetric matrices (i.e. $\boldsymbol{\Omega}$ and $\boldsymbol{N}$) as:

$$\nabla \boldsymbol{u}^{\boldsymbol{T}} = \boldsymbol{\Omega} + \boldsymbol{B} + \boldsymbol{N}\boldsymbol{A}^{-\boldsymbol{1}}, \tag{2.69}$$

$$\boldsymbol{O}^{\boldsymbol{T}} \nabla \boldsymbol{u}^{\boldsymbol{T}} \boldsymbol{O} = \bar{\boldsymbol{\Omega}} + \bar{\boldsymbol{B}} + \bar{\boldsymbol{N}}\boldsymbol{\Lambda}^{-\boldsymbol{1}}, \tag{2.70}$$

where $\boldsymbol{B}$ presents the purely extensional and $\boldsymbol{\Omega}$ and $\boldsymbol{N}$ the rotation parts of the transpose of the velocity gradient tensor and $\bar{\boldsymbol{\Omega}} = \boldsymbol{O}^{\boldsymbol{T}}\boldsymbol{\Omega}\boldsymbol{O}$, $\bar{\boldsymbol{B}} = \boldsymbol{O}^{\boldsymbol{T}}\boldsymbol{B}\boldsymbol{O}$ and $\bar{\boldsymbol{N}} = \boldsymbol{O}^{\boldsymbol{T}}\boldsymbol{N}\boldsymbol{O}$. As shown in Fattal and Kupferman (2004) and Afonso et al. (2012), this decomposition always exists and is unique. It can be represented for a two dimensional case as:

$$\boldsymbol{O}^{\boldsymbol{T}} \nabla \boldsymbol{u}^{\boldsymbol{T}} \boldsymbol{O} = \begin{pmatrix} m_{11} & m_{12} \\ m_{21} & m_{22} \end{pmatrix}, \tag{2.71}$$

$$\bar{\boldsymbol{B}} = \begin{pmatrix} m_{11} & 0 \\ 0 & m_{22} \end{pmatrix}, \tag{2.72}$$

$$\bar{\boldsymbol{\Omega}} = \begin{pmatrix} 0 & \frac{\lambda_2 m_{12} + \lambda_1 m_{21}}{\lambda_2 - \lambda_1} \\ -\frac{\lambda_2 m_{12} + \lambda_1 m_{21}}{\lambda_2 - \lambda_1} & 0 \end{pmatrix}, \bar{\boldsymbol{N}} = \begin{pmatrix} 0 & \frac{m_{12} + m_{21}}{\lambda_2^{-1} - \lambda_1^{-1}} \\ -\frac{m_{12} + m_{21}}{\lambda_2^{-1} - \lambda_1^{-1}} & 0 \end{pmatrix}, \tag{2.73}$$

Using the decomposition presented in (2.69), one can reformulate equation (2.65) as follows:

$$\frac{D\boldsymbol{A}}{Dt} = \boldsymbol{\Omega}\boldsymbol{A} - \boldsymbol{A}\boldsymbol{\Omega} + 2\boldsymbol{B}\boldsymbol{A} + \frac{F(\boldsymbol{A})}{Wi} H(\boldsymbol{A}). \tag{2.74}$$

Applying the chain derivative rule for $\boldsymbol{\Theta} = \boldsymbol{O}^{\boldsymbol{T}}\boldsymbol{A}\boldsymbol{O}$, equation 2.74 can be transformed to a principal coordinate system (i.e. the conformation tensor for every mesh cell is different from its neighbouring cells, so this coordinate system is not global and unique for every cell) and be written as (Afonso et al., 2012):

$$\frac{D\boldsymbol{\Theta}}{Dt} = \boldsymbol{\Theta}\boldsymbol{\Phi} - \boldsymbol{\Phi}\boldsymbol{\Theta} + \bar{\boldsymbol{\Omega}}\boldsymbol{\Theta} - \boldsymbol{\Theta}\bar{\boldsymbol{\Omega}} + 2\bar{\boldsymbol{B}}\boldsymbol{\Theta} + \frac{F(\boldsymbol{\Theta})}{Wi} H(\boldsymbol{\Theta}), \tag{2.75}$$

where $\boldsymbol{\Phi} = \boldsymbol{O^T}\frac{D\boldsymbol{O}}{Dt} = -\frac{D\boldsymbol{O^T}}{Dt}\boldsymbol{O} = -\boldsymbol{\Phi}^T$. Considering that $\boldsymbol{\Phi}$ and $\bar{\boldsymbol{\Omega}}$ are anti-symmetric matrices, one can conclude that the evolution equation for $\boldsymbol{\Theta}$ is independent of these tensors and equation 2.75 reduces to:

$$\boldsymbol{\Theta\Phi} - \boldsymbol{\Phi\Theta} = \boldsymbol{\Theta}\bar{\boldsymbol{\Omega}} - \bar{\boldsymbol{\Omega}}\boldsymbol{\Theta}, \tag{2.76a}$$

$$\frac{D\boldsymbol{\Gamma_i}}{Dt} = 2\bar{\boldsymbol{B}}_{\boldsymbol{ii}}\boldsymbol{\Gamma}_{\boldsymbol{i}} + \frac{F(\boldsymbol{\Gamma_i})}{Wi}H(\boldsymbol{\Gamma_i}), \tag{2.76b}$$

for off-diagonal (2.76a) and diagonal (2.76b) terms (no summation over ii) of equation 2.75. Following the approach presented by Afonso et al. (2012), for any continuous, invertible and differentiable function (i.e. $\mathbb{K}()$), the kernel-conformation constitutive law can be applied as:

$$\mathbb{K}(\boldsymbol{A}) = \boldsymbol{O}\mathbb{K}(\boldsymbol{\Theta})\boldsymbol{O^T}, \tag{2.77}$$

which suggests that the kernel function is only operating on the magnitude of the extension matrix and not in the eigenvectors of deformations. Using the chain derivative rule on the diagonal matrix $\mathbb{K}()$, one can obtain:

$$\frac{\partial\mathbb{K}(\boldsymbol{\Theta})}{\partial t} = \frac{\partial\boldsymbol{\Theta}}{\partial t}\boldsymbol{J}, \tag{2.78}$$

where $\boldsymbol{J}$ is a diagonal gradient matrix defined as:

$$\boldsymbol{J} = diag(\frac{\partial\mathbb{K}(\Gamma_1)}{\partial\Gamma_1}; \frac{\partial\mathbb{K}(\Gamma_2)}{\partial\Gamma_2}; \frac{\partial\mathbb{K}(\Gamma_3)}{\partial\Gamma_3}). \tag{2.79}$$

The evolution equation for kernel-conformation tensor, in its principal coordinate system, can be presented as:

$$\frac{D\mathbb{K}(\boldsymbol{\Theta})}{Dt} = 2\bar{\boldsymbol{B}}\boldsymbol{\Theta J} + \frac{F(\boldsymbol{\Theta})}{Wi}H(\boldsymbol{\Theta})\boldsymbol{J}. \tag{2.80}$$

Applying the chain derivative rule for the conformation tensor, as follows:

$$\frac{D\mathbb{K}(\boldsymbol{A})}{Dt} = \frac{D\boldsymbol{O}}{Dt}\mathbb{K}(\boldsymbol{\Theta})\boldsymbol{O^T} + \boldsymbol{O}\frac{D\mathbb{K}(\boldsymbol{\Theta})}{Dt}\boldsymbol{O^T} + \boldsymbol{O}\mathbb{K}(\boldsymbol{\Theta})\frac{D\boldsymbol{O^T}}{Dt}. \tag{2.81}$$

equation 2.80 can be rewritten as:

$$\frac{D\mathbb{K}(\boldsymbol{A})}{Dt} = \boldsymbol{\Omega}\mathbb{K}(\boldsymbol{A}) - \mathbb{K}(\boldsymbol{A})\boldsymbol{\Omega} + 2\boldsymbol{O}\bar{\boldsymbol{B}}\boldsymbol{\Theta J}\boldsymbol{O^T} + \frac{F(\boldsymbol{\Theta})}{Wi}\boldsymbol{O}H(\boldsymbol{\Theta})\boldsymbol{J}\boldsymbol{O^T}. \tag{2.82}$$

Choosing the log function for the transformation of the conformation tensor, we have:

$$\mathbb{K}(\boldsymbol{A}) = log(\boldsymbol{A}) = \boldsymbol{O}(log(\boldsymbol{\Theta}))\boldsymbol{O^T}, \tag{2.83}$$

Using (2.83) as the kernel function for transformation of conformation tensor, the gradient matrix $\boldsymbol{J}$ may be defined as:

$$\boldsymbol{J} = diag(\frac{\partial log(\Gamma_1)}{\partial\Gamma_1}; \frac{\partial log(\Gamma_2)}{\partial\Gamma_2}; \frac{\partial log(\Gamma_3)}{\partial\Gamma_3}) = \boldsymbol{\Theta^{-1}}. \tag{2.84}$$

Implementing equation 2.84 in 2.82, for the Oldroyd-B constitutive equation, $F(\boldsymbol{\Theta}) = 1$ and $H(\boldsymbol{A}) = \boldsymbol{I} - \boldsymbol{A}$, the final form of the evolution equation will appear as follows:

$$\frac{D\mathbb{K}(\boldsymbol{A})}{Dt} = \boldsymbol{\Omega}\mathbb{K}(\boldsymbol{A}) - \mathbb{K}(\boldsymbol{A})\boldsymbol{\Omega} + 2\boldsymbol{B} + \frac{1}{Wi}(e^{\boldsymbol{\Theta}} - \boldsymbol{I}). \tag{2.85}$$

Unfortunately, all of the kernel transformations previously presented by Afonso et al. (2012), have an unbounded nature. In appendix A, using the bounded properties of Atan (arc tangent) function, this scenario is extended to a bounded transformation for the conformation tensor of viscoelastic fluids that can be applied for a large class of constitutive equations. Despite the success of this novel approach, for consistency, the results shown in Chapters 3,4 and 5 were obtained using the standard log-conformation approach.

2.4 Numerical Schemes

In openFoam the user has a wide range of choices for the numerical schemes and discretization of terms, such as derivatives appearing in the governing equations that can be set in the $fvSchemes$ dictionary in the system directory. In this section it is described how to specify the schemes in this dictionary and more information about the employed discretization schemes is also provided. Generally, the terms that must be assigned a numerical scheme range from different types of derivatives such as gradient ∇ and divergence $\nabla.$ to the interpolation of values from a set of points to another. The set of terms which the discretization scheme must be specified are listed in Table 2.1. Every keyword described in Table 2.1 is related to a specific sub-dictionary containing information about terms of a particular type , e.g divSchemes $\nabla.$ contains all divergence terms such as $\nabla.\boldsymbol{u}$. Each sub-dictionary contains keyword entries for each term

Table 2.1: Main keywords in fvSchemes (Greenshields, 2015).

Keyword	Category of mathematical terms
gradSchemes	Gradient ∇
interpolationSchemes	Point to point value interpolation
laplacianSchemes	Laplacian ∇^2
divSchemes	Divergence $\nabla.$
timeScheme	First and second order derivatives of time $\partial/\partial t, \partial^2/\partial t^2$

specified within, including: a default discretization scheme. Subsequently, the user may use other entries whose names correspond to particular terms specified, e.g. grad(p) or grad(u) for ∇p and ∇u, respectively.

2.4.1 Gradient Schemes

In the gradSchemes sub-dictionary, the user can define gradient terms. The options that OpenFoam provides for the discretization of gradient terms can be selected from those presented in Table 2.2. In this thesis the Gauss discretization scheme is employed

Table 2.2: Discretization schemes available in gradSchemes (Greenshields, 2015).

Discretization scheme	Description
Gauss $< interpolationScheme >$	Second order, Gaussian integration
leastSquares	Second order, least squares
fourth	Fourth order, least squares
cellLimited $< gradScheme >$	Cell limited version of one of the above schemes
faceLimited $< gradScheme >$	Face limited version of one of the above schemes

in simulations for the gradient terms which is the standard finite volume discretization of Gaussian integration. In reference to a gradient term $\nabla \boldsymbol{\phi}$, discretization of gradient terms is performed by integrating over a control volume and transforming the volume integral into a surface integral using Gauss's theorem as follows:

$$\int_A \phi ds = \sum_f \phi_f A_f, \tag{2.86}$$

where A denotes the surface area of the control volume and A_f denotes the area of a face for the control volume. ϕ_f is the interpolated value of ϕ from cell centres to face f. The choices of interpolation scheme are presented from Table 2.4. Initial simulations

Table 2.3: Behaviour of interpolation schemes used in divSchemes (Greenshields, 2015).

Schemes	Description
linear	Linear interpolation (central differencing)
cubicCorrection	Cubic scheme
midPoint	Linear interpolation with symmetric weighting
Upwinded convection schemes	
upwind	Upwind differencing
linearUpwind	Linear upwind differencing
skewLinear	Linear with skewness correction
filteredLinear2	Linear with filtering for high-frequency ringing
TVD schemes	
limitedLinear	limited linear differencing
vanLeer	van Leer limiter
MUSCL	MUSCL limiter
limitedCubic	Cubic limiter

Table 2.4: Interpolation schemes. (Greenshields, 2015).

suggest that the linear scheme is an effective choice, so the Gauss linear scheme is used in all of the simulations for discretization of terms involving gradient operator.

2.4.2 Laplacian schemes

In the laplacianSchemes sub-dictionary Laplacian terms are defined. Here, the Gauss integral scheme is the only choice of discretization. For a Laplacian term $\nabla.(k\nabla\phi)$, discretization of diffusion terms is done after integration over the control volume and converting it into a surface integral as:

$$\int_A n.(k\nabla\phi)ds = \sum_f k_f(n.\nabla_f\phi)A_f, \tag{2.87}$$

where $\nabla_f\phi$ is the the gradient at the face. The face normal gradient can be approximated using the scheme

$$n.\nabla_f\phi = \frac{\phi_N - \phi_P}{|\boldsymbol{d}|}. \tag{2.88}$$

This approximation is second order accurate when the vector $\boldsymbol{d}$ between the center of the cell of interest P and the center of a neighboring cell N is orthogonal to the face plane, i.e. parallel to A. In the case of non-orthogonal meshes, a correction term could be introduced which is evaluated by interpolating cell centered gradients obtained from Gauss integration. In this discretization method a selection of inputs are required to define both the interpolation scheme for the diffusion coefficient (as was already presented in Table 2.4) and a surface normal gradient scheme (i.e. snGradScheme). The choices provided in OpenFoam for snGradScheme is presented in Table 2.6. In

Table 2.5: Behaviour of interpolation schemes used in divSchemes (Greenshields, 2015).

Schemes	Numerical behaviour
corrected	Unbounded, second order, conservative
uncorrected	Bounded, first order, non-conservative
limited	Blend of corrected and uncorrected
bounded	First order for bounded scalars
fourth	Unbounded, fourth order, conservative

Table 2.6: Behaviour of surface normal schemes used in laplacianSchemes (Greenshields, 2015).

this thesis a linear interpolation scheme with corrected snGradScheme is used in all simulations.

2.4.3 Divergence schemes

The divSchemes sub-dictionary contains divergence terms. Similar to the Laplacian Scheme, the Gauss integral scheme is the only choice of discretization in divergence schemes. For a divergence term $\nabla.(\rho\phi\boldsymbol{u})$, discretization of convection terms is performed by integrating over a control volume and transforming the volume integral into a surface integral using the Gauss's theorem as follows:

$$\int_A n.(\rho\phi\boldsymbol{u})dA \approx \sum_f n.(A\rho\boldsymbol{u})_f\phi_f = \sum_f F\phi_f, \tag{2.89}$$

where F is the mass flux through the face defined as $n.(A\rho\boldsymbol{u})_f$. The value ϕ_f on face f can be evaluated in a variety of ways and the interpolation scheme is selected from Table 2.4. The choice of interpolation determines numerical accuracy as shown in Table 2.7

2.4.4 Time schemes

The first order time derivative $\partial/\partial t$ terms are specified in the ddtSchemes sub-dictionary. The discretization scheme for each term can be selected from those listed in Table 2.8. In the simulations carried out in this thesis the Euler scheme is used for the terms with time derivative. Discretization of the time derivative $\partial(\rho\phi)/\partial t$ is carried out by integrating it over the control volume of a grid cell as:

$$\int_V \frac{\partial \rho\phi}{\partial t} dV \approx \frac{\rho_P^n \phi_P^n - \rho_P^0 \phi_P^0}{\Delta t} V_P, \tag{2.90}$$

where $\phi_P^n \equiv \phi_P(t + \Delta t)$ represents the new value at the time step we are solving for and $\phi_P^0 \equiv \phi_P(t)$ stands for the old value obtained in the previous time step.

Overall, the steady-state numerical simulations presented in this thesis have the order of accuracy of two. Some limited simulations for unsteady flows were also carried out that have an order of accuracy of one.

Table 2.7: Behaviour of interpolation schemes used in divSchemes (Greenshields, 2015).

Schemes	Numerical behaviour
linear	Second order, unbounded
skewLinear	Second order, (more) unbounded, skewness correction
cubicCorrected	Fourth order, unbounded
upwind	First order, bounded
linearUpwind	First/second order, bounded
QUICK	First/second order, bounded
TVD schemes	First/second order, bounded
SFCD	Second order, bounded
NVD schemes	First/second order, bounded

Table 2.8: Discretization schemes available in ddtSchemes. (Greenshields, 2015).

Schemes	Numerical behaviour
Euler	First order, bounded, implicit
localEuler	Local-time step, first order, bounded, implicit
CrankNicholson	Second order, bounded, implicit
backward	Second order, implicit
steadyState	Does not solve for time derivatives

Chapter 3

Finite aspect ratio inertialess viscoelastic Taylor-Couette flow[1,2]

Both in rheometry and in fundamental fluid mechanics studies, the Taylor–Couette geometry is used frequently to investigate viscoelastic fluids. In order to ensure a constant shear rate in the gap between the inner and outer cylinders, such studies are usually restricted to the small-gap limit where the assumption of a linear velocity distribution is well justified. In conjunction with a sufficiently large aspect ratio (i.e. ratio of cylinder height to gap), the flow is then assumed to be viscometric. In this chapter demonstrate, using a perturbation technique with the curvature ratio (i.e. ratio of the half-gap to the mid-radius of the cylinders) as the perturbation parameter, full nonlinear simulations using a finite-volume technique, and supporting experiments, it is demonstrated that, even in the creeping-flow (inertialess) narrow-gap limit, for viscoelastic fluids end effects due to finite aspect ratio always give rise to a secondary motion. Using the constant-viscosity Oldroyd-B model it is shown that this secondary motion, as has been observed in related pressure-driven flows with curvature, such as the viscoelastic Dean flow, is solely a consequence of the combination of gradients of the first normal-stress difference and curvature. These results show that end effects can significantly change the flow characteristics, especially for small aspect ratios, and has important consequences for the onset criteria for purely elastic instabilities in this geometry.

[1]Work from this chapter has been published in: Davoodi, M., et al. "Secondary flows due to finite aspect ratio in inertialess viscoelastic Taylor–Couette flow." Journal of Fluid Mechanics 857: 823-850, 2018.

[2]Experiments conducted by S. Lerouge, Paris Diderot University

3.1 Mathematical formulation

In this section the mathematical formulation for creeping viscoelastic TC flow is presented. Here, the problem is investigated for the particular case that the inner cylinder is rotating while the other three surfaces (i.e. the other cylinder and the two end faces) are stationary. To probe the viscoelastic behaviour, the Oldroyd-B model is chosen, as this is the simplest differential constitutive equation capable of predicting many complex phenomena due to viscoelasticity (Alves and Poole, 2007; Poole et al., 2007c).

3.1.1 Coordinate system

Considering the geometry of the problem, a cylindrical polar coordinate system is used (Figure 3.1). Introducing the following change of variable, one can write:

$$\tilde{x} = \tilde{r} - \tilde{R}, \tag{3.1}$$

$$\frac{1}{\tilde{r}} = \frac{1}{\tilde{x} + \tilde{R}}, \tag{3.2}$$

$$\frac{\partial}{\partial \tilde{r}} = \frac{\partial}{\partial \tilde{x}} \frac{\partial \tilde{x}}{\partial \tilde{r}} = \frac{\partial}{\partial \tilde{x}}, \tag{3.3}$$

where $\tilde{R}$ is the mid radius ($\tilde{R} = \tilde{R}_i + \tilde{a}$, with $\tilde{R}_i$ and $\tilde{a}$ the radius of the inner cylinder and the half-width of the gap, respectively) and $\tilde{r}$, θ, $\tilde{z}$ are the components of the polar cylindrical coordinate system.

3.1.2 Non-dimensionalization

It is convenient to use dimensionless parameters in this problem. The relationships between dimensional and dimensionless parameters are:

$$\begin{gathered} x = \frac{\tilde{x}}{\tilde{a}}, z = \frac{\tilde{z}}{\tilde{a}\Lambda}, \Lambda = \frac{\tilde{b}}{\tilde{a}}, \beta = \frac{\tilde{\eta}_s}{\tilde{\eta}_t}, Wi = \frac{\tilde{\lambda}\tilde{R}_i\tilde{\omega}}{\tilde{a}}, \tau = \frac{\tilde{\tau}\tilde{a}}{\tilde{\eta}_t\tilde{R}_i\tilde{\omega}}, P = \frac{\tilde{P}\tilde{a}}{\tilde{\eta}_t\tilde{R}_i\tilde{\omega}}, \\ v_r = \frac{\tilde{v}_r}{\tilde{R}_i\tilde{\omega}}, v_\theta = \frac{\tilde{v}_\theta}{\tilde{R}_i\tilde{\omega}}, v_z = \frac{\tilde{v}_z}{\tilde{R}_i\tilde{\omega}}, \boldsymbol{D} = \frac{\boldsymbol{D}\tilde{a}}{\tilde{R}_i\tilde{\omega}}, \delta = \frac{\tilde{a}}{\tilde{R}}, B = 1 + \delta x, \end{gathered} \tag{3.4}$$

where $\tilde{x}$ is the variable defined in equation 3.1, $\tilde{z}$ is the axial variable in the polar cylindrical coordinate system, $\tilde{b}$ is the half-height of the cylinders, Λ is the aspect ratio, β is the solvent-to-total viscosity ratio, $\tilde{\eta}_t$ is the total viscosity of the fluid ($\tilde{\eta}_t = \tilde{\eta}_s + \tilde{\eta}_p$ with $\tilde{\eta}_p$ and $\tilde{\eta}_s$ the polymeric and solvent parts of the viscosity, respectively), Wi is the Weissenberg number, $\tilde{\lambda}$ is the corresponding relaxation time of the fluid, $\tilde{\omega}$ is the angular velocity of the moving inner wall, $\tilde{\boldsymbol{\tau}}$ is the stress tensor, $\tilde{P}$ is the pressure, $\tilde{\boldsymbol{u}}$ is the velocity vector, $\tilde{v}_r$, $\tilde{v}_\theta$ and $\tilde{v}_z$ are components in the $\tilde{r}, \theta$ and $\tilde{z}$ directions of velocity in the polar cylindrical coordinate system and $\tilde{\boldsymbol{D}}$ is the rate-of-deformation

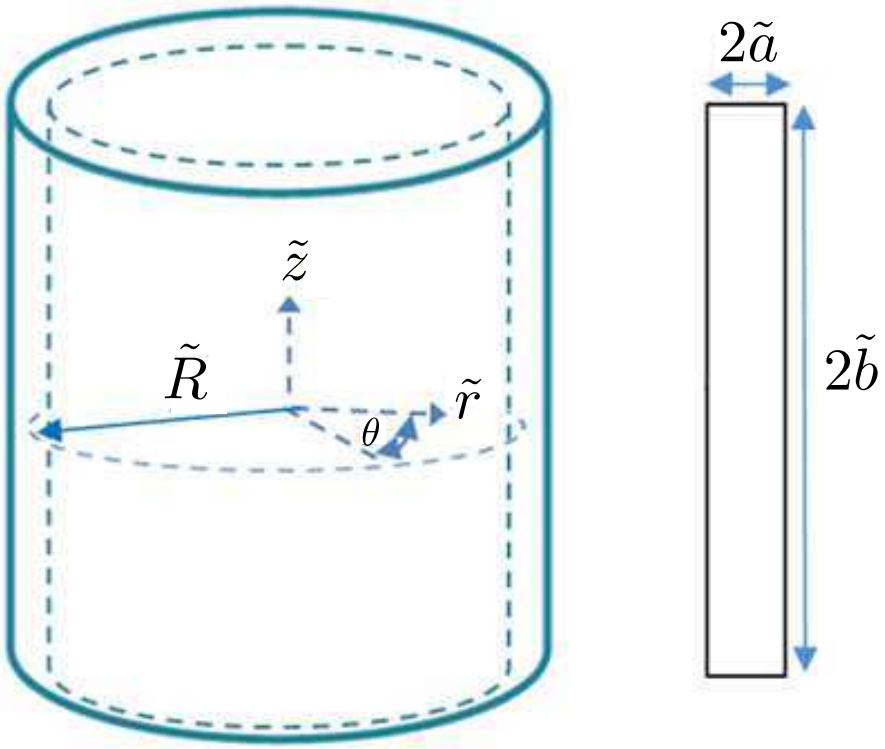

Figure 3.1: Schematic of the narrow-gap TC set-up investigated including polar cylindrical coordinate system: (a) concentric-cylinder set-up; and (b) axisymmetric 'slice' used in analytical method.

tensor ($\tilde{\boldsymbol{D}} = (\tilde{\nabla}\boldsymbol{u} + \nabla\tilde{\boldsymbol{u}}^T)/2$). Finally, δ is the curvature ratio and B represents the local dimensionless curvature.

3.2 Analytical methods

The governing equations in this problem are conservation of mass and momentum. These equations using the change of variable defined in equation 3.1 in a polar cylindrical coordinate system assuming axisymmetry and creeping flow (i.e. $Re \to 0$) can be presented in dimensionless form as follows:

$$\frac{\partial v_r}{\partial x} + \frac{\delta}{B} v_r + \frac{1}{\Lambda}\frac{\partial v_z}{\partial z} = 0, \tag{3.5}$$

$$\frac{\partial P}{\partial x} + \beta\left(\frac{\partial^2 v_r}{\partial x^2} + \frac{\delta}{B}\frac{\partial v_r}{\partial x} - \frac{\delta^2}{B^2} v_r + \frac{1}{\Lambda^2}\frac{\partial^2 v_r}{\partial z^2}\right) + \frac{\partial \tau_{rr}}{\partial x} + \frac{\delta}{B}(\tau_{rr} - \tau_{\theta\theta}) + \frac{1}{\Lambda}\frac{\partial \tau_{rz}}{\partial z} = 0, \tag{3.6}$$

$$\beta\left(\frac{\partial^2 v_\theta}{\partial x^2} + \frac{\delta}{B}\frac{\partial v_\theta}{\partial x} - \frac{\delta^2}{B^2} v_\theta + \frac{1}{\Lambda^2}\frac{\partial^2 v_\theta}{\partial z^2}\right) + \frac{\partial \tau_{r\theta}}{\partial x} + 2\frac{\delta}{B}\tau_{r\theta} + \frac{1}{\Lambda}\frac{\partial \tau_{\theta z}}{\partial z} = 0, \tag{3.7}$$

$$\frac{1}{\Lambda}\frac{\partial P}{\partial z} + \beta\left(\frac{\partial^2 v_z}{\partial x^2} + \frac{\delta}{B}\frac{\partial v_z}{\partial x} + \frac{1}{\Lambda^2}\frac{\partial^2 v_z}{\partial z^2}\right) + \frac{\partial \tau_{rz}}{\partial x} + \frac{\delta}{B}\tau_{rz} + \frac{1}{\Lambda}\frac{\partial \tau_{zz}}{\partial z} = 0. \tag{3.8}$$

To simulate the viscoelastic behaviour, the Oldroyd-B constitutive equation is used to calculate the stress components. This model considers a Newtonian behaviour for the solvent contribution ($\boldsymbol{\tau_s}$) of the fluid and an upper convected Maxwell model for the polymeric part ($\boldsymbol{\tau}$) of the stress tensor.

As TC flow is a wall-driven problem, there is no pressure gradient in the θ direction. However, the presence of the secondary flow causes a pressure distribution in both the r and z directions (see equations 3.6 and 3.8) that is an unknown function of x, z and of the rheological parameters. It is usual to eliminate the pressure gradient in the equations (Robertson and Muller, 1996; Jitchote and Robertson, 2000). To achieve this, the derivative of equation 3.6 with respect to z can be subtracted from the product of Λ and the derivative of equation 3.8 with respect to x.

In the following section the mathematical methods used to derive an approximate analytical solution to the creeping flow of viscoelastic fluids in the narrow-gap TC system are presented. The employed Oldroyd-B model is classified as a quasi-linear equation (Bird et al., 1987); in order to linearize this constitutive equation, a perturbation method is employed. Finally, to cope with the partial differential form of the equations, a separation-of-variables method is used to transform the problem into two

linear ordinary differential equations (Myint-U and Debnath, 2007; Norouzi and Biglari, 2013).

3.2.1 Exact solution for finite-aspect-ratio planar Couette flow

A previous study carried out by Theofilis et al. (2004) has obtained an exact analytical solution for rectangular cavity flows of Newtonian fluids. In this section we derive an alternative solution to this problem and will compare our results with the solution presented in the literature in Appendix B. In the case that $\delta = 0$, equations 3.5 and 3.6-3.8, represent the conservation of mass and momentum in a rectangular coordinate system. For the particular case of Newtonian planar Couette flow (i.e. $\delta = 0$ and polymer stress terms equal to zero) – which from herein onwards will be denoted using a zero superscript inside square brackets (i.e. [0]) – due to the rectilinear distribution of velocity (i.e. no secondary motions in either radial or axial directions; $v_r^{[0]} = v_z^{[0]} = 0$), the momentum equation can be simplified to:

$$\frac{\partial^2 v_\theta^{[0]}}{\partial x^2} + \frac{1}{\Lambda^2}\frac{\partial^2 v_\theta^{[0]}}{\partial z^2} = 0. \tag{3.9}$$

Considering the change of variable introduced in equation 3.1, equation 3.9 should be solved subject to the following boundary conditions at the walls:

$$v_\theta^{[0]}|_{x=1} = v_\theta^{[0]}|_{z=1} = v_\theta^{[0]}|_{z=-1} = 0, \tag{3.10}$$

$$v_\theta^{[0]}|_{x=-1} = 1. \tag{3.11}$$

Equation 3.9 is a linear partial differential equation. To solve it, a separation-of variables method can be used. The velocity may be written as:

$$v_\theta^{[0]} = T(x)\Xi(z) + \frac{1-x}{2}, \tag{3.12}$$

where the second term on the right-hand side of equation 3.12 solves the equation 3.9 when $\Lambda \to \infty$ and is the solution to the 1D case. Using the above definition (equation 3.12), equation 3.9 can be rewritten as two linear ordinary differential equations:

$$\frac{\partial^2 \Xi_n(z)}{\partial z^2} - \kappa_n^2 \Lambda^2 \Xi_n(z) = 0, \tag{3.13}$$

$$\frac{\partial^2 T_n(x)}{\partial x^2} + \kappa_n^2 T_n(x) = 0. \tag{3.14}$$

where κ_n are unknown eigenvalues. The solutions to equations 3.13 and 3.14 are obtained as follows:

$$\Xi_n(z) = B_n sinh(\kappa_n \Lambda z) + C_n cosh(\kappa_n \Lambda z), \tag{3.15}$$

$$T_n(x) = D_n sin(\kappa_n x) + E_n cos(\kappa_n x). \tag{3.16}$$

The solution to equation 3.16 should be solved subject to $T_n(x)|_{x=1} = 0$, hence $E_n = -D_n tan(\kappa_n)$, so

$$T_n(x) = F_n(cos(\kappa_n)sin(\kappa_n x) - sin(\kappa_n)cos(\kappa_n x)) = E_n sin(\kappa_n(x-1)), \tag{3.17}$$

where $F_n = D_n/cos(\kappa_n)$. The boundary condition $T_n(x)|_{x=-1} = 0$ suggests that $-E_n sin(2\kappa_n) = 0$. To get a non-trivial solution to the problem, $\kappa_n = n\pi/2$, where $n \in [0, 1, 2, ...]$, thus

$$v_\theta^{[0]} = \frac{1-x}{2} + \sum_{n=1}^{\infty} \Xi(z) sin(\frac{n\pi}{2}(1-x)), \tag{3.18}$$

Using a Fourier series (Myint-U and Debnath, 2007), one can write

$$\frac{1-x}{2} = \sum_{n=1}^{\infty} \frac{2(-1)^{n+1}}{n\pi} sin(\frac{n\pi}{2}(1-x)). \tag{3.19}$$

Imposing the boundary conditions $v_\theta^{[0]}|_{z=\pm 1} = 0$ leads to $\Xi_n(z)|_{z=\pm 1} = \frac{2(-1)^{n+1}}{n\pi}$, so that the coefficients B_n and C_n for $\Xi_n(z)$ are, respectively, $B_n = 0$ and $C_n = 2(-1)^n/(n\pi cosh(n\pi\Lambda/2))$. Therefore the final solution may be presented as

$$v_\theta^{[0]} = \frac{1-x}{2} + \sum_{n=1}^{\infty} \frac{2(-1)^{n+1}}{n\pi} sin(\frac{n\pi}{2}(1-x)) \frac{cosh(\frac{n\pi}{2}\Lambda z)}{cosh(\frac{n\pi}{2}\Lambda)}. \tag{3.20}$$

According to the rectilinear flow theorem of viscoelastic fluids (Reiner, 1945; Rivlin, 1957, 1997; Green and Rivlin, 1997; Ericksen, 1956), this solution is valid for both Newtonian fluids and, due to its constant shear viscosity, the Oldroyd-B model. Essentially this is the planar Couette flow solution in a straight duct of rectangular cross-section for arbitrary aspect ratio. The dependence of equation 3.20 on an even function of z indicates symmetry along the line $z = 0$. Assuming the viscosity of air to be negligibly small in comparison to the viscosity of any tested liquid, and neglecting surface tension (i.e. also assuming a flat interface), the present solution can be applicable for planar Couette geometries with a flat stress-free free surface at the 'top' and a wall at the 'bottom' if the solution is used for the region $-1 < z < 0$ and $-1 < x < 1$. Such a situation will be used for experimental validation.

3.2.2 Exact solution for flow rate

Using equation 3.20 for the velocity distribution, one can obtain the following equation for the flow rate of the finite-aspect-ratio planar Couette flow:

$$Q^{[0]} = \int_{-1}^{1} \int_{-1}^{1} v_\theta^{[0]} dx dz, \tag{3.21}$$

$$Q^{[0]} = 2 + 2\sum_{n=1}^{\infty} (\frac{2}{n\pi})^3 \frac{(-1)^n - 1}{\Lambda} tanh(\frac{n\pi\Lambda}{2}), \tag{3.22}$$

where $Q^{[0]}$ stands for flow rate in the planar Couette flow. These solutions can be easily compared to the dimensionless 1D solution (the first term on the right-hand side of equation 3.22 as $Q_{1D} = 2$, in our non-dimensional notation).

3.2.3 Perturbation method

As already discussed, a perturbation method is used to linearize the quasi-linear Oldroyd-B model. The perturbation parameter is considered to be the curvature ratio δ. The series forms of the parameters up to the first order of expansion are

$$\psi = \delta\psi^{[1]}, \tag{3.23}$$

$$v_\theta = v_\theta^{[0]} + \delta v_\theta^{[1]}, \tag{3.24}$$

$$P = P^{[0]} + \delta P^{[1]}, \tag{3.25}$$

$$\boldsymbol{\tau} = \boldsymbol{\tau}^{[0]} + \delta\boldsymbol{\tau}^{[1]}, \tag{3.26}$$

Here, ψ is the secondary flow streamfunction, which is related to the lateral components of the velocity vector via

$$v_r = \frac{1}{\Lambda}\frac{\partial\psi}{\partial z} \tag{3.27}$$

$$v_\theta = -\frac{\partial\psi}{\partial x} \tag{3.28}$$

In the case that the curvature ratio goes to zero ($\delta \to 0$), one should note that the effect of curvature will be eliminated, so the flow will be rectilinear (i.e. no secondary flow). So, in these cases, ψ will be zero and consequently the series form of the streamfunction in equation 3.23 must have only the first-order term.

3.2.4 Perturbation solution

After substituting 3.23, 3.24 and 3.26 into the polymeric part of the Oldroyd-B constitutive equation, the linearized form of the zeroth order of the stress tensor for the chosen polar cylindrical coordinate system can be obtained. In the absence of curvature, U_r^0 and U_z^0 are equal to zero (i.e. no secondary flow in the straight Couette flow) and the zeroth-order stress tensor for the polymeric contribution of the Oldroyd-B constitutive equation can be obtained as follows

$$\tau_{rz}^{[0]} = \tau_{rr}^{[0]} = \tau_{zz}^{[0]} = 0, \tag{3.29}$$

$$\tau_{\theta\theta}^{[0]} = 2Wi(1-\beta)[(\frac{\partial v_\theta^{[0]}}{\partial x})^2 + \frac{1}{\Lambda^2}(\frac{\partial v_\theta^{[0]}}{\partial z})^2], \tag{3.30}$$

$$\tau_{r\theta}^{[0]} = (1-\beta)(\frac{\partial v_\theta^{[0]}}{\partial x}), \tag{3.31}$$

$$\tau_{z\theta}^{[0]} = (1-\beta)\frac{1}{\Lambda}(\frac{\partial v_\theta^{[0]}}{\partial z}). \tag{3.32}$$

Using the same approach and collecting the effective terms in the calculation up to first order of the streamfunction, the corresponding stress components related to the polymeric contribution of the Oldroyd-B constitutive equation may be calculated as follows:

$$\tau_{rr}^{[1]} = 2(1-\beta)\frac{1}{\Lambda}(\frac{\partial^2\psi^{[1]}}{\partial x \partial z}). \tag{3.33}$$

$$\tau_{zz}^{[1]} = -2(1-\beta)\frac{1}{\Lambda}(\frac{\partial^2\psi^{[1]}}{\partial x \partial z}). \tag{3.34}$$

$$\tau_{rz}^{[1]} = (1-\beta)(\frac{1}{\Lambda^2}\frac{\partial^2\psi^{[1]}}{\partial z^2} - \frac{\partial^2\psi^{[1]}}{\partial x^2}). \tag{3.35}$$

Substituting the perturbed forms of flow parameters (equations 3.23-3.26 and 3.29-3.32) into the momentum equations (3.6–3.8) and collecting all the coefficients of order δ, the resulting expression is the same as equation 3.9. Therefore, the solution to the planar Couette flow (equation 3.20) is the zeroth-order solution of the perturbation method as well. Formally speaking, due to the singularity of both the stress and the shear rate at the corner, this perturbation approach may not be strictly valid in this location near the moving and stationary walls (Hinch, 1993). Despite this limitation, this approach is continued to derive what is best termed as an 'approximate' analytical solution for the problem. In order to confirm the reasonableness of this approach, we will compare the linearized analytical solution with full nonlinear numerical simulations. To calculate the solution of the secondary flow up to the first order of perturbation expansion, the same method is employed as was used in the zeroth-order solution. After collecting the terms with the coefficient of order δ^1, the resulting coefficient expression is

$$\nabla^4\psi^{[1]} = \frac{1}{\Lambda}\frac{\partial\tau_{\theta\theta}^{[0]}}{\partial z}, \tag{3.36}$$

where the biharmonic operator ∇^4 is defined as $\nabla^4 = \partial^4/\partial x^4 + (2/\Lambda^2)(\partial^4/\partial z^2\partial x^2) + (1/\Lambda^4)(\partial^4/\partial z^4)$. In the case of Newtonian fluids in the creeping-flow limit, $\tau_{\theta\theta}^{[0]}$ is identically zero, as there is no normal-stress in fully developed planar Couette flow and the right-hand side of equation 3.36 is identically zero. So, equation 3.36 will be a homogeneous equation and therefore the general solution to a homogeneous equation with homogeneous boundary condition is zero (Myint-U and Debnath, 2007) (i.e. there must be no secondary flow for Newtonian fluids in the inertialess limit). This reasoning illustrates that, in creeping TC flow, the secondary flow arises due to the existence of non-zero gradients of the first normal-stress difference in viscoelastic fluids (more precisely from the $\tau_{\theta\theta}/r$ term in equation 3.6). Solution of the non-homogenous linear equation 3.36 can be obtained using standard mathematical approaches (Winters, 1987; Jitchote and Robertson, 2000; Robertson and Muller, 1996; Myint-U and Debnath, 2007) subject to zero boundary conditions for velocity in the r and z directions (due to the large size of these equations, they are not presented here).

3.3 Geometric configuration and problem definition

A schematic of the TC geometry is shown in section 3.1 in Figure 3.1. To probe the effect of aspect ratio $\Lambda = \tilde{b}/\tilde{a}$ in the creeping flow of viscoelastic fluids in both tall and shallow TC systems, 21 different geometries $\Lambda = 0.2, 0.3, 0.4, 0.5, 0.6, 0.7, 0.8, 0.9, 1.0, 1.25, 1.5, 1.75, 2.0, 2.5, 3.0, 3.25, 3.5, 3.75, 4.0, 10$ and 20) have been modelled. The implementation of correct boundary conditions at the walls can significantly influence the flowfields and stability criteria in numerical methods. This issue finds notable importance in cases dealing with singularities as occurs here in the corner of the moving and stationary walls. The prescribed boundary condition for the stress tensor at walls in OpenFOAM is defined based on 1D shear flow of Newtonian fluids (zero gradient stress at the wall) (Pimenta and Alves, 2017). Owing to the important role of first normal-stress differences arising from viscoelastic behaviour in the appearance of the secondary flow in the present case, it was discovered via initial simulations that implementation of the zero-gradient-stress boundary condition at the wall is not a good choice for this problem. In fact, using this boundary condition converged solutions could not be obtained for any Weissenberg number without 'regularizing' the wall velocity, i.e. varying the wall velocity smoothly from 0 to 1 over a finite distance (Sousa et al., 2016). In marked contrast, via use of the linear extrapolation approach (Pimenta and Alves, 2017), converged solutions could be obtained without recourse to regularization. In this approach, the stress tensor components at interior faces are obtained by linearly interpolating the cell-centred values, while for the boundary face the value extrapolated in the previous time step is used. This results in an explicit Dirichlet boundary condition, which uses information from the direct neighbours (cells sharing a face) of the cell owning the boundary face (Pimenta and Alves, 2017).

3.4 Comparison of numerical simulation with analytical solution and effect of mesh

In this section a number of representative data analysing the effect of mesh on the flow distribution are presented to give an overview of numerical accuracy. Comparison of the analytical solutions and the numerical simulations is presented in Table 3.1.

In this table, five different uniform meshes are shown respectively to study the mesh dependence via the maximum value of the secondary flow (ψ_{max}) and its position (x_{max}, z_{max}). Since the secondary flow is driven by the high shear rate near the corner region between the moving and the stationary walls, to capture this phenomenon better, the mesh should be extremely fine in this region. The presented data suggest that the equivalent of the M3 mesh $200 \times 100\Lambda$ is a good choice for simulation. The small difference between the results of the analytical calculations and the numerical

Table 3.1: Mesh study for the case $Wi = 0.1, \beta = 0.5, \delta = 0.1, \Lambda = 1$.

Mesh	ψ_{max}	x_{max}	z_{max}
M1=50×25	5.994×10^{-5}	-0.655	0.593
M2=100×50	5.989×10^{-5}	-0.652	0.596
M3=200×100	6.021×10^{-5}	-0.650	0.598
M4=400×200	6.035×10^{-5}	-0.649	0.599
M5=800×400	6.041×10^{-5}	-0.649	0.599
Analytical	6.248×10^{-5}	-0.565	0.636

simulations can be attributed to the fact that in the corner between the moving wall and the stationary wall a velocity jump exists that causes a singularity in the stress field. Consequently, the chosen perturbation method loses strict validity in this region (Hinch, 1993) and, most likely, this issue is the root cause of the small difference between the approximate analytical solution and the numerical data in terms of the location of the peak streamfunction. Certainly, the mesh-dependence study suggests that the small difference is not simply due to mesh effects in the numerical simulation.

3.5 Experiments undertaken by Prof. Sandra Lerouge (Université Paris Diderot, France)

3.5.1 Experimental set-up

The experiments are performed in a transparent TC device fitted to a stress-controlled rheometer (Physica MCR 301) also working in strain-controlled mode via a computer-controlled feedback loop. The TC cell is embedded in a transparent cubical container that ensures temperature control through a water-bath circulation. This configuration of the tank minimizes optical distortions of the images due to refraction caused by the curved interfaces. The rheological properties and the flow behaviour are determined in a Mooney-type TC geometry with inner radius $13.33[mm]$, gap width $1.13[mm]$ and height $40[mm]$. For flow visualizations, the geometrical configuration that matches most accurately the problem at hand with the current set-up was investigated and is illustrated in Figure 3.2.

The inner rotating cylinder has a $13.445[mm]$ radius (i.e. $\tilde{R} - \tilde{a}$) and height $\tilde{b} = 10[mm]$. In this set-up, due to the stress-free surface, we are essentially investigating just one half of the problem described. The gap width is $2\tilde{a} = 1[mm]$, which gives an aspect ratio $\Lambda = \frac{\tilde{b}}{\tilde{a}} = 20$ and curvature ratio $\delta = \frac{\tilde{a}}{\tilde{R}} = 0.04$.

3.5.2 Working fluids

Aqueous polymer solutions with constant shear viscosity ($\tilde{\eta}_t = 239 \pm 2[mPa.s]$) yet exhibiting elastic properties were prepared by the author by adding $500[ppm]$ (w/w) of

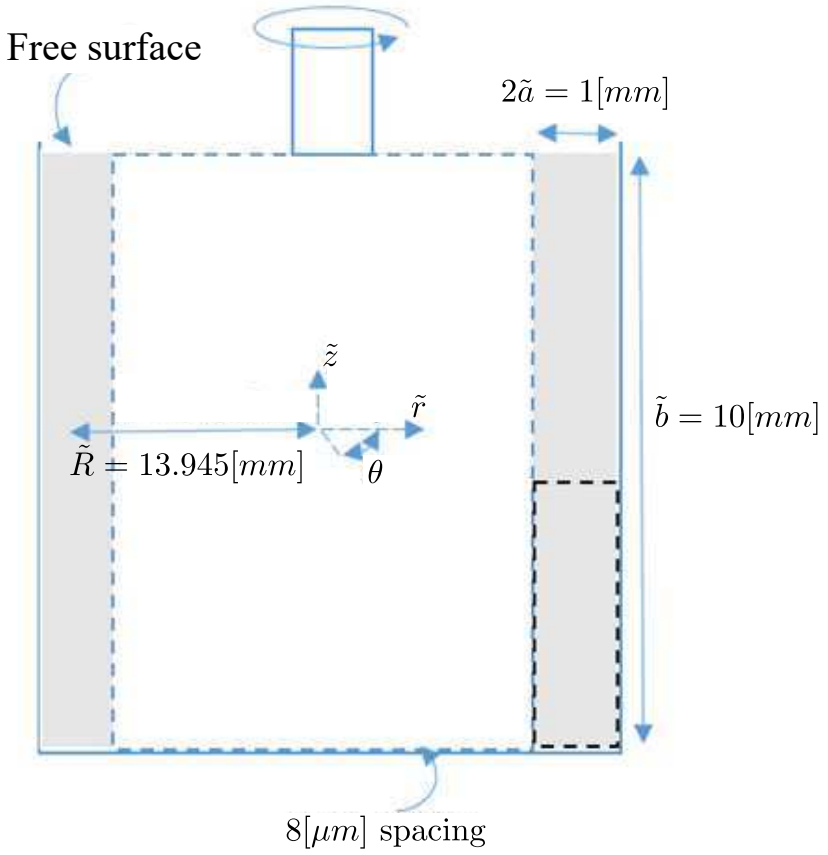

Figure 3.2: Schematic representation of the TC geometry used for optical visualizations. The dashed rectangle highlights the field of observation of a radial plane illuminated with laser light. Not to scale.

a high-molecular-weight polymer (polyethylene oxide (PEO) of $M_w = 4 \times 10^6 [g.mol^{-1}]$ supplied by Sigma Aldrich) to 42.9% (w/w) aqueous solvent solution ($\tilde{\eta}_s = 214 \mp 2[mPa.s]$) of the same polymer with a much lower molecular weight (polyethylene glycol (PEG) of $M_w = 8000[g.mol^{-1}]$ supplied by Sigma Aldrich). These fluids were then shipped to Paris for the experiments. This produces a so-called Boger fluid (James, 2009; Boger, 1977). The viscosity ratio for this fluid is estimated to be 0.89 (i.e. $\beta = \tilde{\eta}_s/\tilde{\eta}_t = 214/239$). For comparison with the Newtonian case, a glycerine aqueous solution 92% (w/w) is used to match the viscosity ($\tilde{\eta}_N = 240.5 \mp 0.7[mPa.s]$). For the two samples, the temperature was set to $20 \mp 0.1[^oC]$. The variations of the viscosity and shear stress with shear rate for both Newtonian and viscoelastic fluids are presented in Figure 3.3.

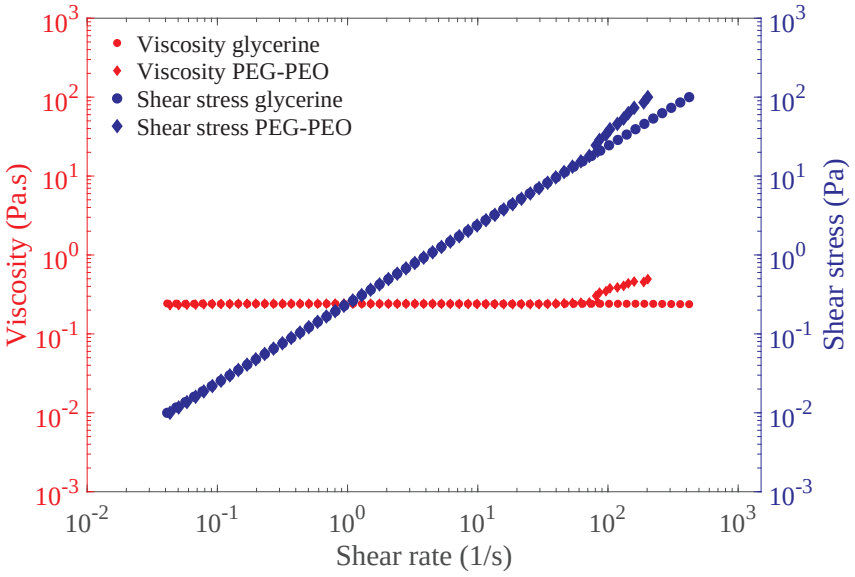

Figure 3.3: Shear stress and shear viscosity as functions of the shear rate for the glycerine solution and for the PEG–PEO solution at $\tilde{T} = 20[^oC]$. The data were collected in stress-controlled mode by increasing the shear stress with sampling of five second per data point.

As can be observed, around a shear rate of $\approx 80[s^{-1}]$ an instability is observed and a deviation between the apparent viscosity of Newtonian and viscoelastic material appears; however, before this critical value, the viscosities of the two fluids are equal and independent of shear rate. To calculate the relaxation time of the polymeric solution, a capillary breakup extensional rheometer (CaBER) (Rodd et al., 2005) test was carried out by the author in Liverpool giving a relaxation time of $0.27 \mp 0.03[s]$.

3.5.3 Experimental protocol

The gap of the TC device is illuminated with a laser sheet propagating along the velocity gradient direction and extending along the vorticity axis. The images of the gap in the velocity gradient/vorticity plane are recorded using a charge-coupled device (CCD) camera equipped with a macro lens. Two configurations were tested to obtain information regarding the azimuthal structure of the flow. In the first approach, a small amount of sample containing the fluorescent dye is injected along a vertical line which is typically $10[mm]$ long (the height of the TC cell) but which also fills the whole gap ($1[mm]$) along the radial direction. This dye is placed slightly upstream from the observation field (typically $1[cm]$ along the azimuthal direction upstream from the observation field) and is illuminated with green laser light (wavelength $532[nm]$). A supplementary movie available at https://doi.org/10.1017/jfm.2018.746 is included to highlight how such a passive tracer is advected in a Newtonian fluid following a step shear rate to demonstrate our flow visualization technique. In the second approach, flow visualizations are performed by seeding the sample with anisotropic reflective particles (Iriodin, Merck). The structure of the flow is probed by illuminating a cross-section of the gap with red laser light (wavelength $638[nm]$).

3.6 Results and discussion

In this section a discussion based on a comparison between the analytical, numerical and experimental observations is carried out.

3.6.1 Planar Couette flow

The flow distribution of the Newtonian creeping-flow finite-aspect-ratio planar Couette flow (zeroth order of the perturbation solution) is shown in Figure 3.4. In order to better understand the effect of aspect ratio, it is useful to define a modified form of aspect ratio as

$$\Lambda^* = \frac{\Lambda}{\Lambda + 1}. \tag{3.37}$$

Using this definition, when the aspect ratio (Λ) changes from zero to infinity, the modified form of the aspect ratio (Λ^*) varies from zero to one, respectively. Owing to the absence of curvature and inertia in this case, the flow has a quasi-linear distribution with no secondary flow. According to the rectilinear flow theorem of viscoelastic fluids (Reiner, 1945; Rivlin and Ericksen, 1997; Green and Rivlin, 1997; Rivlin, 1957), the solution of the velocity profile for viscoelastic fluids with a constant shear viscosity (the Oldroyd-B model) is identical to the Newtonian flow distribution in rectilinear cases. However, it should be noted that the velocity profile for Oldroyd-B fluids generates a

normal-stress distribution that consequently influences the pressure distribution, which is different from the Newtonian case.

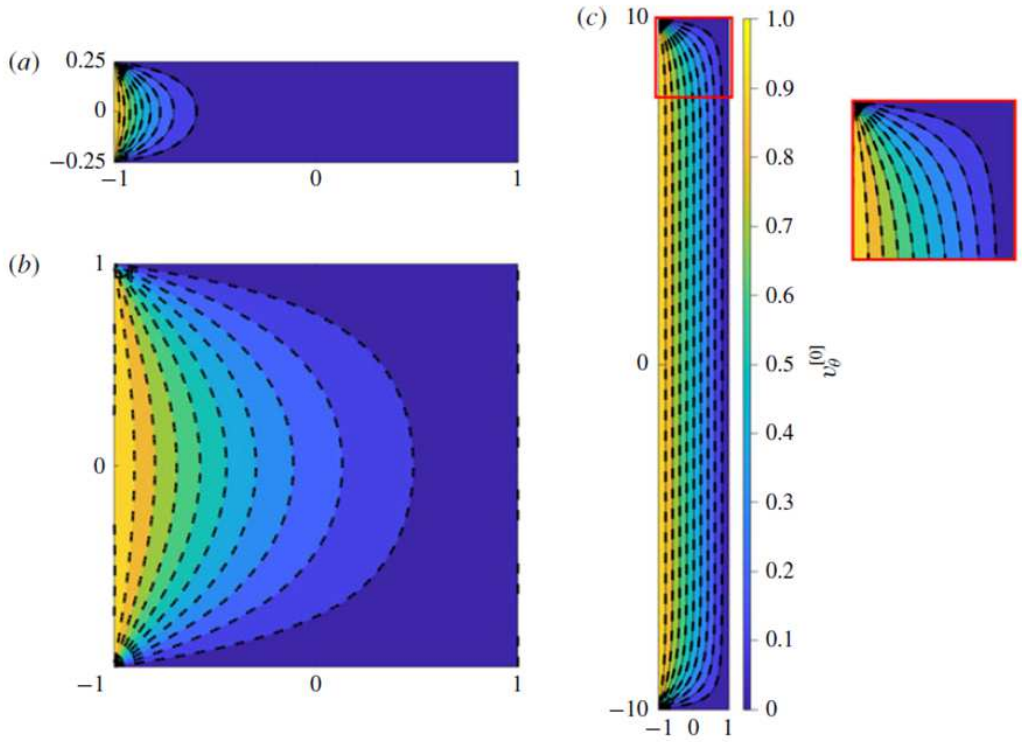

Figure 3.4: Velocity contours for planar Couette flow ('zeroth-order' solution, (equation 3.20)) for: (a) $\Lambda^*(\Lambda) = 0.2(0.25)$; (b)$\Lambda^*(\Lambda) = 0.5(1)$; and (c) $\Lambda^*(\Lambda) = 0.909(10)$. Analytical solution (filled contours); full nonlinear solution of Navier–Stokes using finite-volume solver (– – –).

In Figure 3.4, and all of the other results relating to the contours of the velocity and the streamfunction, the moving wall is the vertical left-hand sidewall. To check the accuracy of the derived zeroth-order solution ($\delta = 0$), a comparison between numerical simulations and the analytical solution is carried out (as shown in Figure 3.4). Also a comparison between the presented analytical solution and the solution obtained in Theofilis et al. (2004) is presented in Appendix B. In numerical simulations, flow distributions for three different aspect ratios $\Lambda^*(\Lambda) = 0.2(0.25), 0.5(1)$ and $0.909(10)$ with both ANSYS Fluent and OpenFOAM software have been simulated. The geometry consists of three stationary walls and one moving wall. To ensure the flow is fully developed, the non-dimensional length (made dimensionless using $\tilde{a}$) of this domain is chosen to be 1, Λ and 10 with the number of mesh points 50, 500 and $50 \times \Lambda$ in the x, θ and z directions, respectively. As is clear from inspection of Figure 3.4, the numerical simulations exhibit a good agreement with the analytical solution.

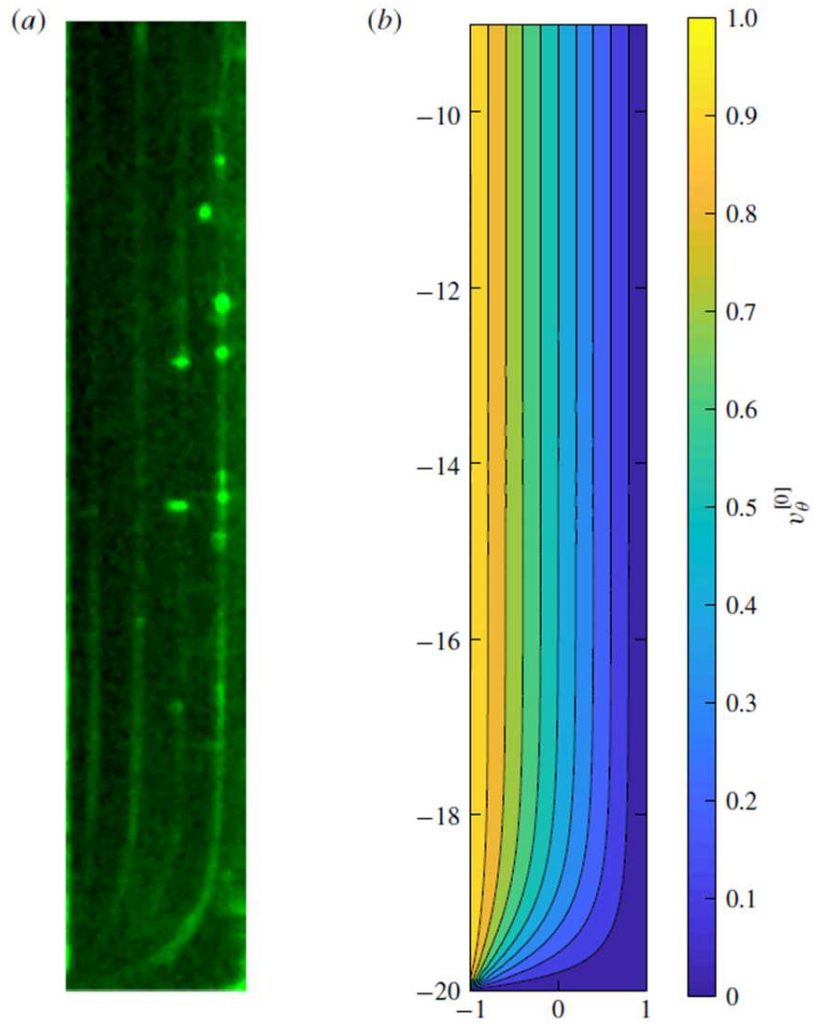

Figure 3.5: Effect of confining wall for a Newtonian fluid in steady planar Couette flow with aspect ratio $\Lambda = \frac{\tilde{b}}{\tilde{a}} = 20$. (a) Snapshot of the lower part of the gap which reflects the advection after five revolutions of a fluorescent dye initially injected at a given location slightly upstream with respect to the observation field. The glycerine solution is sheared at $\tilde{\dot{\gamma}} = 30[s^{-1}]$ ($Re \approx 5 \times 10^{-2}$). The bright fluorescent dots are due to small bubbles. (b) Creeping-flow axial velocity computed analytically from equation 3.20.

As can be seen, in small aspect ratios, the flow distribution is significantly influenced by the effect of the confining walls (Figure 3.4a,b) while, when the aspect ratio increases, the effect of the confining walls is limited to the region near the corner between the moving wall and the stationary wall, and the flow distribution in the middle tends towards the 1D linear solution (Figure 3.4c).

Experimental results in Paris were undertaken for a 92% (w/w) Newtonian glycerine/water solution in a geometrical configuration corresponding to $\Lambda = \frac{\tilde{b}}{\tilde{a}} = 20$. Figure 3.5(a) displays a snapshot of the lower part of the gap taken $14[s]$ after shear start-up at $\tilde{\dot{\gamma}} = 30s^{-1}$ ($Re \approx 5 \times 10^{-2}$). The viscous diffusion time being $\approx 4 \times 10^{-3}[s]$, the velocity profile is fully developed. The fluorescent dye, which is initially injected $\approx 1[cm]$ upstream with respect to the observation field, is convected along the azimuthal direction. The fluorescent lines in the picture represent lines of iso-velocity visible after approximately five revolutions. They provide information about the structure of the streamlines in the azimuthal direction. Away from the bottom wall, the picture is compatible with the solution of planar Couette flow; while close to the bottom wall, the confining effect is clearly observed. The analytical solution computed for the same geometrical conditions ($\Lambda = \frac{\tilde{b}}{\tilde{a}} = 20$) and $Re = 0$ is displayed in Figure 3.5(b). The steady velocity distribution is in good qualitative agreement with the experimental observations. For clarity, it should be reiterated that the creeping flow of a Newtonian fluid is purely azimuthal (θ) with no motion in the lateral directions, i.e. confirming no secondary flow is observed for creeping Newtonian fluid flow.

As was previously reported by Taylor (1923) and discussed in detail in Chapter 1, in the narrow-gap limit, the flow in the TC system for infinite aspect ratio should exhibit a linear distribution along the radial direction. In Figure 3.6(a), the velocity distributions across the gap centreline (i.e. along $z = 0$) for different aspect ratios are shown using both analytical and numerical results. The Figure 3.6 shows that the narrow-gap limit is approximately reached by $\Lambda^* = 0.909(\Lambda = 10)$ where the profile is linear, while for smaller normalized aspect ratios Λ^* the velocity distribution becomes strongly nonlinear.

In Figure 3.6(b,c), the variation of non-dimensional flow rate per unit length, which is normalized with the 1D flow-rate solution ($Q^{[0]}/Q_{1D}$), and its variation with aspect ratio are depicted. In finite-aspect-ratio cases, the flow rate is always smaller than the 1D flow through an equivalent area. This issue is clearly related to the effect of the confining walls resulting in a reduction of the fluid velocity in the region near to the wall. Interestingly, for the unit-aspect-ratio case ($\Lambda^* = 0.5$), the flow rate is reduced to exactly half of the equivalent 1D approximation. Figure 3.6(c) shows that the effect of normalized aspect ratio is exactly symmetric about $\Lambda^* = 0.5$, highlighting that the asymptotic behaviours as $\Lambda^* \to 0$ and $\Lambda^* \to 1$ are equivalent.

Figure 3.7 shows that, as the normalized aspect ratio decreases, the ratio of the wall

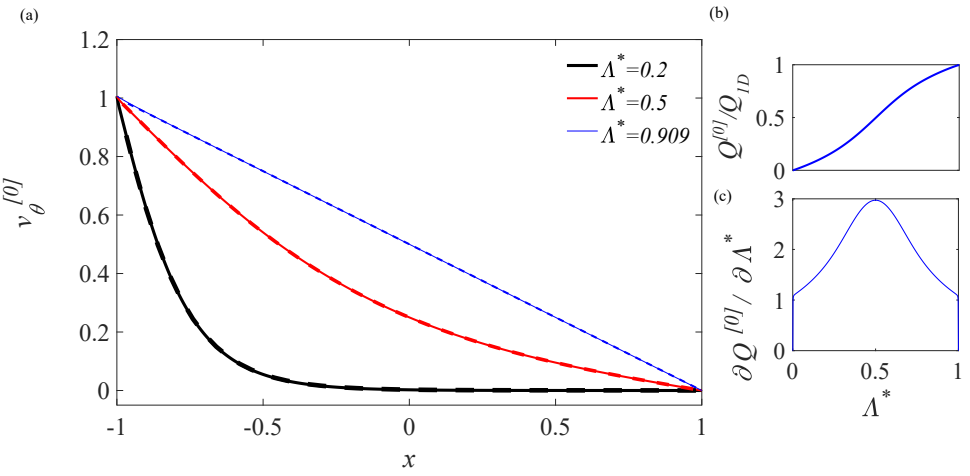

Figure 3.6: (a) Variation of streamwise velocity component across the gap centreline with Λ^*: analytical (solid); numerical (dashed). (b) Flow rate for planar Couette normalized by 1D Couette flow rate (linear velocity distribution) versus Λ^* (c) Variation of the flow-rate slope for planar Couette normalized by the 1D Couette flow rate (linear velocity distribution) versus Λ^*.

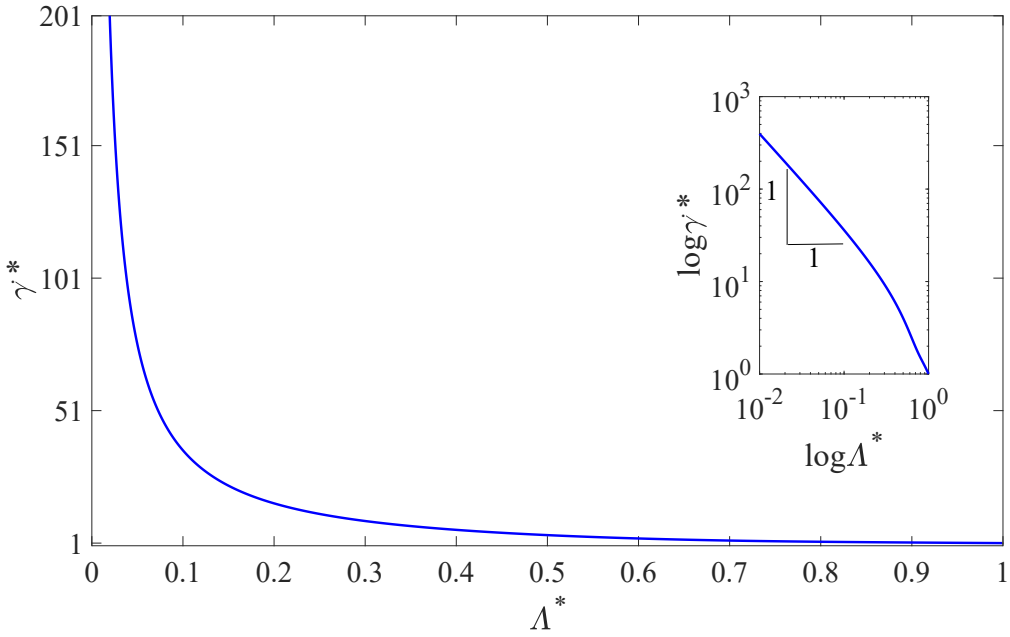

Figure 3.7: Effect of normalized aspect ratio Λ^* on the shear rate normalized with the shear rate of the 1D solution ($\dot{\gamma}_{1D}$) of planar Couette flow at $x = -1, z = 0$. Inset: $\dot{\gamma} = f(\Lambda^*)$ in log–log scale

shear rate at the centreline (i.e. at $x = -1, z = 0$) for the two-dimensional (2D) case over the shear rate of the 1D case increases and tends to infinity exhibiting an inverse relationship with the modified aspect ratio ($\dot{\gamma}^* \approx \frac{1}{\Lambda^*}$) in the limit $\Lambda^* \to 0$ (see inset in figure 3.7). The shear rate at higher aspect ratios tends to its 1D solution as can be expected, i.e. as $\Lambda^* \to 1, \tilde{\dot{\gamma}}^* \to 1$. By $\Lambda^* = 0.95(0.975)$ the shear rate is within 10%(5%) of the 1D value.

3.6.2 Relevance to purely elastic instabilities

The criterion presented by McKinley et al. (1996b) can be used to predict the onset of the purely elastic instability as presented in equation 1.2. In this presentation, when the M parameter reaches a critical value, the instability sets in where the critical magnitude for this parameter (i.e. M_{cr}) must be determined from either careful experiments or detailed calculations; e.g. for a 1D TC flow for the Oldroyd-B model with $\beta = 0.5$ using a linear stability analysis, it is determined to be $M_{cr} = 5.92$ (Larson et al., 1990). In the notation used here, for the limiting case of Oldroyd-B fluids in shear flows (i.e. $\tilde{\tau}_{ss} = 2\tilde{\eta}_p\tilde{\lambda}\tilde{\dot{\gamma}}^2$ assuming $\tilde{\dot{\gamma}} = \tilde{R}_i\tilde{\omega}/2\tilde{a}$ for a 1D case) and considering $\tilde{U} = \tilde{R}_i\tilde{\omega}$ and $\tilde{\Re} = \tilde{R}$, this criterion can be estimated as (McKinley et al., 1996b):

$$M = \sqrt{\delta(1-\beta)}Wi. \tag{3.38}$$

As shown in Figures 3.6 and 3.7, the shear rate along the centreline can be significantly influenced by the effect of the confining walls. So, from equation 3.38, one can expect that the aspect ratio will play an important role in triggering the critical condition where the instability starts. However, as the shear rate is singular at the corner, M is also singular here based on our analysis. Thus the analysis here is restricted to just centreline conditions.

In Figure 3.8 the effect of the modified aspect ratio on the M parameter is depicted along the centreline (based on the zeroth-order analytical solution) for a nominal situation of $\beta = 0.5, Wi = 0.1$ and $\delta = 0.1$. For this particular case, the M parameter for modified aspect ratios of 0.2, 0.5 and 0.8 are calculated as 0.08941, 0.0448 and 0.02745, respectively. Here, setting a constant $M_{cr} = 5.92$ (i.e. the value calculated from a linear stability analysis in the 1D limit) provides an estimate of the critical values of Wi for instability onset, which are 26.56, 21.57, 13.21 and 6.62 for modified aspect ratios of 1 (1D case), 0.8, 0.5 and 0.2, respectively. Once again the centreline values of shear rate are used for this estimate.

Table 3.2 shows the critical values of Wi where the numerical simulation predicts the onset of unsteadiness/instability in comparison to these analytical estimates assuming M_{cr} remains the same as the 1D linear stability result (Larson et al., 1990).

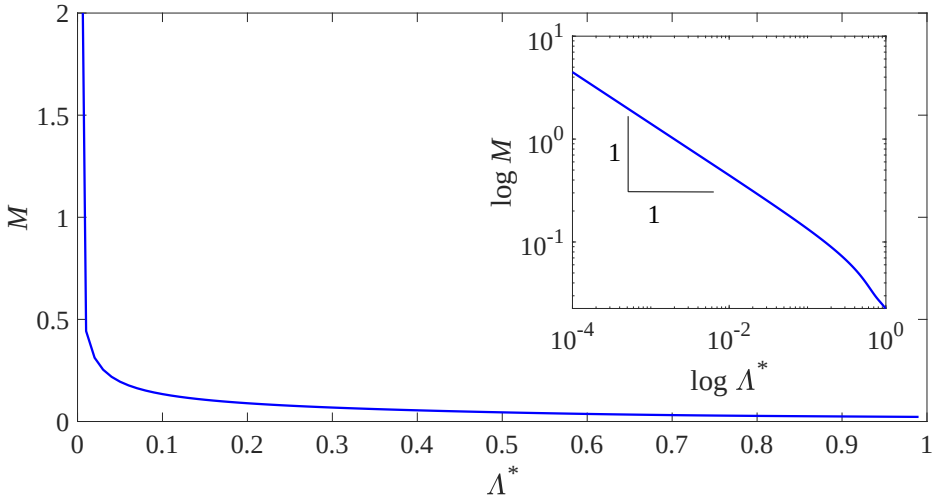

Figure 3.8: Effect of normalized aspect ratio Λ^* on the M parameter at $x = -1, z = 0$ for the $\beta = 0.5, Wi = 0.1, \delta = 0.1$ case.

Table 3.2: Critical values of Wi for onset of time-dependent flow determined via numerical simulations for case where $\delta = 0.1$ and $\beta = 0.5$ at different aspect ratios.

$\Lambda^*(\Lambda)$	0.2(0.25)	0.5(1)	0.8(4)
Wi_{cr}(numerical)	6	7	10
Wi_{cr}(analytical) (assuming $M_{cr} = 5.92$)	6.62	13	21

Our numerical data suggest that M_{cr} is not a constant but changes with the aspect ratio. The critical values of M where the onset of instability is observed numerically for normalized aspect ratios of 0.2, 0.5 and 0.8 are 1.34, 1.56 and 2.23, respectively. At these values, the numerical results show that the flow becomes time-dependent. Our analysis would indicate that purely elastic instabilities are more likely to occur at lower Weissenberg numbers for lower-aspect-ratio geometries even when just the centreline shear rates are considered in the analysis. Thus, if one wanted to promote such instabilities, for example to enhance mixing, this could be achieved via small-aspect-ratio geometries. This result may also have important applications for small-angle neutron scattering or flow birefringence studies, which tend to use smaller-aspect-ratio devices.

3.6.3 Viscoelastic narrow-gap Taylor–Couette flow for arbitrary aspect ratio

As previously discussed with reference to equation 3.36, in the creeping TC flow with finite aspect ratio of viscoelastic fluids, secondary flows are already likely to develop below the purely elastic instability threshold due to the existence of gradients of the first normal-stress difference (from the $\tau_{\theta\theta}/r$ term in 3.6). The combined effect of curvature and the first normal-stress difference results in the movement of the fluid element in the radial direction (as can be seen in equation 3.6), but conservation of mass requires the flow to be replaced and, as a result, a pair of secondary flow vortices appears. This mechanism is similar to the one which activates the Dean vortices in creeping viscoelastic flows in curved pipes (Robertson and Muller, 1996; Jitchote and Robertson, 2000), but in the current study the flow is driven by wall motion rather than by a pressure gradient.

The structure of these secondary flows is presented for three different aspect ratios in Figure 3.9 based on both the analytical solution and numerical simulations. Only the 'lower' half of the geometry is depicted in all cases due to the symmetry about $z = 0$. The results show that the secondary flows are always located close to the region near the corner of the moving and stationary walls, which is related to the presence of strong gradients in the shear rate and consequently the normal stresses in this region. Remarkably, the formation of the secondary flow vortices can be captured experimentally. Figure 3.10 displays a time sequence of images of the lower part of the gap during shear start-up at $\tilde{\dot{\gamma}} = 30[s^{-1}](Re = 5 \times 10^{-2})$ (as in the Newtonian case) and $Wi \approx 18$ for the $500[ppm]$ (w/w) of PEO in 42.9% (w/w) aqueous solution of PEG at $\tilde{T} = 20[^{o}C]$. Note that the purely elastic instability for this system is triggered for $\tilde{\dot{\gamma}} = 80[s^{-1}]$ (see Figure 3.3). Close to the bottom wall, the iso-velocity lines exhibit successive foldings due to the development of a vortex from the corner between the moving wall and the fixed bottom wall. The iso-velocity lines and the structure of the

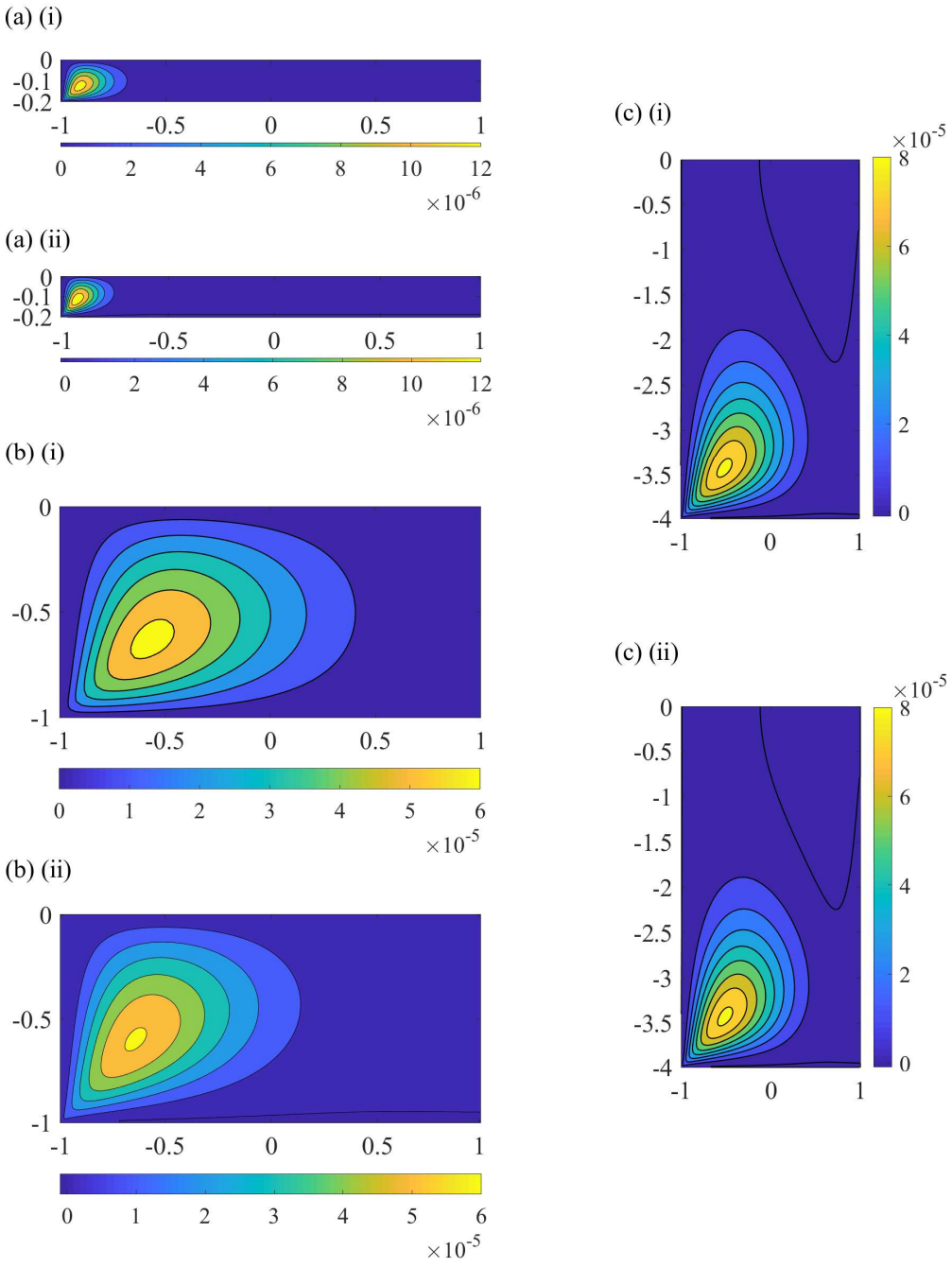

Figure 3.9: Analytical (i) and numerical (ii) estimation of the structure of secondary-flow streamlines for $Wi = 0.1, \beta = 0.5, \delta = 0.1$ (a)$\Lambda^*(\Lambda) = 0.167(0.2)$; (b)$\Lambda^*(\Lambda) = 0.5(1)$; (c)$\Lambda^*(\Lambda) = 0.8(4)$. Owing to the symmetry about $z = 0$ only the lower half of the geometry is depicted

corner vortex can be observed during several tens of seconds before homogenization due to molecular diffusion of the fluorescent dye.

In order to better capture the structure of the corner vortex at long times, flow visualizations were also performed using anisotropic reflective particles seeded in the sample. In this configuration the gap of the TC device is illuminated with red laser light. Figure 3.11(a) is obtained by taking a moving average over $100[s]$ of sequential images when the steady-state regime is achieved. From this picture, iso-light contours can be extracted (Figure 3.11b). The position of the eye of the corner secondary flow and its structure show a good qualitative agreement with the result obtained based on the analytical solution for the case $\delta = 0.04, \Lambda = 20, Re = 0, Wi = 18, \beta = 0.89$ (Figure 3.11c). It should be noted that, strictly speaking, the analytical solution is being used outside of its range of validity at this Weissenberg number, and so this comparison is best viewed as purely qualitative in terms of secondary flow structure. The location of the eye of maximum vortex (or the centre of the secondary flow) is given in Figure 3.12 based on analytical and numerical results. The location of the maximum vortex starts to move from a region close to the moving wall in the radial direction while its position stays constant in z, when the aspect ratio increases from 0.1 to 1. As the aspect ratio increases from 1 to 2, the location of the maximum vortex migrates to a new position in both the radial and z directions. Finally, it can be seen that, by further increasing the aspect ratio, the eye of the vortex remains at a constant radial location while it migrates towards the top wall (i.e. $z \to 1$). Although these trends are the same for both the analytical and numerical results, there is a systematic quantitative variation between the two approaches as had already been observed in section 3.4 where the mesh dependence was discussed for the square aspect-ratio case.

To analyse the range of validity of the perturbation method, the variation of the maximum value of the secondary flow streamfunction with Wi for both the analytical and the numerical solutions are presented in Figure 3.13. The data show that this parameter increases linearly with an increase in the Weissenberg number in the range of $0 < Wi < 1.1$, confirming that the approximate analytical solution data for this range is in an acceptable agreement with the full nonlinear numerical simulation. As shown in Figure 3.6(b), the flow rate decreases with a decrease in the aspect ratio. Figure 3.13 shows that the same trend may also be observed for the maximum value of the secondary flow streamfunction, which may seem, at first glance, reasonable but, as the secondary flow is driven by a gradient induced by the confining walls, this is counter-intuitive, as these effects would be expected to increase as the confining walls become more important ($\Lambda \to 0$). This confusion can be attributed to the manner in which velocity components and, consequently, the secondary flow streamfunction are made dimensionless. As also shown in Figure 3.6(b), a decrease in the aspect ratio is

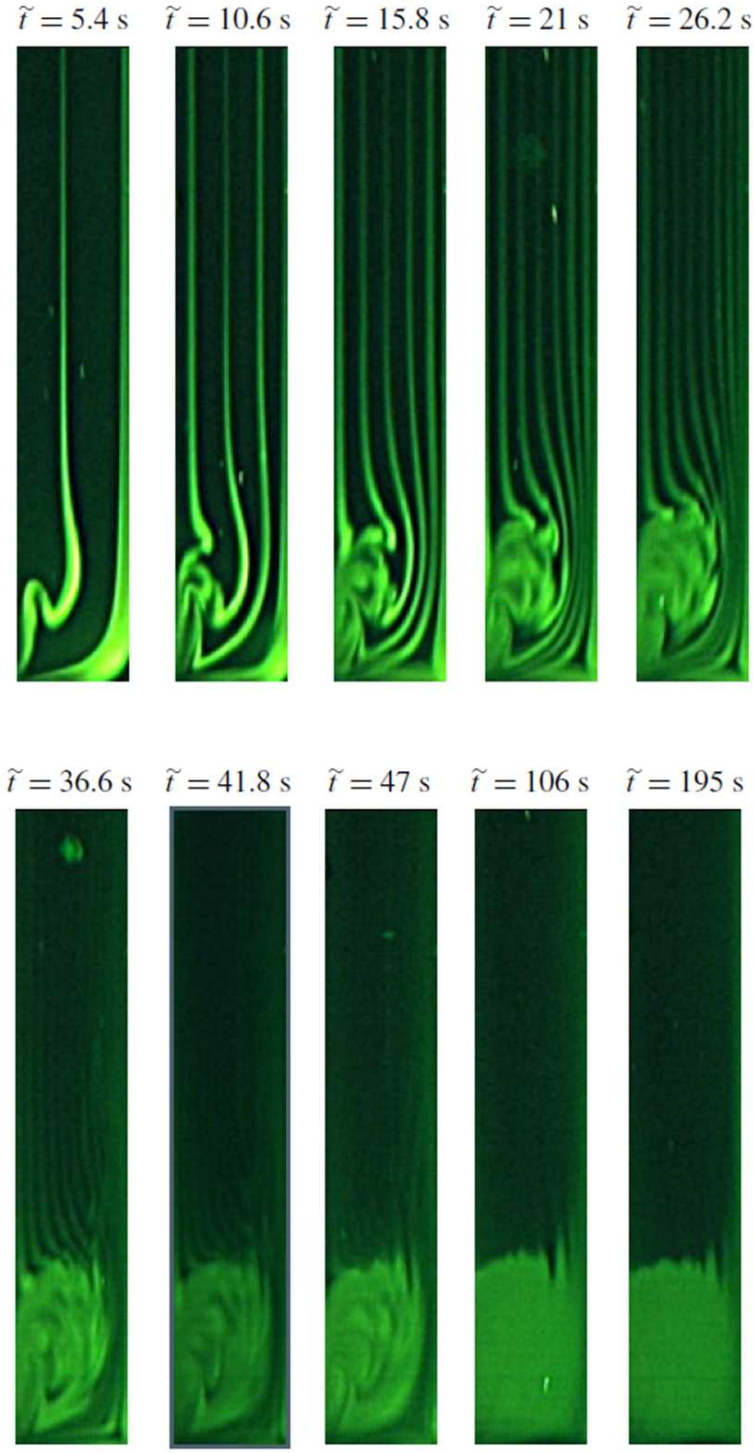

Figure 3.10: Time sequence of images illustrating the formation of the corner secondary flow structure for a 500 ppm (w/w) of PEO in 42.9% (w/w) aqueous solution of PEG at $\tilde{T} = 20[^oC]$. The applied shear rate is $\tilde{\dot{\gamma}} = 30[s^{-1}](\delta = 0.04, Wi = 18, \beta = 0.89, Re = 5 \times 10^{-2})$. The observation field covers 56% of the height of the cylinders in the z direction and the full gap ($1[mm]$) in the radial direction.

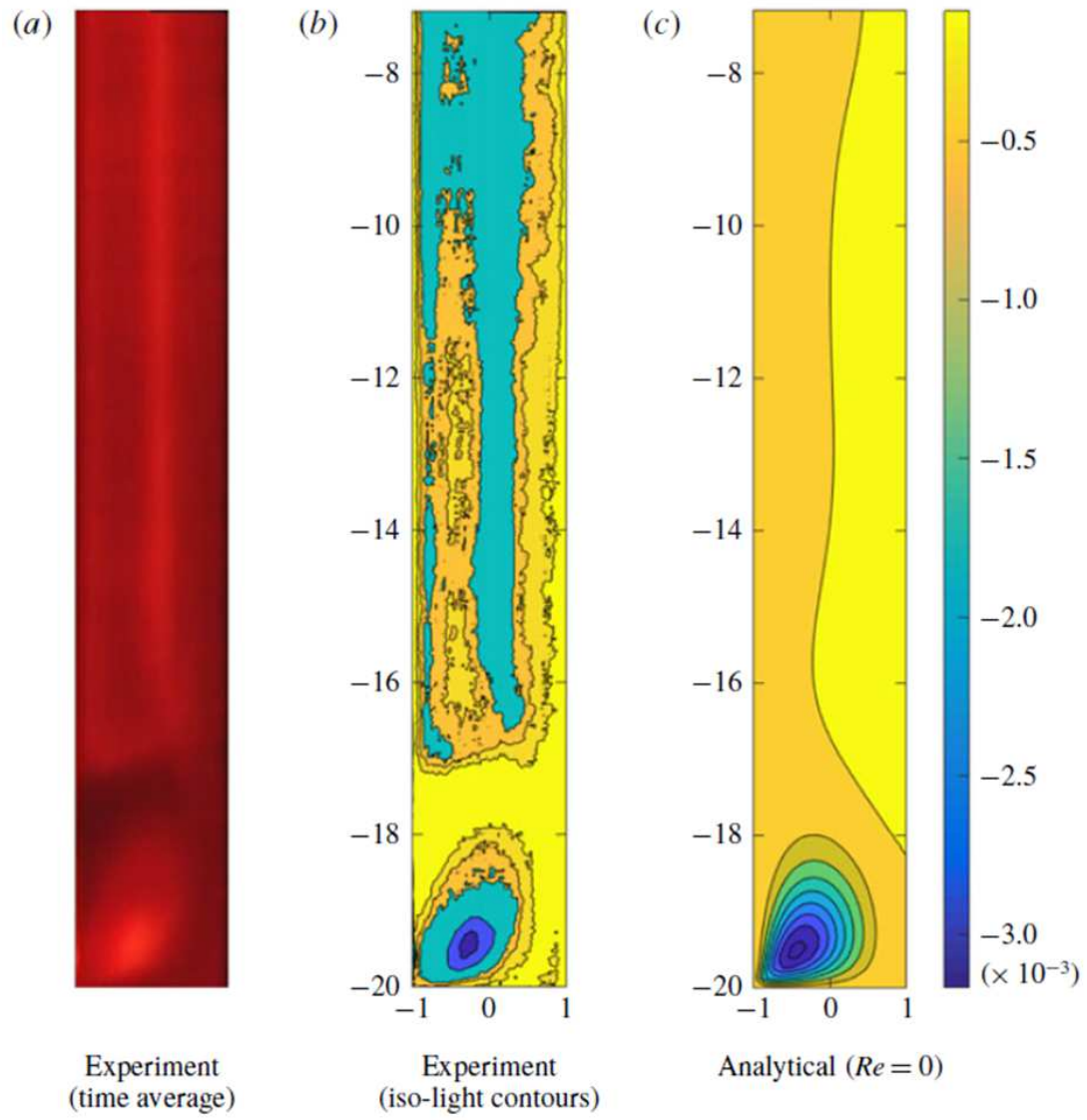

Figure 3.11: Comparison of the corner secondary flow between the analytical ($x_{\psi_{min}} = -0.45, z_{\psi_{min}} = -19.46$) and experimental observation ($x_{\psi_{min}} = -0.52, z_{\psi_{min}} = -19.72$) of 500[$ppm$] (w/w) of PEO in 42.9% (w/w) aqueous solution of PEG at $\tilde{T} = 20[^oC]$. The applied shear rate is $\dot{\gamma} = 30[s^{-1}]$. Experiments: $\delta = 0.04, \Lambda = 20, Re = 5 \times 10^{-2}, Wi = 18, \beta = 0.89$. Analytical:$\delta = 0.04, \Lambda = 20, Re = 0, Wi = 18, \beta = 0.89$.

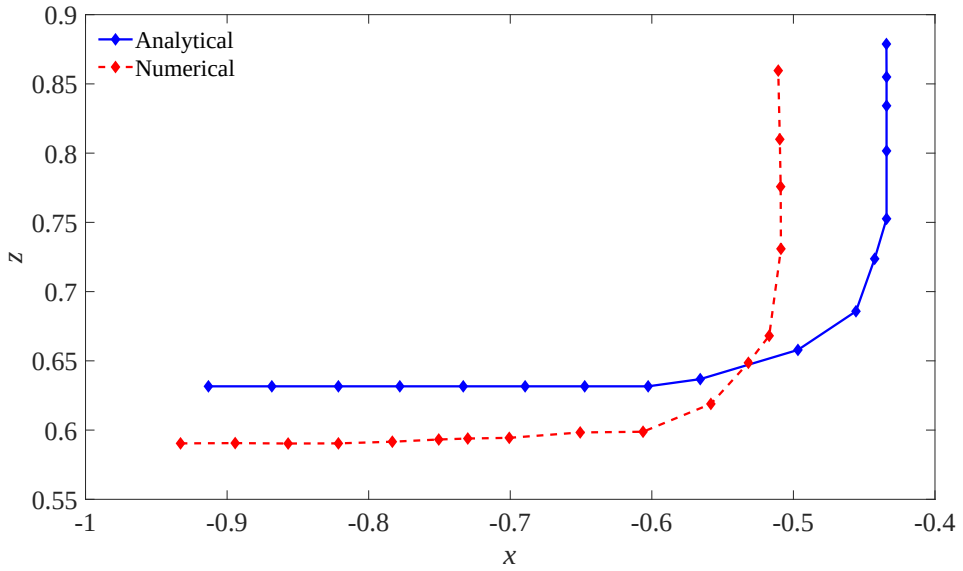

Figure 3.12: Locations of the eyes of maximum vortices for $Wi = 0.1, \beta = 0.5, \delta = 0.1$ in different aspect ratios Λ =0.2, 0.3, 0.4, 0.5, 0.6, 0.7, 0.8, 0.9, 1.0, 1.25, 1.5, 1.75, 2.0, 2.5, 3.0, 3.5 and 4.0 (diamonds, from left to right, respectively).

followed by a decrease in the magnitude of the average velocity throughout the gap. To better discuss the effect of confining walls on the secondary flow, it is better to use the mean value of the main velocity as the reference velocity in Figure 3.13(b) rather than the wall velocity. In this manner, one can see how the magnitude of the secondary flow streamfunction is scaled with respect to the mean value of the velocity at the same aspect ratio. Using this normalization, it can be shown that, although the magnitude of the main velocity is decreased as the aspect ratio decreases, the ratio of the magnitude of the secondary flow velocity relative to the mean velocity increases, confirming the fact that lateral components of the velocity get stronger as the confining effect of the walls increases ($\Lambda \to 0$).

3.6.4 Conclusions

In this chapter, based on both a linear analytical perturbation approach and full nonlinear numerical simulations using a finite-volume technique, the effect of confining walls on the inertialess, viscoelastic narrow-gap TC system was investigated and compared with experimental observations. The results show that, for any finite aspect ratio, a pair of secondary flow vortices exists for any non-zero elasticity (i.e. $Wi > 0$), in excellent qualitative agreement with the experiments. This secondary flow appears due to the presence of gradients of the first normal-stress difference (more precisely from the $\tau_{\theta\theta}/r$ term in equation 3.6). The confining walls on the top and bottom of the geometry can

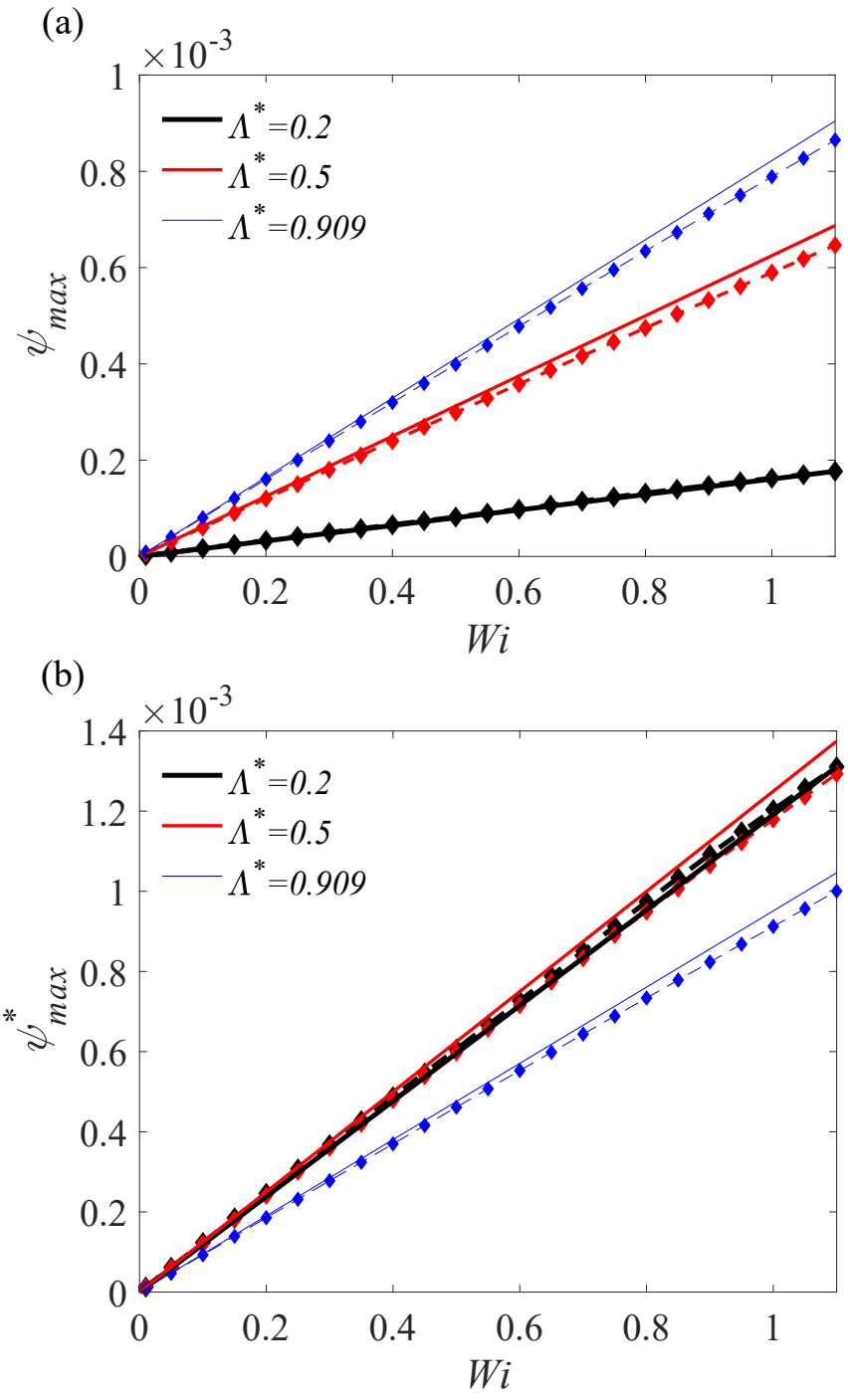

Figure 3.13: Variation of ψ_{max} with Wi for $\beta = 0.5$, $\delta = 0.1$ in different aspect ratios of $\Lambda^*(\Lambda) = 0.2(0.25)$, $\Lambda^*(\Lambda) = 0.5(1)$ and $\Lambda^*(\Lambda) = 0.909(10)$ (a) normalized with wall velocity and (b) normalized with mean value of main velocity. The solid line shows the analytical solution and the dashed line with diamonds highlights the numerical data.

significantly influence the flow distribution through the gap, and the average velocity in the narrow gap is always smaller than the 1D case.

The confining effect of the walls can modify the threshold of the purely elastic instability which is known to occur in TC systems. Based on full nonlinear simulations, the M_{cr} parameter of McKinley et al. (1996b) is not a constant for the finite-aspect-ratio cases but a weak function of the aspect ratio of the geometry. Nevertheless the values of the M parameter obtained (1.3–2.2) are broadly consistent with values obtained in purely elastic instabilities for other flows (McKinley et al., 1996b; Alves and Poole, 2007; Zilz et al., 2012; Sousa et al., 2016; Pakdel and McKinley, 1998). The analysis here would indicate that purely elastic instabilities are more likely to occur at lower Weissenberg numbers for lower-aspect-ratio geometries and this could be used to promote such instabilities, e.g. to enhance mixing. The results in this chapter may also have important applications for TC devices used in small-angle neutron scattering or flow birefringence experiments, which tend to use smaller aspect ratios and are therefore more probe to purely-elastic instabilities which would be unwanted in these cases.

Chapter 4

Control of symmetry-breaking instability in cross-slot geometries [1]

The cross-slot stagnation point flow is one of the benchmark problems in non-Newtonian fluid mechanics as it allows large strains to develop and can therefore potentially be used for extensional rheometry measurements or, once instability arises, as a mixing device. In such a flow, beyond a critical value in which the ratio of elastic force to viscous force is high enough, elasticity can break symmetry even in the absence of significant inertial forces (i.e. creeping flow), which is perhaps an unwanted phenomenon if the device is to be used as a rheometer but beneficial from a mixing perspective. In this chapter, a passive control mechanism is introduced to the cross-slot by adding a cylinder at the geometric centre to replace the "free" stagnation point with "pinned" stagnation points at the surface of the cylinder. In the current modified geometry, effects of the blockage ratio (the ratio of diameter of the cylinder to the width of the channel), the Weissenberg number (the ratio of the elastic forces to viscous forces) and extensibility parameters (α and L^2 parameters) are investigated in 2D numerical simulations using both the simplified Phan-Thien and Tanner (sPTT) and finitely extensible non-linear elastic (FENE-P) models (Appendix E). It is shown that the blockage ratio for fixed solvent-to-total viscosity ratio has a stabilizing effect on the associated symmetry-breaking instability. The resulting data show that the suggested modification, although significantly changing the flow distribution in the region near the stagnation point, does not change the nature of the symmetry-breaking instability or, for low blockage ratio, the critical condition for onset. Using both numerical and physical experiments coupled with a supporting analytic analysis, it can be concluded that this instability cannot therefore be solely related to the extensional flow near the stagnation point but it is more likely related to streamline curvature and the high deformation rates near the corners i.e. a classic "curved streamlines" purely-elastic

[1] Work from this chapter has been submitted to Journal of Fluid Mechanics.

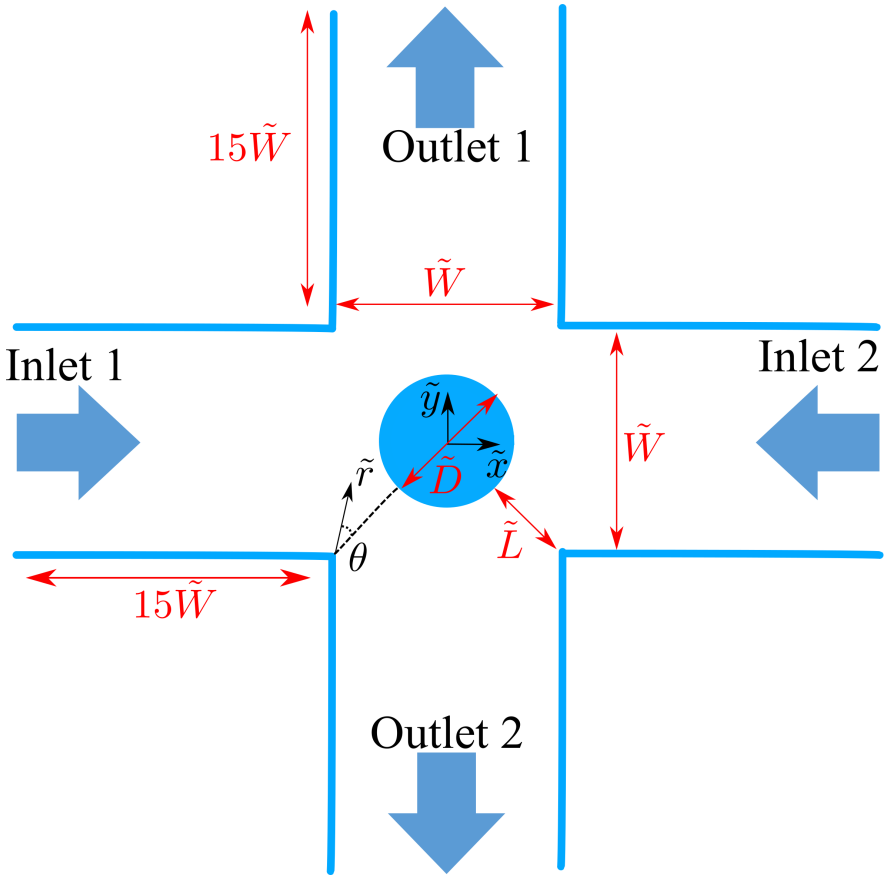

Figure 4.1: Schematic of the cross-slot geometry with a cylinder and the coordinate systems used in the problem. Not to scale. The angle theta is measured with respect to the diagonal line $|x| = |y|$.

instability following the Pakdel-McKinley paradigm encapsulated in equation 1.2. The work in this chapter also suggests that the proposed geometric modification can be an effective approach to enabling higher flow rates to be achieved whilst retaining steady symmetric flow allowing effective control of flow in the cross-slot.

4.1 Geometric configuration and problem definition

A schematic of the geometry and employed coordinate systems are shown in Figure 4.1. The length of inlet/outlet arms are set to be 15 times of the width of channel in order to allow fully-developed conditions at the cross-slot, which we confirmed in our numerical simulation to be sufficient. In the numerical procedure, a constant bulk velocity $\tilde{U}_B$ at the inlets, and Neumann boundary condition at the outlets were assumed. At the walls, the no-slip boundary conditions were imposed and the values of the extra stress components were linearly extrapolated using the method introduced in Pimenta and Alves (2017). In order to better understand effects of the proposed geometry modification on the cross-slot symmetry-breaking instability, besides the no-slip boundary condition,

a number of additional simulations using a complete slip boundary condition at the cylinder wall were also carried out (i.e. normal velocity component is fixed to zero while the tangential component is set to have zero gradient). No finite disturbances are introduced in the simulations to induce the onset of symmetry-breaking instability. Instead, the instability is naturally triggered from accumulation of numerical error via machine level precision.

4.2 Non-dimensionalization

It is convenient to use dimensionless parameters in this problem. The relationships between dimensional and dimensionless parameters are:

$$x = \frac{\tilde{x}}{\tilde{W}}, y = \frac{\tilde{y}}{\tilde{W}}, r = \frac{\tilde{r}}{\tilde{W}}, \Phi = \frac{\tilde{D}}{\tilde{W}}, \boldsymbol{U} = \frac{\tilde{\boldsymbol{U}}}{\tilde{U}_B}, Re = \frac{\tilde{\rho}\tilde{U}_B\tilde{W}}{\tilde{\eta}_t},$$
$$Wi = \frac{\tilde{\lambda}\tilde{U}_B}{\tilde{W}}, \beta = \frac{\tilde{\eta}_s}{\tilde{\eta}_t}, N_1 = \frac{\tilde{\tau}_{xx} - \tilde{\tau}_{yy}}{\tilde{\eta}_t\tilde{U}_B/\tilde{W}}, \dot{\epsilon} = \frac{\tilde{\dot{\epsilon}}}{\tilde{U}_B/\tilde{W}}, \boldsymbol{\Omega} = \frac{\tilde{\boldsymbol{\Omega}}}{\tilde{U}_B/\tilde{W}}$$

were $\tilde{x}$, $\tilde{y}$ and $\tilde{r}$ are the variables related to the corresponding rectangular and polar coordinate systems, $\tilde{W}$ is the width of the channel, $\tilde{D}$ is the diameter of the cylinder, Φ is the blockage ratio parameter which may change between zero (the standard cross-slot geometry with no cylinder) to $\sqrt{2}$ (fully blocked cross-slot geometry) values, $\tilde{\boldsymbol{U}}$ is the velocity vector, $\tilde{U}_B$ is the imposed bulk velocity at the inlet arms, Re is the Reynolds number which is set to be 0.01 for all simulations in order to model creeping flow, Wi is the Weissenberg number, β is the solvent-to-total viscosity ratio and $\tilde{\eta}_t$ is the total viscosity (i.e. $\tilde{\eta}_t = \tilde{\eta}_s + \tilde{\eta}_p$), N_1 is the non-dimensional first normal-stress difference, $\tilde{\dot{\epsilon}}$ is the strain rate and $\tilde{\boldsymbol{\Omega}}$ is the vorticity tensor.

4.3 Mesh dependency study

In this section, a number of representative results analysing the effect of mesh on the 2D flow distribution are presented to give an overview of numerical accuracy. The block-structured mesh generation in OpenFoam, requires the flow domain to be divided into sixteen smaller sub-domain blocks. In Figure 4.2, a schematic definition of the different blocks used in the mesh generation steps for a nominal blockage ratio of $\Phi = 55\%$ is illustrated. Here, two different meshes were used and the characteristics of these meshes are presented in Table 4.3. The cell growth rate (GR) is defined based on the ratio of the first cell size to the last cell size in a specific direction. Note that, owing to the symmetry of the domain, only mesh information for a quarter of the geometry is presented but the full geometry is used in all simulations.

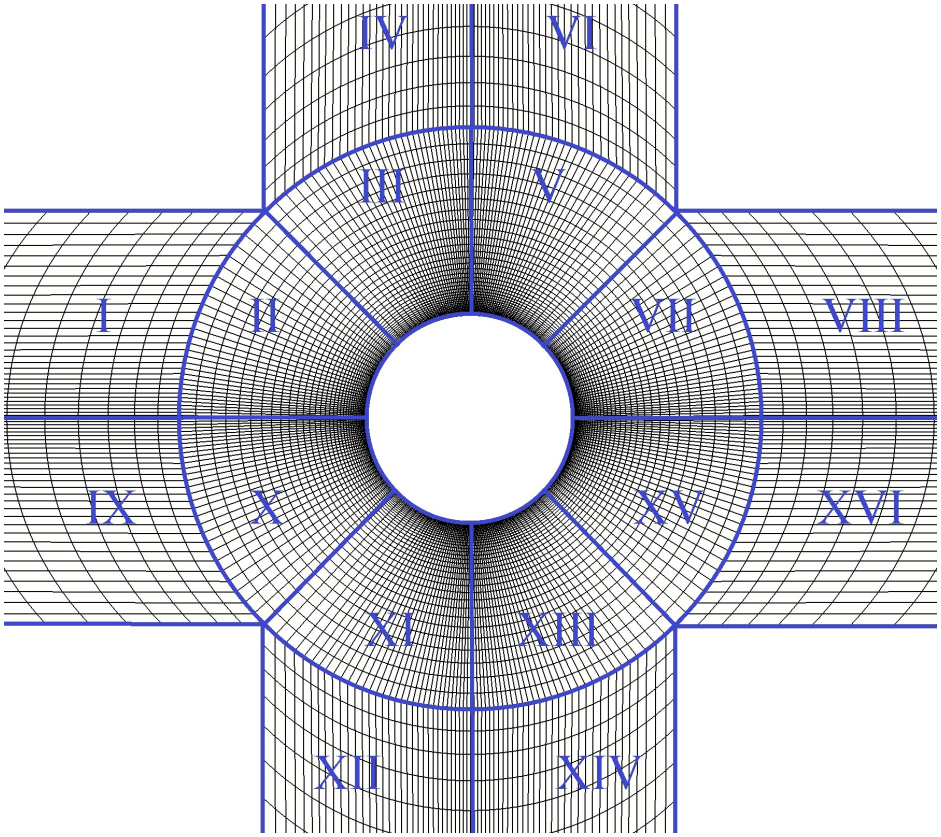

Figure 4.2: Schematic representation of the geometry and definition of the blocks used to generate the mesh

Table 4.1: Main characteristics of meshes in different blocks (NR × NT (GRR, GRT))[a] problems.

Block	**I**	**II**	**III**	**IV**	**NCV**[b]
M1	60×30 (0.05, 5)	36×30 (25, 5)	36×30 (25, 0.2)	60×30 (20, 0.2)	23040
M2	120×60 (0.05, 5)	72×60 (25, 5)	72×60 (25, 0.2)	120×60 (20, 0.2)	92160

[a] NR, NT: number of cells in radial and tangential directions; GRR, GRT: Cell grow rate in radial and tangential directions.

[b] NCV: total number of control volumes.

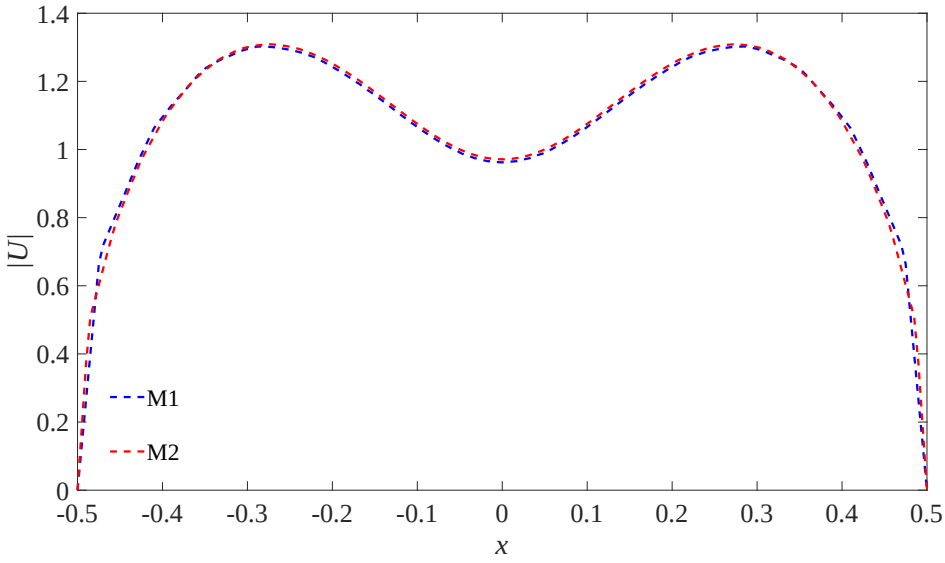

Figure 4.3: Distribution of velocity magnitude, at the entrance region of the outlet arms (i.e. along the line $y = \pm 0.5$) for different meshes for Newtonian creeping flow. M1 and M2 results are shown in blue and red, respectively.

In Figure 4.3, the effect of mesh refinement on the flow distribution of creeping Newtonian flow are presented (i.e. $Re = 0.01$). In this figure, the distribution of velocity magnitude at the entrance region of the outlet arms, are presented for the meshes introduced in Table 4.3. The results show that the mean average errors between M1 and M2 are less than 1.3%. Therefore, the remaining results presented here were obtained using the M1 except for simulations corresponding to $\Phi = 10\%$ in which meshes similar in density to M2 were used. For the standard cross-slot geometry a mesh similar to the work by Cruz et al. (2016) consisted of five blocks were used. The total number of cells for the standard cross-slot geometry is 13005.

4.4 Experiments

4.4.1 Experimental set-up

A schematic diagram of the experimental rig is shown in Figure 4.4. Flow through the microfluidic system was driven using two identical individually-controlled high precision syringe pumps (PHD Ultra Harvard Apparatus). One of the pumps drives fluid into the two opposed inlets, while the other one withdraws fluid simultaneously from the two outlets of the device (all at equal volumetric flow rates). According to the manufacturer, the mass flow rate ($\tilde{m}$) certified accuracy is 0.35% at the lowest free pulsation-free delivering rate, which set the lowest flow rate used.

For the purpose of this study, two geometries including one standard cross-slot device and one modified cross-slot geometry with $\Phi = 55\%$ were designed. These

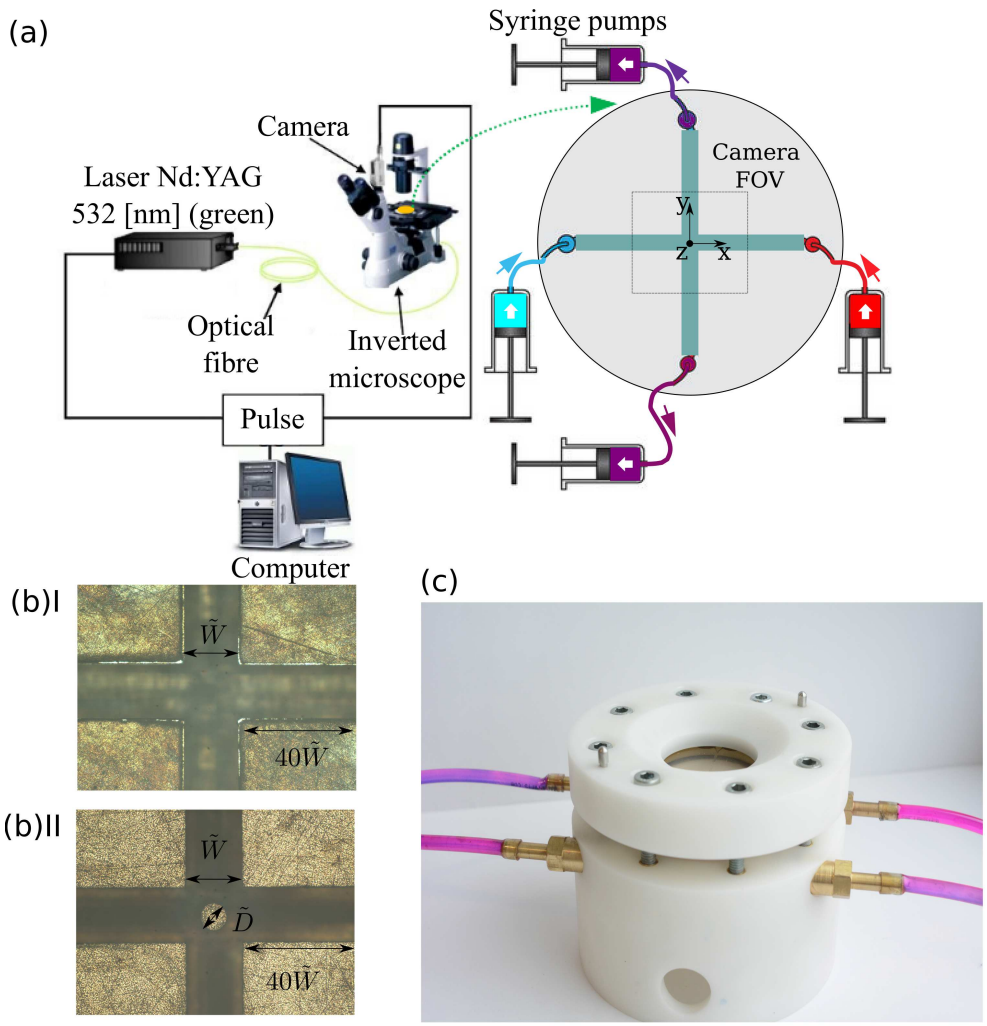

Figure 4.4: (a) A schematic illustrating the experimental apparatus of a microfluidic cross-slot device allowed for direct observation of the $x-y$ plane. The origin is placed at the geometric centre of the device. The rig is mounted on an inverted microscope fitted with a filter cube. A pulsed Nd:YAG laser is used to excite the dyed fluid, and a CCD camera enables the instability formation to be captured (notes: 1-not to scale; 2-camera FOV to be captured (field of view): 4 [mm] $\times$ 4 [mm]). (b) The prototype microfluidic device rigs for I: standard cross-slot geometry and II: the cross-slot with cylinder geometry. The channels were micro-machined in brass and encased in poly-oxymethylene. A 6.5[mm] thick upper wall fabricated from borosilicate glass to obtain seal while allowing the flow structure to be visualised. (c) Photograph illustrating the experimental rig set-up assembled.

geometries were micro-machined into two pieces of brass using CNC machining with a rectangular cross-section channel. Here, to best approximate a 2D channel, the channel height is selected to be twice of its width, $\tilde{H} = 2000 \pm 10[\mu\text{m}]$ and $\tilde{W} = 1000 \pm 10[\mu\text{m}]$, respectively. The device was encased in polyoxymethylene, an insulating material also known as ACETAL. The cross-section dimensions of the cross-slot flow device were quantified using a Nikon EPIPHOT TME inverted microscope with 100 times magnification, 470 pixels = 1000[μm]. The combined length of the channel inlet and outlet is $80\tilde{W} = 80 \pm 0.1$[mm] to ensure fully-developed flow at the central region of the geometry for all flow rates studied. The cross-slot geometry was enclosed by a 6.5[mm] thick upper wall fabricated from borosilicate glass to maintain sealing while still allowing the flow structure to be visualised.

Rhodamine-B (ACROS Organics) was chosen as a fluorescent dye to capture the flow patterns in the cross-slot micro-geometry (Ross et al., 2001; Huang et al., 2013, 2014). The dyed fluid was prepared by dissolving 30 ppm of Rhodamine-B in half of the working fluid. The optical set-up is composed of an inverted microscope (DMI, Leica Microsystems GmbH) fitted with an appropriate filter cube (excitation BP $530 - 545$[nm], dichroic mirror 565[nm], barrier filter $610 - 675$[nm], Leica Microsystems GmbH), and a pulsed Nd:YAG laser (Solo-PIV III laser, wavelength 532[nm], New Wave Research) that is used to excite this fluorescent Rhodamine-B dye with illumination and a CCD (charge couple device) camera.

4.4.2 Working fluids

The Newtonian working fluid used in the experiments is a mixture of glycerine (relative density 1.26, ReAgent Chemical Services) and distilled water with a nominal concentration of 70 percent glycerine (by weight). The density ($\tilde{\rho}$) and viscosity ($\tilde{\eta}_s$) of the mixed solution were measured at $\tilde{T} = 20[^\circ\text{C}]$. A density meter (Anton Paar DMA 35N) with a quoted precision of $0.001[\text{g/cm}^3]$ was used for quantifying the fluid density. A controlled-stress torsional rheometer (Anton Paar MCR302) was utilised to measure the fluid viscosity using a 60[mm] and 1° cone with a shear rate range from $1[\text{s}^{-1}]$ to $200[\text{s}^{-1}]$. The measured values of the density ($\tilde{\rho}$) and viscosity ($\tilde{\eta}_s$) are $1184[kg/m^3]$ and $35.50[mPa.s]$, respectively.

To elucidate the role of elasticity, a mixture of 70 percent glycerine and distilled water (by weight) and 190 ppm polyacrylamide (PAA, $\text{M}_\text{w} = 18 \times 10^6[\text{g.mol}^{-1}]$, Sigma-Aldrich). Initially, the required amount of PAA is added to distilled water, and the resultant liquid is slowly mixed using a magnetic stirrer. In another container, the necessary amount of glycerine is also added to distilled water and mixed using a magnetic stirrer. After 24 hours, the result is two clear, transparent, and colourless solutions. The PAA and glycerine solutions are then combined in a unique container, and the resultant polymer solution is thus left to mix gently in a magnetic stirrer (24 hours).

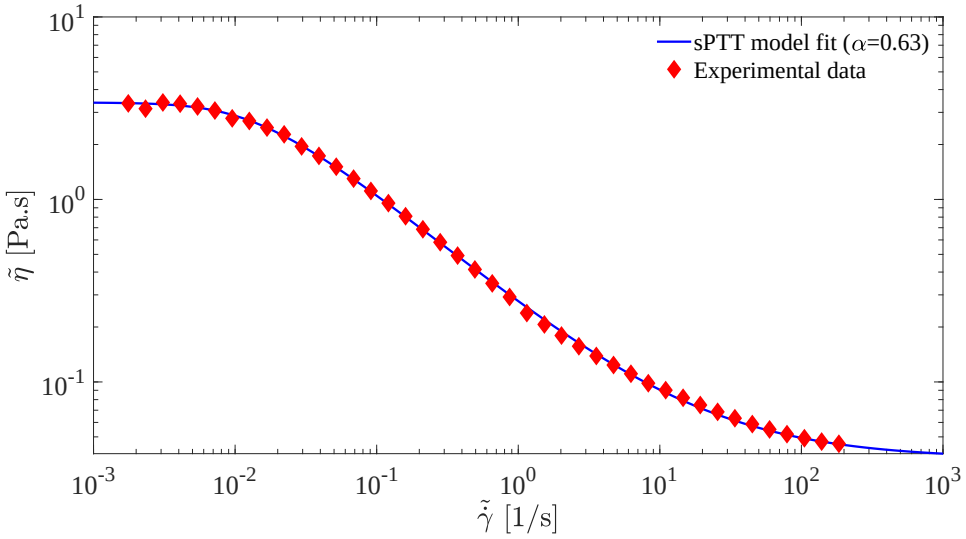

Figure 4.5: Analytical fit based on the sPTT model ($\alpha = 0.63, \tilde{\eta_0} = 3360[mPa.s], \tilde{\eta_\infty} = 35.5[mPa.s]$) and the experimental shear viscosity data of 190 ppm polyacrylamide (PAA) in 70:30 glycerine/water solution versus the shear rate at $\tilde{T} = 20[°\text{C}]$.

All rheology measurements were conducted at $\tilde{T} = 20 \pm 0.1[°\text{C}]$. The working fluid characterisation includes measuring viscosity, density, and relaxation time. Figure 4.5 displays the experimental data for viscosity of the viscoelastic fluid as a function of applied shear rate and an analytical fit based on a single mode sPTT model with $\alpha = 0.63, \tilde{\eta}_0 = 3.36[Pa.s]$ and $\tilde{\eta}_\infty = 35.5[mPa.s]$. The relaxation time of the fluid were measured using small amplitude oscillatory shear. Analysing the storage modulus ($\tilde{G'}$) and the loss modulus ($\tilde{G''}$) using a Maxwell model is a common approach to estimate the relaxation time of viscoelastic fluids (Bird et al., 1987). Here, a four mode generalized Maxwell model is used to estimate the average relaxation time. The response of the generalized Maxwell model for the oscillatory test is as follows:

$$\tilde{G'} = \sum_{i=1}^{4} \frac{\tilde{\eta}_i \tilde{\lambda}_i \tilde{\omega}^2}{1 + \tilde{\lambda}_i^2 \tilde{\omega}^2}, \tag{4.1}$$

$$\tilde{G''} = \sum_{i=1}^{4} \frac{\tilde{\eta}_i \tilde{\omega}}{1 + \tilde{\lambda}_i^2 \tilde{\omega}^2}, \tag{4.2}$$

where the unknown $\tilde{\lambda}_i$ and $\tilde{\eta}_i$ values of the model are determined by minimizing the deviation between the model and experimental data of the frequency sweep test subject to the constraints that the total viscosity is equal to $3.36[Pa.s]$ and the solvent mode has $35.5[mPa.s]$. Finally, the average relaxation time of our working fluid may be estimated as

$$\bar{\tilde{\lambda}} = \sum_{i=1}^{4} \frac{\tilde{\eta}_i \tilde{\lambda}_i}{\tilde{\eta}_i}. \tag{4.3}$$

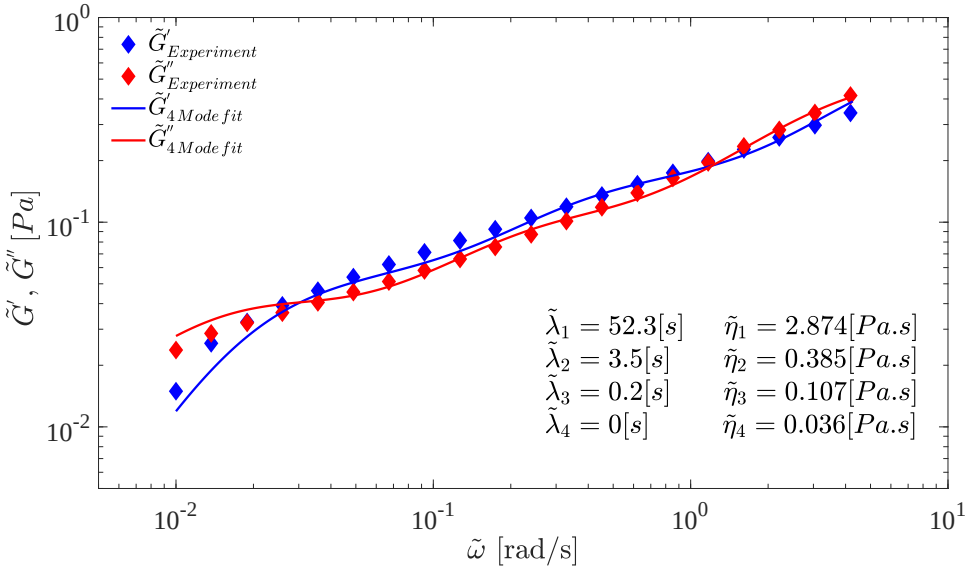

Figure 4.6: Variation of the storage and loss modulus versus the frequency for the solution of 190 ppm polyacrylamide (PAA) in 70:30 glycerine/water at $\tilde{T} = 20[°C]$.

Here, the Anton Paar MCR302 is used to measure the rheological properties of the working fluid. Both the amplitude and frequency sweep tests are carried out at $T = 20[°C]$, using a 60[mm] and 1° cone. Figure 4.6 shows the results of the frequency sweep test in the range of 0.01 to 4 Hz at 10% strain amplitude. Our experimental results suggest an average relaxation time of $\tilde{\bar{\lambda}} = 45.05[s]$.

4.4.3 Experimental protocol

Experiments are conducted over a range of $0.1 < \bar{Wi} < 200$ by programming the syringe pumps to perform ramps in $\bar{Wi}$ with small step increases in mass flow rate ($0.001 < \dot{m}/\tilde{\rho} < 0.2[nl/s]$). Here, $\bar{Wi}$ is defined based on the average relaxation time of the fluid obtained from equation 4.3. The camera is synchronised with the laser at a repetition rate of 8.875[Hz]. All images shown in this work were captured from the top view using an 8× microscope objective (Leica Microsystems GmbH), and the camera FOV (field of view), 4 [mm] × 4 [mm] which thoroughly covers the central region of the device containing the field of interest. The flow visualisation technique applied here consists of pumping dyed fluid (Rhodamine-B) from one of the inlets while undyed fluid is pumped in the other inlet; both inlets are kept at the same flow rate using the same syringe pump but two identical syringes. Fluid motion starts from rest and at least fifty images were captured through the upper glass cover of the cross-slot cell. To assure the flow distribution has reached its steady-state situation, after changing the flow rate approximately a 30-40 minute wait at each step is applied.

4.5 Results and Discussion

In this section, results related to the influence of the geometric modification on the flowfield and on the associated steady symmetry-breaking instability in the cross-slot geometry are presented. In this chapter a series of 2D numerical simulations, experimental results and a supporting approximate analytical solution are used to determine the M parameter (equation 1.2) to show that this instability cannot be solely related to the extensional flow near the stagnation point and is more likely related to streamline curvature and the high deformation rates near the re-entrant corners.

In the standard cross-slot geometry, fluid particles experience a complex deformation due to the existence of shear-dominated and elongational-dominated flows near the corners and stagnation point, respectively. A suitable parameter that can be used to visualise different types of flow is the flow-type parameter ζ (Lee et al., 2007):

$$\zeta = \frac{||\tilde{\boldsymbol{D}}|| - ||\tilde{\boldsymbol{\Omega}}||}{||\tilde{\boldsymbol{D}}|| + ||\tilde{\boldsymbol{\Omega}}||}, \tag{4.4}$$

where, $||\tilde{\boldsymbol{D}}|| = (\frac{\tilde{\boldsymbol{D}}:\tilde{\boldsymbol{D}}}{2})^{1/2}$ and $||\tilde{\boldsymbol{\Omega}}|| = (\frac{\tilde{\boldsymbol{\Omega}}:\tilde{\boldsymbol{\Omega}}}{2})^{1/2}$ are magnitudes of deformation (i.e. $\tilde{\boldsymbol{D}} = \frac{(\nabla\tilde{\boldsymbol{U}}+\nabla\tilde{\boldsymbol{U}}^T)}{2}$) and vorticity tensors (i.e. $\tilde{\boldsymbol{\Omega}} = \frac{(\nabla\tilde{\boldsymbol{U}}-\nabla\tilde{\boldsymbol{U}}^T)}{2}$), respectively. The ζ parameter may vary within the range $[-1, 1]$ in which $\zeta = -1$ characterizes a solid-like rotational deformation, $\zeta = 1$ a pure extensional and $\zeta = 0$ a simple shear flow. Results shown in the left column of Figure 4.7 highlight the effect of elastic stress on the streamline distribution superimposed on the flow-type parameter for small values of Wi number before the onset of the symmetry-breaking purely-elastic instability. As shown, following Figure 4.1, the inlets are located on the left and right sides while the outlets are on the top and bottom. Due to the existence of these opposite inlets and outlets, a point with zero velocity appears at the centre of the geometry (a stagnation point) resulting in a planar elongational flowfield in this area. As shown in Figure 4.7, in the creeping flow of Newtonian fluids, this extensional-dominated flow appears in the shape of four strands stretched along the centrelines of the inlet/outlet arms. These strands are located at the mid-distance between the two walls where, due to symmetry, the shear rate is zero (see Figure 4.8), and due to a non-zero value of the streamwise gradient of velocity, a purely-elongational flow is observed. This issue can also be illustrated by plotting the xy component of the vorticity tensor (Ω_{xy}) as shown in the right hand column of Figure 4.7.

By increasing the Weissenberg number up to a limit (here, $Wi = 0.17$ for $\beta = \frac{1}{9}$ and $\alpha = 0.02$), the velocity distribution in the fully developed channel exhibits a flatter distribution in comparison to the Newtonian flowfield, due to shear-thinning, and consequently the elongational dominated flow expands to a wider region. As shown in Figure 4.8, by increasing the value of Weissenberg number beyond this limit, three shear-free locations appear in the velocity profile, leading to three strands of elongational-

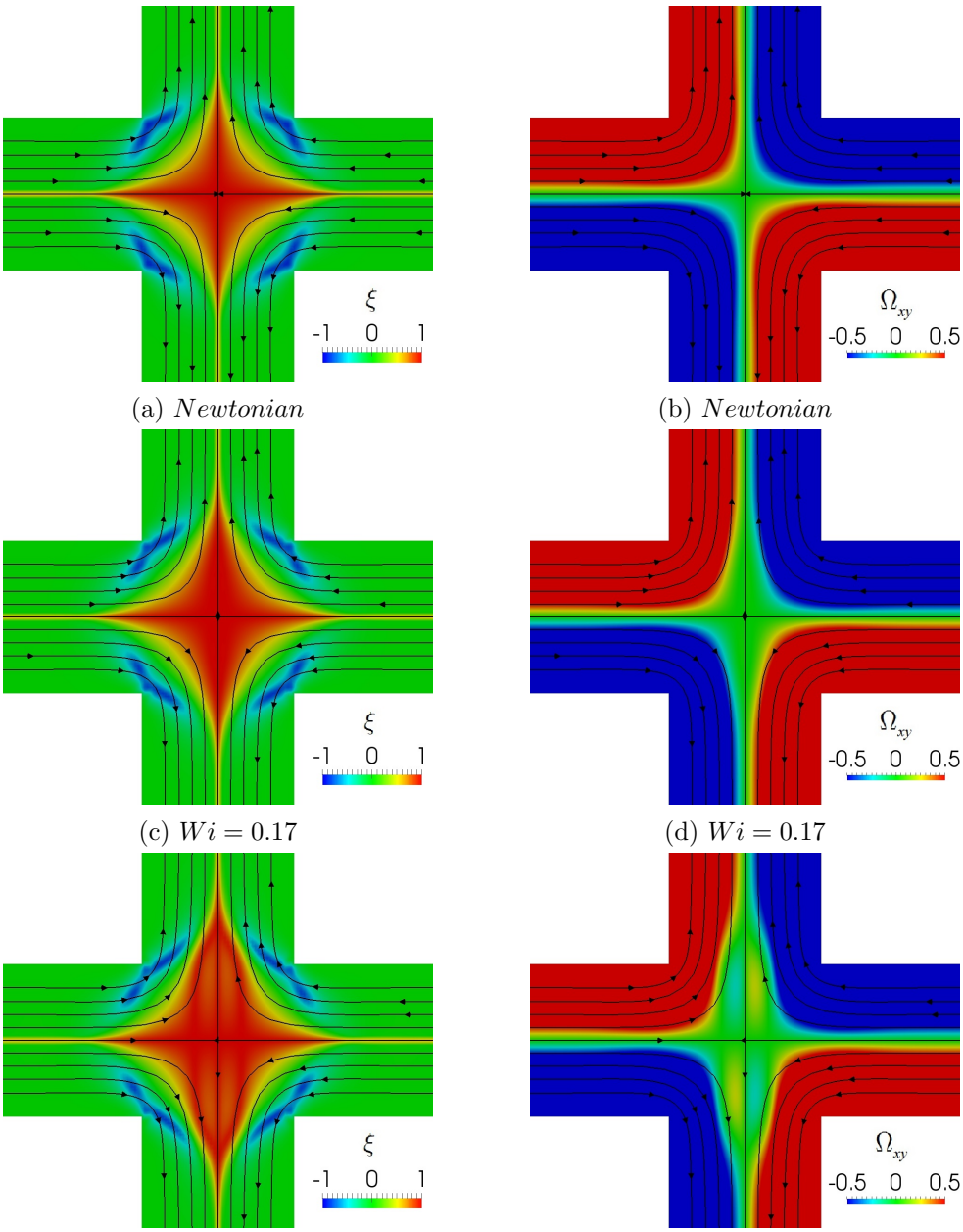

(a) *Newtonian* (b) *Newtonian*

(c) $Wi = 0.17$ (d) $Wi = 0.17$

(e) $Wi = 0.3$ (f) $Wi = 0.3$

Figure 4.7: Distribution of the flow-type parameter and the xy component of the vorticity tensor (Ω_{xy}) for Newtonian and viscoelastic fluids with $\alpha = 0.02$, $\beta = 1/9$, in a standard-shape cross-slot geometry ($\Phi = 0\%$). Streamlines are superimposed in all cases.

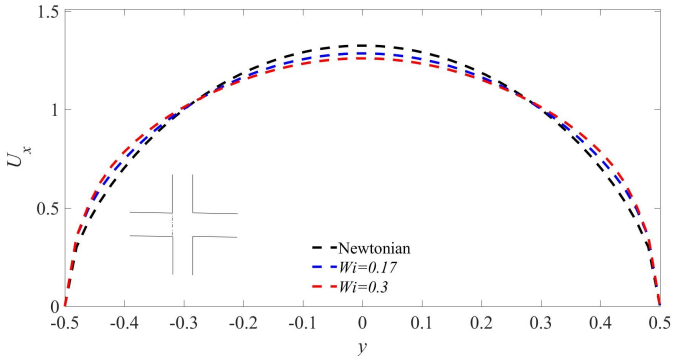

(a)

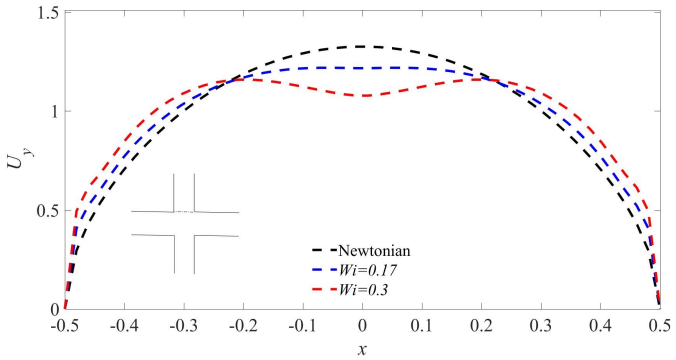

(b)

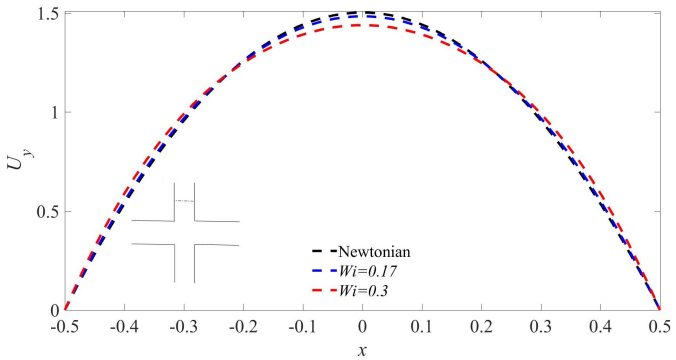

(c)

Figure 4.8: Comparison of non-dimensional velocity distribution along (a) the vertical line at $x = -0.5$, (b) the horizontal line at $y = 0.5$, (c) the horizontal line at $y = 1$ between Newtonian and viscoelastic fluids with $\alpha = 0.02$, $\beta = 1/9$, in a standard-shaped cross-slot geometry ($\Phi = 0\%$).

dominated fields at the outlet arms (along the line $y = \pm 0.5$). As the flow redevelops we expect the flow further downstream to eventually exhibit its approximately parabolic fully-developed distribution (i.e. with only one shear-free point), so these strands join together as we move further downstream through the outlet arms. The results in Figures 4.7 and 4.8 show that the effect of elasticity on the flowfield, even prior to any purely-elastic instability, is significant and changes the flow type downstream of the stagnation point in quite a fundamental way.

Previous studies (Arratia et al., 2006; Gardner et al., 1982) conducted in the standard cross-slot geometry have shown that beyond a critical value of the Wi number, elasticity can break symmetry even in the creeping-flow regime. This change of flow distribution can be related to the existence of multiple solutions to the hydrodynamic problem due to the non-linear nature of the elastic force in viscoelastic fluids. In other words, due to the existence of the non-linear upper-convective derivative operator (equation 2.4) in the governing equations, the problem may exhibit more than one solution leading to bifurcation of solutions after a critical value of Weissenberg number. The modifying effects of adding a cylinder to the flowfield and the associated symmetry-breaking instability is presented in Figure 4.9 (for a nominal case of $\Phi = 50\%$). The results suggest that once the cylinder is added, although the flow distribution in the geometric central region changes significantly, i.e. the shear-free elongational dominated regime with a single stagnation point is replaced with a shear flow around the cylinder wall containing four stagnation points stretched towards the inlet/outlet arms, the steady symmetry-breaking nature of the instability essentially does not change.

By increasing the blockage ratio, the average velocity passing through the central region of the cross-slot geometry (i.e. through $\tilde{L}$ in Figure 4.1) increases which will consequently increase the local shear rate and hence the first normal-stress difference in this region (see Figure 4.10). On the other hand, by changing the size of the cylinder, the local values of streamline curvature are also changed. These two issues suggest that the proposed geometry modification may be used as an effective approach to control the kinematic properties of the flowfield that are known to play an important role in the onset of the instability (see equation 1.2) if the instability is of the "curved streamlines" type. Figure 4.10 illustrates the transition from steady symmetry-breaking instability at the standard cross-slot geometry by performing increasing blockage ratio simulations at a constant value of $Wi = 0.7$ with $\alpha = 0.02, \beta = 1/9$, suggesting a stabilizing effect of the blockage ratio as symmetry is progressively returned to the flow as Φ increases.

In order to better characterize the magnitude of the observed instability in the numerical simulations, we define an asymmetry parameter as the ratio of the x-component of velocity to the mean value of velocity in the inlet arms , i.e. $AP = \frac{\tilde{U}_x}{\tilde{U}_B}$, at the $x = 0, y = 0.5$ location. Using this definition, if the flow retains its symmetric distri-

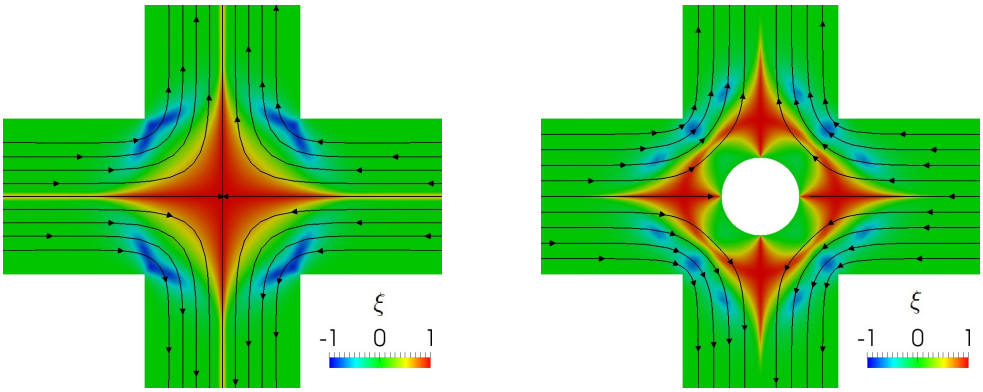

(a) Newtonian, $\Phi = 0\%$ (b) Newtonian, $\Phi = 50\%$

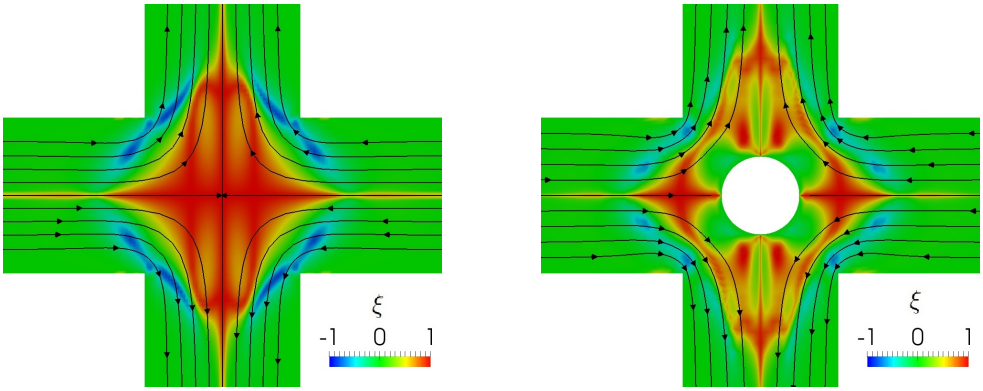

(c) $Wi = 0.51, \Phi = 0\%$ (d) $Wi = 0.65, \Phi = 50\%$

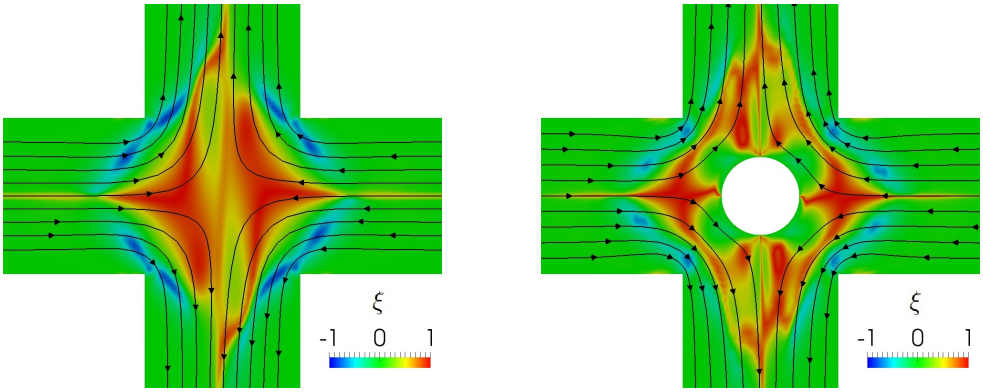

(e) $Wi = 0.515, \Phi = 0\%$ (f) $Wi = 0.66, \Phi = 50\%$

Figure 4.9: Distribution of the flow-type parameter for Newtonian and viscoelastic fluids with $\alpha = 0.02$, $\beta = 1/9$.

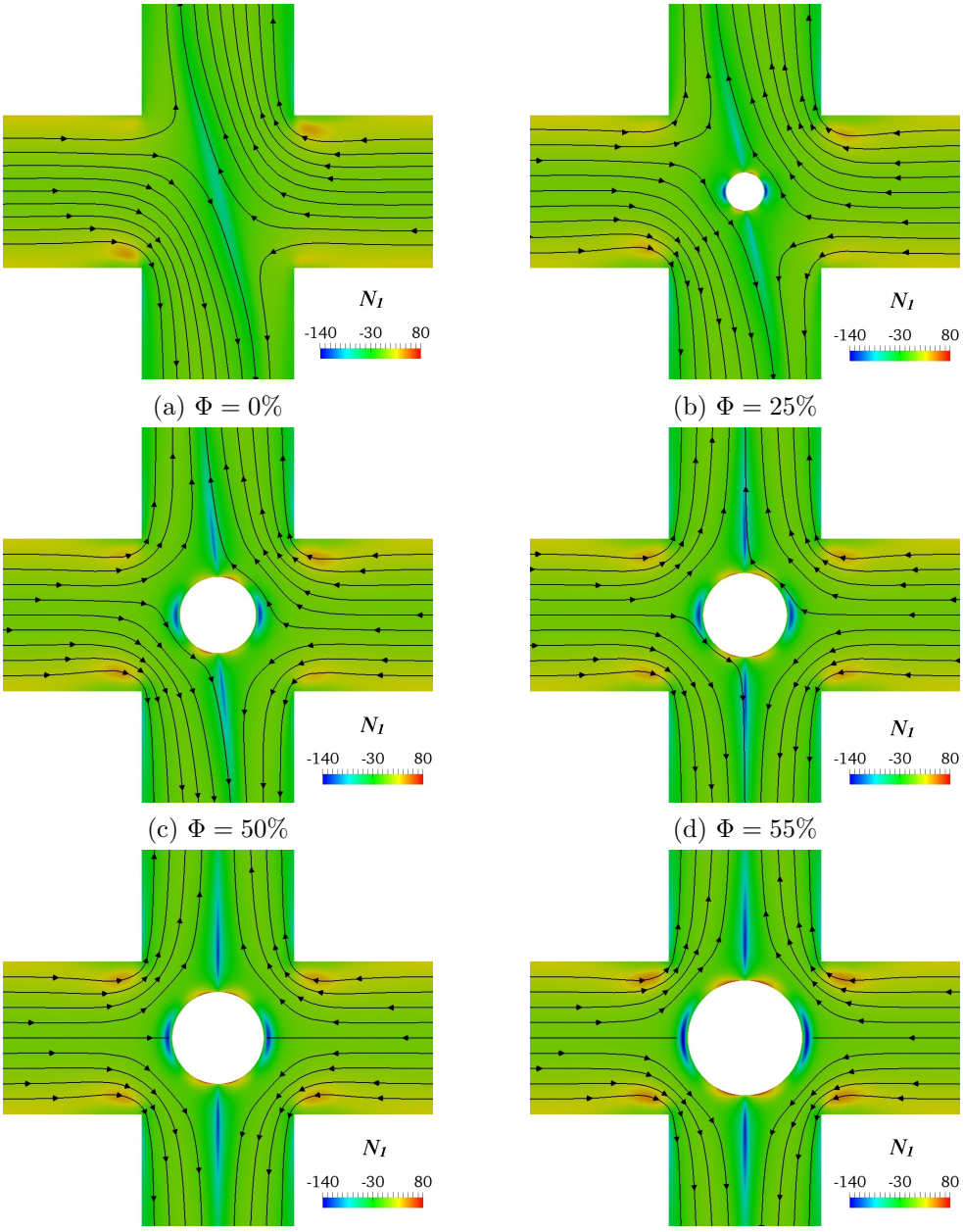

(a) $\Phi = 0\%$ (b) $\Phi = 25\%$

(c) $\Phi = 50\%$ (d) $\Phi = 55\%$

(e) $\Phi = 60\%$ (f) $\Phi = 75\%$

Figure 4.10: Effect of the geometry modification on streamlines superimposed onto contour plots of non-dimensional first normal-stress difference for $Wi = 0.7, \alpha = 0.02$, $\beta = 1/9$. Beyond $\Phi = 60\%$ symmetry is returned to the flow.

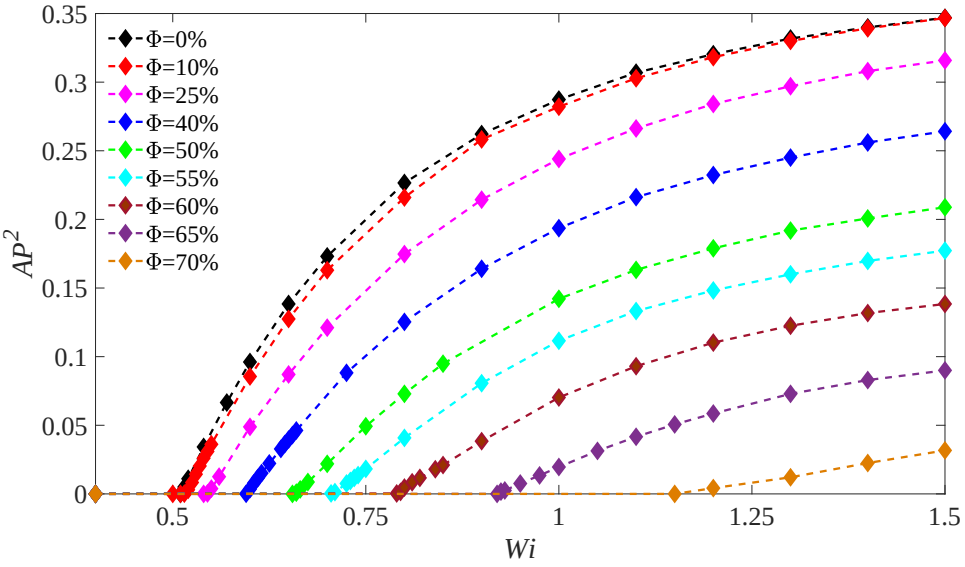

Figure 4.11: Effect of Weissenberg number on the symmetry-breaking instability for $\alpha = 0.02$, $\beta = 1/9$ and different blockage ratios Φ.

bution, the x component of velocity at this location will be equal to zero, while once instability is triggered, due to the asymmetric distribution of the resulting flow, $\tilde{U}_x$ exhibits a non-zero value.

Previous studies (Poole et al., 2007a,c) showed that by increasing the Weissenberg number, the symmetry-breaking exhibits a supercritical growth close to the bifurcation point. In Figure 4.11, the variation of the asymmetry parameter is plotted versus the Weissenberg number for different values of blockage ratios, which all exhibit a similar supercritical characteristic behaviour for the instability as was observed previously in the standard cross-slot (Poole et al., 2007b). In Figure 4.12, we show the effect of the blockage ratio for different constant values of the Weissenberg number with $\beta = 1/9, \alpha = 0.02$. These results reveal a stabilizing effect of the addition of the cylinder at the geometrical centre of the cross-slot problem characterizing a supercritical behaviour close to the bifurcation point (i.e. $AP^2 = a(1-\Phi)+b$ where values of a and b are shown in Figure 4.12).

A previous experimental study in the standard cross-slot geometry conducted by Sousa et al. (2018) has also shown that by increasing the Weissenberg number to higher values, one can potentially trigger a second time-dependent instability. Numerical simulations of shear-thinning sPTT fluids conducted by Cruz et al. (2016) has shown that critical values of Weissenberg number for the onset on instability for both the steady symmetry-breaking and the time-dependent instabilities are a function of the cross-section aspect ratio ($AR = \frac{height}{width}$) and the shear-thinning properties of the fluid (i.e. the α parameter in the sPTT model). Cruz et al. (2016) show that once the aspect ratio

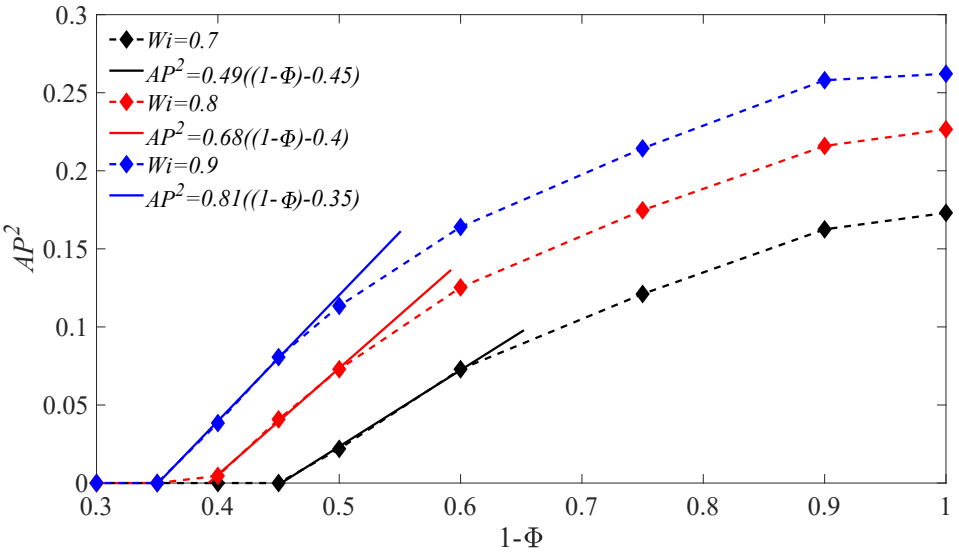

Figure 4.12: Effect of blockage ratio parameter on the symmetry-breaking instability for $\alpha = 0.02$, $\beta = 1/9$.

is sufficiently small, depending on the value of α parameter, the flow distribution can potentially switch from the steady symmetry state to the time-dependent instability directly.

In order to test the hypothesis that a cylinder can delay the steady symmetry-breaking, the analysis from 2D numerical simulations is extended to a series of experiments using the flow visualization approach introduced in section 4.4. For this purpose, two cross-slot geometries are used with the cross section aspect ratio of two, $AR = 2$, one standard cross-slot geometry and one cross-slot geometry with a cylinder at the geometrical centre with $\Phi = 55\%$. This geometry is selected to best approximate a 2D channel and observe the steady asymmetry based on the results of Cruz et al. (2016).

Here, a florescence dyed fluid is injected from the right inlet while undyed fluid is pumped in from the left inlet; both at the same flow rate, to visualise the flow distribution in the studied geometries. By increasing the flow rate, the Weissenberg number can be changed from 0.1 up to 200. These results suggest that beyond a critical value of the Weissenberg number, $\bar{W}i_{cr} \approx 0.46$, the symmetry of flow is broken in agreement with previous studies (Arratia et al., 2006; Sousa et al., 2018). In the standard cross-slot geometry, Figure 4.13 shows the flow distribution in symmetric Newtonian flows and a steady asymmetry flow for 190 ppm polyacrylamide (PAA) in 70:30 glycerine/water viscoelastic fluids at $\bar{W}i = 0.8$ and $Re = 6e-6$. To better investigate the symmetry-breaking instability we define an experimental asymmetry parameter as $AP_e = \frac{(\tilde{H}11-\tilde{H}12)+(\tilde{H}22-\tilde{H}21)}{2\tilde{W}}$. A schematic definition of $\tilde{H}11, \tilde{H}12, \tilde{H}21$ and $\tilde{H}22$ are illustrated in figure 4.13 (a).

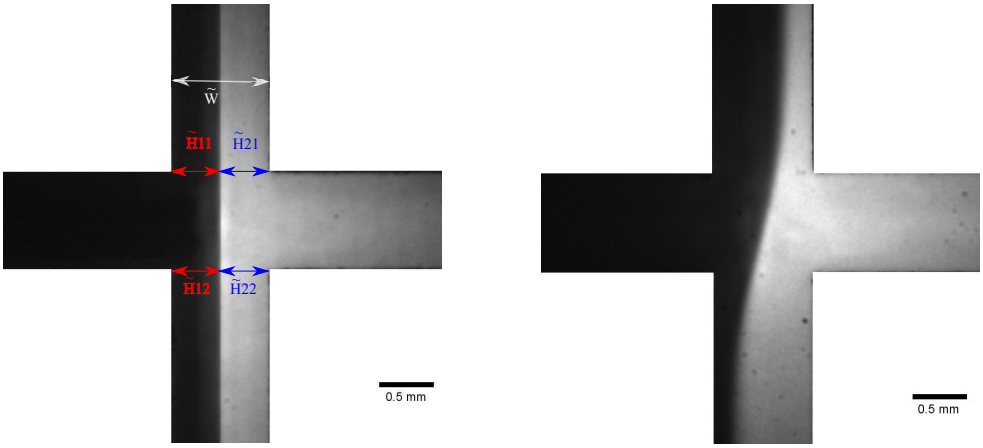

(a) steady symmetry ($\bar{W}i = 0$) (b) steady asymmetry ($\bar{W}i = 0.8$)

Figure 4.13: Visualisation of the flow pattern and schematic representative of characteristic lengths used in definition of asymmetry parameter in our experiment for the standard cross-slot geometry ($\Phi = 0\%$) at $Re = 6e-6$ for solutions of (a) 70:30 glycerine/water Newtonian fluid and (b) 190 ppm polyacrylamide (PAA) in 70:30 glycerine/water viscoelastic fluids at $\bar{W}i = 0.8$. Fluid with the fluorescence dye injected from right inlet arm whereas the fluid without dye is injected from left.

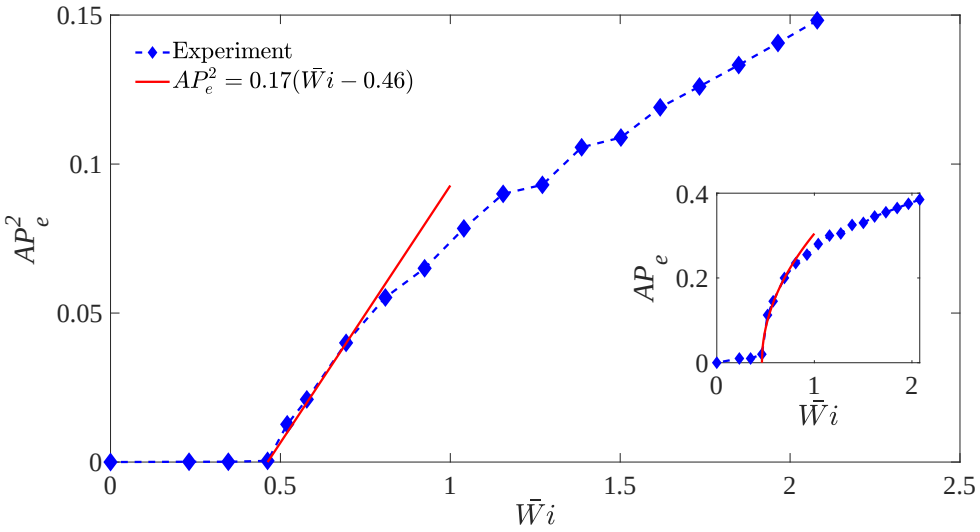

Figure 4.14: Variation of the asymmetry parameter against the Weissenberg number for 190 ppm polyacrylamide (PAA) in 70:30 glycerine/water viscoelastic fluids in standard cross-slot geometry.

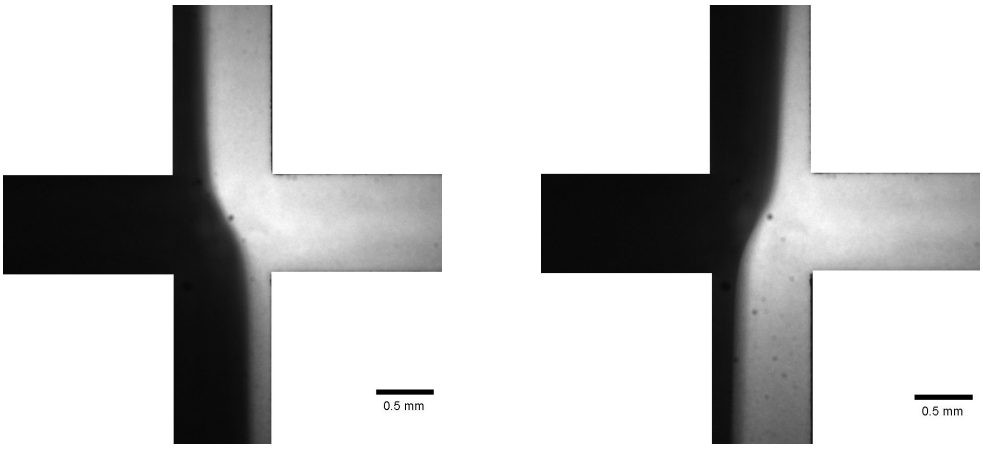

(a) instant 1 (b) instant 2

Figure 4.15: Flow visualisation at different instants of the oscillation cycle at the centre of the standard cross-slot geometry at $\bar{W}i = 277$. Fluid with the fluorescence dye injected from right inlet arm where as the fluid without dye is injected from left.

In Figure 4.14, we show that the symmetry-breaking instability in the standard cross-slot geometry, near the bifurcation point follows a supercritical growth, as was also observed in our 2D numerical simulations. As the Weissenberg number is increased to higher values, a time dependent symmetry-breaking instability develops at $\bar{W}i \approx 92$ which oscillates between two states (see Figure 4.15). Unfortunately the experimental protocol was insufficient to characterise this time dependency more quantitatively.

Following the benchmark of the experimental protocol, the standard cross-slot geometry was replaced with a modified geometry with $\Phi = 55\%$. In Figure 4.16, the symmetric distribution of flowfield for both the Newtonian fluid and 190 ppm polyacrylamide (PAA) in 70:30 glycerine/water viscoelastic fluids at $\bar{W}i = 2.3$ and $Re = 2e-5$ are presented. Here, unlike the standard cross-slot geometry that the purely-elastic symmetry-breaking instability was triggered at $\bar{W}i_{cr} = 0.46$, we were able to retain a symmetric flowfield up to $\bar{W}i_{cr} \approx 3.5$, qualitatively supporting the 2D numerical simulations regarding the stabilizing effect of the addition of a cylinder.

In the experiments, unlike the prediction from 2D numerical simulations, it can be noticed that by increasing the Weissenberg number to higher values, the flowfield switches to an unsteady oscillatory instability (Figure 4.17) directly with no evidence of a steady symmetry-breaking instability. This issue may potentially be related to the effect of finite cross-section aspect ratio in the experiments which was neglected in our 2D simulations. Having shown experimentally that the cylinder does indeed stabilise the flowfield significantly, numerical simulations are now used to probe additional effects and to see how the blockage ratio delays onset can be quantified.

Figure 4.18, shows the "stability diagram" for the modified geometry. Here, above the black dashed-line (the data are shown by red filled diamonds) are the regions in

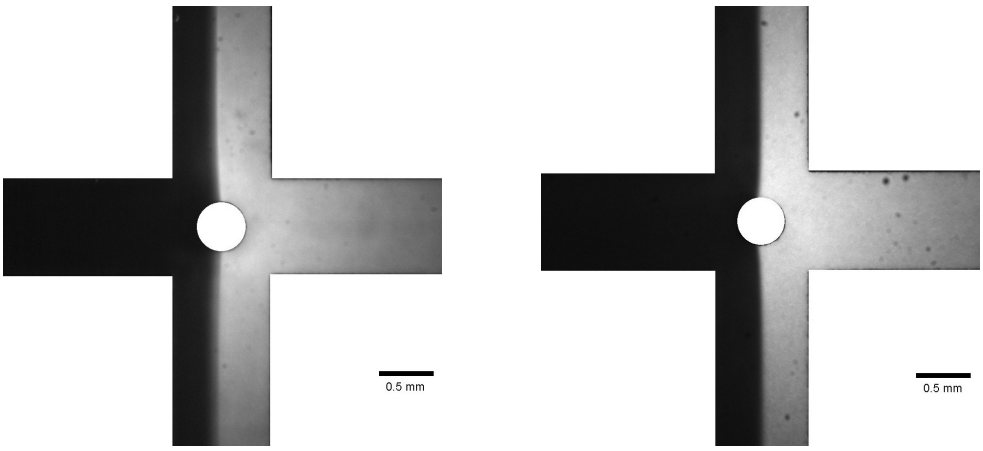

(a) steady symmetry ($Wi = 0$) (b) steady symmetry ($Wi = 2.3$)

Figure 4.16: Visualisation of the flow pattern in cross-slot geometry with $\Phi = 55\%$ at $Re = 2e-5$ for solutions of (a) 70:30 glycerine/water Newtonian fluid and (b) 190 ppm polyacrylamide (PAA) in 70:30 glycerine/water viscoelastic fluids at $\bar{Wi} = 2.3$. Fluid with the fluorescence dye injected from right inlet arm where as the fluid without dye is injected from left.

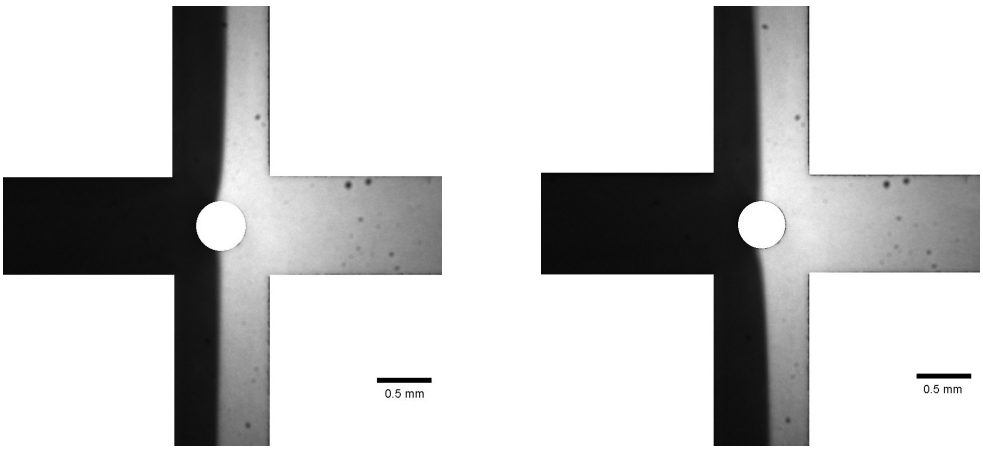

(a) instant 1 (b) instant 2

Figure 4.17: Flow visualisation at different instants of the oscillation cycle at the centre of the cross-slot geometry with $\Phi = 55\%$ and $\bar{Wi} = 18.5$. Fluid with the fluorescence dye injected from right inlet arm where as the fluid without dye is injected from left.

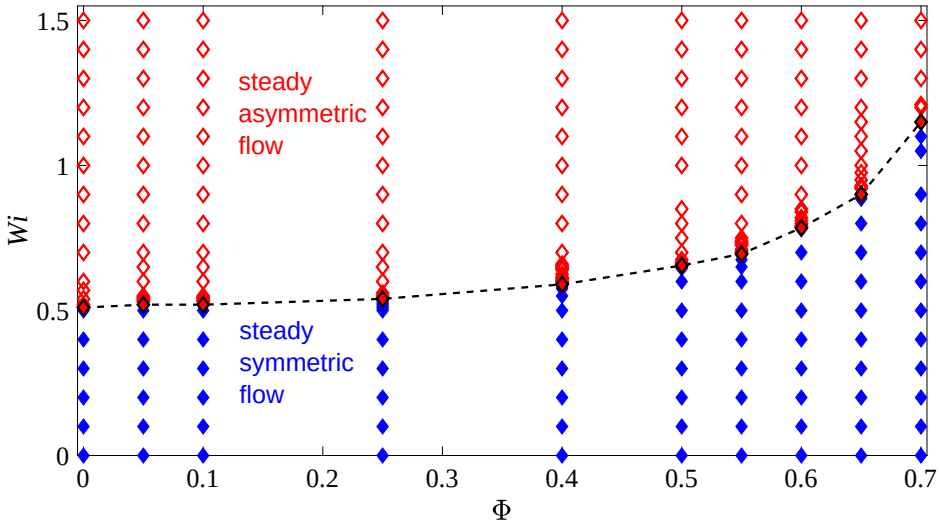

Figure 4.18: Boundary between the symmetric and asymmetric flow for different Wi numbers and blockage ratio for $\alpha = 0.02$, $\beta = 1/9$.

which the flow exhibits a steady asymmetric distribution. The simulations suggest that as the size of the cylinder approaches to zero, its modifying effects on the critical conditions of triggering the symmetry-breaking instability fades away and the critical value of the Weissenberg number for the onset of the instability approaches to the critical value of Weissenberg number in the standard cross-slot geometry. One should note that a combination of conservation mass (i.e. $\frac{\partial U_r}{\partial r} + \frac{1}{r}\frac{\partial U_\theta}{\partial \theta} = 0$) with the no-slip boundary condition (i.e. velocity at the cylinder wall is equal to zero and due to the no-slip boundary condition $\frac{\partial U_\theta}{\partial \theta}|_{r=\Phi} = 0$) requires the strain rate at the stagnation point at the cylinder to become zero. So, by replacing the free-stagnation point with pinned stagnation points, independent of the cylinder size, a non-zero value of strain rate at the stagnation point is replaced with a zero value once the no-slip boundary condition is applied (as confirmed in Figure 4.19).

By changing the applied boundary condition at the cylinder surface at a constant blockage ratio, the onset sensitivity of the purely-elastic instability with the magnitude of the strain rate at the vicinity of cylinder is analysed. In Figures 4.19 and 4.20, the strain rate distribution along the symmetry lines for both the Newtonian and viscoelastic fluids before the onset of instability is plotted using both slip and no-slip boundary conditions at the cylinder surface. As can be seen, by replacing the no-slip boundary condition with a slip boundary condition, although the zero strain rate value at the stagnation point is replaced by a larger non-zero value (approximately 3.5 times larger than the maximum value of strain rate at the standard cross-slot geometry), the critical value of the Weissenberg number in which the instability is triggered stays almost constant (i.e. $Wi_{cr} \approx 0.51$)

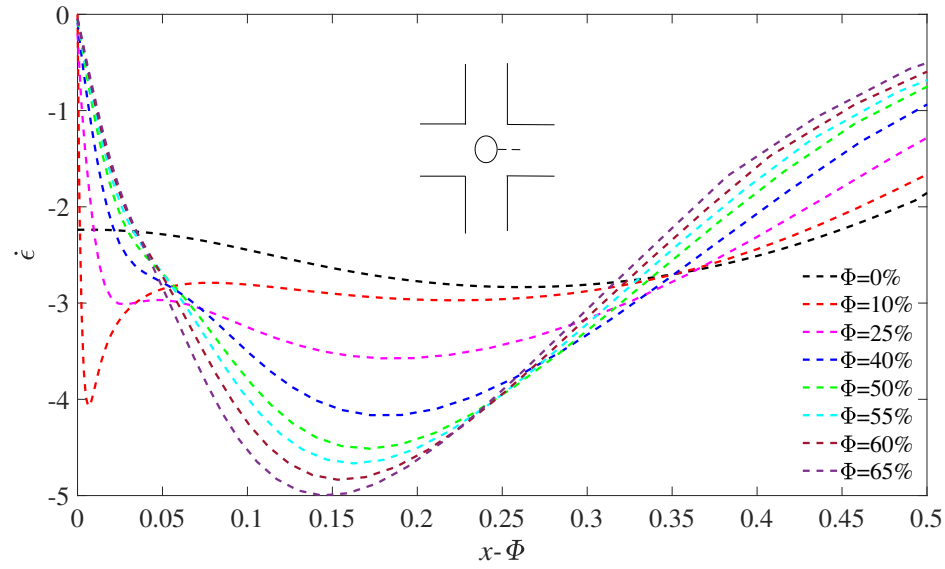

(a)

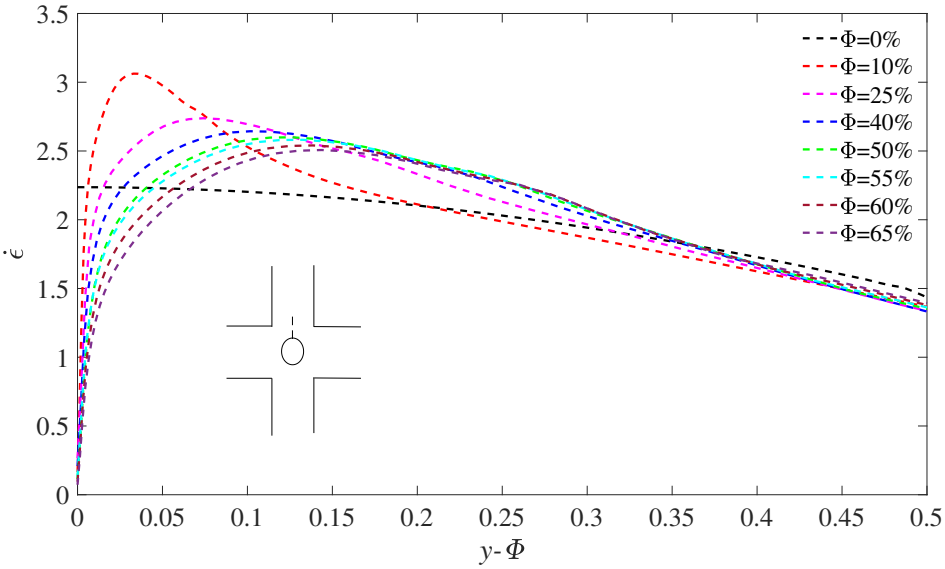

(b)

Figure 4.19: Effect of blockage ratio parameter on the flow strain rate before the start of instability for $\alpha = 0.02$, $\beta = 1/9$ along (a) horizontal lines downstream (b) vertical line upstream. (The critical values of Wi number for $\Phi = 0\%, 25\%, 40\%, 50\%, 55\%, 60\%, 65\%$ are $0.51, 0.54, 0.59, 0.66, 0.7, 0.78, 0.9$, respectively)

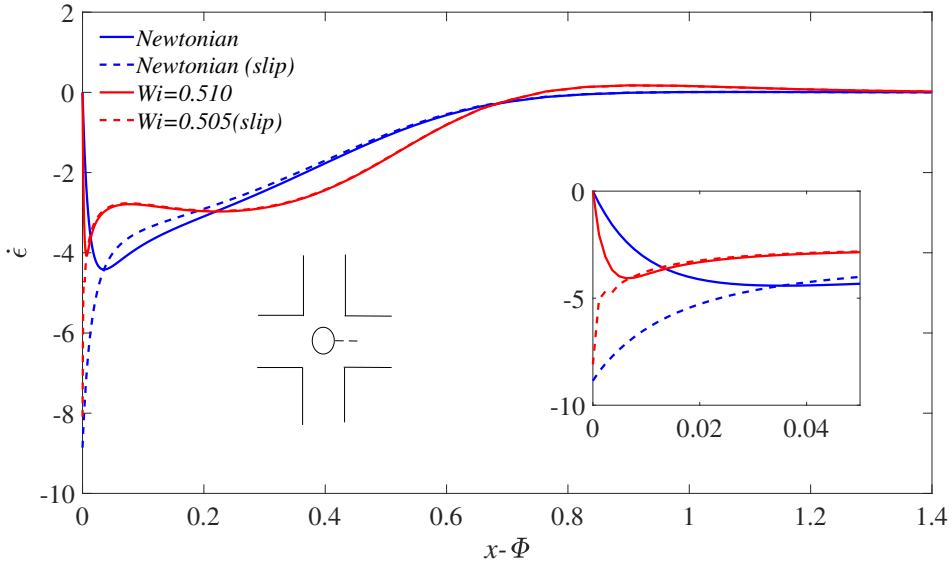

(a)

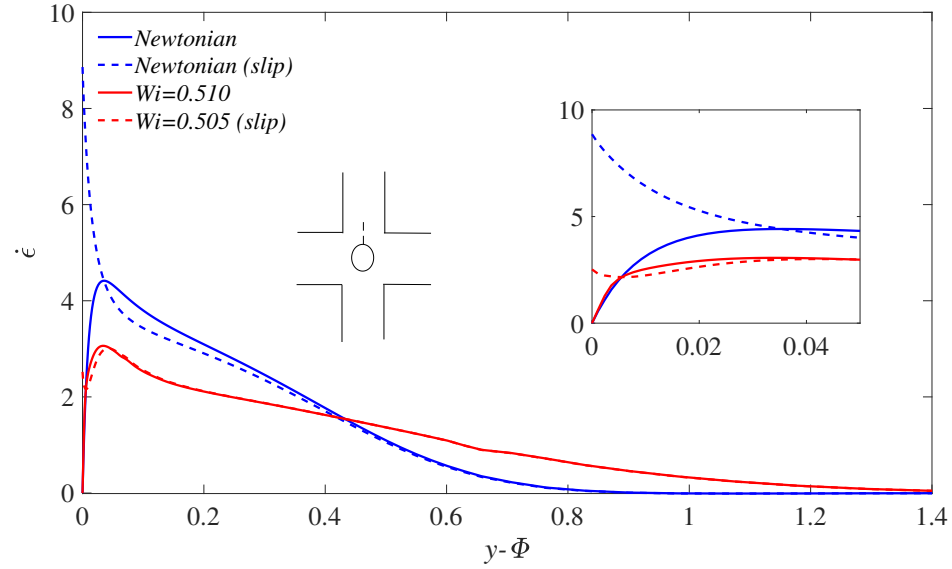

(b)

Figure 4.20: Effect of slip boundary condition at the cylinder on flow strain rate along (a) horizontal lines downstream (b) vertical line upstream for creeping Newtonian flows and viscoelastic fluids before the start of purely-elastic instability for $\alpha = 0.02$, $\beta = 1/9$ and $\Phi = 5\%$

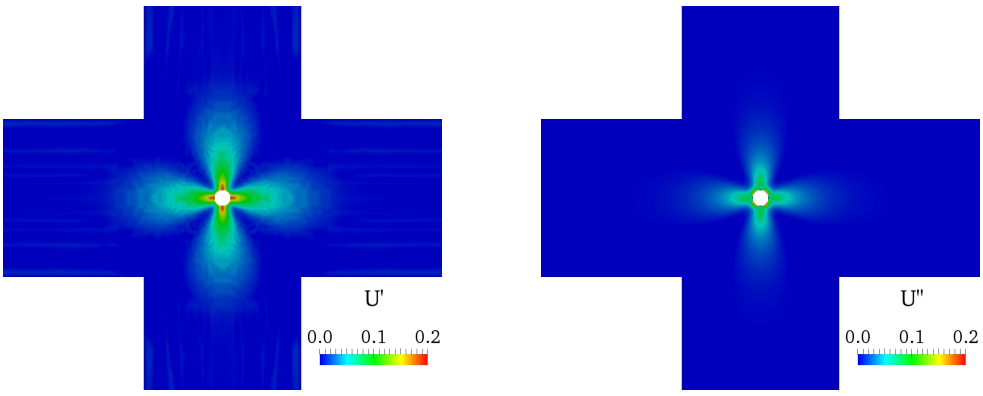

(a) $U' = |U_{0\%B}| - |U_{10\%B}|$ (b) $U'' = |U| - |U_s|$, with $\Phi = 10\%$

Figure 4.21: Effect of (a) geometry modification and (b) slip boundary condition on the velocity field of creeping Newtonian fluid flows.

As is shown in Figure 4.21, the effects of the geometry modification and change of the boundary condition for $\Phi = 10\%$, is essentially local and mainly influences the flow distribution near the central region. The results presented in Figures 4.18-4.21 show that in the limit where the blockage ratio tends to zero ($\Phi \to 0$), even by applying fundamental changes to the kinematic characteristics of flowfield at the vicinity of the stagnation point (changing both the strain rate value and the curvature of streamlines), the critical value of the Weissenberg number in which the instability is triggered tends towards its critical value for the standard cross-slot geometry (i.e. $Wi_{cr} = 0.51$). These data strongly suggest the symmetry-breaking instability in the cross-slot geometry is probably triggered due to the high shear rate and high curvature of streamlines at a location away from the geometric centre and closer to the corner regions and is essentially independent of the kinematic properties of the flow near the stagnation point.

From the results presented it can be concluded that the high shear rate along with the high streamline curvature near the four cross-slot corners is potentially responsible for the transition to an asymmetric flow pattern and therefore the ideas developed by McKinley et al. (1996a) are applied to investigate this possibility. Following the numerical procedure explained by Cruz et al. (2016), the local distribution of the M parameter (equation 1.2) is plotted in Figure 4.22. The local illustration of the M parameter can be an effective way to observe the location of instability-driving regions within the flowfield. As expected from previous results, the maximum value of the M parameter appears near the corners which is related to the high curvature of streamlines here and shear rate in this region (Hinch (1993)).

One of the interesting properties of the M parameter is related to its ability to scale the purely-elastic instabilities with respect to both rhelogiocal and geometrical prop-

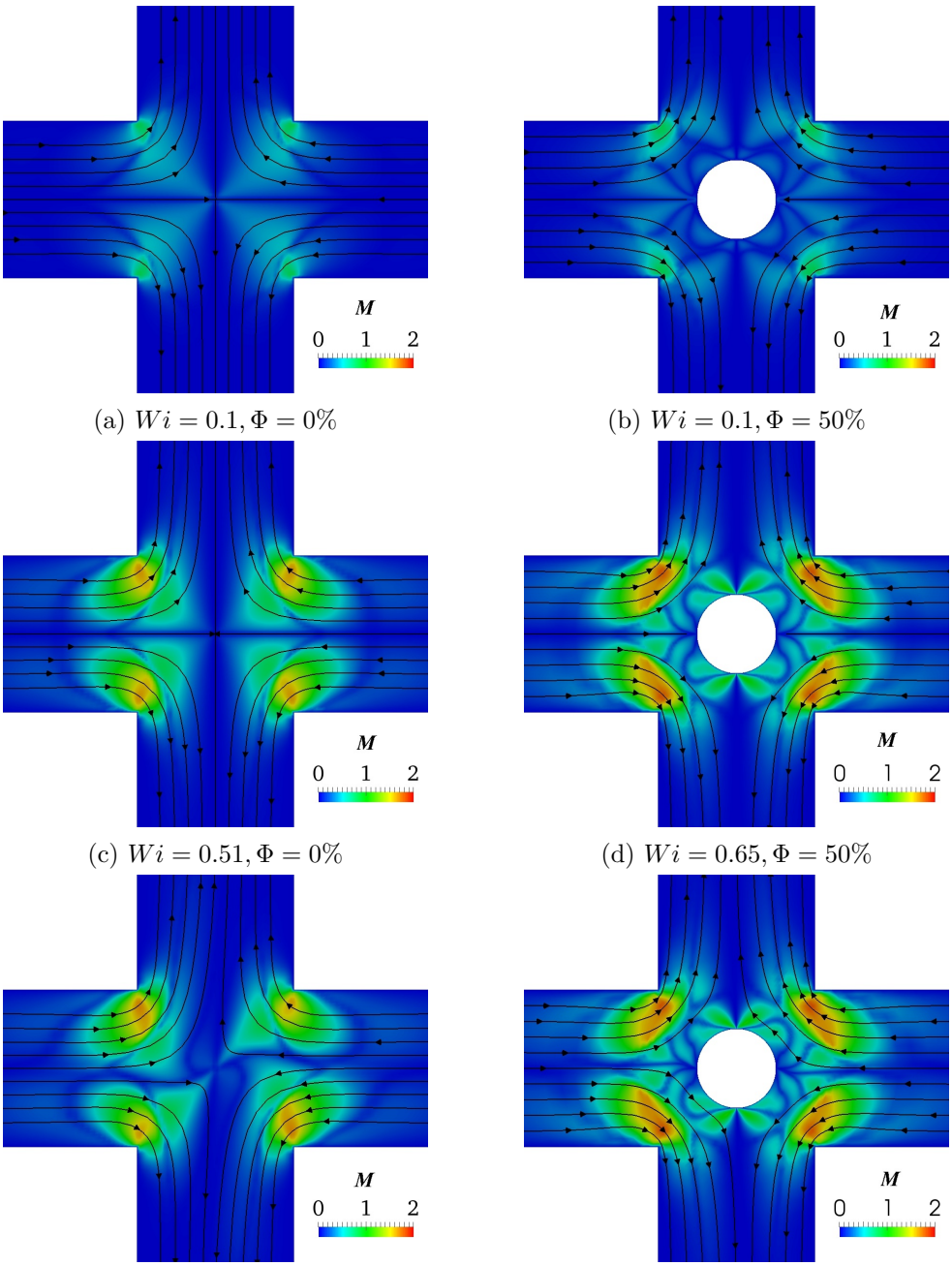

(a) $Wi = 0.1, \Phi = 0\%$ (b) $Wi = 0.1, \Phi = 50\%$

(c) $Wi = 0.51, \Phi = 0\%$ (d) $Wi = 0.65, \Phi = 50\%$

(e) $Wi = 0.52, \Phi = 0\%$ (f) $Wi = 0.66, \Phi = 50\%$

Figure 4.22: Illustrative contours of M parameter for $\alpha = 0.02$, $\beta = 1/9$.

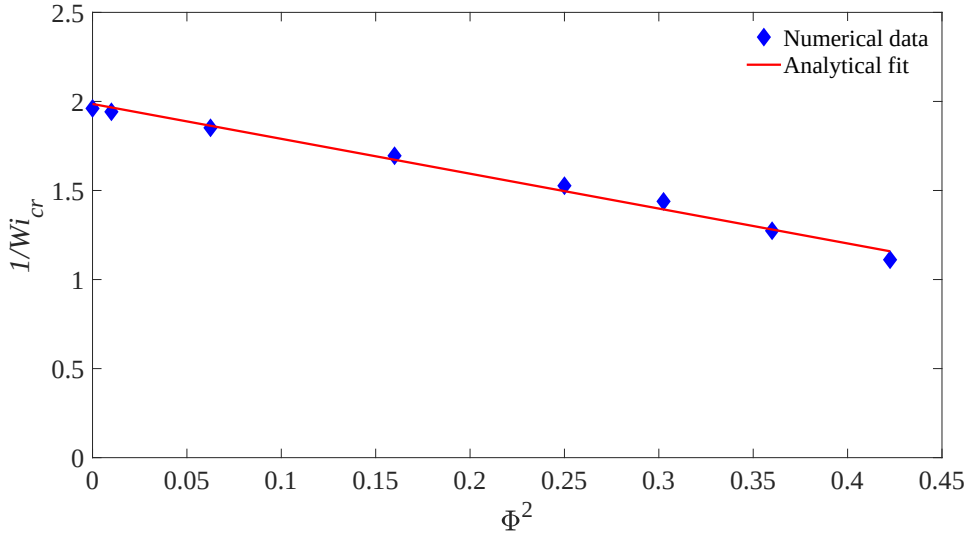

Figure 4.23: Variation of critical values of Weissenberg number against the blockage ratio parameter for $\alpha = 0.02$, $\beta = 1/9$ (Analytical fit $\frac{1}{Wi_{cr}} = -1.9578\Phi^2 + 1.9858$).

erties of the problem (Pakdel and McKinley, 1998; McKinley et al., 1996b; Alves and Poole, 2007; Zilz et al., 2012). Here, the approach suggested by McKinley et al. (1996b) to model the effect of blockage ratio is also applied. An initial analysis suggested that neither $\tilde{D}$ nor $\tilde{W}$ provide a good approximation of the characteristic curvature of the streamlines in the cross-slot cylinder geometry and in fact this characteristic length scale is influenced by both of these parameters. In Appendix C, using an approximate analytical solution for creeping Newtonian flows, it is shown that the streamline curvature should scale as:

$$\frac{1}{\tilde{\Re}} = \frac{1}{\tilde{W}}(a + b\Phi^2), \tag{4.5}$$

where a and b are undetermined constants. The results presented in Figure 4.22, clearly show that the highest value of the M parameter appears in the vicinity of the corner's shear-dominated regions. Assuming a steady-state purely shear flow for an Oldroyd-B fluid (of which the sPTT model approaches in the $\alpha \to 0$ limit), one may scale the normal-stress component in equation 1.2 as:

$$\tilde{\tau}_{ss} = 2\tilde{\lambda}\tilde{\eta}_p\tilde{\dot{\gamma}}. \tag{4.6}$$

Here, using $\tilde{U}_b$ and $\tilde{\Re}$ as references for the velocity field and the length scale, the reference shear rate may be expressed as $\tilde{\dot{\gamma}} = \frac{\tilde{U}_b}{\tilde{\Re}}$. Substitution of these equations into the dimensionless M criteria (equation 1.2), results in the following condition for the

onset criteria of purely-elastic instability in the modified cross-slot geometry:

$$M_c = \sqrt{\frac{\tilde{\lambda}\tilde{U}_b}{\tilde{W}}(a + b\Phi^2)2(1-\beta)\frac{\tilde{\lambda}\tilde{U}_b}{\tilde{W}}(a + b\Phi^2)}, \tag{4.7}$$

where a, b and M_c are now the unknown constants. However, factoring out the quantity $(\frac{\tilde{\lambda}\tilde{U}_b}{\tilde{W}})^2$ and some rearrangement one can simplify the equation into:

$$\frac{1}{Wi_{cr}} = \bar{a} + \bar{b}\Phi^2, \tag{4.8}$$

where, $\bar{a} = \frac{a\sqrt{2(1-\beta)}}{M_c}$ and $\bar{b} = \frac{b\sqrt{2(1-\beta)}}{M_c}$ are unknown constants. Figure 4.23 shows the fit obtained based on equation 4.8 and our 2D numerical simulations. From this prediction (equation 4.8), one can show $\frac{\partial Wi_{cr}}{\partial \Phi} = 0$ once $\Phi \to 0$, suggesting that in the limit $\Phi \to 0$, the modifying effect of the addition of a cylinder on the critical kinematic properties of flowfield and the onset criteria of instability fades away (Figure 4.18 also illustrates this point). Bearing in mind that equation 4.8 is obtained using a pure-shear flow assumption (i.e. equation 4.6) and the scaling of streamline curvature is obtained using a Taylor expansion in the vicinity of corners, the good agreement between the analytical prediction (equation 4.8) and numerical simulations, once again suggests that the instability is triggered due to the high shear flow near the corners and not the elongational dominated flow at the stagnation point itself. Finally, to test the sensitivity of our chosen model parameters, in Appendix D we show how the extensibility parameter in the sPTT modifies the critical conditions and in Appendix E we show that the same results can be observed with the FENE-P model.

4.6 Conclusions

In this chapter a passive control mechanism is introduced to the cross-slot geometry by the addition of a cylinder at the geometric centre of the problem. A series of numerical simulations and an approximate analytical analysis, using the definition of the M parameter introduced by McKinley et al. (1996b) was used, to scale and analyse the stabilizing effect of the proposed geometrical modification on the onset criteria for a purely-elastic instability and compare these results to new experimental data. The results in this chapter suggest that in the limit that $\Phi \to 0$ replacing the finite strain rate "free" stagnation point flow with a zero strain rate "pinned" stagnation points at the cylinder surface does not affect the onset for the purely-elastic instability. The simulations were extended by applying a complete slip boundary condition at the cylinder and changing the maximum strain rate from zero to approximately 3.5 times of the strain rate in the standard cross-slot geometry, to show that the kinematic properties of the flow distribution around the stagnation point do not play any significant role in the onset of the purely-elastic symmetry-breaking instability and that the critical values of the Weissenberg number for which the instability is triggered, in both cases, tend toward its critical value for the standard cross-slot geometry (i.e. $Wi \approx 0.51$). Finally, by plotting the local distribution of the M parameter, it is shown that the location of instability-driving regions appears in the vicinity of the corners which can be attributed to the high deformation rate and high streamline curvature in this region. Finally how the effect of blockage ratio scales with the onset criteria is shown and thus can be successfully used to control onset conditions.

Chapter 5

Stabilisation of purely-elastic instabilities in cross-slot geometries using interfacial tension

In this chapter of the thesis, two-phase viscoelastic fluid flows in the cross-slot geometry are simulated using a volume of fluid method (described in chapter 2). The stress components of the viscoelastic material are simulated using the simplified Phan-Thien and Tanner (sPTT) model with a log-conformation approach. The combined effects of the capillary number (the ratio of the interfacial stress to the viscous stress), the Weissenberg number (the ratio of the elastic stress to viscous stress), extensibility parameter of the sPTT model (α) and the solvent-to-total viscosity ratio (β) of each of the two phases and the ratio of the total viscosities of two fluids (the K parameter) are investigated in a 2D geometry. It is shown that the interfacial tension force plays an important role in the shape of the interface of the two fluids near the free stagnation point. By reducing the interfacial tension force the interface of the two fluids becomes curved and this can consequently change the curvature of streamlines in this region. In this scenario, for fixed values of β, Wi, α and K parameters the interfacial tension is shown to have a stabilising effect on the associated steady symmetry-breaking instability. Using the definition of the Pakdel-McKinley M parameter (equation 1.2), an approximate analytical expression is obtained that shows the critical Weissenberg number Wi_{cr} scales with the capillary number as $\frac{1}{Wi_{cr}} = -\frac{0.0185}{Ca} + 1.938$ in agreement with the numerical data. The K parameter is shown to change the location of the stagnation point and the interface position of the two fluids for a fixed value of Ca number. By increasing the K parameter, the local value of the Weissenberg number near the corners of the geometry is significantly increased and a combination of this kinematic change in the flowfield with a stratification of viscosity (Yih, 1967) and jump of elastic normal stresses across the interface (Wilson and Rallison, 1997) can consequently lead

to a time-dependent instability. Finally, as in single phase flow,the Weissenberg number has a destabilising effect.

5.1 Geometric configuration and problem definition

A schematic of the studied problem is presented in Figure 5.1. As shown inlets are located at the left (fluid-1) and right (fluid-2) side arms while outlets are located at the top and bottom arms. Width of the channels $\tilde{W}$ for all inlets and outlets are the same. Fluids are injected at the inlets with an equal constant bulk velocity $\tilde{U}_B$. A zero gradient boundary condition for the stress and velocity components is applied at the outlets to simulate fully developed conditions. At the walls, values of the stress components are calculated using an extrapolation method as suggested by Pimenta and Alves (2017) and no-slip is assumed for the velocities. For the phase indicator parameter C, constant values of 1 and 0 are used at the left and right inlet arms and a zero gradient at the outlet and walls.

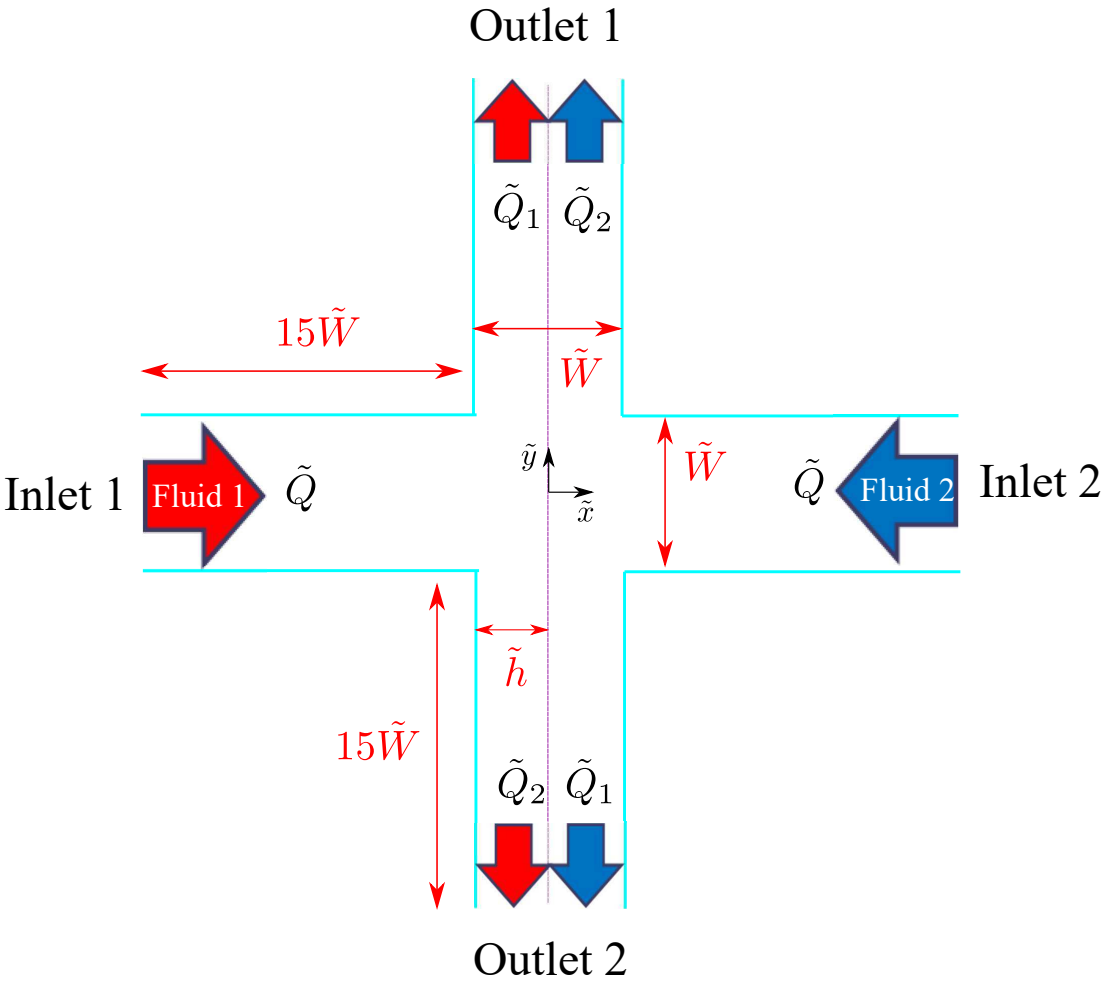

Figure 5.1: Schematic of the cross-slot geometry for two-phase flow problem. Not to scale. $\tilde{h}$ is indicating the passage width of fluid-1 in the outlet arms.

5.2 Non-dimensionalization

To better characterise the flowfield and the important parameters playing a role in this problem, the use of following dimensionless parameters are adopted:

$$x = \frac{\tilde{x}}{\tilde{W}}, y = \frac{\tilde{y}}{\tilde{W}}, \boldsymbol{U} = \frac{\tilde{\boldsymbol{U}}}{\tilde{U}_B}, \boldsymbol{\tau} = \frac{\tilde{\boldsymbol{\tau}}}{\tilde{\eta}_{1,t}\tilde{U}_B/\tilde{W}}, p = \frac{\tilde{p}}{\tilde{\eta}_{1,t}\tilde{U}_B/\tilde{W}}, Re_i = \frac{\tilde{\rho}_i\tilde{U}_B\tilde{W}}{\tilde{\eta}_{i,t}},$$
$$Wi_i = \frac{\tilde{\lambda}_i\tilde{U}_B}{\tilde{W}}, \beta_i = \frac{\tilde{\eta}_{i,s}}{\tilde{\eta}_{i,t}}, Ca = \frac{\tilde{\eta}_{1,t}\tilde{U}_B}{\sigma}, K = \frac{\tilde{\eta}_{2,t}}{\tilde{\eta}_{1,t}}, AP_{tp} = \frac{\tilde{Q}_1 - \tilde{Q}_2}{\tilde{Q}}, St = \frac{\tilde{f}\tilde{U}_B}{\tilde{W}}, \tag{5.1}$$

where i index can be either 1 or 2 (i.e. $i = \{1, 2\}$) indicating properties of fluid-1 and fluid-2 , $\tilde{x}$, $\tilde{y}$ are the variables related to the rectangular coordinate system, $\tilde{W}$ is the width of the channel, $\tilde{\boldsymbol{U}}$ is the velocity vector, $\tilde{U}_B$ is the imposed bulk velocity at the inlet arms, $\tilde{\boldsymbol{\tau}}$ is the total stress tensor, p is the pressure, Re_i is the Reynolds number corresponding to each phase which is set to be 0.01 for all simulations in order to model creeping flow, Wi_i is the Weissenberg number defined for each phases, β_i is the solvent-to-total viscosity ratio of each of two phases and $\tilde{\eta_{i,t}}$ is the total viscosity of each of the phases (i.e. $\tilde{\eta}_{i,t} = \tilde{\eta}_{i,s} + \tilde{\eta}_{i,p}$), Ca is the capillary number defined based on the properties of fluid-1, K is the ratio of total viscosity of fluid-2 to fluid-1, $\tilde{Q}$ is the imposed flow rate at the inlets (i.e. $\tilde{Q} = \tilde{W}\tilde{U}_B$), $\tilde{Q}_1$ and $\tilde{Q}_2$ are defined in Figure 5.1 and AP_{tp} is the asymmetry parameter used in our two-phase flow simulations to quantify the asymmetry of flow magnitude (before onset of any symmetry-breaking instability $\tilde{Q}_1 = \tilde{Q}_2$ so $AP_{tp} = 0$, but once the symmetry of the flow is broken $\tilde{Q}_1 \neq \tilde{Q}_2$ and AP_{tp} exhibits a non-zero value). St is the Strouhal number and $\tilde{f}$ is the frequency of the time dependent instability. A previous study conducted by Wilson and Rallison (1997) has shown that a non-zero value of the normal stress jump at the interface of viscoelastic fluids may trigger an instability in three-layer planar flows. In this thesis, to mainly concentrate on and study the effect of interfacial stress on the symmetry-breaking instability in the cross-slot geometry, the values of $Wi_1 = Wi_2$, $\beta_1 = \beta_2$ and the extensibility parameter of two fluids $\alpha_1 = \alpha_2$ are fixed.

5.3 Results and discussion

In this section results related to the 2D simulation of two-phase flows of both Newtonian and viscoelastic fluids in the cross-slot geometry are presented.

5.3.1 Analytical solution for two-phase flow of fully-developed Newtonian fluids in a channel

Although it is well known that in the limit of no inertia or surface tension channel flows of Newtonian fluids with a viscosity stratification are linearly unstable (Yih, 1967), nev-

ertheless in this section an exact analytical solution for the pressure driven, creeping two-phase flow of Newtonian fluids in between two parallel plates is derived. This solution will then provide a partial benchmark solution for the non-linear simulations in the cross-slot geometry (i.e. in the outlet arms once the flow has gone sufficiently far downstream of the cross-slot that it becomes "fully developed"). To avoid instability the numerical simulations include interfacial tension (Hooper and Boyd, 1983; Barmak et al., 2016). A schematic of the problem and the employed coordinate system is shown in Figure 5.2.

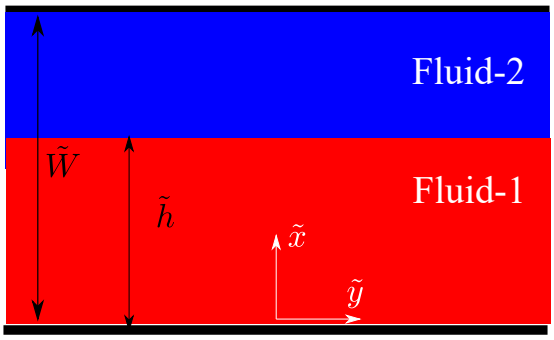

Figure 5.2: Schematic of the parallel plate geometry for two-phase flow problem and the employed coordinate system. Not to scale. Choice of coordinate system is in order to model "outlet" arms in cross-slot.

The Navier-Stokes equation in dimensionless form for fluid-1 and fluid-2 can be written as:

$$(\frac{d^2U_i}{dx^2}) = G, \qquad i = 1 \tag{5.2}$$

$$K(\frac{d^2U_i}{dx^2}) = G, \qquad i = 2 \tag{5.3}$$

where x is the dimensionless variable in the rectangular coordinate system (i.e. $x = \frac{\tilde{x}}{\tilde{W}}$), U_i is the dimensionless velocity in the $\tilde{y}$ direction with respect to the reference bulk velocity (i.e. $U_i = \frac{\tilde{U}_i}{\tilde{U}_B}$) and G is the dimensionless pressure gradient defined as $G = \frac{\frac{\partial \tilde{p}}{\partial \tilde{y}}}{\tilde{\eta}_1 \tilde{U}_B}$. Note that to get a rectilinear one dimensional flow distribution, the pressure drop in both phases should be equal, otherwise it will lead to a pressure gradient in the lateral direction of the flow stimulating a secondary motion. Solutions to equations 5.2 - 5.3 may be presented as follows:

$$U_1 = \frac{1}{2}Gx^2 + C_1x + C_2, \tag{5.4}$$

$$U_2 = \frac{1}{2}\frac{G}{K}x^2 + C_3x + C_4. \tag{5.5}$$

Equation 5.4 and 5.5 should be solved subject to the continuity of tangential velocity and the shear stress at the interface i.e. $x = \tilde{h}/\tilde{w} = h$ as:

$$U_1|_{x=h} = U_2|_{x=h}, \tag{5.6}$$

$$\frac{dU_1}{dx}|_{x=h} = K\frac{dU_2}{dx}|_{x=h}, \tag{5.7}$$

and the no-slip boundary condition at the walls (i.e. at $x = 0$ and $x = 1$) as:

$$U_1|_{x=0} = U_2|_{x=1} = 0. \tag{5.8}$$

Solving these equations with respect to the above mentioned boundary condition leads to:

$$\begin{aligned} C_1 = C_3 = \frac{3(Kh^2 - h^2 + 1)}{h^2(Kh^2 - h^2 - 2h + 3)}, \\ C_2 = 0, C_4 = -\frac{3(Kh - k - h + 1)}{h^2(Kh^2 - h^2 - 2h + 3)}. \end{aligned} \tag{5.9}$$

One should note that along with the unknown constants (C_1, C_2, C_3 and C_4), values of G and h are also unknown but they can be calculated by setting the flow rate of each fluid. In this problem we consider the flow rate in each phase to be equal to $\tilde{U}_B\tilde{W}/2$ (or in our dimensionless form equal to 0.5). Using the flow rate constraint for fluid-1, one can calculate the unknown pressure gradient G as:

$$G = -\frac{6(Kh - h + 1)}{h^2(Kh^2 - h^2 - 2h + 3)}, \tag{5.10}$$

which is equal in both fluids. Setting the flow rate equal to 0.5 for fluid-2, leads to the following constraint for the h variable:

$$\frac{0.5 + (0.5 - 0.5K^2)h^4 + (4K - 2)h^3 + (3 - 6K)h^2 + (2K - 2)h}{h^2K(3 + (K - 1)h^2 - 2h)} = 0. \tag{5.11}$$

The unknown value of h can be obtained, now, by solving equation 5.11 numerically. In this thesis, a bisection method has been used to solve this equation.

In order to better understand the effect of viscosity ratio, it is useful to define a modified form of viscosity ratio ratio as:

$$K^* = \frac{K}{K + 1}. \tag{5.12}$$

Using this definition, when the viscosity ratio K changes from zero to infinity, the modified form of the viscosity ratio K^* varies from zero to one, respectively. Note, a similar idea was used in Chapter 3 for aspect ratio. From equation 5.11, in the limits that $K \to 0$ and $K \to \infty$ the h parameter tends toward one and zero, respectively. Similarly for $K = 1$ (i.e. fluids in each phase has identical properties), one can show analytically that $h = 0.5$. From equation 5.11 one can say by changing the viscosity ratio parameter, the term $h(1 - h)$ should show two roots at $K^* = 0$ and $K^* = 1$. Figure 5.3 shows the variation of the $h(1 - h)$ parameter with the normalized viscosity ratio parameter K^* and numerical results obtained from the outlet arms from cross-slot

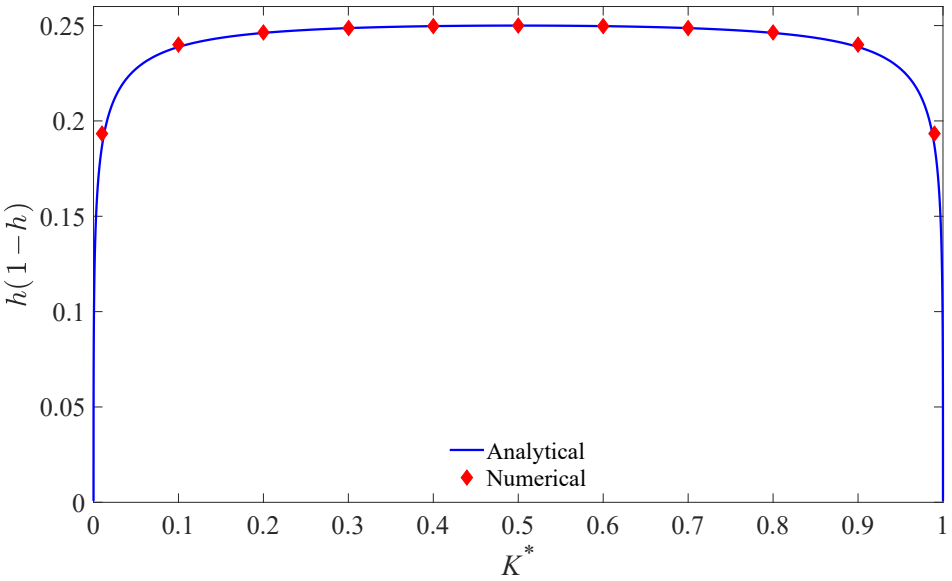

Figure 5.3: Variation of the height of the interface between two fluids with viscosity ratio for Newtonian fluids. Numerical simulations from outlet arms of cross-slot $5\tilde{W}$ downstream with $Ca = 0.005$.

simulations sufficiently far downstream that the flow is fully developed. As shown, the effect of the normalized viscosity ratio parameter is exactly symmetric about $K^* = 0.5$ (i.e. $K = 1$), highlighting that the asymptotic behaviours as $K \to \infty$ and $K \to 0$ are equivalent. From equations 5.10 - 5.11 and results presented in Figure 5.3, one can realize by increasing the viscosity of one of the two fluids, considering that the pressure drop should be equal in both phases, to retain a rectilinear flow, the average velocity reduces and so the area that the fluid requires to satisfy the constant flow rate constraint increases. Note that the results presented in Figure 5.3 were carried out at a high value of the interfacial tension ($Ca = 0.005$) (Hooper and Boyd, 1983; Barmak et al., 2016) to avoid the instability predicted by Yih (1967).

5.3.2 Two-phase flow simulations of Newtonian fluids

To better understand the effect of important parameters playing a role in this problem the simulation of Newtonian fluids in creeping flows ($Re = 0.01$) is first probed.

In Figure 5.4, results related to the effect of viscosity ratio parameter K are presented. As can be seen, by increasing the viscosity of fluid-1 (shown in red for $C = 1$), the interface of the two fluids shift towards "the right" and a "dimple" starts to grow near the stagnation point. The mechanism responsible for the shift of the interface of the two fluids in the fully-developed regions of the outlet arms is identical to the one previously discussed in section 5.2.1. By increasing the viscosity of fluid-1, the average

velocity at a constant pressure gradient is reduced, so the fluid requires more space to satisfy the constant flow rate constraint. As is well known, in two phase flow problems, a jump of normal forces appears at the interface of two fluids that is balanced by the effect of interfacial tension as follows (Rybczynski, 1911; Taylor and Acrivos, 1964; Davoodi and Norouzi, 2016; Norouzi et al., 2019):

$$\tilde{\boldsymbol{\tau}}_{1,xx} - \tilde{\boldsymbol{\tau}}_{2,xx} - \tilde{p}_1 + \tilde{p}_2 = \frac{1}{\Re}\tilde{\sigma}, \tag{5.13}$$

where in the Newtonian problem $\tilde{\tau}_{i,xx} = \tilde{\eta}_i(\frac{\partial \tilde{U}_{i,x}}{\partial \tilde{x}})$. One can show that at the stagnation point, because $\frac{\partial U}{\partial x} = \frac{\partial U_{1,x}}{\partial x} = \frac{\partial U_{2,x}}{\partial x} = constant$, if $\tilde{\eta}_2 < \tilde{\eta}_1$ then $\tilde{\tau}_{2,xx} < \tilde{\tau}_{1,xx}$, that can potentially lead to the presence of a positive curvature at the interface. In the inlet arms, a higher pressure is required to flow the fluid with higher viscosity and consequently a pressure difference at the two inlet arms appear. Unfortunately due to the complex deformation that the fluid experiences near the stagnation point, a detailed discussion on the pressure distribution in the vicinity of the interface of the two fluids relies on numerical results. In Figure 5.4 (ii), the distribution of $\tau_{xx} - p$ in the central region of the geometry is depicted. As can be seen, by increasing the viscosity of fluid-1, a jump of the normal force at the interface of the two fluids is observed that leads to the appearance of a dimple with a positive curvature at the interface of the two fluids (i.e. the left hand side terms in equation 5.13 finds a positive value that balances with the interfacial stress, interfacial tension times by the curvature of interface, on the right hand side).

Figure 5.5 shows the effect of the viscosity parameter on the magnitude of the velocity. As shown in Figure 5.4, by increasing the viscosity of fluid-1, the h parameter increases leading to a reduction in the associated area which fluid-2 requires to pass in the outlet arms. To satisfy the constant flow rate constraint in the outlet arms, the mean value of velocity in fluid-2 increases which also leads to a higher shear rate near the corners of the cross-slot geometry (not shown explicitly). Preliminary experiments in square microfluidic geometries ($1 < K < 60, Ca = 0.006$) exhibited good qualitative agreement with the patterns shown in Figure 5.4 (Oliveira, 2019). As discussed earlier, in two-phase flow problems a jump in the normal forces appears at the interface of the two fluids which is balanced by interfacial tension times by curvature. From equation 5.13, one can realize by increasing the interfacial tension to balance a constant jump in the normal force, a smaller curvature is required. As shown in Figure 5.6, by increasing the interfacial tension (i.e. reducing the Ca number) the curvature appearing at the interface of the two fluids reduces and eventually, below a critical value of Ca, leads to a flat interface (see Figure 5.6 (b)). This change in curvature at the interface, consequently changes the flow distribution and normal stress.

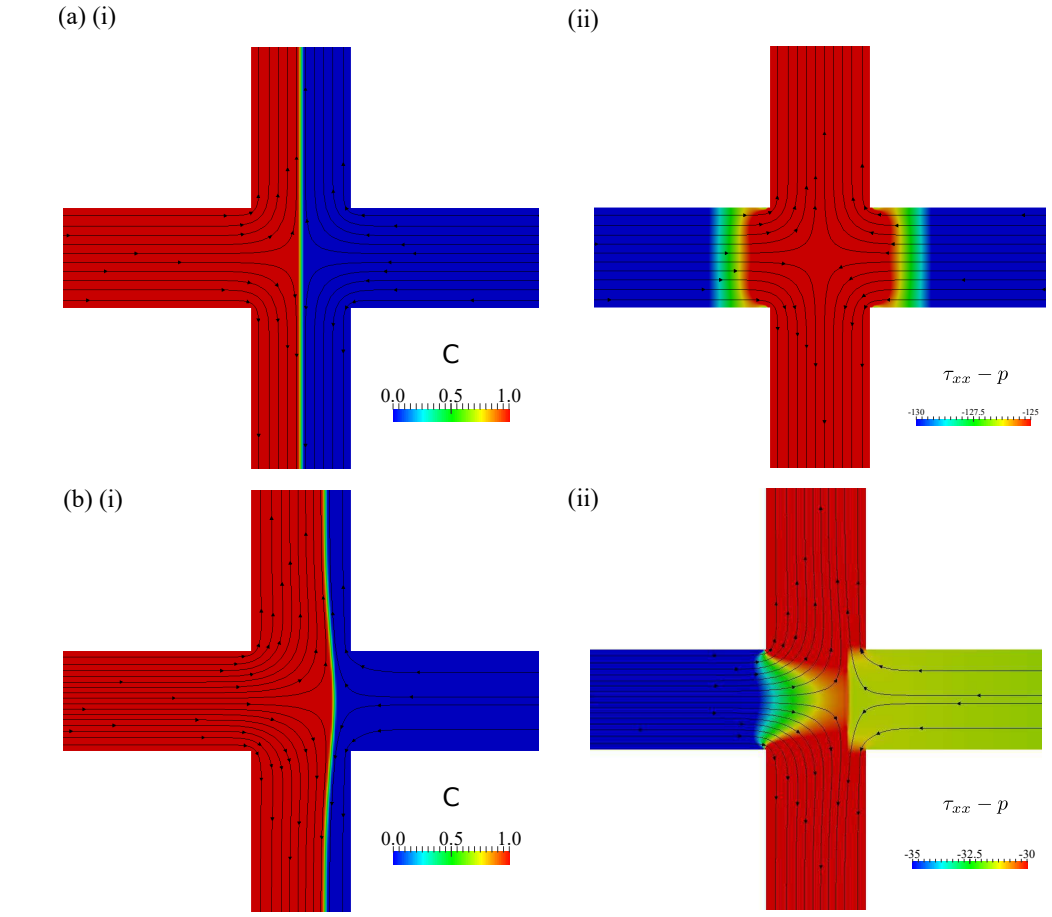

Figure 5.4: Streamlines superimposed on (i) the phase indicator parameter C , and (ii) the $\tau_{xy} - p$ term for (a) $K = 1$, (b) $K = 0.001$, with $Ca = 0.005$.

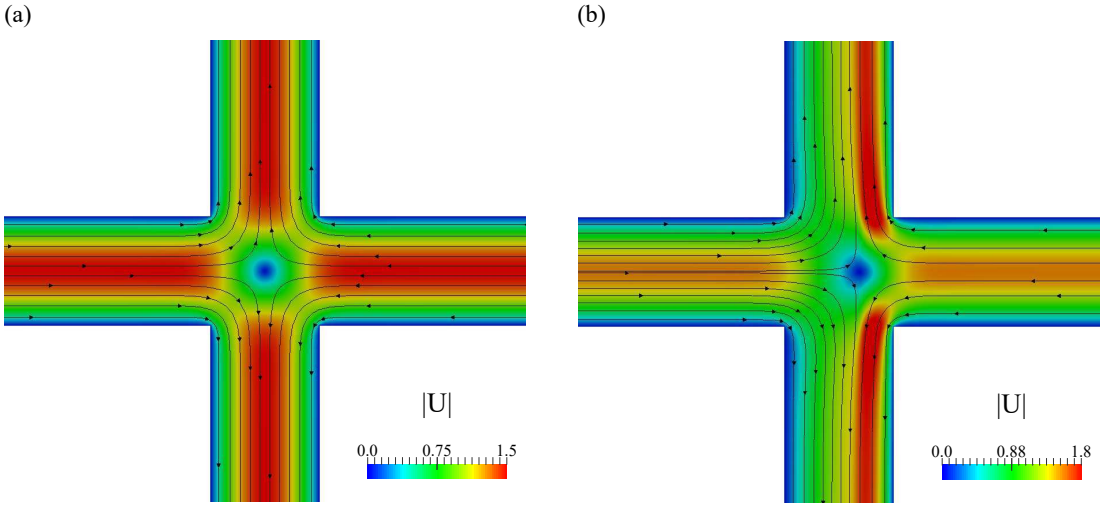

Figure 5.5: Streamlines superimposed on the velocity magnitude for (a) $K = 1$, (b) $K = 0.001$, with $Ca = 0.005$.

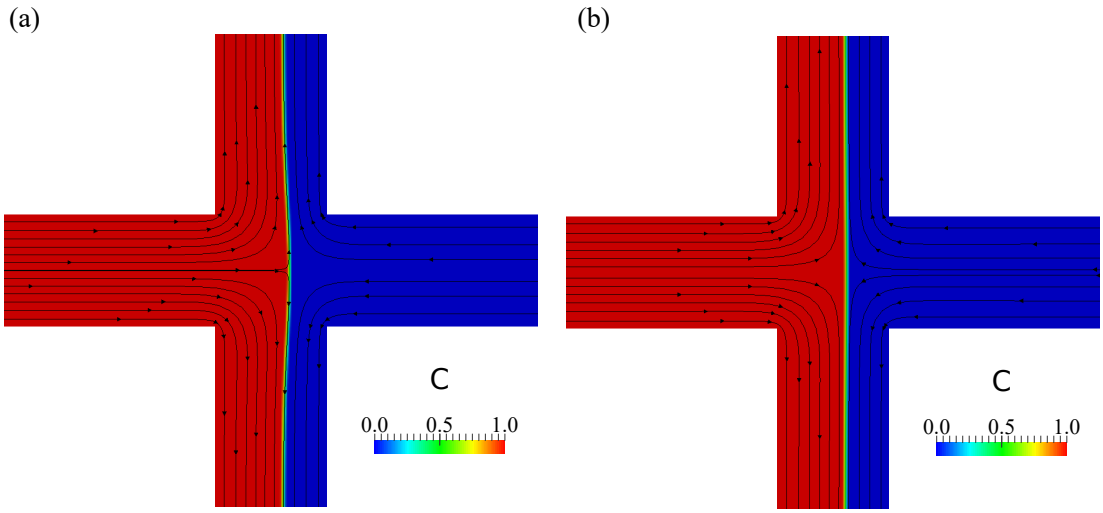

Figure 5.6: Effect of interfacial tension on the interface shape of two fluids for (a)$Ca = 0.1$, (b)$Ca = 0.005$, with $K = 0.1$.

5.3.3 Validation of two-phase flow solver with single phase viscoelastic solver

In Figure 5.7 the effect of the Weissenberg number on the symmetry-breaking instability at $Ca = \infty$ is illustrated. Imposing the value of interfacial tension $\tilde{\sigma} = 0$, the interfacial force applied on the interface of two fluids is set to zero (the $\tilde{\boldsymbol{F}}$ term in equation 2.63). In this case, by setting the rheological properties of two fluids to be equal, one can expect conservation of momentum equation 2.63 for the two-phase flow problem reduces to its equivalent equation 2.56 in a single phase problem. In Figure 5.8, a comparison between the results obtained using the rheoFoam and rheoInterFoam solvers is presented that shows both good quantitative and qualitative agreements between these two solvers. The rheoFoam solver is a single-phase flow solver and rheoInterFoam is a two-phase flow solver which were introduced in the rheoTool package in OpenFOAM (Pimenta and Alves, 2017). Both solvers predict a supercritical growth of the asymmetry parameter AP_{tp} near the critical value of the Weissenberg number $Wi_{cr} = 0.515$. The present results gives us confidence in the correct implementation of the viscoelastic constitutive equation in the two-phase flow solver.

5.3.4 Effect of interfacial tension on the symmetry-breaking instability

As is well known, the interfacial tension acts along a surface which suggests that by increasing the interfacial tension, the interface of two fluids should exhibit a flatter surface (as was also discussed in the Newtonian flow problem). In Figure 5.9, this stabilizing effect of the interfacial tension is illustrated. The results suggest that at fixed values of Wi_i, α_i and the β_i parameter, once the instability is triggered, by increasing

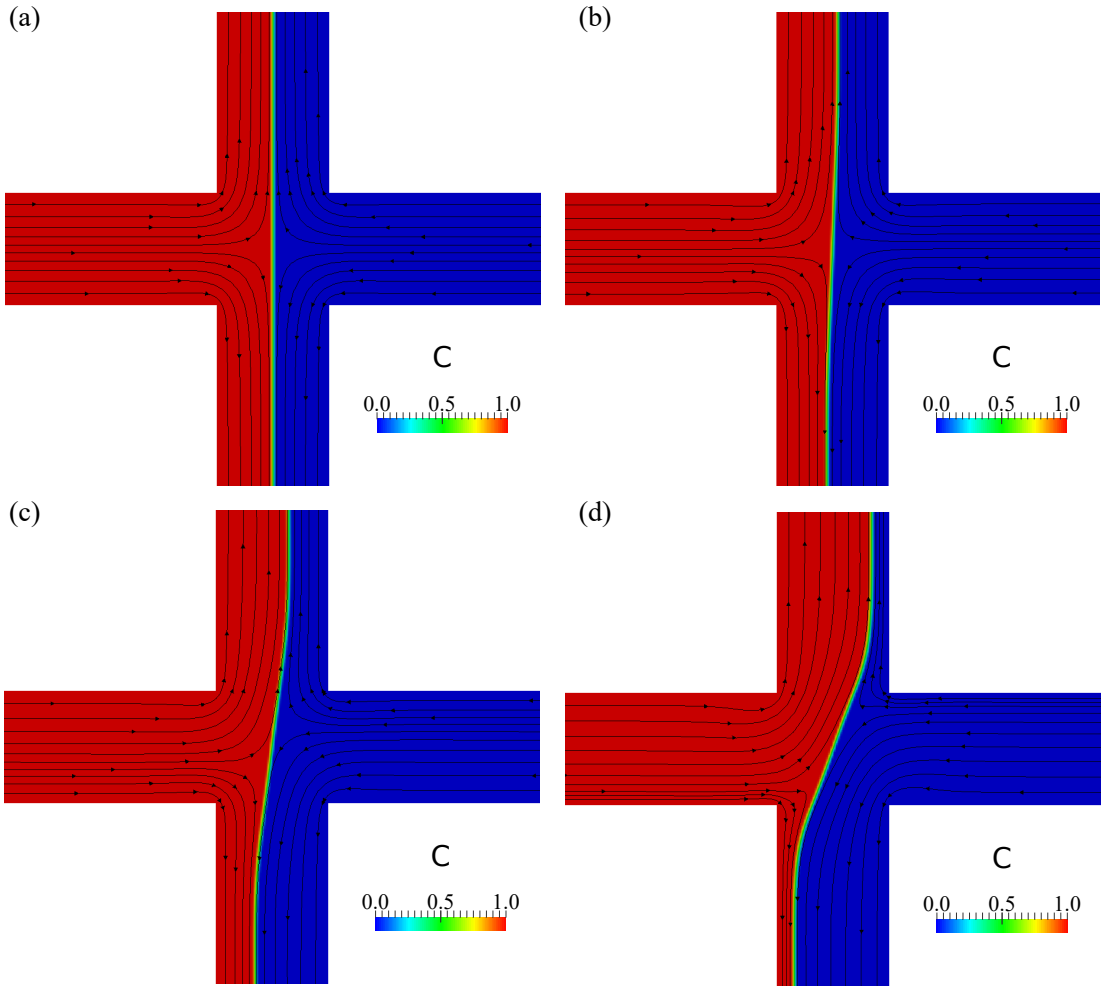

Figure 5.7: Effect of viscoelasticity on the symmetry-breaking instability of two fluids for (a)$Wi = 0.4$, (b)$Wi = 0.515$, (c)$Wi = 0.55$, (d)$Wi = 1$, with $K = 1, \alpha_i = 0.02, Ca = \infty$ and $\beta_i = 1/9$.

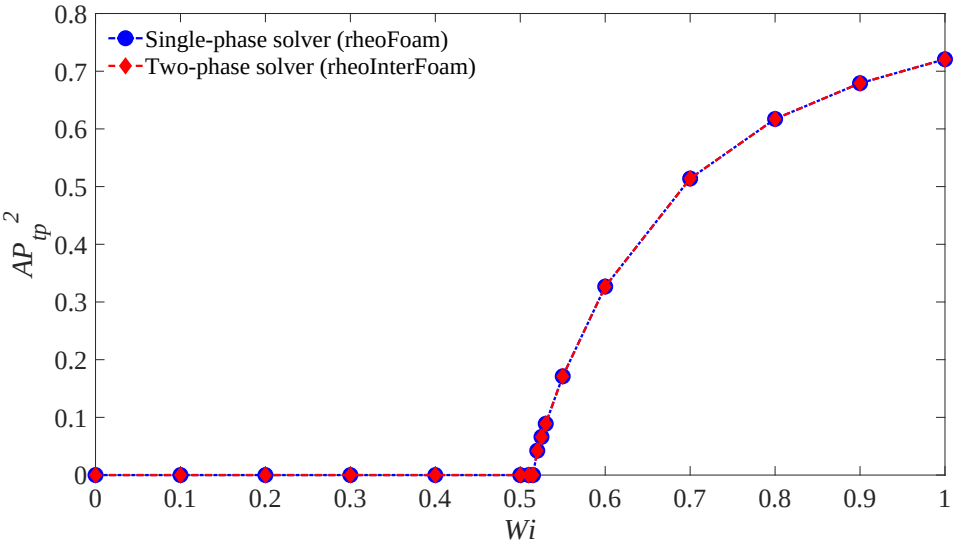

Figure 5.8: Comparison of the symmetry-breaking instability between single-phase and two phase flow solvers for $\beta_i = 1/9$ and $\alpha_i = 0.02$.

the interfacial tension (i.e. reducing the Ca number) the interface of the two fluids exhibits a flatter surface and so has a stabilizing effect. The variation of the AP_{tf} parameter with Wi_i is plotted in Figure 5.10 showing the supercritical nature of this instability as is also observed in the single phase case (Figure 5.8).

In a single-phase flow problem in the cross-slot geometry the curvature parameter can be estimated using the width of the channel as $1/\tilde{\Re} = 1/(a\tilde{W})$ in equation 1.2 where a is an unknown constant which scales this reference length. Here, due to the presence of the normal stress jump in equation 5.13, an additional curvature modification appears with a contribution from the interfacial tension. Assuming a constant jump of the normal stress $\tilde{b}[N.m^{-2}]$ on the interface of the two fluids (i.e. considering the left hand side of equation 5.13 to be equal to a constant $\tilde{b}[N.m^{-2}]$), the radius of the interfacial curvature can be scaled as $\tilde{\Re} = \tilde{\sigma}/\tilde{b}$. Strictly speaking, the normal stress jump at the interface is a weak function of the capillary number. Here for the sake of scaling, it is assumed to be a constant in order to make progress. At the end a comparison between the prediction obtained using this assumption and the results in the 2D numerical simulations will be carried out to show that the jump of normal stress at the interface of two fluids should be a weak function of the Ca number and is therefore a valid approximation in this analysis.

An initial analysis suggests that neither $\tilde{\sigma}/\tilde{b}$ nor $a\tilde{W}$ provide a good approximation of the characteristic curvature of the streamlines in the two-phase cross-slot flow problem and in fact this characteristic length scale is influenced by both of these parameters. Introducing the modifying effect of the interfacial tension on the curvature radius of

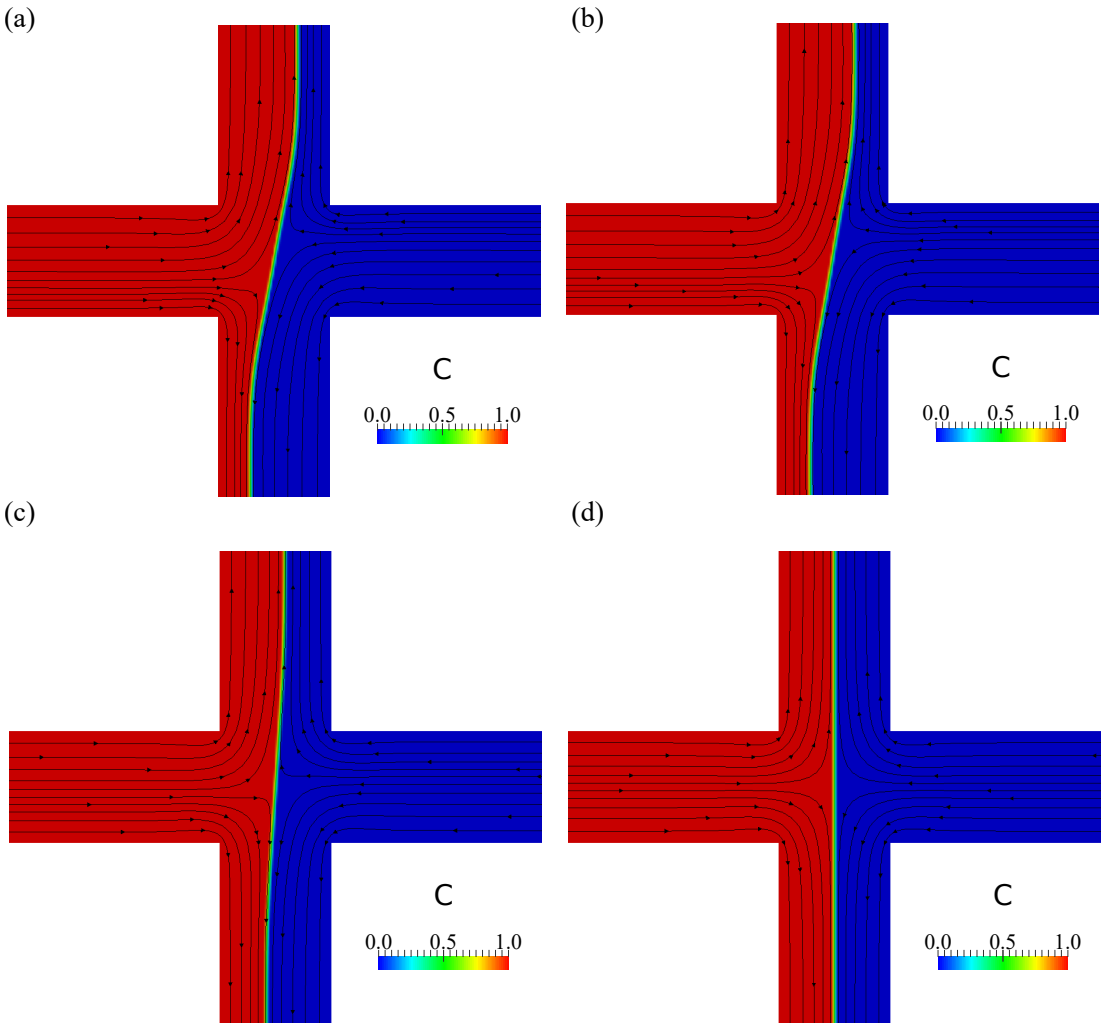

Figure 5.9: Effect of interfacial tension on the symmetry-breaking instability of two fluids for (a)$Ca = \infty$, (b)$Ca = 1$, (b)$Ca = 0.1$, (c)$Ca = 0.005$, with $Wi_i = 0.6, K = 1, \alpha_i = 0.02$ and $\beta_i = 1/9$.

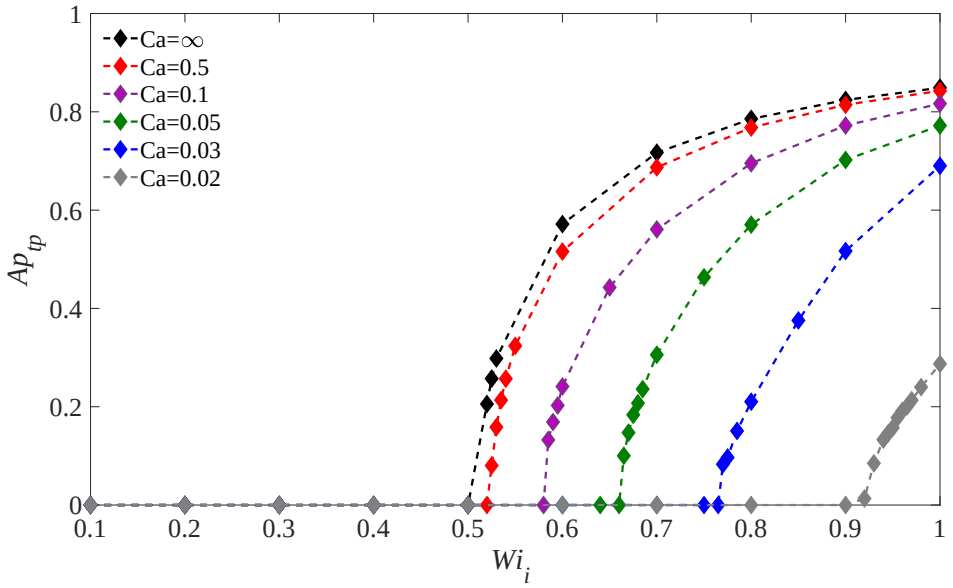

Figure 5.10: Effect of Weissenberg number on the symmetry-breaking instability for $\alpha_i = 0.02, \beta_i = 1/9, K = 1$ and different capillary numbers.

the flow using a linear combination, the reference curvature may be presented as:

$$\frac{1}{\tilde{\Re}} = \frac{1}{a\tilde{W} + \tilde{\sigma}/\tilde{b}}. \tag{5.14}$$

Assuming the modification applied to the streamline curvature due to the interfacial tension is small (i.e. $a\tilde{W} >> \tilde{\sigma}/\tilde{b}$), using a Taylor expansion one can rewrite equation 5.14 as:

$$\frac{1}{\tilde{\Re}} = \frac{1}{a\tilde{W}} + \frac{\tilde{\sigma}}{\tilde{b}a^2\tilde{W}^2}. \tag{5.15}$$

In this presentation a and $\tilde{b}$ are undetermined constants. Assuming a steady-state purely shear flow for an Oldroyd-B fluid (of which the sPTT model approaches in the $\alpha \to 0$ limit), one may scale the normal-stress component in equation 1.2 as:

$$\tilde{\tau}_{ss} = 2\tilde{\lambda}\tilde{\eta}_p\tilde{\dot{\gamma}}. \tag{5.16}$$

Here, using $\tilde{U}_b$ and $\tilde{\Re}$ as references for the velocity field and the length scale, the reference shear rate may be expressed as $\tilde{\dot{\gamma}} = \frac{\tilde{U}_b}{\tilde{\Re}}$. Substitution of these equations into the dimensionless M criteria (equation 1.2), results in the following condition for the onset criteria of a purely-elastic instability in the two-phase cross-slot flow problem:

$$M_c = \sqrt{\frac{\tilde{\lambda}\tilde{U}_b}{\tilde{W}}(a' + \frac{b'}{Ca})2(1-\beta)\frac{\tilde{\lambda}\tilde{U}_b}{\tilde{W}}(a' + \frac{b'}{Ca})}, \tag{5.17}$$

where $a' = 1/a$, $b' = \tilde{\eta}_t\tilde{U}_B/\tilde{b}a^2\tilde{W}$ and M_c are unknown constants. However, factoring out the quantity $(\frac{\tilde{\lambda}\tilde{U}_b}{\tilde{W}})^2$ and some rearrangement one can simplify the equation into:

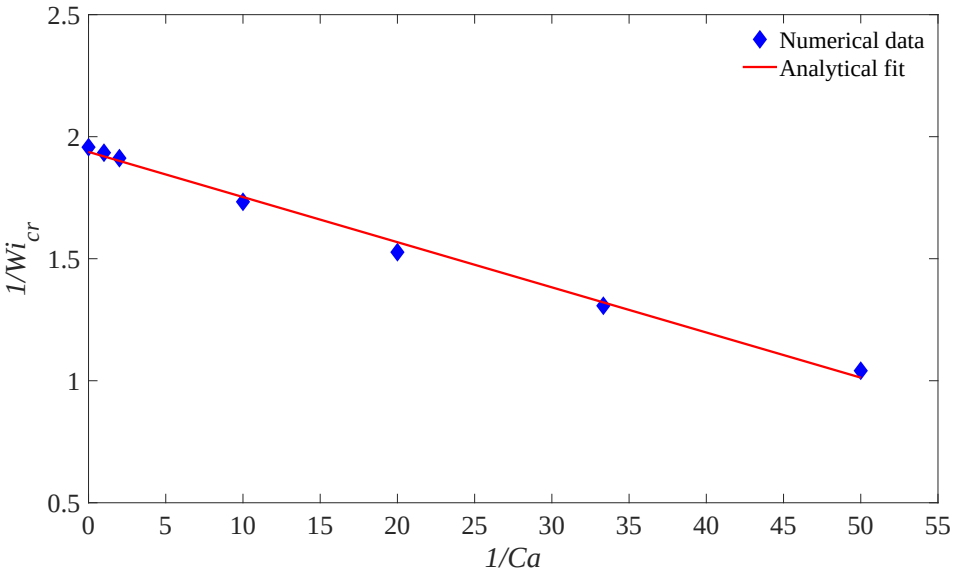

Figure 5.11: Variation of critical values of Weissenberg number against the capillary number for $\beta_i = 1/9, \alpha_i = 0.02$ and $K = 1$. Analytical fit $\frac{1}{Wi_{i,cr}} = -\frac{0.0185}{Ca} + 1.938$.

$$\frac{1}{Wi_{cr}} = \bar{a} + \frac{\bar{b}}{Ca}, \tag{5.18}$$

where, $\bar{a} = \frac{a'\sqrt{2(1-\beta)}}{M_c}$ and $\bar{b} = \frac{b'\sqrt{2(1-\beta)}}{M_c}$ are unknown constants. Figure 5.11 shows a good agreement between the fit obtained based on equation 5.18 and 2D numerical simulations. This simple correlation allows the prediction of the onset of a purely-elastic instability in the two-phase cross-slot flow as a function of the capillary number.

Finally, the modifying effect of the total viscosity ratio parameter K is briefly depicted in Figures 5.12- 5.14. As shown in Figure 5.12, reducing the K parameter pushes the interface of the two fluids towards the right and has an initial stabilizing effect. However, the simulations show that a further reduction of the K parameter below a critical value triggers a time-dependent instability that might be appearing due to a combination of an increase in the shear rate of fluid-2 near the corner (i.e. an increase in the local value of the Weissenberg number in this region) or the stratification of viscosity (Yih, 1967) or a jump of elastic normal stresses across the interface (Wilson and Rallison, 1997). Results presented in Figure 5.13 show the time dependent nature of this instability at two different instances in time. The frequency of this instability was calculated using a fast Fourier transformation as shown in Figure 5.14.

5.4 Conclusions

In this chapter, a series of 2D numerical simulations were carried out to investigate the combined effect of interfacial tension and the total viscosity ratio parameter K on

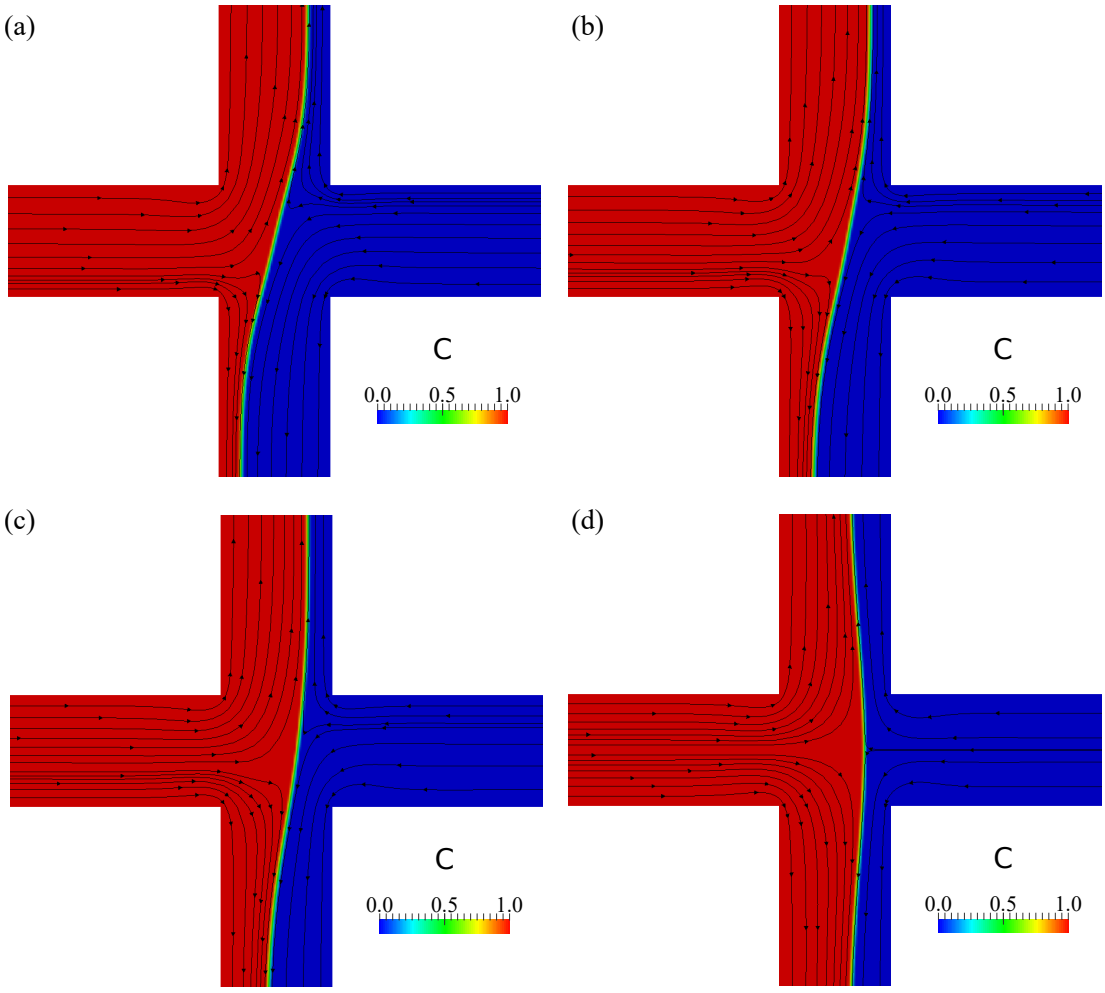

Figure 5.12: Effect of the viscosity ratio parameter on the symmetry-breaking instability of two fluids for (a)$K = 1$, (b)$K = 0.5$, (c)$K = 0.1$, with $Wi = 1, Ca = 0.005, \alpha_i = 0.02$ and $\beta_i = 1/9$.

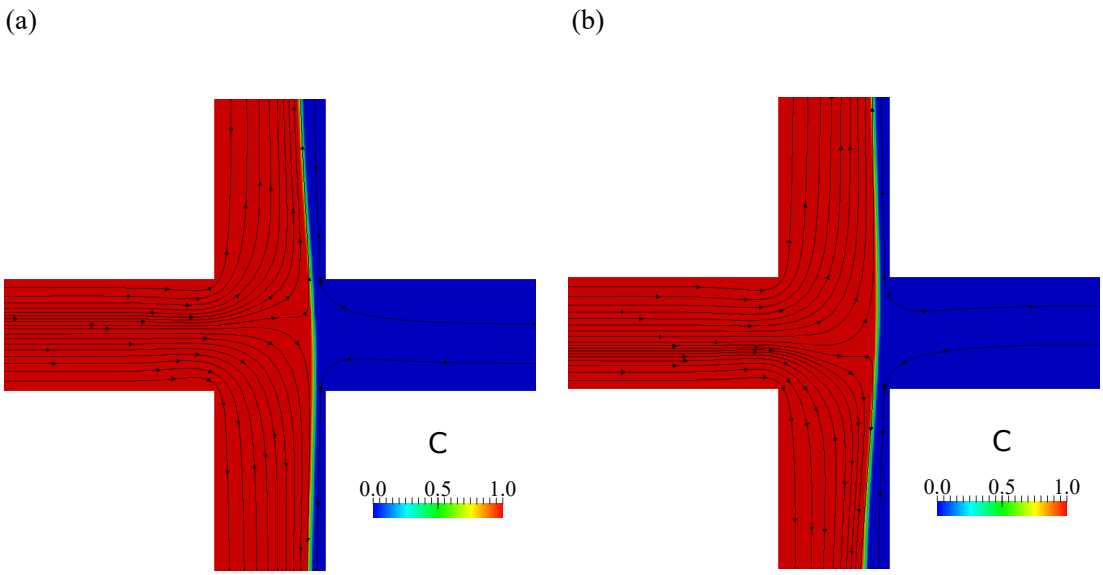

Figure 5.13: Effect of the viscosity ratio parameter on the onset of time-dependent symmetry-breaking instability in three different instances for $K = 0.001, Wi = 1, Ca = 0.005, \alpha_i = 0.02$ and $\beta_i = 1/9$.

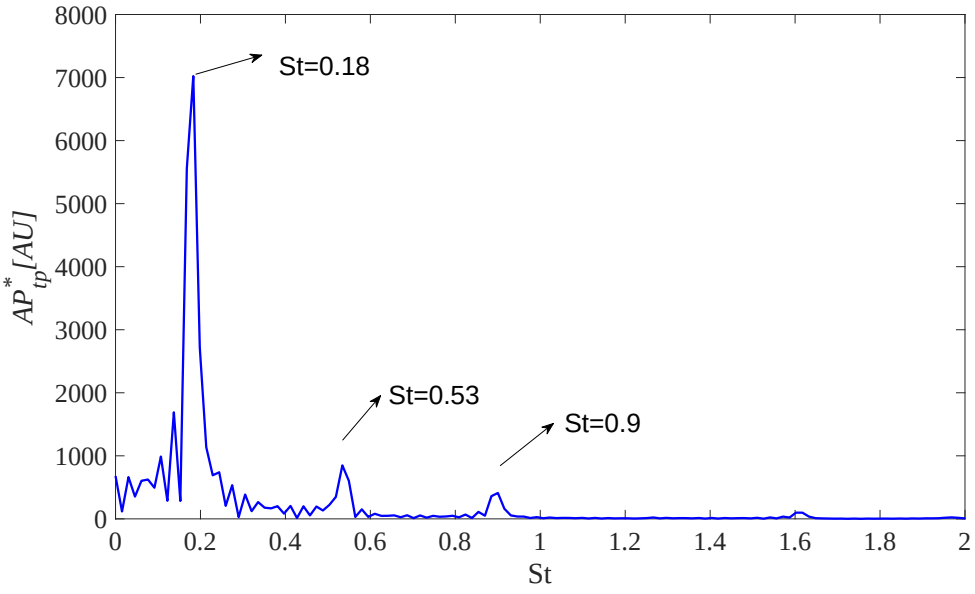

Figure 5.14: Frequency analysis using the fast Fourier transformation approach for the time-dependent symmetry-breaking instability with $K = 0.001, Wi_i = 1, Ca = 0.005, \alpha_i = 0.02$ and $\beta_i = 1/9$.

the onset of instability in the cross-slot geometry. Simulations for creeping Newtonian flows, with significant interfacial tension ($Ca = 0.005$), suggests that by reducing the K parameter, the interface of two fluids displace to a new location. To study the effect of this phenomenon, an analytical solution for the creeping fully-developed flows of two fluids with a flat interface in between two parallel plates is obtained. Using this analytical solution it has been shown that by increasing the viscosity of one of the fluids, the pressure drop changes and so the average velocity passing through the line between the wall and the interface of the two fluids for the fluid with higher viscosity reduces. To satisfy a constant flow rate in both fluids the area required for the fluid to flow with a higher viscosity needs to be increased. The mechanism behind the relocation of the interface in the fully-developed region downstream of the cross-slot is similar to the one discussed analytically in a planar channel. Interestingly, when the K parameter exhibits a non-unitary value a dimple appears at the interface of the two fluids in the vicinity of the stagnation point, which is related to the jump of the normal forces at the interface of the two fluids. The results suggest that by increasing the interfacial tension between two fluids the interface exhibits a flatter shape which is related to the balance of the interfacial stress with the jump of the normal stress.

Furthermore, at a constant capillary number, by increasing the Weissenberg number beyond a critical value such that a purely-elastic instability arises, the flow distribution and consequently the interface of the two fluids becomes asymmetric. Once the instability is triggered, by reducing the capillary number (i.e. increasing the interfacial tension) at a constant Weissenberg number the interface of the two fluids becomes flatter and eventually regains symmetry once again. Finally, the modification of the interfacial stress on the streamline curvature is introduced in the onset criteria of instability using the definition of the M parameter (Equation 1.2). An analytical expression is obtained that can be successfully used to predict how the critical Weissenberg number scales with the capillary number.

Chapter 6

Conclusions

The research carried out in this thesis aimed to contribute to a better understanding of purely-elastic instabilities of vicoelastic fluids such that the onset could be controlled in some manner. To do so flows of viscoelastic fluids in two main geometries were studied: the Taylor-Couette and the cross-slot. A series of geometrical (aspect ratio, geometric modification) and rheological (interfacial tension) parameters were introduced and these were shown to be effective in achieving this aim.
The results obtained in this thesis have shown that the M parameter can successfully predict the onset condition of purely-elastic instabilities in complex flow regimes such as ones observed in the modified cross-slot geometry and the two-phase flows in cross-slot. In the confined Taylor-Couette geometry, the results exhibited a correct scaling of the onset condition of the purely elastic instability using the M parameter but our investigation has revealed that the M parameter is not constant and is in fact a function of aspect ratio. However for the other geometries studied the M parameter was very powerful in correctly predicting the scaling of the various parameters (i.e. Φ and Ca)

6.1 Taylor-Couette geometry

All of the previous studies related to purely-elastic instabilities in the Taylor-Couette geometry were limited to the flow of viscoelastic fluids in between sufficiently tall cylinders where the one-dimensional assumption of the base flow could be applied. In this thesis, an investigation was carried out to study the effect of confining walls on the base flow and on the onset criteria of purely-elastic instability in the Taylor-Couette geometry. As a first step, an exact analytical solution was represented for the planar Couette flow of creeping Newtonian fluids which, due to the rectilinear distribution of the flow-field, the solution is also valid for constant viscosity viscoelastic fluids (such viscoelastic fluids can be modelled using the Oldroyd-B constitutive model). Results obtained using both the analytical solution and full non-linear numerical simulations in geometries with large aspect ratios suggest that the flowfield along the symmetry gap line tends toward the prediction of the velocity distribution obtained in a one-dimensional flow.

In such geometries, the modification of the flowfield due to the presence of confining walls is mainly restricted to a region located near the stationary top and bottom walls of the geometry. Further investigations in shallow geometries has shown that by reducing the aspect ratio, the modification of stationary walls on the top and bottom of the geometry will affect a larger domain of the flowfield and that the one-dimensional assumption of velocity distribution will not be valid any more. Following this, using the curvature ratio as a perturbation parameter, an approximate analytical solution for the base flow of viscoelastic fluids in the Taylor-Couette geometry was obtained. The results so obtained using both the approximate analytical solution and the full non-linear simulations suggest that due to a combination of streamline curvature and the presence of the first normal-stress difference a pair of secondary flows exists in the confined Taylor-Couette geometry which is absent for its equivalent creeping Newtonian flows before the start of any instability. Experiments conducted by a collaborator, Prof. Sandra Lerouge (Université Paris Diderot, France), confirmed the presence of this secondary flow in good qualitative agreement with the analytical prediction. Once these base flow modifications were understood, the effect of the aspect ratio on the onset condition of the purely-elastic instability was investigated. The parameter that can properly scale the onset criteria of purely-elastic instabilities is the so-called M parameter (McKinley et al., 1996b). Initial results using the global distribution of the M parameter suggests that due to the singularity of the normal-stress, the maximum value of the M parameter is singular and its global maximum is located at the corner of the moving and stationary walls. Thus, the analysis was restricted to just centreline conditions which showed that M_{cr} is not a constant but changes with aspect ratio. The obtained results suggest that by reducing the aspect ratio, the shear rate across the gap centreline increases whilst the curvature remains unchanged, so from the definition of the M parameter, one can expect that the critical Weissenberg number for the onset of the time-dependent instability *decreases* by reducing the aspect ratio parameter, which was confirmed with complimentary non-linear numerical simulations.

6.2 Cross-slot geometry

Due to the presence of opposite inlets and outlets in cross-slot stagnation point flows, a planar elongation flow is obtained at the centroid region which is of great interest for extensional rheometry. Previous studies conducted in this geometry has shown that beyond a critical value of the Weissenberg number a purely-elastic instability is triggered that can break the symmetry distribution of the flowfield - whilst remaining steady - which is an unwanted phenomenon if the device is to be used as a rheometer. In this thesis, a series of investigations were carried out to study different geometrical and rheological parameters which are playing a role in the onset criteria of the

symmetry-breaking purely-elastic instability in the cross-slot geometry. As a part of an investigation in this thesis, a geometrical modification was introduced to the standard cross-slot geometry by adding a cylinder to the geometric centre of the domain. The results presented in the thesis suggest that by increasing the size of the cylinder, one can potentially reduce the curvature of the streamlines in the centroid region and delay the onset of the instability to higher values of the Weissenberg number.
In a further investigation, the effect of interfacial tension on the curvature of the interface of two fluids and the onset criteria of the purely-elastic instability was investigated. Results obtained, once again using the M parameter, in both the modified cross-slot geometry and the two-phase flow problems, have shown the important role of the streamline curvature near the corners of the geometry on the onset criteria of the instability and that the instability is of "the curved streamlines" type which answered an open question from the literature.

6.2.1 The cross-slot cylinder geometry

In the cross-slot geometry, fluid particles passing through the line between the corners of the geometry and the stagnation point experience a complex deformation due to the presence of high shear rate and high strain rate regions at the vicinity of re-entrant corners and the stagnation point, respectively. Considering the presence of high streamline curvature, according to the definition of the M parameter (equation 1.2), both of these regions can potentially provide a suitable condition for a disturbance to grow and consequently trigger the purely-elastic instability. From the previous studies conducted in the literature, it is not clear if instabilities in the cross-slot are driven via curvature and high deformation rate near the stagnation point or from a region closer to the corner.

The free stagnation point is observed frequently in problems such as flow past a droplet or bubble, and in the standard cross-slot geometry, due to the presence of opposite flows in the inlet and outlet arms. In such problems the strain rate at the stagnation point exhibits a non-zero value. In contrast to the free stagnation point condition, in problems that the stagnation point is pinned at a solid object, due to a combination of the no-slip boundary condition and conservation of mass, the strain rate at the stagnation is equal to zero. In this thesis it was suggested to replace the free stagnation point with a non-zero strain rate value with zero strain rate pinned stagnation points by adding a cylinder at the geometric centre of the domain. By changing the size of the cylinder one can control the streamline curvature in the central region of the geometry. Also the addition of a cylinder to the problem will block the flowfield and, as a consequence, changes the velocity profile in this region. Numerical simulations with supporting experimental results suggest that the addition of a cylinder has a stabilizing effect on the onset of purely-elastic instabilities. As a part of this

research an approximate analytical expression for the velocity distribution along the gap between the corners of the geometry and the stagnation point was derived. Using the definition of the M parameter and this approximate analytical expression, the stabilizing effect of the introduced geometrical modification was obtained analytically. According to the analysis presented in this thesis, the stabilizing effect of the addition of a cylinder to the cross-slot geometry is related to the change of streamline curvature near the re-entrant corner regions. The obtained results suggest that once the blockage parameter approaches to zero the modification of the cylinder wall on the flowfield is local and the critical condition in which the instability is triggered is the same as the onset condition in the standard cross-slot geometry. In a following step, to study the effect of the stagnation point region on the onset condition of the purely-elastic instability for small blockage ratios, a complete slip boundary condition was applied at the cylinder wall to replace the zero strain rate value for the no-slip boundary condition with a non-zero strain rate at the stagnation points, this value is approximately three times larger than the strain-rate value at the stagnation point of the standard cross-slot geometry. The obtained results suggest that the kinematic properties of the flow distribution around the stagnation point do not play any significant role in the onset of the purely-elastic symmetry-breaking instability and that the critical values of the Weissenberg number which the instability is triggered, in both no-slip and complete slip boundary conditions cases, tend toward its critical value for the standard cross-slot geometry (i.e. $Wi \cong 0.51$).

Finally, by plotting the local distribution of the M parameter, it was shown that the location of instability-driving regions appears in the vicinity of the corners which can be attributed to the high deformation rate and high streamline curvature in this region.

6.2.2 Stabilisation of purely-elastic instabilities in cross-slot geometries using interfacial tension

In this chapter of the thesis, a series of 2D numerical simulations were carried out to investigate the effect of the interfacial tension on the onset condition of the purely-elastic instability in the stagnation point cross-slot flow problem. In this study, two different fluids were injected in inlet arms with the same flow rate and relaxation times and the value of the solvent-to-total viscosity ratio parameter of the two fluids was set to be identical. Using this protocol, one can study the effect of interfacial tension and the total viscosity ratio parameter (i.e. the K parameter) on the onset criteria of the symmetry-breaking instability. As a first step, to study the effect of the K parameter, an investigation was carried out to obtain an analytical expression for the velocity distribution of the two-phase flow problem in between two parallel plates in the fully-developed regime. The presented analytical solutions are functions of the location of the interface of the two fluids h that can be obtained by solving a mass conservation

constraint. The results suggest that by reducing the value of the K parameter the interface of two fluids move from the symmetry centreline toward a new location to provide the fluid with a higher viscosity a larger passage to flow through. This relocation of the interface is related to a combined influence of the pressure gradient and the conservation of mass. The K parameter was shown to exhibit a similar effect on the flowfield of creeping Newtonian fluids in the cross-slot geometry in the outlet arms. By reducing the K parameter, the interface of the two fluids moves towards the "right" (to provide a larger area for the fluid with the higher viscosity to pass). Interestingly, as the K parameter finds a non-zero value a dimple starts to appear at the interface of the two fluids in the vicinity of the stagnation point region, which is related to the jump of the normal forces at the interface of the two fluids. The results suggest that by increasing the interfacial tension between two fluids the interface of the two-fluids exhibits a flatter shape which is related to the balance of the interfacial stress with the jump of the normal force. At the interface of the two fluids, the interfacial tension times by the curvature of the interface balance a jump of the normal force, so by increasing the interfacial tension a smaller curvature is required to balance this force and the interface becomes flatter.

The problem was then extended to the investigation of the purely-elastic instability in the presence of interfacial tension. At a constant capillary number, by increasing the Weissenberg number beyond a critical value, the flow distribution and consequently the interface of the two fluids obtains an asymmetric distribution which is related to the non-linear effect of the elastic stress. These results suggest that once the instability is triggered, by reducing the capillary number (i.e. increasing the interfacial tension) at a constant Weissenberg number, the interface of the two fluids finds a flatter distribution and eventually, below a critical value of the capillary number, the flow exhibits symmetry once again. Following this, the modification of the interfacial stress on the streamline curvature was introduced in the definition of the M parameter to obtain an analytical expression which can be used to understand onset conditions. Once the instability is triggered, at constant capillary and Weissenberg numbers, the K parameter has been shown to have a stabilizing effect down to a critical value. However, the simulations show that a further reduction of the K parameter below a critical value triggers a time-dependent instability that might be appearing due to a combination of an increase in the shear rate of fluid-2 near the corner (i.e. an increase in the local value of the Weissenberg number in this region) or the stratification of viscosity (Yih, 1967) or a jump of elastic normal stresses across the interface (Wilson and Rallison, 1997). Results presented in Figure 5.13 show the time dependent nature of this instability at two different instances in time. The frequency of this instability was calculated using a fast Fourier transformation as shown in Figure 5.14.

6.3 Suggestion for further work

The research carried out in this thesis can assist in a range of future studies to investigate the behaviour of Newtonian and complex fluid systems. Suggestions for future works in the TC geometry are given below.

As discussed previously, the approximate analytical solution presented in this thesis was limited to the first order of perturbation expansion and assuming a steady-state. One thing that would be interesting to do in the future is to extend this problem to study unsteady flows by including the time derivatives in the problem and to extend the perturbation expansion by including higher order terms. One could hope such analytical investigations, potentially, provide more valuable insights on the time dependent structure of the flowfield and the instability which appears for higher values of the Weissenberg number.

For all of the linear stability analysis conducted in the past, the base flowfield was assumed to be one dimensional. In such studies, unfortunately, the explicit analysis of end effects will be difficult, because the departures from the linear solution are not in any sense small near the end walls. Hence an appreciation of the full problem in qualitative terms is a useful preliminary objective. In the future, it would be interesting to employ the present perturbation solution from this thesis as a base flow to conduct a linear stability analysis and investigate the modifying effect of the confining walls on the onset criteria of pure-elastic instability in the TC geometry and compare them with full 3D numerical simulations and experimental results.

For the cross-slot geometry, the solid cylinder could be replaced by a droplet. One of the main differences between the free and pinned stagnation points in fluid mechanics is related to the magnitude of the strain-rate at this point. The combination of the no-slip boundary condition with the conservation of mass requires, when fluid passes a solid object, to obtain a zero strain rate at the stagnation point, while in free stagnation point problems, the strain rate can obtain a non-zero value. An interesting project that would be worth doing in the future would be to replace the cylinder at the geometric center of the cross-slot geometry with a droplet of another fluid. In this way, one can possibly study the proposed geometry modifications in this thesis in different non-zero strain rates (by changing the properties of the fluid in the drop phase, different tangential velocity profile at the interface of the two fluids will be obtained and, as a consequence, different strain rates at the stagnation point can be obtained). This study would be subject to the assumption that the droplet stays at the center of the cross-slot geometry which, of course, may not be true. Preliminary simulations suggested the set-up may not be stable but only a limited parameter range was studied.

One other interesting topic to work on would be the investigation of the addition of a cylinder on the OSCER geometry (Haward et al., 2012a). A previous study by Haward et al. (2012a) has shown that the instability in this modified geometry is triggered due to a combination of the high elongational flow and streamline curvature at the stagnation-point of the geometry. As discussed in this thesis, by replacing a free-stagnation point by pinned stagnation points at the cylinder walls, a non-zero value of the strain rate will be replaced by a zero value and this fundamental change in the flowfield in this region might potentially lead to delay of instability to higher values of the Weissenberg number and provide more insight regarding the kinematics of the flowfield in such ideal elongational dominated flows.

Also, as a part of this thesis an analytical platform has been developed by applying a bounded transformational on the conformation tensor (presented in Appendix A). Using this analytical platform a solver has been developed by modifying the rheoFoam platform and including a bounded evolution equation of the conformation tensor. One of the things that would be interesting to do in the future would be to test this solver for the lid-driven cavity flow of viscoelastic fluids (this problem is known as one of toughest problem from numerical simulation point of view in rheology, due to the singularity of strain rate near the moving lid and stationary walls). It would be also nice to conduct some analytical approximation, similar to the one conducted for Taylor-Couette flow, to check the accuracy of these two solutions.

Appendix A

A bounded-transformation for viscoelastic conformation constitutive laws

In this Appendix the previous kernel-conformation transformation studies are extended by using the bounded properties of Atan (arc tangent) function to formulate and suggest a transformation for the conformation tensor of viscoelastic fluids that can be applied for a large class of constitutive equations. This transformation is motivated based on numerical evidence that the high Weissenberg number problem is caused by the failure of numerical approaches in dealing with the large growth of deformation rate developed by the conformation tensor. Similar type of problems may be observed in hydrodynamic problems such as flow in confined Couette geometries or lid-driven cavity flows that in the corner of moving and stationary walls, singularities of deformation and conformation rates exist.

In all of the previously suggested transformations, the applied function had an unbounded nature (i.e. $\lim_{\boldsymbol{A}\to\infty} Log_a(\boldsymbol{A}) = \lim_{\boldsymbol{A}\to\infty} root^a(\boldsymbol{A}) = \infty$). Here in this Appendix it is suggested to take advantage of the bounded nature of Atan function (i.e. $\lim_{\boldsymbol{A}\to\infty} Atan(\boldsymbol{A})) = \pi/2$) for the transformation of conformation tensor. In this way, one would expect that numerical approaches to be less likely to become divergent when a large growth of deformation rate is appeared in hydrodynamic problems. The merit of the new formulation is assessed by simulating confined Couette flows of viscoelastic materials using an Oldroyd-B constitutive equation in the OpenFoam platform and modifying the rheoFoam solver (Pimenta and Alves, 2017). By using this newly formulated constitutive law and adding boundedness properties to the conformation tensor, it is shown that one can consequently provide a higher computational chance to obtain solutions to these types of problem.

Here, in this part of the thesis a combination of log and Atan functions for the transformation of conformation tensor is suggested to be used:

$$\mathbb{K}(\boldsymbol{A}) = Atan(log(\boldsymbol{A})) = \boldsymbol{O}Atan(log(\boldsymbol{\Theta}))\boldsymbol{O^T}, \tag{A.1}$$

In this manner, the log function reduces the magnitude of the $\boldsymbol{A}$ tensor (Fattal and Kupferman, 2004) while, Atan will add the bounded properties to this transformation. Using (A.1) as the kernel function for the transformation of conformation tensor, the gradient matrix $\boldsymbol{J}$ may be defined as:

$$\boldsymbol{J} = diag(\frac{\partial Atan(log(\Gamma_1)}{\partial \Gamma_1}; \frac{\partial Atan(log(\Gamma_2)}{\partial \Gamma_2}; \frac{\partial Atan(log(\Gamma_3)}{\partial \Gamma_3}) = (\boldsymbol{\Theta}(ln(\boldsymbol{\Theta}))^2 + 1)^{-1}. \tag{A.2}$$

Implementing equation A.2 in 2.82, for the Oldroyd-B constitutive equation, $F(\boldsymbol{\Theta}) = 1$ and $H(\boldsymbol{A}) = \boldsymbol{I} - \boldsymbol{A}$, the final form of the evolution equation will be appeared as follows:

$$\begin{aligned} \frac{D\mathbb{K}(\boldsymbol{A})}{Dt} &= \boldsymbol{\Omega}\mathbb{K}(\boldsymbol{A}) - \mathbb{K}(\boldsymbol{A})\boldsymbol{\Omega} + 2\boldsymbol{B}\boldsymbol{O}\frac{1}{ln(\boldsymbol{\Theta})^2 + 1}\boldsymbol{O}^{\boldsymbol{T}} \\ &+ \frac{1}{Wi}(\boldsymbol{O}\frac{1}{(ln(\boldsymbol{\Theta})^2 + 1)\boldsymbol{\Theta}}\boldsymbol{O}^{\boldsymbol{T}} - \boldsymbol{O}\frac{1}{ln(\boldsymbol{\Theta})^2 + 1}\boldsymbol{O}^{\boldsymbol{T}}). \end{aligned} \tag{A.3}$$

This newly transformed evolution equation for the conformation tensor is embedded in the rheoFoam solver (Pimenta and Alves, 2017) and its merit is assessed by simulating creeping flow of Oldroyd-B fluids in a planar confined Couette geometry with aspect ratio of one (i.e. $\Lambda = 1$), a cross-slot geometry and flow past a confined cylinder and comparing it with log-conformation results.

A.1 Fully developed planar Couette flow

As a first step, to check the accuracy of the formulation obtained in equation A.3, a comparison between the results obtained using *Atan*-conformation and *Log*-conformation solvers in a fully-developed planar Couette flow problem is carried out. The schematic of the studied problem is presented in Figure A.1 and the employed mesh is similar in density to $M3$ mesh from Table 3.1. As shown in Figure A.1, $\tilde{U}_w$ is the wall velocity and $\tilde{L}$ is the length of the square cross section.

The velocity distribution ($U_z = \frac{\tilde{U}_z}{\tilde{U}_w}$) using both the *Atan*-conformation (filled contours) and *Log*-conformation (solid lines) solvers with $\beta = \frac{\tilde{\eta}_s}{\tilde{\eta}_t} = 0.5$ and $Wi = \frac{\tilde{\lambda}\tilde{U}_w}{\tilde{L}} = 0.1$ for creeping flow (i.e. $Re = \frac{\tilde{\rho}\tilde{U}_w\tilde{L}}{\tilde{\eta}_t} = 0.01$) are presented in Figure A.2 which shows a satisfactory agreement between the two solvers. In such a problem, due to the presence of a jump in velocity at the corner of the moving and stationary walls the stress distribution is singular. As shown in Figure A.3 both solvers were able to capture the distribution of the stress tensor in a good agreement with each other. This issue provides confidence that the use of a bounded transformation on the conformation tensor should not affect the final results even in such singular problems.

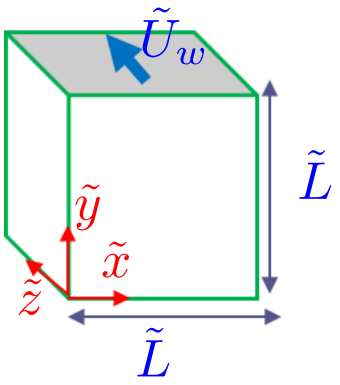

Figure A.1: A schematic of the planar Couette geometry with the employed coordinate system.

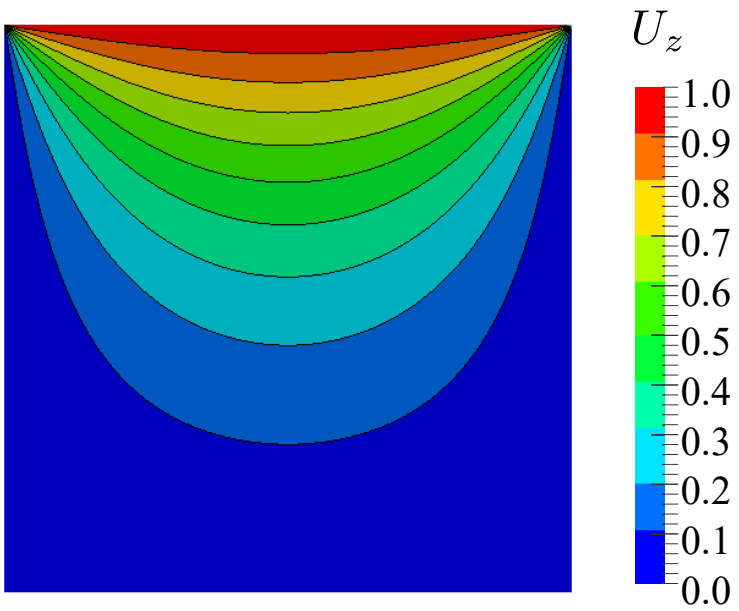

Figure A.2: Velocity contours for planar Couette flow with $\beta = 0.5$ and $Wi = 0.1$. Results obtained with the *Atan*-conformation solver (filled contours); *log*-conformation (solid lines).

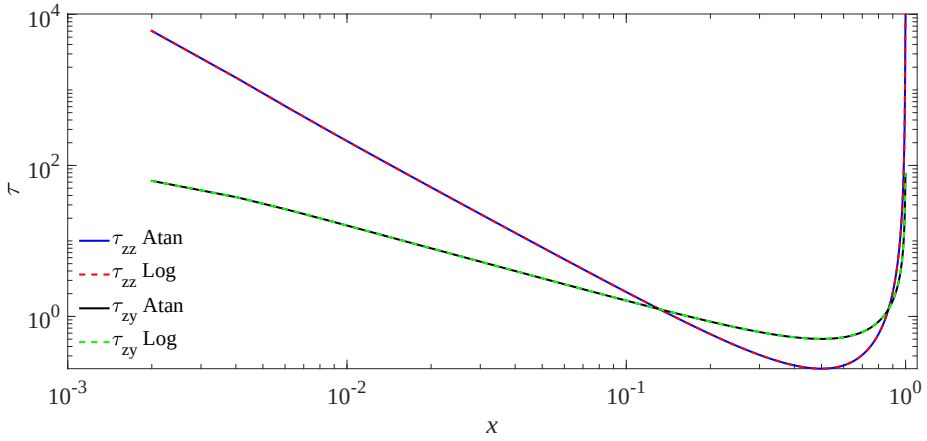

Figure A.3: Stress distribution obtained using Log (dashed lines) and Atan (solid lines) transformations along the moving wall at $y = 1$ for planar Couette flow with $\beta = 0.5$ and $Wi = 0.1$.

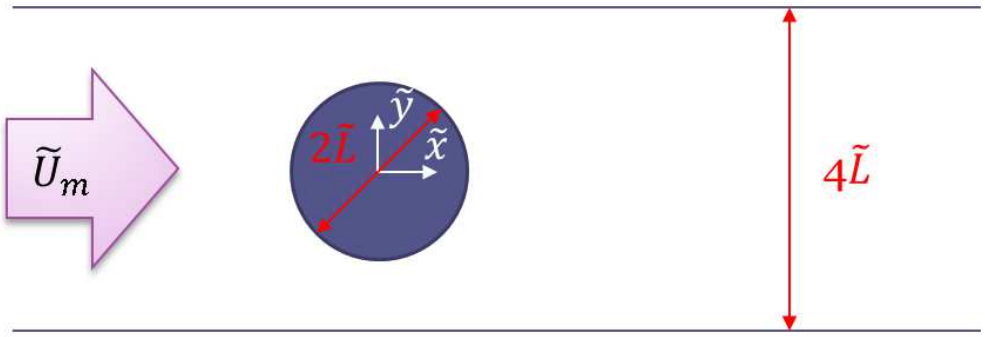

Figure A.4: A schematic of the confined cylinder geometry with the employed coordinate system.

A.2 Flow past a confined cylinder

In fluid mechanics the flow passing a confined cylinder geometry is considered as one of the challenging problems due to the complex flow distribution (Alves et al., 2001). The schematic of the studied problem is presented in Figure A.4 and the employed mesh is similar to the one used in Alves et al. (2001). As shown in Figure A.4, $\tilde{U}_m$ is the mean velocity passing through the entrance region and $2\tilde{L}$ is the size of the cylinder located between two walls of parallel plates with a distance of $4\tilde{L}$. The x component of the velocity distribution ($U_x = \frac{\tilde{U}_x}{\tilde{U}_m}$) using both the *Atan*-conformation (filled contours) and *log*-conformation (solid line) solvers with $\beta = \frac{\tilde{\eta}_s}{\tilde{\eta}_t} = 0.59$ and $Wi = \frac{\tilde{\lambda}\tilde{U}_w}{\tilde{L}} = 0.6$ for the creeping flow (i.e. $Re = \frac{\tilde{\rho}\tilde{U}_w\tilde{L}}{\tilde{\eta}_t} = 0.01$) are presented in Figure A.5 which shows a satisfactory agreement between the two solvers. In Figure A.6 the evolution of the drag coefficient in time for both solvers is presented. Here $C_d = \frac{\tilde{F}_x}{\tilde{\eta}\tilde{U}_m\tilde{L}}$ where $\tilde{F}_x$ is the force applied on the cylinder in x direction. The satisfactory results obtained in Figure

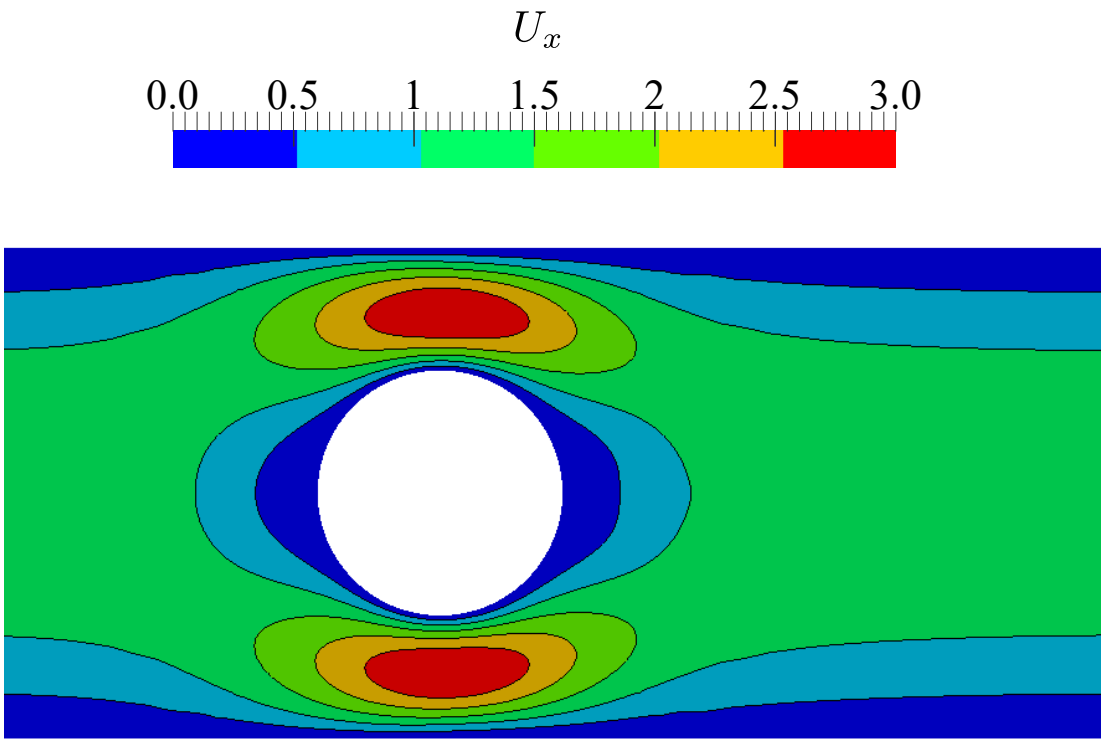

Figure A.5: Distribution of the x component of the velocity with $\beta = 0.59$ and $Wi = 0.6$. Results obtained with the *Atan*-conformation solver (filled contours); *log*-conformation (slid lines).

A.6 in between the two solvers gives us confidence in the correct implementation of equation A.3 for prediction of stress evolution in such complex flows.

A.3 Cross-slot stagnation point flow

As a final test case, in this section the results obtained using the *Atan*-conformation solver is benchmarked against the *Log*-conformation solver. In Figure A.7 the variation of the asymmetry parameter with the Weissenberg number is plotted. The agreement between these two solvers suggest that the results obtained with the *Atan*-conformation solver is consistent with results obtained using the *Log*-conformation solver.

A.4 Conclusions

In solvers using the kernel-conformation concept, a transformation function is introduced and applied to the conformation tensor after a change of coordinate system. This new coordinate system consists of the principal axis of the stress tensor (i.e. the eigenvectors of the stress tensor). Generally, this transformation function can be in the form of any continuous function. In the past lots of different functions (sinh, square root, log and ...) have been suggested and studied to be applied on the conformation

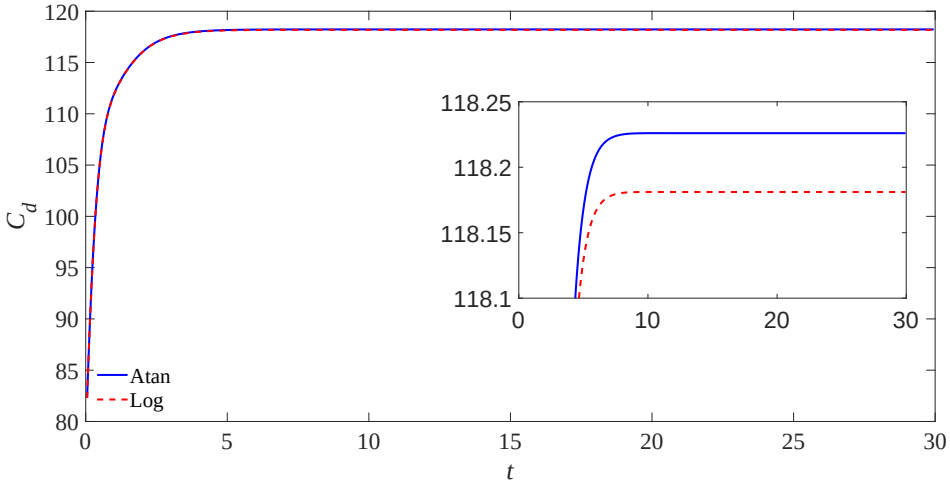

Figure A.6: Evolution of drag coefficient in time for Log-conformation (red dashed line) and Atan-conformation (blue solid line) solvers with $\beta = 0.59$ and $Wi = 0.6$.

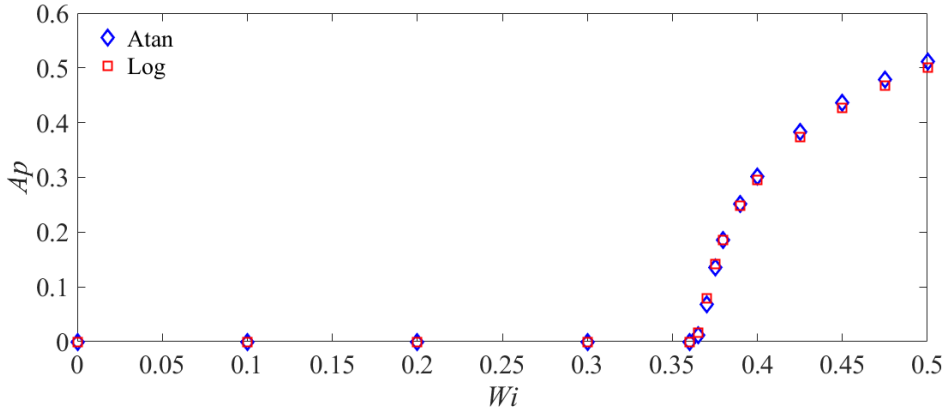

Figure A.7: Variation of asymmetry parameter versus Wi number for *Log*-conformation (red square symbol) and *Atan*-conformation (blue diamond symbol) solvers with $\beta = 1/9$.

tensor so during the numerical procedure, the solvers deal with a smaller magnitude conformation tensor in the transformed constitutive equations. In this way, numerical approaches are less likely to diverge. Interestingly, all of the previous studied transformation functions which had unbounded natures (as an example $log(\infty) = \infty$). By employing this newly introduced bounded transformation on the conformation tensor, a boundedness nature was added to the transformed evolution equation of stress tensor (here this evolution equation will always vary between 0 and $\pi/2$ since $Atan(\infty) = \pi/2$). In this Appendix results obtained using the newly introduced *Atan*-conformation solver (equation A.3) were benchmarked against the *Log*-conformation solver in three different problems. These numerical simulations suggests that when this bounded transformation is applied on the Oldroyd-B constitutive law, this numerical approach will have a good chance to simulate these types of complex flows. The presented simulations have shown a good agreement with previously reported results to predict the flowfield and stress-distributions in singular problems such as the one observed in planar Couette flow and complex problems such as flow past a confined cylinder and flow in a cross-slot geometry.

Appendix B

Comparison between analytical solution for Newtonian fully-developed finite aspect ratio planar Couette flow and Theofilis et al. (2004)

A previous study carried out by Theofilis et al. (2004) has derived an analytical solution for the rectangular cavity flows of Newtonian fluids. Applying an appropriate change of coordinate system to model the problem defined in this thesis and after correcting a typos in equation (2.5) in Theofilis et al. (2004), one can represent their solution as:

$$v_\theta^{[0]} = \sum_{n=0}^{\infty} \frac{4(-1)^n}{(2n+1)\pi} \frac{sinh((2n+1)\pi(-x+1)/2\Lambda)}{sinh((2n+1)\pi/\Lambda)} cos((2n+1)\pi z/2). \tag{B.1}$$

In Figure B.1, the solution obtained in equation 3.20 is compared against the independent solution presented in equation B.1 adopted from Theofilis et al. (2004). As can be seen there is excellent global agreement. One subtle difference is the slight change in boundary condition at the corner which we confirmed remains essentially local.

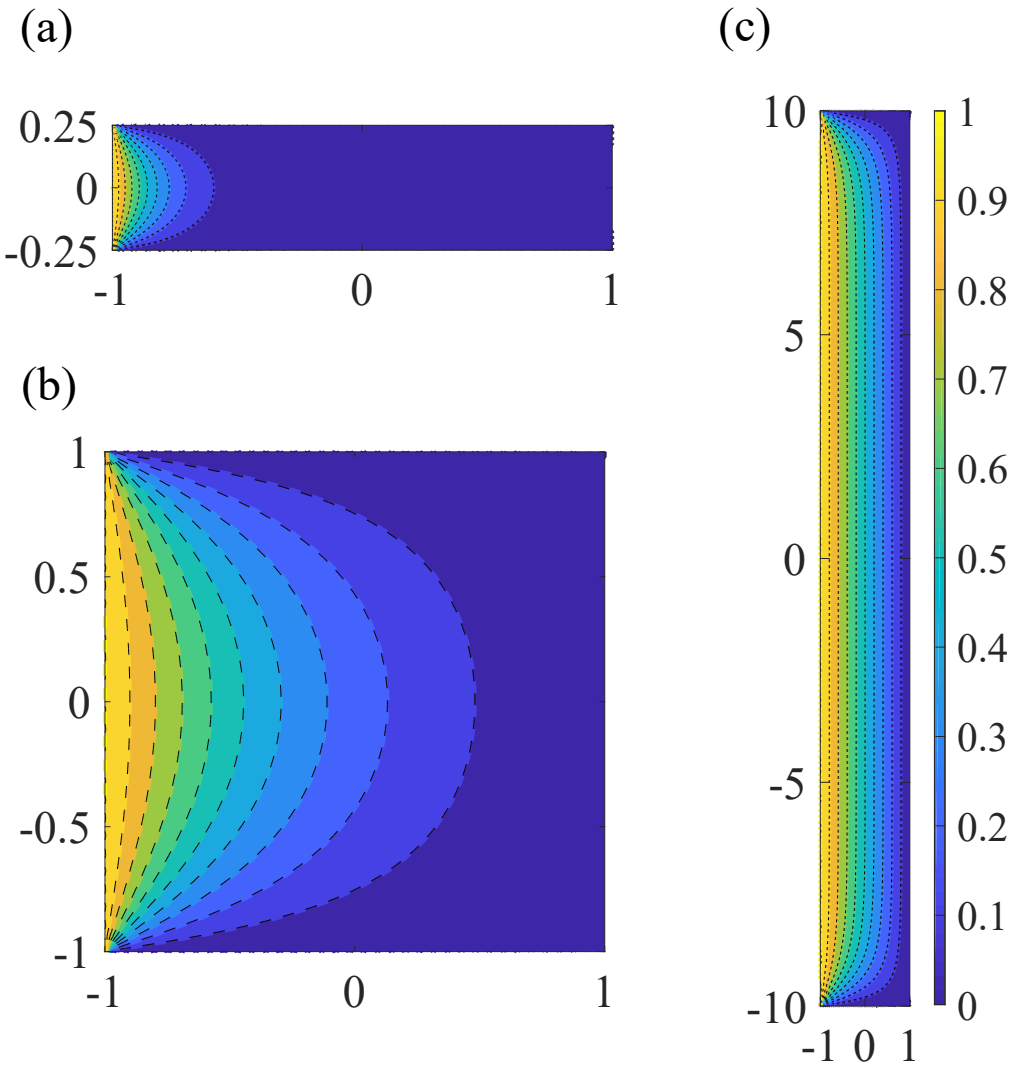

Figure B.1: Velocity contours for planar Couette flow (a) $\Lambda = 0.25$; (b) $\Lambda = 1$; (c)$\Lambda = 10$. The solution obtained in this thesis in equation 3.20(filled contours), the solution presented in equation B.1 adopted from Theofilis et al. (2004) (- - -).

Appendix C

Analytical approach for determining the M_{Cr} parameter in the modified cross-slot geometry

In this Appendix, an approximate analytical solution for the flow distribution of a creeping Newtonian fluid along a diagonal line between the corners and a stagnation point is obtained (a schematic of the problem is depicted in Figure 4.1). Moving to a cylindrical coordinate system, the components of the velocity vector in terms of the stream function are:

$$\tilde{U_\theta} = \frac{\partial \tilde{\psi}}{\partial \tilde{r}}, \qquad \tilde{U_r} = -\frac{1}{\tilde{r}}\frac{\partial \tilde{\psi}}{\partial \theta}. \tag{C.1}$$

For steady Newtonian flows, the conservation of momentum equation using the definition of stream function, in non-dimensional form may be presented as:

$$\nabla^4 \tilde{\psi} = 0. \tag{C.2}$$

Separation of the stream function into a function of a radial line $f(\tilde{r})$ and a function of the angular polar angle which is periodic with the wave number of m allows the general form of the analytical solution for equation C.2 to be obtained as:

$$\tilde{\psi} = (C_1 \tilde{r}^m + C_2 \tilde{r}^{-m} + C_3 \tilde{r}^{m+2} + C_4 \tilde{r}^{m-2}) e^{im\theta}. \tag{C.3}$$

The analytical solution obtained by Moffatt (1964) for the creeping flow of Newtonian fluids around a sharp corner of 270^o suggests that the stream function must have the following form:

$$\tilde{\psi} = A\tilde{r}^{1.5445}(cos(0.3415\pi)cos(1.5445\theta) - cos(1.158\pi)cos(0.4555\theta)). \tag{C.4}$$

Using the general form of the stream function solution (equation C.3), the aim here is to find an approximate analytical expression for the stream function which as

$r \to 0$ the solution asymptotes to the exact solution presented by Moffatt (1964) (i.e. equation C.4). One should note that $1 < m < 3$, which implies that the velocity is not singular at $\tilde{r} = 0$ and the velocity gradient has a bounded value far from the corner. Equation C.4 suggests that as $\tilde{r} \to 0$ the stream function must have wave numbers (the m parameter in equation C.3) of 0.4555 and 1.5445. Using the suggested values for m in equation C.3, the stream function will appear in the following form:

$$\tilde{\psi} = A\tilde{r}^{1.5445}(cos(0.3415\pi)cos(1.5445\theta) - cos(1.158\pi)cos(0.4555\theta)) + B\tilde{r}^{2.4555}cos(0.4555\theta). \tag{C.5}$$

Considering the following constraints:

$$\tilde{U_\theta} \mid_{\tilde{r}=\tilde{L}} = 0, \tag{C.6}$$

$$\int_0^{\tilde{L}} \tilde{U_\theta} d\tilde{r} = \frac{1}{2}\tilde{U_B}\tilde{W}. \tag{C.7}$$

The unknown constants can then be calculated as:

$$A = \frac{0.994\tilde{W}\tilde{U}_B}{\tilde{L}^{1.5445}}, \qquad B = \frac{0.848\tilde{W}\tilde{U}_B}{\tilde{L}^{2.4555}}, \tag{C.8}$$

using equation C.1, one can then calculate the components of the velocity vector along the line $\theta = 0$ as:

$$\tilde{U_\theta} = 3.5551\tilde{U}_B(\frac{\tilde{r}}{\tilde{W}})^{0.5445} - 4.8749\tilde{U}_B(\frac{\tilde{r}}{\tilde{W}})^{1.4555}, \qquad \tilde{U_r} = 0. \tag{C.9}$$

A comparison between the presented analytical solution and the numerical result is shown in Figure C.1 where a good agreement can be observed.

Knowing the functional form of the velocity (equation C.5), the curvature of the streamline may be calculated as (Haward et al., 2016a; Cruz et al., 2016):

$$\tilde{\Re} = (\mid \tilde{\boldsymbol{u}} \mid)^3 / (\mid \tilde{\boldsymbol{u}} \times \frac{D\tilde{\boldsymbol{u}}}{D\tilde{t}} \mid), \tag{C.10}$$

where $\frac{D\tilde{\boldsymbol{u}}}{D\tilde{t}}$ is the material derivative of the velocity vector.
Using the definition of the stream function, one can calculate $1/\Re$ as follows:

$$\frac{1}{\tilde{\Re}} = \frac{1.538(\tilde{L})^{0.911} - 3.811\tilde{r}^{0.911}}{(4.163(\tilde{L})^{0.911} - 4.163\tilde{r}^{0.911})\tilde{r}}. \tag{C.11}$$

One should notice that the present analytical solution is only an approximate solution for creeping Newtonian fluid flow between the corner of the cross-slot geometry and the stagnation point and so the obtained stream function does not satisfy the boundary conditions at the walls and does not present a correct θ dependency away from $\theta = 0$.

To include the effect of the cylinder at the center of the cross-slot geometry, we consider the diagonal gap length $\tilde{L}$ to be:

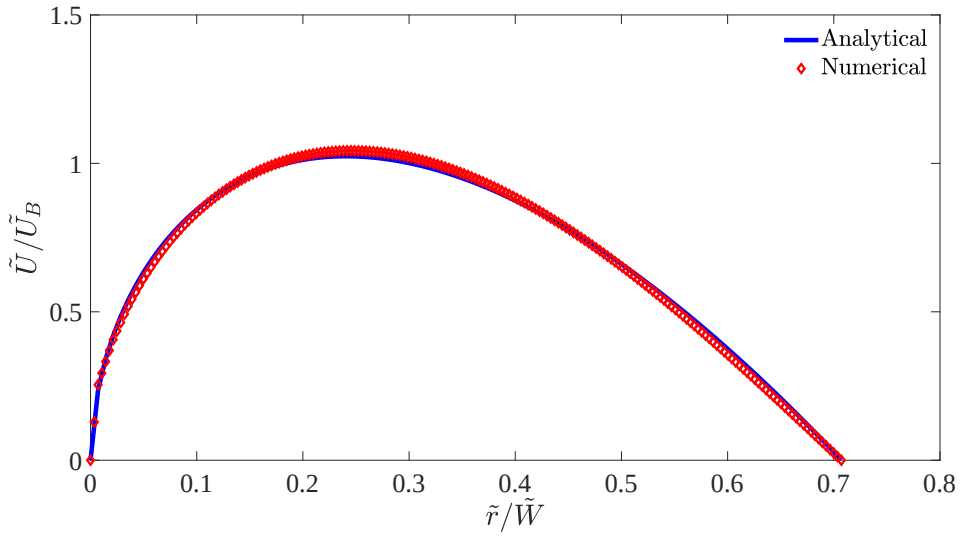

Figure C.1: Velocity distribution along the radial direction at $\theta = 0$ for both the analytical and numerical simulations for standard cross-slot, Newtonian fluid and $Re = 0.01$.

$$\tilde{L} = \frac{\sqrt{2}}{2}\tilde{W} - \frac{\tilde{D}}{2}. \tag{C.12}$$

Using equation C.12 and some simplification with a Taylor expansion around the corner of the cross-slot geometry, the $1/\tilde{\Re}$ term can be expressed as:

$$\frac{1}{\tilde{\Re}} = \frac{0.369}{\tilde{W}(\frac{\tilde{r}}{\tilde{W}})}(1-3.388(\frac{\tilde{r}}{\tilde{W}})^{0.911}(1+0.6492\Phi))(1+1.366(\frac{\tilde{r}}{\tilde{W}})^{0.911}(1+0.642\Phi)). \tag{C.13}$$

Here it is assumed that, prior to instability, viscoelasticity does not significantly affect the scaling correlation between the streamline curvature and the blockage ratio and will proceed to scale the M parameter with the blockage ratio parameter based on equation C.13. In the end the accuracy of this hypothesis is checked by plotting the obtained approximate analytical expression with the numerical results.

For an Oldroyd-B fluid, assuming steady-state simple shear, the second term on the right hand side of equation 1.2 can be simplified to:

$$\frac{\tilde{\tau}_{11}}{\tilde{\eta}_0\tilde{\dot{\gamma}}} = 2(1-\tilde{\beta})\tilde{\lambda}\tilde{\dot{\gamma}}. \tag{C.14}$$

Considering $\tilde{U}_B$ as the reference velocity, and using the formulated $\tilde{\Re}$ parameter as the reference length (i.e. equation 4.5), after some simplifications, one can state:

$$\frac{1}{Wi_c} = \frac{a\sqrt{2(1-\beta)}}{M_c} + \Phi^2\frac{b\sqrt{2(1-\beta)}}{M_c} \equiv a^* + b^*\Phi^2 \tag{C.15}$$

so that a plot of the reciprocal of the critical condition ($1/Wi_c$) against Φ^2 should be linear with intercept a^* and slope b^* (Figure 4.23, shows this plot confirming the approximate analysis).

Appendix D

Effect of extensibility parameter in sPTT model in the modified cross-slot geometry

In this Appendix, the effect of the extensibility parameter α of the sPTT model on the purely-elastic symmetry-breaking instability of cross-slot problem is investigated. In the limiting case where $\alpha \to 0$ the sPTT model reduces to the Oldroyd-B model which predicts a constant viscosity for the viscoelastic materials and the elastic stress in a pure shear flow can be scaled as $2\tilde{\lambda}\tilde{\eta}_p\tilde{\dot{\gamma}}^2$. In the sPTT model, for a non-zero value of α, due to shear-thinning properties of viscosity, the magnitude of first normal-stress difference reduces and scales as $2\tilde{\lambda}\tilde{\eta}_p\tilde{\dot{\gamma}}^n$, where $n < 2$. This matter suggests that the local value of the Weissenberg number (the ratio of elastic to viscous stress) reduces as the α parameter increases once the flow is subject to a constant shear rate. In Figure D.1 the variation of the asymmetry parameter versus the Wi number for different values of α are plotted, showing a supercritical growth near the bifurcation point. As can be seen, by increasing the extensibility parameter the critical value of the Weissenberg number for the onset of symmetry-breaking instability is delayed to higher values which is a consequence of the shear-thinning of the first normal-stress difference. In Figure D.2, the variation of the critical Weissenberg number Wi_{cr} with the α parameter is shown.

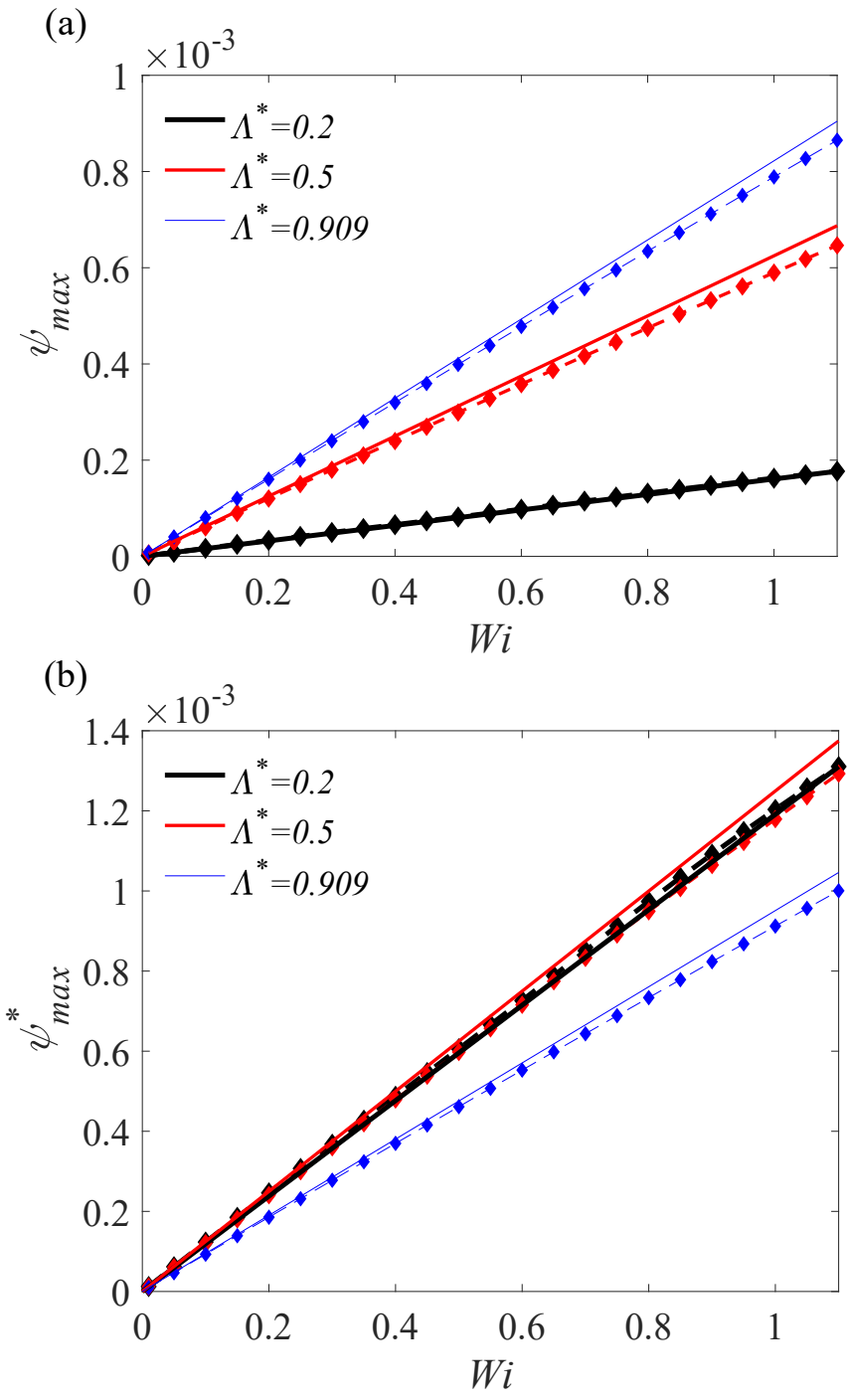

Figure D.1: Effect of extensibility parameter on symmetry-breaking instability of flow for $\Phi = 50\%$, $\beta = 1/9$.

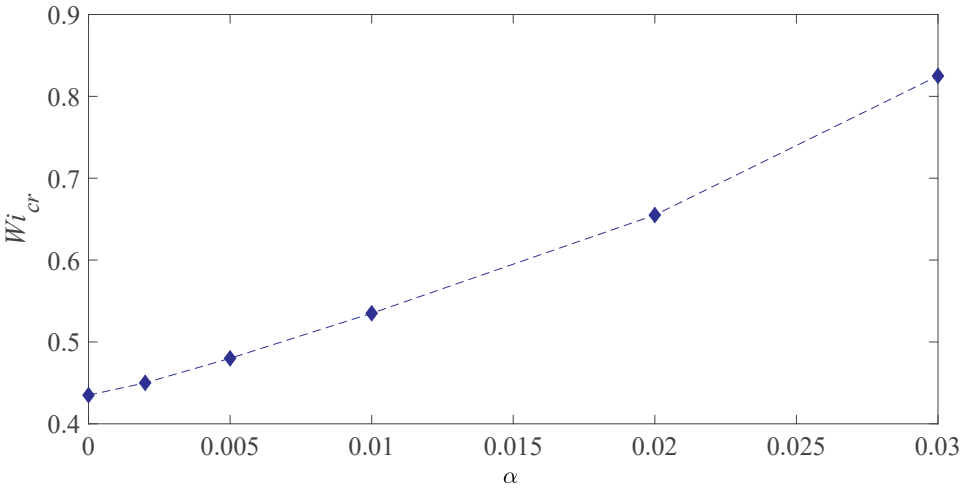

Figure D.2: Effect of extensibility parameter on critical Weissenberg number for $\Phi = 50\%, \beta = 1/9$.

Appendix E

2D simulations using the FENE-P model in the standard cross-slot geometry

In this Appendix, the FENE-P model is used as an additional constitutive equation to match the rheological properties of our model with the sPTT constitutive equation. Expanding the upper-convective derivative in equation 2.8, the FENE-P model can be rewritten as:

$$\tilde{\tau} + \tilde{\lambda}((\overset{\nabla}{\tilde{\boldsymbol{\tau}}}\ \frac{1}{f_2}) + \tilde{\boldsymbol{\tau}}(\overset{\nabla}{\frac{1}{f_2}})) = \frac{a\tilde{\eta}_p}{f_2}(\nabla\tilde{\boldsymbol{u}} + \nabla\tilde{\boldsymbol{u}}^T) - a\tilde{\eta}_p(\frac{D}{D\tilde{t}}(\frac{1}{f_2}))\boldsymbol{I}. \tag{E.1}$$

In ideal steady-state shear/extensional flows, the term $(\overset{\nabla}{\frac{1}{f_2}})$ is equal to zero and in the limit where L^2 finds a large value, the FENE-P model reduces to (Oliveira, 2009):

$$(1 + \frac{\tilde{\lambda}(Tr(\tilde{\boldsymbol{\tau}}))}{\tilde{\eta}_p L^2})\tilde{\boldsymbol{\tau}} + \tilde{\lambda}\ \overset{\nabla}{\tilde{\boldsymbol{\tau}}} = \tilde{\eta_p}(\nabla\tilde{\boldsymbol{u}} + \nabla\tilde{\boldsymbol{u}}^T). \tag{E.2}$$

This issue suggests that in "viscometric" flows, assuming $L^2 >> 1$, both the FENE-P and sPTT models are identical when $\alpha = \frac{1}{L^2}$ (Cf Equation E.2 and equations 2.6). In Figure E.1, this point is illustrated by plotting viscometric functions of both the SPTT and FENE-P models with $\alpha = 2e-4$ and $L^2 = 5000$, respectively, with $\beta = 1/9$. Simulations with $L^2 = 5000$ and $\alpha = 2e-4$ parameters shown in Figure E.2 suggests that once the viscometric functions are fit in between two models the instability is triggered at almost same critical value of the Weissenberg number which may, at a first glance, suggest that the critical condition in which the instability is triggered is related to the steady-state viscometric properties of the model.

Here, one should note that very large values of L^2 in FENE-P and very small values of α in sPTT models may potentially conceal the difference between these two models since in the limit $L^2 \to \infty$ or $\alpha \to 0$ both the FENE-P and sPTT models will reduce to the Oldroyd-B model (Bird et al., 1987).

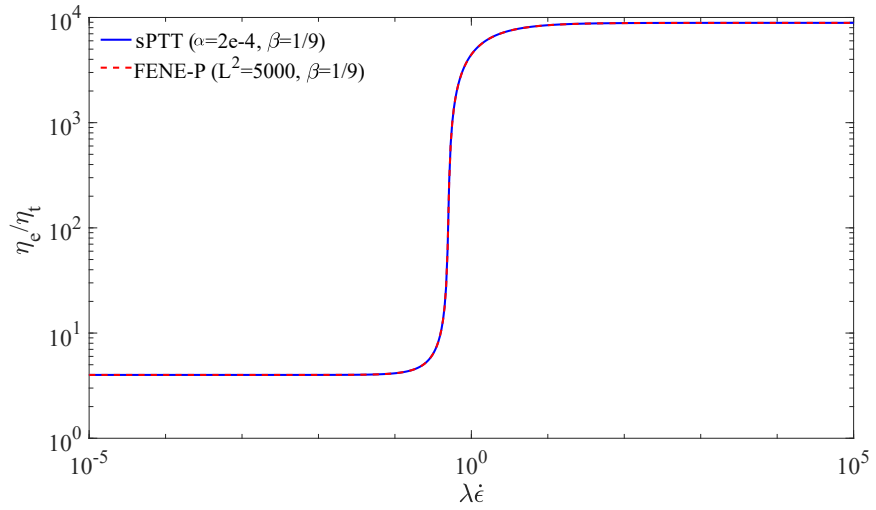

(a)

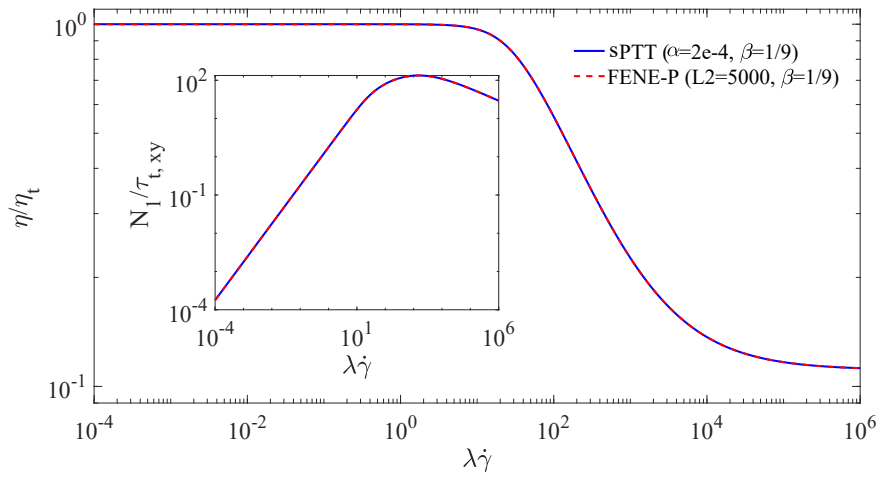

(b)

Figure E.1: Comparison of rheological properties; (a) elongational viscosity, (b) shear viscosity and the first normal-stress, between sPTT ($\alpha = 2e-4$) and FENE-P ($L^2 = 5000$) models with $\beta = 1/9$, in standard pure shear and planar elongational flows.

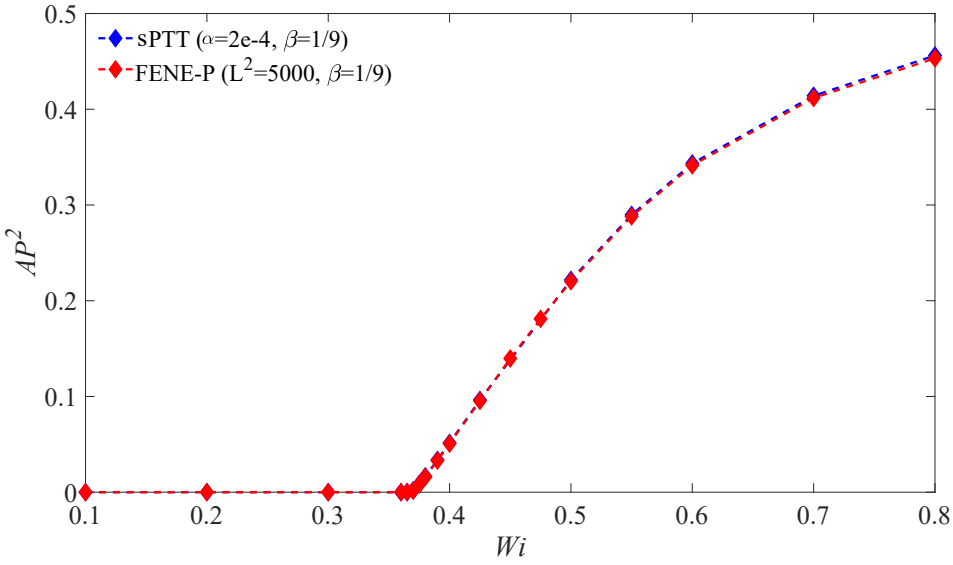

Figure E.2: Variation of Asymmetry parameter with the Weissenberg number for sPTT ($\alpha = 2e-4$) and FENE-P ($L^2 = 5000$) models with $\beta = 1/9$ in a standard cross-slot geometry.

In another attempt to better investigate the effect of rheological properties of the fluids, the viscometric functions using a smaller value of L^2 are fit and a larger value of the α parameter in these two models is used. Figure E.3, shows the fit obtained between viscometric function of SPTT model with $\alpha = 0.02$ and FENE-P model with $L^2 = 58$ at a fixed value of $\beta = 0.2$. Interestingly, as shown in Figure E.4, although the steady-state viscometric functions between the two constitutive equations are in good agreement, the critical values of the Weissenberg number for the onset of the instability are significantly different in these two models. This issue provides further evidence that the kinematic properties of the flow triggering the instability are, most probably, related to the non-homogeneous kinematics properties of the complex flows and not solely related to the viscometric flows at the corners or stagnation point themselves.

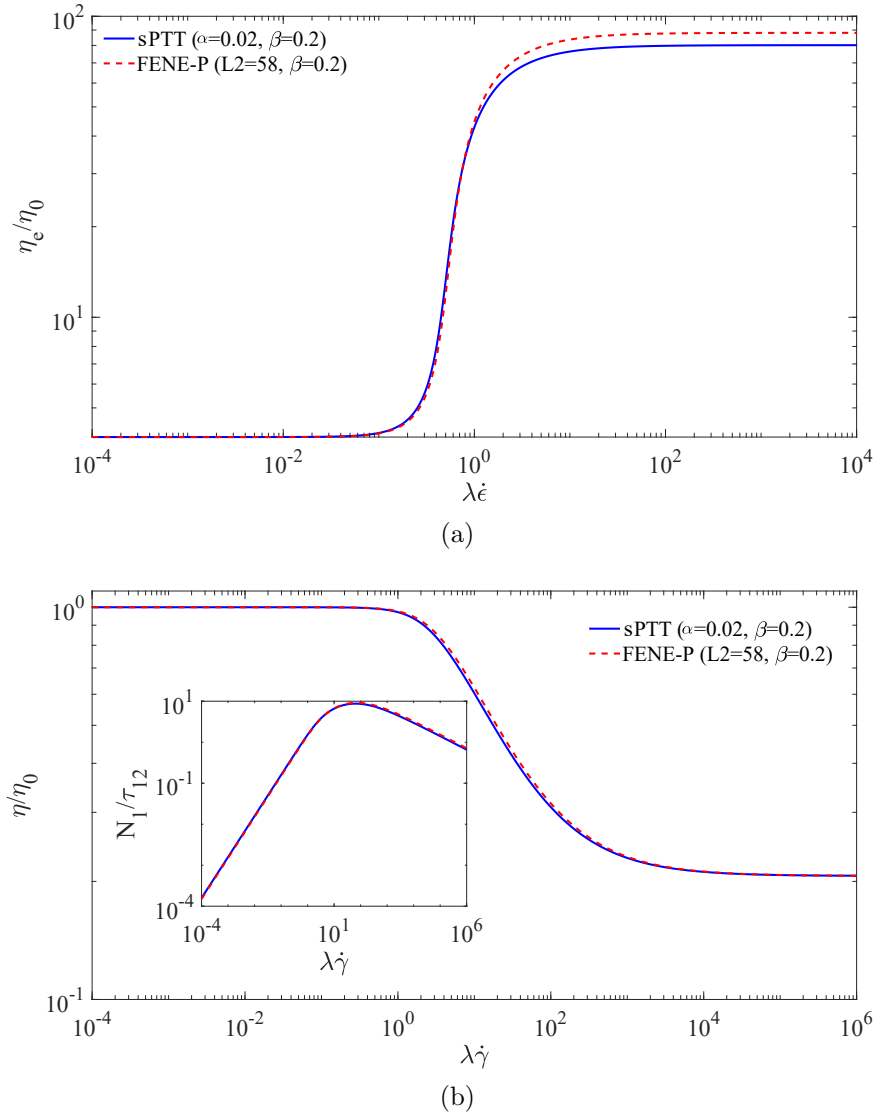

Figure E.3: Comparison of rheological properties; (a) elongational viscosity, (b) shear viscosity and the first normal-stress, between sPTT ($\alpha = 0.02$) and FENE-P ($L^2 = 58$) models with $\beta = 0.2$, in standard pure shear and planar elongational flows.

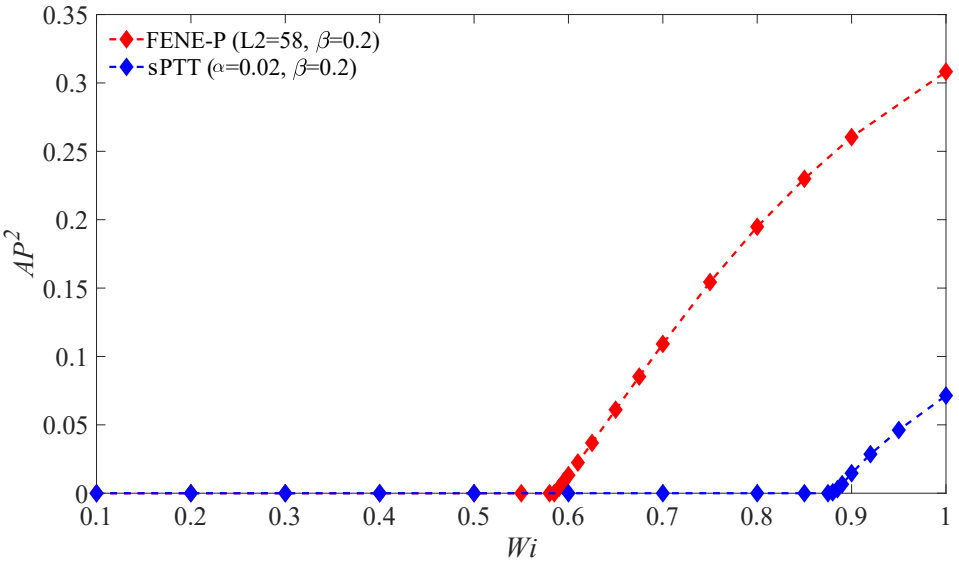

Figure E.4: Variation of Asymmetry parameter with the Weissenberg number for sPTT ($\alpha = 0.02$) and FENE-P ($L^2 = 58$) models with $\beta = 0.2$ in a standard cross-slot geometry.

References

DE Abbott and SJ Kline. Experimental investigation of subsonic turbulent flow over single and double backward facing steps. *Journal of Basic Engineering*, 84(3):317–325, 1962.

WM Abed, AF Domingues, RJ Poole, and DJC Dennis. Heat transfer enhancement in a cross-slot micro-geometry. *International Journal of Thermal Sciences*, 121:249–265, 2017.

AM Afonso, MA Alves, and FT Pinho. Purely elastic instabilities in three-dimensional cross-slot geometries. *Journal of Non-Newtonian Fluid Mechanics*, 165(13-14):743–751, 2010.

AM Afonso, FT Pinho, and MA Alves. The kernel-conformation constitutive laws. *Journal of Non-Newtonian Fluid Mechanics*, 167:30–37, 2012.

M Akiyama and KC Cheng. Graetz problem in curved pipes with uniform wall heat flux. *Applied Scientific Research*, 29(1):401–418, 1974.

N Ali, M Sajid, Z Abbas, and T Javed. Non-Newtonian fluid flow induced by peristaltic waves in a curved channel. *European Journal of Mechanics-B/Fluids*, 29(5):387–394, 2010.

MA Alves and RJ Poole. Divergent flow in contractions. *Journal of Non-Newtonian Fluid Mechanics*, 144(2-3):140–148, 2007.

MA Alves, FT Pinho, and PJ Oliveira. The flow of viscoelastic fluids past a cylinder: finite-volume high-resolution methods. *Journal of Non-Newtonian Fluid Mechanics*, 97(2-3):207–232, 2001.

K Arora, R Sureshkumar, and B Khomami. Experimental investigation of purely elastic instabilities in periodic flows. *Journal of Non-Newtonian Fluid Mechanics*, 108(1-3): 209–226, 2002.

PE Arratia, CC Thomas, J Diorio, and J P Gollub. Elastic instabilities of polymer solutions in cross-channel flow. *Physical Review Letters*, 96(14):144502, 2006.

N Balci, B Thomases, M Renardy, and C R Doering. Symmetric factorization of the conformation tensor in viscoelastic fluid models. *Journal of Non-Newtonian Fluid Mechanics*, 166(11):546–553, 2011.

BR Baliga and SV Patankar. A control volume finite-element method for two-dimensional fluid flow and heat transfer. *Numerical Heat Transfer*, 6(3):245–261, 1983.

I Barmak, A Gelfgat, H Vitoshkin, A Ullmann, and N Brauner. Stability of stratified two-phase flows in horizontal channels. *Physics of Fluids*, 28(4):044101, 2016.

TB Benjamin. Bifurcation phenomena in steady flows of a viscous fluid. i. theory. *Proceedings of the Royal Society of London. A. Mathematical and Physical Sciences*, 359(1696):1–26, 1978a.

TB Benjamin. Bifurcation phenomena in steady flows of a viscous fluid ii. experiments. *Proceedings of the Royal Society of London. A. Mathematical and Physical Sciences*, 359(1696):27–43, 1978b.

JF Berret, G Porte, and JP Decruppe. Inhomogeneous shear flows of wormlike micelles: ma master dynamic phase diagram. *Physical Review E*, 55(2):1668, 1997.

S Berti, A Bistagnino, G Boffetta, A Celani, and S Musacchio. Two-dimensional elastic turbulence. *Physical Review E*, 77(5):055306, 2008.

RB Bird, PJ Dotson, and NL Johnson. Polymer solution rheology based on a finitely extensible bead—spring chain model. *Journal of Non-Newtonian Fluid Mechanics*, 7(2-3):213–235, 1980.

RB Bird, RC Armstrong, and O Hassager. *Dynamics of Polymeric Liquids*. vol. 1: Fluid mechanics. 1987.

C Bisgaard. Velocity fields around spheres and bubbles investigated by laser-doppler anemometry. *Journal of Non-Newtonian Fluid Mechanics*, 12(3):283–302, 1983.

DV Boger. A highly elastic constant-viscosity fluid. *Journal of Non-Newtonian Fluid Mechanics*, 3(1):87–91, 1977.

DV Boger and K Walters. *Rheological Phenomena in Focus*, volume 4. Elsevier, 2012.

Jeremiah U Brackbill, Douglas B Kothe, and Charles Zemach. A continuum method for modeling surface tension. *Journal of computational physics*, 100(2):335–354, 1992.

T Burghelea, E Segre, and V Steinberg. Elastic turbulence in von Karman swirling flow between two disks. *Physics of fluids*, 19(5):053104, 2007.

W Cherdron, F Durst, and JH Whitelaw. Asymmetric flows and instabilities in symmetric ducts with sudden expansions. *Journal of Fluid Mechanics*, 84(1):13–31, 1978.

M Couette. On a new apparatus for the study of friction of fluids. *Compt. Rend*, 107: 388–390, 1888.

FA Cruz, RJ Poole, AM Afonso, FT Pinho, PJ Oliveira, and MA Alves. Influence of channel aspect ratio on the onset of purely-elastic flow instabilities in three-dimensional planar cross-slots. *Journal of Non-Newtonian Fluid Mechanics*, 227: 65–79, 2016.

PA Dashner and WE VanArsdale. A phenomenological theory for elastic fluids. *Journal of Non-Newtonian Fluid Mechanics*, 8(1-2):59–67, 1981.

AR Davies and J Devlin. On corner flows of Oldroyd-B fluids. *Journal of Non-Newtonian Fluid Mechanics*, 50(2-3):173–191, 1993.

M Davoodi and M Norouzi. An investigation on the motion and deformation of viscoelastic drops descending in another viscoelastic media. *Physics of Fluids*, 28(10): 103103, 2016.

T Alziary De Roquefort and G Grillaud. Computation of taylor vortex flow by a transient implicit method. *Computers & Fluids*, 6(4):259–269, 1978.

WR Dean. Note on the motion of fluid in a curved pipe. *The London, Edinburgh, and Dublin Philosophical Magazine and Journal of Science*, 4(20):208–223, 1927.

WR Dean. The streamline motion of fluid in a curved pipe. *Phil. Mag.*, 5:673–693, 1928.

WR Dean and PE Montagnon. On the steady motion of viscous liquid in a corner. In *Mathematical Proceedings of the Cambridge Philosophical Society*, volume 45, pages 389–394. Cambridge University Press, 1949.

RJ Donnelly and D Fultz. Experiments on the stability of viscous flow between rotating cylinders ii. visual observations. *Proceedings of the Royal Society of London. Series A. Mathematical and Physical Sciences*, 258(1292):101–123, 1960.

D Drikakis. Bifurcation phenomena in incompressible sudden expansion flows. *Physics of Fluids*, 9(1):76–87, 1997.

WA Eckerle and LS Langston. Horseshoe vortex formation around a cylinder. In *ASME 1986 International Gas Turbine Conference and Exhibit*, pages V001T01A109–V001T01A109. American Society of Mechanical Engineers, 1986.

B Eckhardt, TM Schneider, B Hof, and J Westerweel. Turbulence transition in pipe flow. *Annual Review of Fluid Mechanics*, 39:447–468, 2007.

JL Ericksen. Overdetermination of the speed in rectilinear motion of non-Newtonian fluids. *Quarterly of Applied Mathematics*, 14(3):318–321, 1956.

J Eustice. Experiments on stream-line motion in curved pipes. *Proceedings of the Royal Society of London. Series A, Containing Papers of a Mathematical and Physical Character*, 85(576):119–131, 1911.

Y Fan, RI Tanner, and N Phan-Thien. Fully developed viscous and viscoelastic flows in curved pipes. *Journal of Fluid Mechanics*, 440:327–357, 2001.

MA Fardin, C Perge, and N Taberlet. "The hydrogen atom of fluid dynamics"–introduction to the Taylor–Couette flow for soft matter scientists. *Soft Matter*, 10 (20):3523–3535, 2014.

R Fattal and R Kupferman. Constitutive laws for the matrix-logarithm of the conformation tensor. *Journal of Non-Newtonian Fluid Mechanics*, 123(2-3):281–285, 2004.

R Fattal and R Kupferman. Time-dependent simulation of viscoelastic flows at high Weissenberg number using the log-conformation representation. *Journal of Non-Newtonian Fluid Mechanics*, 126(1):23–37, 2005.

RA Figueiredo, Cassio M Oishi, AM Afonso, IVM Tasso, and José Alberto Cuminato. A two-phase solver for complex fluids: Studies of the weissenberg effect. *International Journal of Multiphase Flow*, 84:98–115, 2016.

WH Finlay. Perturbation expansion and weakly nonlinear analysis for two-dimensional vortices in curved or rotating channels. *Physics of Fluids A: Fluid Dynamics*, 1(5): 854–860, 1989.

Marianne M Francois, Sharen J Cummins, Edward D Dendy, Douglas B Kothe, James M Sicilian, and Matthew W Williams. A balanced-force algorithm for continuous and sharp interfacial surface tension models within a volume tracking framework. *Journal of Computational Physics*, 213(1):141–173, 2006.

K Gardner, ER Pike, MJ Miles, A Keller, and K Tanaka. Photon-correlation velocimetry of polystyrene solutions in extensional flow fields. *Polymer*, 23(10):1435–1442, 1982.

H Giesekus. On the stability of flow of viscoelastic fluids i: plane and circular couette flow. *Rheologica Acta*, 5:239, 1966.

H Giesekus. On instabilities in poiseuille and couette flow of viscoelastic fluids. *Progress in Heat and Mass Transfer*, 5:187, 1972.

H Görtler. Einige bemerkungen über strömungen in rotierenden flüssigkeiten. *ZAMM-Journal of Applied Mathematics and Mechanics/Zeitschrift für Angewandte Mathematik und Mechanik*, 24(5-6):210–214, 1944.

AE Green and RS Rivlin. Steady flow of non-Newtonian fluids through tubes. In *Collected Papers of RS Rivlin*, pages 1931–1940. Springer, 1997.

Christopher J Greenshields. Openfoam user guide. *OpenFOAM Foundation Ltd, version*, 3(1):47, 2015.

AK Gurnon, CR Lopez-Barron, APR Eberle, L Porcar, and NJ Wagner. Spatiotemporal stress and structure evolution in dynamically sheared polymer-like micellar solutions. *Soft Matter*, 10(16):2889–2898, 2014.

S J Haward, MSN Oliveira, MA Alves, and GH McKinley. Optimized cross-slot flow geometry for microfluidic extensional rheometry. *Physical Review Letters*, 109(12): 128301, 2012a.

SJ Haward, MSN Oliveira, MA Alves, and GH McKinley. Optimized cross-slot flow geometry for microfluidic extensional rheometry. *Physical Review Letters*, 109(12): 128301, 2012b.

SJ Haward, GH McKinley, and AQ Shen. Elastic instabilities in planar elongational flow of monodisperse polymer solutions. *Scientific Reports*, 6:33029, 2016a.

SJ Haward, RJ Poole, MA Alves, PJ Oliveira, N Goldenfeld, and AQ Shen. Tricritical spiral vortex instability in cross-slot flow. *Physical Review E*, 93(3):031101, 2016b.

T Hayat, S Noreen, and A Alsaedi. Effect of an induced magnetic field on peristaltic flow of non-newtonian fluid in a curved channel. *Journal of Mechanics in Medicine and Biology*, 12(03):1250058, 2012.

D Hill. A theoretical approach for analyzing the restabilization of wakes. In *30th Aerospace Sciences Meeting and Exhibit*, page 67, 1992.

EJ Hinch. The flow of an Oldroyd fluid around a sharp corner. *Journal of Non-Newtonian Fluid Mechanics*, 50(2-3):161–171, 1993.

CW Hirt and BD Nichols. Volume of fluid (vof) method for the dynamics of free boundaries. *Journal of Computational Physics*, 39(1):201–225, 1981.

AP Hooper and WGC Boyd. Shear-flow instability at the interface between two viscous fluids. *Journal of Fluid Mechanics*, 128:507–528, 1983.

MM Hoque, MM Alam, M Ferdows, and OA Bég. Numerical simulation of dean number and curvature effects on magneto-biofluid flow through a curved conduit. *Proceedings of the Institution of Mechanical Engineers, Part H: Journal of Engineering in Medicine*, 227(11):1155–1170, 2013.

Y Thomas Hu and A Lips. Kinetics and mechanism of shear banding in an entangled micellar solution. *Journal of Rheology*, 49(5):1001–1027, 2005.

CY Huang, CA Li, HY Wang, and TM Liou. The application of temperature-sensitive paints for surface and fluid temperature measurements in both thermal developing and fully developed regions of a microchannel. *Journal of Micromechanics and Microengineering*, 23(3):037001, 2013.

CY Huang, CA Li, BH Huang, and TM Liou. The study of temperature rise in a 90-degree sharp bend microchannel flow under constant wall temperature condition. *Journal of Mechanics*, 30(6):661–666, 2014.

D Jacqmin. Calculation of two-phase navier–stokes flows using phase-field modeling. *Journal of Computational Physics*, 155(1):96–127, 1999.

DF James. Boger fluids. *Annual Review of Fluid Mechanics*, 41:129–142, 2009.

W Jitchote and AM Robertson. Flow of second order fluids in curved pipes. *Journal of non-newtonian fluid mechanics*, 90(1):91–116, 2000.

YL Joo and ESG Shaqfeh. Viscoelastic Poiseuille flow through a curved channel: A new elastic instability. *Physics of Fluids A: Fluid Dynamics*, 3(9):2043–2046, 1991.

DD Joseph. *Fluid dynamics of viscoelastic liquids*. Springer-Verlag, New York, 1990.

Z Keshavarz-Motamed and L Kadem. 3d pulsatile flow in a curved tube with coexisting model of aortic stenosis and coarctation of the aorta. *Medical engineering & physics*, 33(3):315–324, 2011.

N Kockmann, C Föll, and P Woias. Flow regimes and mass transfer characteristics in static micromixers. In *Microfluidics, BioMEMS, and Medical Microsystems*, volume 4982, pages 319–330. International Society for Optics and Photonics, 2003.

V Kumar, M Aggarwal, and KDP Nigam. Mixing in curved tubes. *Chemical Engineering Science*, 61(17):5742–5753, 2006.

RR Lagnado and LG im Leal. Visualization of three-dimensional flow in a four-roll mill. *Experiments in Fluids*, 9(1-2):25–32, 1990.

RG Larson, ESG Shaqfeh, and SJ Muller. A purely elastic instability in taylor–couette flow. *Journal of Fluid Mechanics*, 218:573–600, 1990.

JS Lee, R Dylla-Spears, NP Teclemariam, and SJ Muller. Microfluidic four-roll mill for all flow types. *Applied physics letters*, 90(7):074103, 2007.

JY Lee, GG Fuller, NE Hudson, and XF Yuan. Investigation of shear-banding structure in wormlike micellar solution by point-wise flow-induced birefringence measurements. *Journal of Rheology*, 49(2):537–550, 2005.

AI Leonov. Nonequilibrium thermodynamics and rheology of viscoelastic polymer media. *Rheologica Acta*, 15(2):85–98, 1976.

J Leray and J Schauder. Topologie et équations fonctionnelles. In *Annales Scientifiques de l'École Normale Supérieure*, volume 51, pages 45–78, 1934.

S Lerouge, J Decruppe, and JF Berret. Correlations between rheological and optical properties of a micellar solution under shear banding flow. *Langmuir*, 16(16):6464–6474, 2000.

MW Liberatore, F Nettesheim, NJ Wagner, and L Porcar. Spatially resolved small-angle neutron scattering in the 1-2 plane: A study of shear-induced phase-separating wormlike micelles. *Physical Review E*, 73(2):020504, 2006.

CR López-Barrón, NJ Wagner, and L Porcar. Layering, melting, and recrystallization of a close-packed micellar crystal under steady and large-amplitude oscillatory shear flows. *Journal of Rheology*, 59(3):793–820, 2015.

F Magaletti, F Picano, M Chinappi, L Marino, and CM Casciola. The sharp-interface limit of the cahn–hilliard/navier–stokes model for binary fluids. *Journal of Fluid Mechanics*, 714:95–126, 2013.

A Mallock. Determination of the viscosity of water. *Proceedings of the Royal Society of London*, 45(273-279):126–132, 1889.

Olivier Marquet, Denis Sipp, and Laurent Jacquin. Sensitivity analysis and passive control of cylinder flow. *Journal of Fluid Mechanics*, 615:221–252, 2008.

JC Maxwell. On the dynamical theory of gases. *Phil. Trans. R. Soc. Lond.*, 157:49–88, 1867.

GH McKinley. Steady and transient motion of spherical particles in viscoelastic liquids. *Transport Processes in Bubble, Drops, and Particles*, pages 338–375, 2002.

GH McKinley, P Pakdel, and A Öztekin. Rheological and geometric scaling of purely elastic flow instabilities. *Journal of Non-Newtonian Fluid Mechanics*, 67:19–47, 1996a.

GH McKinley, P Pakdel, and A Öztekin. Rheological and geometric scaling of purely elastic flow instabilities. *Journal of Non-Newtonian Fluid Mechanics*, 67:19–47, 1996b.

R Mittal and G Iaccarino. Immersed boundary methods. *Annu. Rev. Fluid Mech.*, 37: 239–261, 2005.

HK Moffatt. Viscous and resistive eddies near a sharp corner. *Journal of Fluid Mechanics*, 18(1):1–18, 1964.

FA Morrison. *Understanding Rheology, Topics in Chemical Engineering*. Oxford University Press, New York, 2001.

F Moukalled, L Mangani, and M Darwish. The finite volume method in computational fluid dynamics. *An advanced introduction with OpenFoam® and Matlab®. Nueva York: Springer. Recuperado de http://www. gidropraktikum. narod. ru/Moukalled-et-al-FVM-OpenFOAM-Matlab. pdf*, 2016.

SJ Muller. Elastically-influenced instabilities in taylor-couette and other flows with curved streamlines: a review. *Korea-Australia Rheology Journal*, 20(3):117–125, 2008.

SJ Muller, RG Larson, and ESG Shaqfeh. A purely elastic transition in taylor-couette flow. *Rheologica Acta*, 28(6):499–503, 1989.

T Mullin. Experimental studies of transition to turbulence in a pipe. *Annual Review of Fluid Mechanics*, 43:1–24, 2011.

T Mullin, Y Toya, and SJ Tavener. Symmetry breaking and multiplicity of states in small aspect ratio taylor–couette flow. *Physics of Fluids*, 14(8):2778–2787, 2002.

T Myint-U and L Debnath. *Linear partial differential equations for scientists and engineers*. Springer Science & Business Media, 2007.

M Norouzi and N Biglari. An analytical solution for Dean flow in curved ducts with rectangular cross section. *Physics of Fluids*, 25(5):053602, 2013.

M Norouzi, MH Kayhani, C Shu, and MRH Nobari. Flow of second-order fluid in a curved duct with square cross-section. *Journal of Non-Newtonian Fluid Mechanics*, 165(7-8):323–339, 2010.

M Norouzi, A Emamian, and M Davoodi. An analytical and experimental study on dynamics of a circulating boger drop translating through newtonian fluids at inertia regime. *Journal of Non-Newtonian Fluid Mechanics*, 267:1–13, 2019.

JG Oldroyd. On the formulation of rheological equations of state. *Proceedings of the Royal Society of London. Series A. Mathematical and Physical Sciences*, 200(1063): 523–541, 1950.

M S N Oliveira. *Private Communication*, 2019.

PJ Oliveira. Alternative derivation of differential constitutive equations of the Oldroyd-B type. *Journal of Non-Newtonian Fluid Mechanics*, 160(1):40–46, 2009.

A Öztekin, B Alakus, and GH McKinley. Stability of planar stagnation flow of a highly viscoelastic fluid. *Journal of Non-Newtonian Fluid Mechanics*, 72(1):1–29, 1997.

P Pakdel and GH McKinley. Elastic instability and curved streamlines. *Physical Review Letters*, 77(12):2459, 1996.

P Pakdel and GH McKinley. Cavity flows of elastic liquids: purely elastic instabilities. *Physics of Fluids*, 10(5):1058–1070, 1998.

L Pan, A Morozov, C Wagner, and PE Arratia. Nonlinear elastic instability in channel flows at low reynolds numbers. *Physical Review Letters*, 110(17):174502, 2013.

CS Peskin. The fluid dynamics of heart valves: experimental, theoretical, and computational methods. *Annual Review of Fluid Mechanics*, 14(1):235–259, 1982.

A Peterlin. Optical effects in flow. *Annual Review of Fluid Mechanics*, 8(1):35–55, 1976.

N Phan-Thien and RI Tanner. A new constitutive equation derived from network theory. *Journal of Non-Newtonian Fluid Mechanics*, 2(4):353–365, 1977.

F Pimenta and MA Alves. Stabilization of an open-source finite-volume solver for viscoelastic fluid flows. *Journal of Non-Newtonian Fluid Mechanics*, 239:85–104, 2017.

RJ Poole, MA Alves, AP Afonso, FT Pinho, and PJ Oliveira. Purely-elastic flow instabilities in a microfluidic cross-slot geometry. In *AIChE Annual Meeting, Conference Proceedings*, 2007a.

RJ Poole, MA Alves, and PJ Oliveira. Purely elastic flow asymmetries. *Physical Review Letters*, 99(16):164503, 2007b.

RJ Poole, MA Alves, and PJ Oliveira. Purely elastic flow asymmetries. *Physical review letters*, 99(16):164503, 2007c.

RJ Poole, A Lindner, and MA Alves. Viscoelastic secondary flows in serpentine channels. *Journal of Non-Newtonian Fluid Mechanics*, 201:10–16, 2013.

RJ Poole, GN Rocha, and PJ Oliveira. A symmetry-breaking inertial bifurcation in a cross-slot flow. *Computers & Fluids*, 93:91–99, 2014a.

Rob Poole, Simon Haward, Paulo Oliveira, and Manuel Alves. Symmetry-breaking bifurcations and enhanced mixing in microfluidic cross-slots. In *APS Meeting Abstracts*, 2014b.

I Proudman and JRA Pearson. Expansions at small reynolds numbers for the flow past a sphere and a circular cylinder. *Journal of Fluid Mechanics*, 2(3):237–262, 1957.

B Purnode and MJ Crochet. Polymer solution characterization with the FENE-P model. *Journal of Non-Newtonian Fluid Mechanics*, 77(1-2):1–20, 1998.

M Reiner. A mathematical theory of dilatancy. *American Journal of Mathematics*, 67 (3):350–362, 1945.

O Reynolds. Xxix. an experimental investigation of the circumstances which determine whether the motion of water shall be direct or sinuous, and of the law of resistance in parallel channels. *Philosophical Transactions of the Royal society of London*, (174): 935–982, 1883.

RS Rivlin. The relation between the flow of non-newtonian fluids and turbulent newtonian fluids. *Quarterly of Applied Mathematics*, 15(2):212–215, 1957.

RS Rivlin. The hydrodynamics of non-Newtonian fluids. i. In *Collected Papers of RS Rivlin*, pages 1842–1863. Springer, 1997.

RS Rivlin and JL Ericksen. Stress-deformation relations for isotropic materials. In *Collected Papers of RS Rivlin*, pages 911–1013. Springer, 1997.

AM Robertson and SJ Muller. Flow of Oldroyd-B fluids in curved pipes of circular and annular cross-section. *International journal of non-linear mechanics*, 31(1):1–20, 1996.

GN Rocha, RJ Poole, MA Alves, and PJ Oliveira. On extensibility effects in the cross-slot flow bifurcation. *Journal of Non-Newtonian Fluid Mechanics*, 156(1-2):58–69, 2009.

LE Rodd, TP Scott, JJ Cooper-White, and GH McKinley. Capillary break-up rheometry of low-viscosity elastic fluids. *Applied Rheology*, 15(1):12–27, 2005.

D Ross, M Gaitan, and LE Locascio. Temperature measurement in microfluidic systems using a temperature-dependent fluorescent dye. *Analytical Chemistry*, 73(17):4117–4123, 2001.

JP Rothstein and GH McKinley. Extensional flow of a polystyrene boger fluid through a 4: 1: 4 axisymmetric contraction/expansion. *Journal of Non-Newtonian Fluid Mechanics*, 86(1-2):61–88, 1999.

W Rybczynski. Uber die fortschreitende bewegung einer flussigen kugel in einem zahen medium. *Bull. Acad. Sci. Cracovie A*, 1:40–46, 1911.

M Sahin. Parallel large-scale numerical simulations of purely-elastic instabilities behind a confined circular cylinder in a rectangular channel. *Journal of Non-Newtonian Fluid Mechanics*, 195:46–56, 2013.

DG Schaeffer. Qualitative analysis of a model for boundary effects in the taylor problem. In *Mathematical Proceedings of the Cambridge Philosophical Society*, volume 87, pages 307–337. Cambridge University Press, 1980.

ESG Shaqfeh. Purely elastic instabilities in viscometric flows. *Annual Review of Fluid Mechanics*, 28(1):129–185, 1996.

KR Shull, CM Flanigan, and AJ Crosby. Fingering instabilities of confined elastic layers in tension. *Physical Review Letters*, 84(14):3057, 2000.

J Soulages, MSN Oliveira, PC Sousa, MA Alves, and GH McKinley. Investigating the stability of viscoelastic stagnation flows in t-shaped microchannels. *Journal of Non-Newtonian Fluid Mechanics*, 163(1-3):9–24, 2009.

PC Sousa, FT Pinho, and MA Alves. Purely-elastic flow instabilities and elastic turbulence in microfluidic cross-slot devices. *Soft matter*, 14(8):1344–1354, 2018.

RG Sousa, RJ Poole, AM Afonso, FT Pinho, PJ Oliveira, A Morozov, and MA Alves. Lid-driven cavity flow of viscoelastic liquids. *Journal of Non-Newtonian Fluid Mechanics*, 234:129–138, 2016.

PJ Strykowski and KR Sreenivasan. On the formation and suppression of vortex 'shedding'at low reynolds numbers. *Journal of Fluid Mechanics*, 218:71–107, 1990.

YY Su and B Khomami. Purely elastic interfacial instabilities in superposed flow of polymeric fluids. *Rheologica Acta*, 31(5):413–420, 1992.

S Sugiyama, T Hayashi, and K Yamazaki. Flow characteristics in the curved rectangular channels: Visualization of secondary flow. *Bulletin of JSME*, 26(216):964–969, 1983.

R Tagg. The Couette-Taylor problem. *Nonlinear Science Today*, 4(3):1–25, 1994.

RI Tanner. *Engineering rheology*, volume 52. OUP Oxford, 2000.

GI Taylor. Stability of a viscous liquid contained between two rotating cylinders. *Philosophical Transactions of the Royal Society of London. Series A, Containing Papers of a Mathematical or Physical Character*, 223(605-615):289–343, 1923.

GI Taylor. The formation of emulsions in definable fields of flow. *Proceedings of the Royal Society of London. Series A, containing papers of a mathematical and physical character*, 146(858):501–523, 1934.

TD Taylor and A Acrivos. On the deformation and drag of a falling viscous drop at low Reynolds number. *Journal of Fluid Mechanics*, 18(3):466–476, 1964.

V Theofilis, PW Duck, and J Owen. Viscous linear stability analysis of rectangular duct and cavity flows. *Journal of Fluid Mechanics*, 505:249–286, 2004.

G Tryggvason, B Bunner, A Esmaeeli, D Juric, N Al-Rawahi, W Tauber, J Han, S Nas, and Y-J Jan. A front-tracking method for the computations of multiphase flow. *Journal of computational physics*, 169(2):708–759, 2001.

HK Versteeg and W Malalasekera. *An introduction to computational fluid dynamics: the finite volume method*. Pearson education, 2007.

K Walters. *Rheometry*. Halsted Press, 1975.

K Walters and RI Tanner. The motion of a sphere through an elastic fluid. *Transport Processes in Bubbles, Drops, and Particles, Hemisphere, New York, NY*, 1:992, 1992.

F Wendt. Turbulente strömungen zwischen zwei rotierenden konaxialen zylindern. *Archive of Applied Mechanics*, 4(6):577–595, 1933.

HJ Wilson and JM Rallison. Short wave instability of co-extruded elastic liquids with matched viscosities. *Journal of non-newtonian fluid mechanics*, 72(2-3):237–251, 1997.

KH Winters. A bifurcation study of laminar flow in a curved tube of rectangular cross-section. *Journal of Fluid Mechanics*, 180:343–369, 1987.

C-S Yih. Instability due to viscosity stratification. *Journal of Fluid Mechanics*, 27(2): 337–352, 1967.

P Yue, JJ Feng, C Liu, and J Shen. A diffuse-interface method for simulating two-phase flows of complex fluids. *Journal of Fluid Mechanics*, 515:293–317, 2004.

P Yue, J Dooley, and JJ Feng. A general criterion for viscoelastic secondary flow in pipes of noncircular cross section. *Journal of Rheology*, 52(1):315–332, 2008.

J Zilz, RJ Poole, MA Alves, D Bartolo, B Levaché, and A Lindner. Geometric scaling of a purely elastic flow instability in serpentine channels. *Journal of Fluid Mechanics*, 712:203–218, 2012.

J Zilz, C Schäfer, C Wagner, RJ Poole, MA Alves, and A Lindner. Serpentine channels: micro-rheometers for fluid relaxation times. *Lab on a Chip*, 14(2):351–358, 2014.